DEVELOPMENT OF MULTIPLEXABLE BIOSENSORS TO QUANTIFY THE SPATIOTEMPORAL DYNAMICS OF RHO GTPASES AND PROTEIN KINASES IN THE SAME LIVING CELL

Chia-Wen Hsu

A dissertation submitted to the faculty of the University of North Carolina at Chapel Hill in partial fulfillment of the requirements for the degree of Doctor of Philosophy in the Division of Chemical Biology and Medicinal Chemistry at the Eshelman School of Pharmacy

Chapel Hill
2012

Approved by:

Klaus M. Hahn, Ph.D.

David S. Lawrence, Ph.D.

Alexander Tropsha, Ph.D.

Brian Kuhlman, Ph.D.

Qisheng Zhang, Ph.D.

ABSTRACT

CHIA-WEN HSU: Development of Multiplexable Biosensors to Quantify the
Spatiotemporal Dynamics of Rho GTPases and Protein Kinases in the Same Living Cell
(Under the direction of Dr. Klaus M. Hahn)

Cell motility is a highly dynamic and heterogenous cellular process regulated by the coordination of multiple Rho GTPases, Src family kinases, and the mitogen-activated protein kinase (MAPK) cascades. However, it has been difficult to monitor more than two protein activities in the same cell due to the overlapping spectra of current biosensors and biological perturbations at high biosensor concentrations. Dye-based biosensors, which rely on an affinity scaffold that binds only to the activated conformation of the endogenous targets and an environment-sensing dye that changes its fluorescence properties to report the specific binder-target interactions, possess great potential to monitor multiple endogenous targets in the same cell. Here, I created novel environment-sensing dyes and exploited novel affinity scaffolds to develop multiplexable dye-based biosensors capable of quantifying the spatiotemporal dynamics of multiple Rho GTPases and protein kinases in the same cell.

Src protein kinase is an upstream regulator of the Cdc42 GTPase. The coordination of Cdc42 and Src at the leading edge has not been well characterized due to lack of multiplexable biosensors to monitor Cdc42 and Src activities in the same living cell. Therefore, I developed novel near infrared merocyanine dyes and a red ratiometric merocyanine dye with an intrinsic ratiometric response that can be used to construct

multiplexible biosensors. The relative timing and the subcellular localization of active Cdc42 and Src during leading edge dynamics and during pinocytosis were revealed using the new dyes.

Src also plays an important role in the MAPK-mediated cell motility. However, the precise roles of MAPKKs and MAPKs at the leading edge remain poorly characterized due to the lack of sensitive biosensors for each target. By taking advantage of the specific interactions between MAPKKs and MAPKs, I developed the first substrate-based biosensor designs to report the activity of endogenous MEK1/2 and MKK3/6. I also developed a sensitive ERK1/2 biosensor based on artificial binders through collaborations with the Plűckthun group.

This work will provide a foundation to study the crosstalk between Rho GTPases, Src family kinases and the MAPK cascades via multiplexed live cell imaging.

DEDICATION

To my parents Chun-Tseng Hsu and Yu-Yun Lin for their constant support and care throughout out my life.

To my husband Wei Sun for his unlimited love throughout my graduate studies.

ACKNOWLEDGEMENTS

First I would like to express my most sincere thanks to my advisor Prof. Klaus Hahn. His great insight, patience, and critical thinking have nurtured me to be a better scientist. I am happy to have so many exciting, challenging, and highly interdisciplinary projects that forced me to exploit my creativity as much as I can and immerse myself in various disciplines. As a foreign student, I am fortunate to have an advisor like Prof. Hahn who is willing to take his time to improve my writing and presentation skills. More importantly, because of his close mentorship, I have become a chemist who not only knows how to make useful tools but also knows how to quantify cell biology to extract new information.

I also truly appreciate the support and the valuable advice from my doctoral committees: Prof. Alex Tropsha, Prof. Brian Kuhlman, Prof. David Lawrence, and Prof. Qisheng Zhang. I thank Prof. Tropsha and his former student Yetain Chen for their computation model of ERK that gave us a good starting point of biosensor designs. I am grateful to have a joint journal club with Prof. Kuhlman and his group, where I learned a lot about photosensory proteins and generated many ideas when designing MEK biosensors. I truly appreciate the critical questions and the advice from Prof. Lawrence. I still remember that he told me to be brave when I was about to give up the MEK biosensor project. I thank Prof. Zhang for his kindness to let me work as his teaching assistant during my fifth year.

My graduate life could not be so colorful without my brilliant and hardworking labmates: Chris MacNevin, Li Li, Dmitriy Gremyachinskiy, Yi Wu, Hui Wang, Jason Yi, Marie Rougie, Jon Zawistowski, Scott Slattery, Chris Welch, Brian Mehl, Andrei Karginov, Peihsuan Chu, Onur Dagliyan, Jianrong Wu, Akash Gulyani, Evan Trudeau, Xin Zou, Tamara Davis, and Janet Doolittle. I benefited a lot from daily interactions with these "in-house" experts with diverse backgrounds and critical thinking. I give my special thanks to Dr. Chris MacNevin. I feel comfortable to work on chemistry-related projects in a cell biology lab because I know Chris is always there and ready to answer my chemistry problems throughout my graduate studies. I am very grateful to have Dmitriy Gremyachinskiy to be my rotation mentor, who trained me all the essential chemistry skills as well as lab management practice within the intensive six months of our overlap. I truly thank Dr. Li Li for taking her time and for her patience to teach me how to do microinjection, bead loading, and microscopy. I also enjoyed our extensive collaborations and productive discussions. I thank Marie Rougie for teaching me the techniques of cell culture, microscopy and imaging processing. I would like to thank Dr. Yi Wu for guiding me into protein engineering and for his continued encouragement when I worked on the caging project. I thank Dr. Hui Wang for teaching me molecular cloning skills, and for providing me many advice and remarkable ideas during troubleshooting. I thank Evan Trudeau for helping me prepare some of the ERK biosensor proteins and clone all the p38 mutant constructs. I thank Dr. Jianrong Wu and Dr. Scott Slattery for helping me understand the scripts in the MetaMorph and the Matlab routines. I thank Onur Dagliyan for his expertise in molecular modeling. I thank Dr. Yi Wu, Dr. Chris Welch, and Dr. Andrei Karginov for generation of several valuable stable cell lines that I found very useful for characterization and applications of my new dye-based biosensors. I truly thank Dr. Jason Yi who frequently shares interesting science stories and makes me more positive about science. I especially thank Dr. Chris MacNevin, Dr. Jon Zawistowiski, Dr. Scott Slattery, and Dr. Li Li for reviewing this dissertation.

Many of the great works I could not have accomplished without my collaborators. I was very happy to work with Dr. Alexei Toutchkine on the ratiometric merocyanine dyes, because it was his astounishing work on dyes that allured me to do my second rotation in the Hahn laboratory. I really appreciate the collaboration work on the optimization of red merocyanine dyes with Dr. Dmitriy Gremyachinskiy, Dr. Chris MacNevin, and Dr. Li Li. This work set a solid foundation for the design of my near infrared merocyanine dyes. Dmitriy also contributed to the intial design and the synthesis of near infrared dyes. I also thank the collaboration efforts on the ERK biosensor project with Dr. Lutz Kummer in the Plückthun group at the University of Zurich. They discovered and characterized a specific artificial binder for phosphorylated ERK that our group has been wanted for more than ten years. I strongly appreciated the support and the fruitful discussions from Dr. Michelle Mendoza in the Blenis group at the Havard University. Most of the valuable constructs and proteins for the MEK biosensor project were generous gifts from them. I thank Dr. Elizabeth Hinde in the Gratton group at the University of California at Irvine on the FLIM projects. She conducted all the *in vitro* lifetime measurements. I also appreciate the joint efforts on FLIM with Dr. Li Li, Dr. Brain Mehl, and Marie Rougie in the Hahn group. The addition of Brian to our lab has enabled us to build a better FLIM scope and image analysis routines. Thus I was able to obtain the first FLIM image of dye-based biosensors with his help. I thank Dr. Tilo Mathes in the Hegemann group for providing valuable reagents and for his support in the caging project. I also thank Dr. Arlene Bridges and Dr. Wanda Bodnar for their assistance in mass spectrometry.

Lastly, I would like to express my greatest thanks to my family and friends for their endless love and support. Everytime I get together with them in Taiwan, I feel fully recharged and get lots of inspirations in both science and life. I am very fortunate to have warm-hearted parents—Chun-Tseng Hsu and Yu-Yun Lin who only wish me to be happy and healthy, have a cheerful brother Shao-Kai Hsu who helps me take care of my parents while I am studying abroad, and have Wei Sun to be my husband who shares all sorts of ups and downs and works long hours together throughout my graduate studies. I especially thank the continued encourgement from my previous undergraduate advisor, Prof. Chao-Tsen Chen at the National Taiwan University. It was a great pleasure to join her group since sophoremore. Most of my synthetic skills and my knowledge of dye chemistry were established through the hardcore training in her group. I also especially appreciate the kindness of Dr. Kuo-Hsiung Lee to give me the opportunity to join this program and to conduct my first rotation in his laboratory. I thank Prof. Michiyuki Mastuda at the Kyoto University, Prof. Peter Hegemann at the Humboldt University at Berlin, and Prof. Chun-Hung Lin at the Academic Sinica for inviting me to present my work at their institutes during my graduate studies. I also appreciate the critical questions and valuable suggestions I got during my postdoctoral interviews in the laboratories of Dr. Jin Zhang, Dr. Ryohei Yasuda, Dr. Loren Looger, Dr. Luke Lavis, Dr. Deborah Morrison and Dr. Menghang Xia. I thank the knowledgeable teachers—Dr. Nigel Caplan, Dr. Gigi Taylor, and the active members in the writing group—Congying Wu, Hung-ching Hsia, Xin Zou, Peihsuan Chu, Zaozao Chen and Wei Sun for their help in improving my academic writing skills. I thank Chen-Yu Hsieh, Po-hung Wang, and Dr. Feng Liu for their chemistry expertise and for constant encouragement throughout my graduate studies. I especially thank Yin-Hsuan Lin, Peihsuan Chu, Jin Hong and Chih-Da Wu for their friendship and their support throughout my time in Chapel Hill.

PREFACE

“When you want something,
all the universe conspires in helping you to achieve it.”
— Paulo Coelho, *The Alchemist*

TABLE OF CONTENTS

LIST OF TABLES

LIST OF FIGURES

LIST OF ABBREVIATIONS

ADP	Adenosine diphosphate
ARF-GAP	ADP ribosylation factor GTPase activating protein
AIE	Aggregation-induced emission
AMP-PNP	Adenylyl-imidodiphosphate
AP-1	Activation protein-1
ATP	Adenosine triphosphate
ATP-γS	Adenosine 5'-O-(3-thio)triphosphate
BCA assay	Bicinchoninic acid assay
Bcl-2	B cell lympoma 2
BHQ	Black hole quencher
BiFC	Bimolecular fluorescence complementation
BODIPY	Boron-dipyrromethene
BSA	Bovine serum albumin
CBD	Cdc42-binding domain
CD site	Common docking site
Cdc42	Cell division control protein 42
Cdk5	Cyclin-dependent kinase 5
CFP	Cyan fluorescent protein homolog
CLIP 170	Cytoplasmic linker protein of 170 kDa
cpFP	Circularly permuted fluorescent protein
cPLA2	Calcium-dependent phospholipase A2
c-Myc	c-Fos and v-myc myelocytomatosis viral oncogene homolog
CREB	Cyclic AMP response element-binding protein
CRIB	Cdc42/Rac interactive binding

DARPin	Designed ankyrin repeat protein
DCDHF	Dicyanomethylenedihydrofuran
DIC	Differential interference contrast
DLK	Dual leucin-zipper kinase
DMEM	Dulbecco's Modified Eagle Medium
DMF	Dimethyl formamide
DMSO	Dimethyl sulfoxide
DTT	Dithiothreitol
DUSP	Dual specificity phosphatase
EA	Ethyl acetate
EDTA	Ethylenediaminetetraacetic acid
EE	Early endosome
EGF	Epidermal growth factor
EGFP	Enhanced green fluorescent protein
eIF-4E	Eukaryotic initiation factor-4E
ELK-1	E twenty-six (ETS)-like transcription factor 1
ER	Endoplasmic reticulum
ERK	Extracellular signal-regulated kinase
ESI	Electrospray ionization
EV	Endocytic vesibles
FAK	Focal adhesion kinase
FBS	Fetal bovine serum
FGF	Fibroblast growth factor
FLIM	Fluorescence lifetime imaging microscopy
fMLP	N-Formyl-methionyl-leucyl-phenylalanine
FP	Fluorescent protein

FRET	Förster resonance energy transfer
FRG	FGD1-related Cdc42-guanine nucleotide exchange factor
GDP	Guanosine diphosphate
GEF	Guanine nucleotide exchange factor
GFP	Green fluorescent protein
GIT	GPCR kinase interacting protein
GPCR	G protein-coupled receptor
GRB2	Growth factor receptor-bound protein 2
GST	Glutathione S-transferase
GTP	Guanosine triphosphate
HEK 293	Human Embryonic Kidney 293 cells
HEPES	4-(2-Hydroxyethyl)-1-piperazineethanesulfonic acid
HePTP	Hematopoietic protein-tyrosine phosphatase
HGF	Hepatocyte growth factor
HPLC	High performance liquid chromatography
HRMS	High-resolution mass spectrometry
HRP	Horseradish peroxidase
HSP27	Heat shock protein-27
HTS	High throughput screening
IPTG	β-D-1-thiogalactopyranoside
IQGAP1	IQ motif containing GTPase activating protein 1
JIP1	c-Jun N-terminal kinase interacting protein 1
JNK	c-Jun N-terminal kinase
KEGG	Kyoto Encyclopedia of Genes and Genomes
KIM	Kinase interaction motif
KSR	Kinase suppressor of Ras

LB-agar	Luria-Bertani agarose
LC-MS	Liquid chromatography-mass spectrometry
LOV2	Light, oxygen, voltage-sensing domain
LRMS	Low-resolution mass spectrometry
LUMO	Lowest unoccupied molecular orbitals
MALDI	Matrix-assisted laser desorption/ionization
MAPK	Mitogen-activated protein kinase
MAPKAPK	MAPK activated protein kinase
MAPKK	Mitogen-activated protein kinase kinase
MAPKKK	Mitogen-activated protein kinase kinase kinase
MBP	Maltose-binding protein
MDCK cells	Madin Darby canine kidney cells
MEF	Mouse embryo fibroblast
MEF2	Myocyte enhancer factor-2
MeOH	Methanol
mRFP1	Monomeric red fluorescent protein
NFκB	Nuclear factor κB
NFAT3	Nuclear factor of activated T cells-3
MLCK	Myosin light chain kinase
MLK3	Mix lineage kinase 3
MK2	MAPK activated protein kinase 2
MKP	MAPK phosphatase
MNK	MAPK interacting kinase
MORG-1	MAPK organizer 1
MP-1	MEK-partner 1
MSK	Mitogen- and stress-activated protein kinase

NES	Nuclear export signal
NIR	Near infrared
NLO	Non-linear optical
NLS	Nuclear localization signal
NMR	Nuclear magnetic resonance
NSCLC	Non-small cell lung cancer
PAK	p21-activated protein kinase
PA-Rac	Photoactivatable Rac GTPase
PBD	Periplasmic binding protein
PDGF	Platelet-derived growth factor
PEA-15	Phospho-enriched protein in astrocytes 15
PET	Photo-induced electron transfer
PI3K	Phosphoinositide 3-kinase
2p-FLIM	Two-photon fluorescence lifetime imaging microscopy
PMA	Phorbol-12-myristate-13-acetate
PMMA	Poly methylmethacrylate
PMSF	Phenylmethanesulfonylfluoride or phenylmethylsulfonyl fluoride
POPC	Palmitoyl oleoyl phosphatidyl choline
PP2A or PP2	Protein phosphatase 2
PPI	Protein-protein interaction
PRISM	Protein-protein interaction prediction by structural matching
PTP	Protein tyrosine phosphatase
PVDF	Polyvinylidene fluoride
PXNα	Paxillin α
Q-TOF	Quadrupole time-of-flight
QY	Quantum yield

RE	Recycling endosomes
RhoGDI	Rho GDP-dissociation factor
rRNA	Ribosomal ribonucleic acid
RSK	Ribosomal protein S6 kinase
RTK	Receptor tyrosine kinase
SASA	Solvent accessible surface area
SDM	Site-directed Mutator
SDS-PAGE	Sodium dodecyl sulfate polyacrylamide gel electrophoresis
Sef	Similar expression to FGF genes
SFK	Src family kinase
SH3	SRC Homology 3 Domain
SNAPP	Simplicial neighborhood analysis of protein packing
SOS	Son of sevenless homolog
SRF	Serum response factor
TAK	TGFβ-activated kinase
TBST	Tris-buffered saline with Tween
TFA	Trifluoroacetic acid
TFIIIB	Pol III-specific transcription factor B
TGFβ	Transforming growth factor β
TICT	Twisted intramolecular charge transfer
+TIP	Plus end tracking protein
TLC	Thin layer chromatography
tRNA	Transfer ribonucleic acid
TPE	Tetraphenylenes
TPL2	Tumor progression locus 2
UV	Ultra-violet

VDW	Val der Waas
VEGF	Vascular endothelial growth factor
VMD	Visual Molecular Dynamics
WASP	Wiscott-Aldrich syndrome protein
WRC	WAVE2-regulatory complex
YFP	Yellow fluorescent protein

Chapter 1

Long wavelength merocyanine dyes for multiplexed live cell imaging

1.1 Summary

Activity of endogenous proteins can be reported by fluorescence changes of a solvatochromic merocyanine dye covalently attached to an affinity reagent that binds only the activated conformation of its target. It has however remained challenging to monitor multiple protein activities simultaneously in the same living cell due to the need for two fluorophores in a ratiometric biosensor and the spectral overlap that can occur when using multiple fluorophores. Here we describe a new class of near infrared and red merocyanine dyes with solvent-sensitive fluorescence properties for *in vitro* assays and for multiplexed live cell imaging. We also demonstrate the use of the new dyes to co-image spatiotemporal dynamics of endogenous Cdc42 and Src family kinases (SFK) in the same living cell. We show that both active Cdc42 and SFK are mainly localized at the leading edge while only SFK is activated throughout pinocytosis.

1.2 Introduction and Background

Biosensors that report protein activity in living cells are valuable tools used to investigate the spatial and temporal regulation of dynamic and complex cell signaling events. Subtle changes in the relative timing and subcellular localization of protein activity during the cross-talk of multiple signaling molecules can lead to diverse cell responses; such spatiotemporal information needs to be studied in living cells because it is often lost in *in vitro* assays or fixed cell experiments, due to the need for long incubation times and/or to the disruption of cellular compartments. Fluorophores for live cell imaging must possess the following properties: sufficient brightness (i.e. large extinction coefficient, high quantum yield), photostability, water solubility, biocompatibility, and emissions at long wavelengths to avoid cellular autofluorescence.

Förster resonance energy transfer (FRET) and solvatochromism have been employed to generate biosensors for reporting protein activity in living cells. It has been difficult to monitor two or more biosensors in the same living cell due to significant spectral overlap of the multiple fluorophores and increasing biological perturbations at high total biosensor concentrations. In our experience, cells expressing two FP-based FRET biosensors usually fail to exhibit normal cell motility. An alternative approach we have been developing uses dye-based biosensors. Biosensors based on dyes can require less biosensor due to their enhanced brightness, and unlike their FP-based counterparts, dye-based biosensors have the ability to sense endogenous, unmodified target molecules. We are able to reduce biological perturbations by combining a FP-based FRET biosensor and a biosensor based on a solvatochromic dye, enabling use to study the coordination of Cdc42, Rac and Rho during cell motility with seconds and submicron resolution (1). Here we have sought to develop new merocyanine dyes for multiplexed imaging of two or more dye-based biosensors in the same living cell, and optimized the best versions of these dyes for intensity-based or lifetime-based imaging.

The first class of new dyes consists of the red-shifted versions of previously reported red merocyanine dyes with optimized properties for live cell imaging. Since addition of each double bond to the conjugated polymethine chain in cyanine dyes usually results in a red shift of approximately 100 nm, red merocyanine dyes with these chemical modifications are likely to be excited by near infrared wavelengths. Thus these red-shifted merocyanine dyes could provide an orthogonal fluorescent channel which can be imaged together with a red dye-based biosensor or commonly used fluorescent proteins. The second class consists of red merocyanine dyes with dual fluorescence changes in both intensity and wavelengths; these dyes do not require a second fluorophore for ratio imaging. In addition, because fluorescence lifetime of a molecule is insensitive to factors that influence dye intensity, biosensors based on solvatochromic dyes do not need a second fluorophore for quantification of protein activity in fluorescence lifetime imaging microscopy (FLIM). Therefore FLIM properties of the new dyes were examined as well. The new dyes were tested on the two published activity sensor designs for endogenous activated Cdc42 GTPase and for Src family kinases (SFK). The best dye-based biosensors for intensity-based or lifetime-based detection were determined by comparing biosensor brightness, dynamic range, photostability, and solvent-dependent fluorescence properties (intensity, lifetime, and wavelength maxima).

1.2.1 Protein-based biosensors for live cell imaging

Protein activity or abundance of analytes in live cells can be quantified by fluorescence changes of fluorescent proteins (FPs) or small organic dyes. The fluorophores are attached to target protein molecules or an affinity reagent that specifically binds the activated conformation of the target proteins or sites of posttranslational modifications. Affinity reagents based on protein scaffolds can be easily obtained from the natural binding partners of the target molecules or artificially designed proteins via high-throughput screening (HTS) or protein engineering. Protein-based affinity reagents also provide more extensive binding interactions than small molecule- and peptide-based binders. While FP-based biosensors still dominate the mainstream for biological applications, an increasing number of chemically modified proteins with unique properties is being developed and applied to live cell studies. Here I summarize recent progress in protein-based biosensors that use fluorescent proteins or organic dyes:

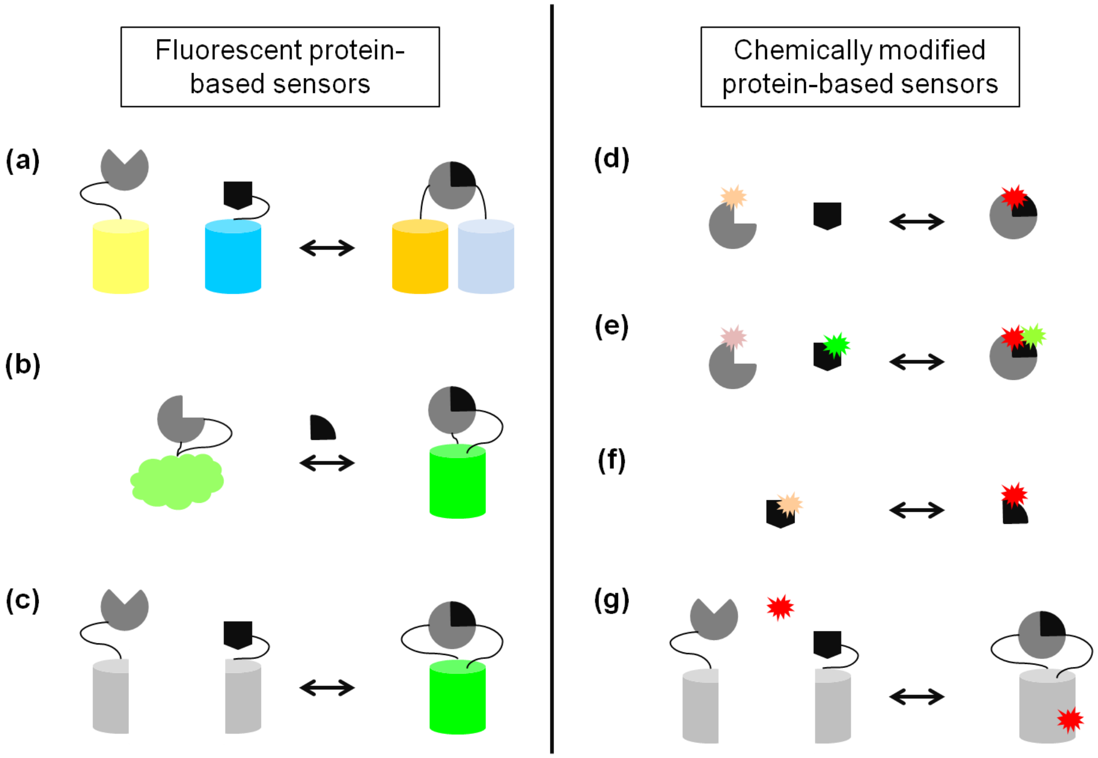

Figure 1.1 Exisitng designs of protein-based biosensors.
The target molecules and affinity reagents for binding of the targets are colored in black and dark grey, respectively. Fragments of a fluorescent protein or a protein tag are colored in light grey. (a) Biosensors based on FRET between two FPs with overlapping spectra. The binding interactions produce change in FRET/donor emission ratios. (b) Biosensors based on circular permuted FPs (cpFPs). Binding of the target molecules induce a conformational change in the cpFP that alters the fluorescence intensity of the cpFP. (c) Biosensors based on BiFC of an N-terminal and a C-terminal fragment consisting an intact fluorescent protein molecule. Upon binding, the two fragments reconstitute the intact fluorescent protein structure and generate fluorescence. (d) Biosensors based on solvatochromic dyes and affinity reagents that bind specifically to the activated targets. Binding interactions usually bring the dye to the more hydrophobic target-binder binding interface, resulting in fluorescence increase in the dye channel. (e) Biosensors based on FRET between two dyes with overlapped spectra. The mechanism is

identical to FP-FRET. Small molecule-FRET usually produces higher dynamic range than FP FRET. (f) Biosensors based on a solvatochromic dye-labeled target protein molecule. Upon conformational changes, the dye is likely in a more hydrophobic or a less hydrophobic environment on the binder surface and therefore displays a fluorescence change (g) Biosensors based on a cell permeable dye and split fragments of a protein tag such as SNAP tags or CLIP tags. The binding interactions enable reconstitution of the protein tags which can form a stable covalent linkage with the corresponding cell permeable dyes.

Fluorescent protein-based biosensors Most biosensor designs are based on fluorescent proteins because FPs can be used for manipulation by transfecting reagents and for genetically targeting to specific tissues by incorporating a tissue-specific promoter sequence in the plasmids for transfection. The fluorescence readouts of FP-based biosensors can be generated through bimolecular fluorescence complementation (BiFC), Förster resonance energy transfer (FRET), and other mechanisms (**Fig 1.1a-c**). BiFC utilizes the fluorescence recovery after *in vivo* reconstitution of the N-terminal and the C-terminal fragments derived from the parent fluorescent protein molecules (**Fig 1.1c**). The available fluorescent protein variants for BiFC include Cerulean, mVenus and GFP. The BiFC methods have been applied to many pairs of binding partners such Ras-Raf (2), actin-cofilin (2), AP1-NFκB (3), Myc-Max-Mad (4), and p53-catalyse (5). The BiFC is easily adapted to a wide variety of protein-protein interactions; however this method suffers from limited temporal resolution because the method takes time for maturation of the reconstituted fluorescent proteins. The fluorescence intensity of a reconstituted fluorescent protein is also usually 10-100 fold weaker than the parent fluorescent protein (6). Because the wavelengths of the existing fluorescent proteins cover the entire visible spectrum (**Fig 1.2**), several pairs of fluorescent proteins capable of undergoing FRET have been developed (7). Cyan fluorescent protein (CFP) and yellow fluorescence protein (YFP) are the most commonly used FRET pair so far. The emission spectrum of CFP is substantially overlapped with the excitation spectrum of YFP, indicating the close potential energies of the CFP-YFP pair. Because the FRET efficiency of the two fluorophores is inversely proportional to the sixth power of the distance between CFP and YFP, excitation of CFP can result in an increase in the emission of YFP through FRET when the two fluorophores are within 10 nm. Binding interactions between two binding partners alter the distance between the two fluorophores and the relative orientations of their dipole moments, thus the change in FRET/donor emission is a function of the protein-protein interactions (**Fig 1.1a**). To report target protein activity or detect amounts of target molecules, one of the fluorophores in the FRET pair is fused to a target-binding domain that specifically recognizes the activated conformations of target proteins (1, 8-12), sites of post-translational modifications (13-24) or small molecules (25-30). Some FRET biosensors (24, 31, 32) are based on the loss of FRET upon enzymatic cleavage of a sequence between the donor and the acceptor fluorophores or conformational changes of the FP-tagged target proteins. The other fluorphore is fused to a docking domain or a recombinant target molecule for achieving specificity of the biosensor designs. Circular permutation of fluorescent proteins not only enables FRET through different orientations of either the donor or the acceptor FP but also provide new biosensor designs based on single fluorophores. Structural changes occurring at the site of permutation can stabilize the hydrogen bonding network or affect the polarity surrounding the chromophore, resulting in a fluorescence intensity change (**Fig 1.1b**). GCaMPs and Pericams are by far the most popular Ca^{2+} biosensors based on circularly permuted GFP and YFP, respectively (33). Marvin *et al* extended this idea to generate a sensitive intensity-based sensor for maltose by inserting a circularly permuted

GFP to a periplasmic binding protein (PBD) (34). Binding of maltose induces a conformational change in PBD and affects the fluorescence intensity of the inserted cpGFP. This approach has great potential to become a generally applicable method to produce single FP-based reporters for a diverse array of analytes. Recently the detection of a ternary complex in live cells has been enabled by combining BiFC and FRET (35). In the BiFC-FRET biosensor design, a pair of split mVenus fluorescent protein fragments is fused to bJun and bFos transcription factors. The binding interactions between bJun and bFos activate the reconstitution of mVenus. The complex is then capable of associating with a Cerulean-tagged p65 transcription factor and undergoes FRET.

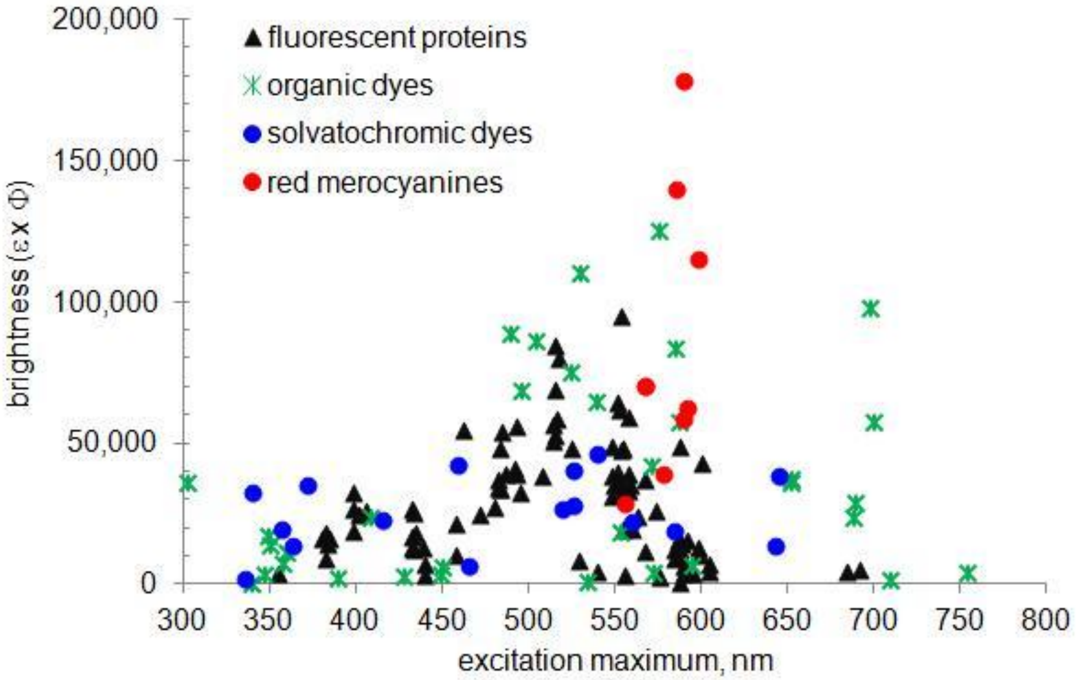

Figure 1. 2 Brightness and excitation maxima of fluorescent proteins and organic dyes.
Brightness is the product of the extinction coefficient ε and the quantum yield Φ of the fluorophore. The values were obtained from references (7, 36-39).

Dye-based biosensors The major advantages of organic dyes over FPs include the relative small size of dyes when compared with FPs and binder molecules, ease of optimization of dye properties through chemical modifications and the diversity of sensing mechanisms such as solvatochromism, FRET, twisted intramolecular charge transfer (TICT), and photo-induced electron transfer (PET). Despite the superior dynamic range, small molecule FRET (**Fig 1.1e**) is less used in protein-based biosensors than FP-based FRET because the latter is much easier in terms of preparation and delivery. Therefore, the current scope of small molecule FRET is focused on detecting metabolites or enzymatic cleavage *in vitro* and in cell lysates. Mie *et al* recently reported a technology to visualize protein-protein interactions in live cells based on the newly developed split SNAP and split CLIP tags (**Fig 1.1g**) (40). They showed that a pair of c-SNAP-tagged bJun and n-SNAP-tagged bFos can form a reconstituted SNAP tag and react with SNAP-Cell TMR Star dyes in HeLa cells. Since protein tags can easily be fused to protein-based affinity reagents, simultaneous labeling of a split SNAP tag and a split CLIP tag with SNAP-Cell Oregon Green and CLIP-Cell TMR-Star also demonstrates great potential for multiplexed imaging of two or more pairs of protein-protein interactions in the same living cell.

Spatial and temporal dynamics of endogenous activated targets can be reported by biosensor designs based on solvatochromic fluorphores (**Fig 1.1d & f)**. Solvatochromic fluorophores such as merocyanine dyes can emit at longer wavelengths than fluorescent proteins (FPs) where the spectral overlap with cellular autofluorescence is greatly diminished (**Fig 1.2**). Importantly, merocyanine dyes exhibit altered fluorescence intensity and/or wavelength maxima in either excitation or emission spectra in response to changes in polarity (hydrophobicity and charge) and hydrogen-bonding interactions in the local environment of the dye molecule. Merocyanine dyes have been employed to generate dye-based biosensor designs (**Fig 1.1 a & c**) for reporting spatiotemporal dynamics of calmodulin (41, 42), S100A4 (43), Cdc42 (44, 45) and Src family kineases (SFKs) (46). Another advantage of the use of solvatochromic dyes is the direct excitation that produces a brighter signal per unit irradiation intensity. Thus less biosensor material is required to obtain sufficient biosensor signals with minimal cellular perturbation. Because of the smaller size and the use of longer wavelengths, dye biosensors are complementary to FP-based FRET biosensors and can be co-imaged with a FRET biosensor in a single living cell (1).

1.2.2 Solvatochromism

The principle of fluorescence can perhaps be best understood by the Jabłoński diagram (**Fig 1.3A**) in which the singlet ground state and the first singlet excited state are denoted as S_0 and S_2, respectively. A fluorophore can be populated at various vibration levels upon excitation. In some cases, fluorophore molecules quickly relax to the lowest excited state S_1 in a process called internal conversion. When the excited electrons return to the ground state, a loss in vibrational energy accompanies with emission, resulting in a red shift of the emission spectra relative to the excitation spectra. The wavelength difference between the absorption maximum and emission maximum is called the Stokes shift. The relative potential energies of the ground state, the excited states and the transition states are influenced by various factors such as temperature, solvent polarity, and intermolecular interactions.

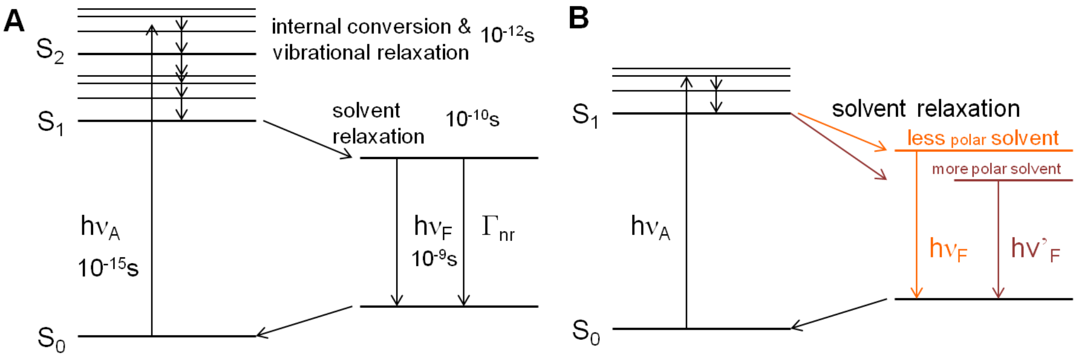

Figure 1.3 Jabloński diagrams of regular fluorescen and solvatochromism.
A. Jabloński diagram. S_0: singlet ground state. S_1: the first excited state. $h\nu_A$: absorption energy. $h\nu_F$: dissipated energy via fluorescence. Γ_{nr}: energy loss via non-radiative processes. **B.** Solvatochromism. Emission maxima are red-shifted if the excited state is more stabilized than the ground state of a molecule in more polar solvents. These diagrams were adapted from: J. R. Lakowicz, *Principles of Fluorescence Spectroscopy*, Springer, New York, NY, USA, 3rd edition, 2006.

Solvatochromism is a term to describe the solvent-sensitive fluorescence behaviors of some molecules (**Fig 1.3B**). These molecules usually possess a large difference in the dipole moments of the ground state and the excited state. Hypsochromic (blue shift) and bathochromic (red shift) transitions in the absorption spectra of a molecule are called as negative solvatochromism and positive solvatochromism, respectively. When a molecule undergoes a positive solvatochromism in a more polar solvent, a red shift in the emission spectra of the molecule is observed. Solvatochromism is determined by the relative stabilization in the ground state and the excited state of the molecule in solvents of various polarities. Because the time for the light-absorbing molecules to be excited to the excited state (femtoseconds) is much shorter than the time for molecules to undergo vibrational or rotational movements (1-100 picoseconds), solvatochromic fluorophores still obey the Frank-Condon principle in which the vibration levels in the ground state are similar to the vibration levels in the excited state. Due to the unique solvent-dependent fluorescence properties of solvatochromic dyes, several solvatochromic dyes have been developed to report protein conformation change, protein-sensor binding interactions and post-translational modifications *in vitro* and in live cell imaging (1, 39, 41, 43-52).

The solvatochromic properties of native tryptophan residues in proteins led to their becoming the first well-investigated class of fluorophores that could be useful for detecting protein conformation changes (53, 54). Since then, many new extrinsic fluorophores with greater brightness and longer wavelengths have been developed to report biological events via probe-target interactions when a probe molecule is in proximity to the target molecule (55). One class of solvatochromic dyes that are especially useful for live cell imaging is merocyanine dyes. A merocyanine molecule consists of an electron donor, an electron acceptor, and a conjugated polymethine chain bridging the donor and the acceptor moieties (**Fig 1.4A**). Depending on its environment and the chemical structure, the ground state resonance structure of a merocyanine dye can fall anywhere along a continuum between neutral, partially charged, and zwitterionic forms. Merocyanines are more attractive for live cell imaging applications than most solvatochromic dyes because merocyanines satisfy several criteria necessary for live cell imaging including brightness, solvent-dependent fluorescence, and long excitation wavelengths. Some merocyanine derivatives are brighter than most fluorescent proteins and/or are more photostable than commonly used imaging dyes such as fluorescein and cyanine dyes (**Fig 1.2**) (45, 56-58).

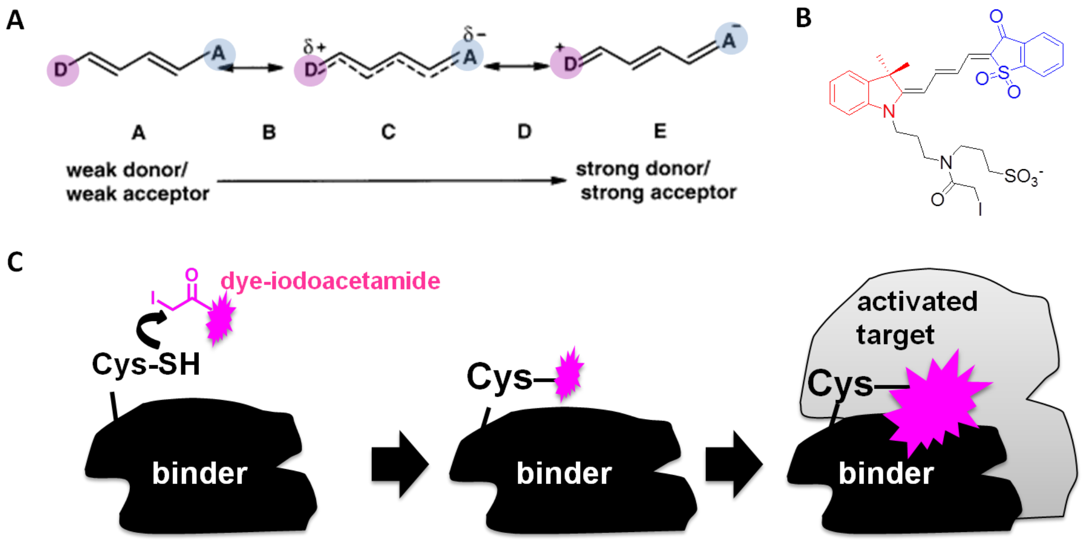

Figure 1.4 Mechanisms of dye-based biosensors.
A. A merocyanine molecule consists of an electron donor (D) and an electron acceptor (A) connected by a conjugated polymethine chain (45, 58). **B.** An example of water-soluble and thiol-reactive merocyanine dye for biosensor applications. The electron donor is colored in red and the electron acceptor is colored in blue. **C.** A typical dye-based biosensor is based on dye-labeled protein-based binder molecules that bind only activated conformation of the target and exhibit fluorescence changes upon binding.

Two examples of biosensor designs based on solvatochromic dyes for live cell imaging applications include MeroCBD for reporting activation of endogenous Cdc42 (44, 45) and SFK merobody for reporting activation of endogenous Src family kinases (SFK) (46). To report protein conformational changes or protein-protein interactions, a merocyanine dye molecule (**Fig 1.4B**) is covalently attached to an engineered cysteine residue on an affinity reagent that binds only activated targets (**Fig 1.4C**). The affinity reagent in MeroCBD is derived from the CRIB domain of Wiscott-Aldrich syndrome protein (WASP)—a direct downstream effector of Cdc42, whereas the affinity reagent that specifically binds the SH3 domain of c-Src was discovered via phage display of a fibronectin scaffold library (59). According to the co-crystal structure (PDB: 1CEE), the binding interface between GTP-bound Cdc42 and WASP contains many hydrophobic residues. Therefore most dye-labeled MeroCBD designs exhibit fluorescence increase upon binding when the merocyanine dye is covalently attached to the binding interface (**Fig 1.5A**). MeroCBD reveals that Cdc42 is highly active at the leading edge during protrusions (**Fig 1.5B**). When a Src family kinase molecule is activated after phosphorylation, the SH3 domain of SFK becomes accessible for the artificial binder (**Fig 1.5C**). When a merocyanine dye is covalently attached to the engineered cysteine residue at the potential binding interface between the affinity reagent and the activated SFK, the dye fluorescence either increases or decreases to reflect abundance of activated SFK in cells. The SFK merobody biosensor is capable of monitoring fluctuation of endogenous SFK activation during leading edge dynamics and macropinocytosis (**Fig 1.5D**). Because merocyanine dyes report changes in total fluorescence intensity that are easily influenced by factors such as varying cell thickness and uneven illumination, a second fluorophore insensitive to protein activation is required as a volume indicator to use for ratiometric imaging. As a result, the broad spectral range of two fluorophores limits the maximum number of biosensors that can be imaged in a single cell using the available wavelengths in the visible region.

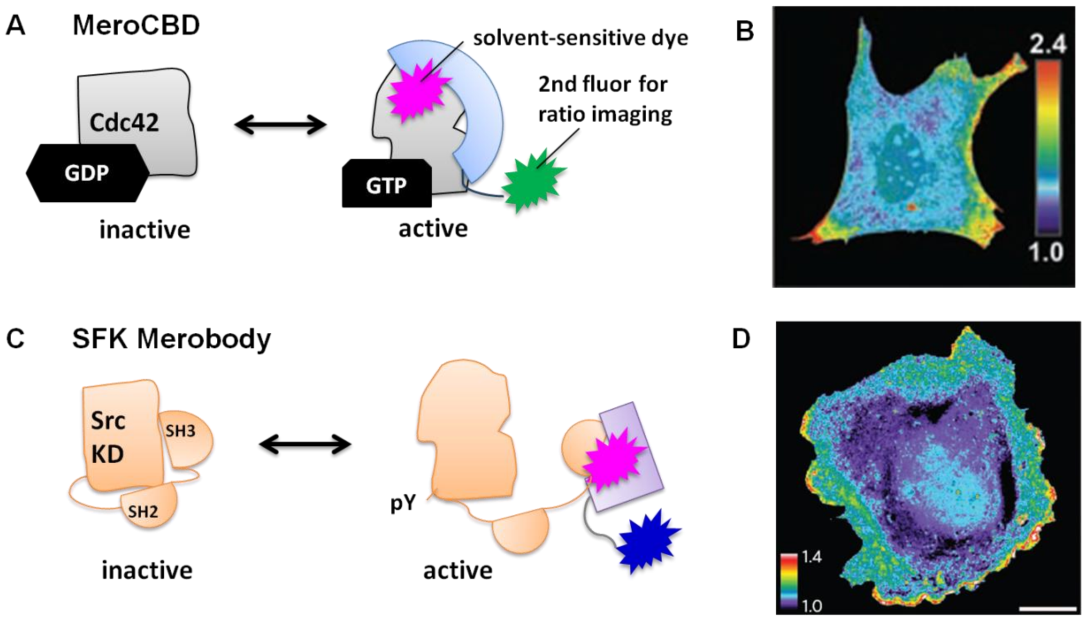

Figure 1.5 Biosensor designs for Cdc42 and SFKs.
A. MeroCBD, a dye-based biosensor for endogenous activated Cdc42 Rho GTPase. The affinity reagent specific to GTP-bound Cdc42 was derived from a substrate of Cdc42. A second fluorophore such as EGFP is fused to the dye-labeled affinity reagent to eliminate factors that affect dye intensity in live cell imaging including varying cell thickness and uneven illumination. **B.** SFK merobody, a dye-based biosensor for endogenous activated Src family kinases (SFKs). The affinity reagent specific to c-Src SH3 domain was obtained through phage display of a library of fibronectin monobodies.

The current obstacles to using solvatochromic dyes inside living cells are the delivery of the highly polar dye conjugate and the lack of bright deep red (700-740 nm) or near infrared (740-780 nm) solvatochromic dyes for multi-color imaging. As bio-orthogonal reactions and site-specific labeling methods (60-84) have been rapidly advanced in recent years, the solvatochromic dyes will be easier to use and provide more novel tools for live cell studies or *in vivo* imaging.

1.2.3 Recent progress of near infrared dye-based probes for live cell imaging applications

Near infrared (NIR) fluorophores with excitation wavelengths ranging from 650 to 900 nm are useful for *in vivo* imaging because of their deeper penetration depth in thick tissues, the diminished contribution of cellular auto-fluorescence to background signal, and the reduced photo-toxicity to live cells. NIR fluorophores are also useful for multiplexed imaging since there are very few bright, photostable near infrared fluorephores that have been routinely used for biological applications. In addition to the most commonly-used cyanine derivatives, several dye scaffolds have progressed for live cell or live animal imaging applications. These near infrared dyes include rigidified cyanines, squaraines, BODIPY derivatives, xanthenes, Si-rhodamines, and dicyanomethylenedihydrofuran (DCDHF) derivatives (**Fig 1.6**).

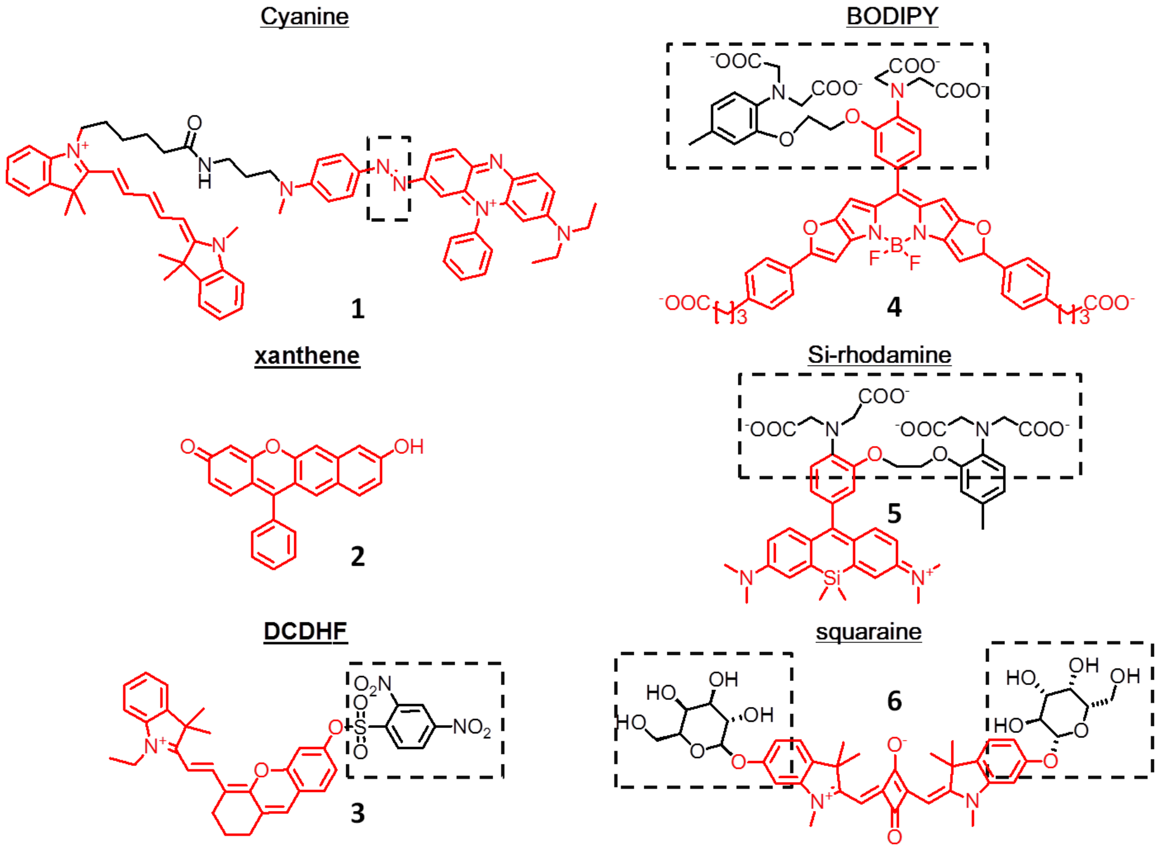

Figure 1.6 Examples of NIR dyes for live cell imaging applications.

The scaffolds of the fluorophores are colored in red. Functional groups for sensing specific cellular events are circled with black dashed lines.

Cyanine derivatives Cyanine dyes are the most popular NIR fluorophores because of their long wavelengths, high extinction coefficients, high quantum yields in aqueous solution, and numerous well-established protocols for preparing dye-conjugates. White *et al* designed a deep-red fluorescent probe with selective response to the surface of both Gram-positive and Gram-negative bacteria in mice injected with bacteria (85). The probe reports the enhanced hydrophobicity surrounding the dye molecule by Förster resonance energy transfer (FRET) of the conjugate of a cyanine energy donor and a bis(zinc(II)-dipicolyamie) energy acceptor. When titrated with POPC/lipid A, the probe showed an approximately four-fold increase in acceptor emission (85). A similar approach was applied by the Nagano group to generate QCy5, the first long wavelength FRET sensor for imaging hypoxia in MCF-7 cells and acute hypoxia in living mice (86). In their sensor design, a Black Hole Quencher (BHQ) derivative serves as the fluorescence quencher for Cy5 and an azobenzene moiety that undergoes reduction in hypoxia. For in vivo imaging, mice injected with QCy5 were imaged with an excitation wavelength of 620 nm and an emission wavelength of 680 nm. However, QCy5 is maximally excited at 605 nm and maximally emits at 645 nm. Okuda *et al* also reported a cyanine-based NIR sensor for hypoxia, GPU-167, which marks the tumor sites in mice with an excitation maxima of 753 nm and an emission maxima at 778 nm (87). Yuan *et al* reported a series of 2,3-dihydro-1H-xanthene-6-ol derivatives with $\lambda_{abs,max}$ ranging from 608 to 698 nm and $\lambda_{em,max}$ ranging from 677 to 718 nm (88). The brightest derivative, compound 3, has an extinction coefficient of 79000 $cm^{-1}M^{-1}$ and a quantum yield of 0.36 in 1:1 PBS-MeOH mixture at pH 7.4. They showed that two derivatives of compound 3 are capable of sensing endogenously generated H_2O_2 in live HeLa cells, macrophages and mice and endogenous thiols in live Bel 7702 cells and mice. Yuan *et al* also describe a new class of cyanine dyes named Changsha (CS) NIR dyes and demonstrated the use of the new dyes to detect endogenous HClO production in RAW264.7 macrophages and mice (88). The parent dye CS2 is maximally excited at 700 nm and emits most at 731 nm with an extinction coefficient of 139,500 $cm^{-1}M^{-1}$ and a quantum yield of 0.41 in ethanol. The probe exclusively responds to HClO over several representative reaction oxygen species (ROS) and reactive nitrogen species. Addition of HClO opens up the OSu-protected derivative, resulting in increases emissions at 745 nm. Other NIR probes based on cyanines have been used to detect pH change (89), mercury ions (90), copper ions (91), singlet oxygen (92), ozone (93) and peroxynitrite (ONOO-) (94, 95).

Dicyanomethylenedihydrofuran (DCDHF) derivatives DCDHF dyes are composed of an amine donor moiety and an acceptor group based on 2-dicyanomethylene-3-cyano-2,5-dihydrofuran (DCDHF) connected with an extensive π-system (96). DCDHF dyes are characterized by a large Stokes shifts and solvent-sensitive change in brightness and lifetime. A lipid-modified derivative, DCDHF-A-6, diffused to the plasma membrane of CHO cells for monitoring membrane dynamics (97). In water the dye is weakly fluorescent with an absorption maximum of 600 nm and an emission maximum of 830 nm. While in toluene solution of 20% poly (methyl methacrylate) (PMMA), DCDHF-A-6 has a quantum yield of 0.71, a blue-shifted absorption maximum at 594 nm and a blue-shifted emission maximum at 686 nm. The extinction coefficients of DCDHF (ε: 29,000-71,000 cm-1M-1) are relatively smaller than cyanines and merocyanines, making it still difficult to generate sufficient signal-to-noise ratios for intensity-based ratio imaging methods. Importantly the fluorescence lifetime of DCDHF derivatives is sensitive to polarity differences in the environment. For example, another dye, DCDHF-N-6, has a quantum yield of 0.017 and a lifetime value smaller than 0.22 ns in ethanol; in PMMA solution the dye becomes brighter with a quantum yield of 0.98 and a lifetime value of 3.2 ns. The photobleaching rates of DCDHF-A-6 and DCDHF-N-6 are 5.4 and 29.5 fold slower than fluorescein. The major issue of DCDHF dyes is their low water solubility caused by the highly planar and hydrophobic conjugated system. Methods to generate more water soluble DCDHF derivatives are being developed to prevent non-specific binding to membrane molecules in living cells (98).

BODIPY derivatives Several near infrared derivatives based on the BODIPY (borondipyrromethane) scaffold by extending the π-conjugated system have been reported (99-103). Most applications of the NIR versions of BODIPY dyes have been in material science. However, Myochin *et al* recently reported a series of near infrared fluorescent probes for detecting matrix metalloproteinases (MMPs) in HT-1080 cells and in mice (100). Among the NIR probes, a probe based on a NIR BODIPY dye and a dark quencher BHQ is cell permeable and shows an increase in quantum yield from 0.001 to 0.127 upon dequenching by the MMP-mediated cleavage of the probes. Interestingly, Hu *et al* reported another new class of near infrared BODIPY derivatives with large Stokes shifts with solvatochromic properties (102). They exploit the advantage of aggregation-induced emission (AIE) of tetraphenylenes (TPE) and create a series of TPE-BODIPY derivatives with various conjugatable linkers. Although these dyes enter cells mainly by endocytosis, these BODIPY dyes might be useful to construct dye-based biosensors to monitor protein conformational changes in live cells.

Xanthene derivatives Two typical classes of xanthenes dyes are fluorescein, rhodamine, and their derivatives, which are usually not excited or emit in the NIR region. A series of new water soluble and low molecular weight semi-naphthofluorone (SNAFR) containing xanthenes derivatives emit at near infrared region with moderate quantum yields of around 0.09 in DMSO and display dual fluorescence changes in both excitation and emission spectra (104). A test dye, SNAFR-6, was capable of rapidly passing through the cell membrane of HEp2 cells and accumulating mainly at endoplasmic reticulum (ER) and lysosomes with low cytotoxcity. This dye is excited maximally at 536 nm, emits maximally at 733 nm and exhibits a photobleaching rate 3.3 fold slower than fluorescein in aqueous solution. Despite the long emission wavelengths and large Stokes shifts of SNAFR dyes, their brightness and photostability will be the focus for future improvement.

Si-Rhodamine (SiR) derivatives The Nagano group at the University of Tokyo recently invented a new class of near infrared fluorophores based on group 14-substituted rhodamine derivatives (105). Group 14 metalloles including silicon, germanium and tin possess unusually low-lying lowest unoccupied molecular orbitals (LUMO) due to the σ*-π* electronic transition between the σ* orbital of the two bonds connecting the group 14 atom and the π* orbital of the butadiene part of the appended fluorophore. As a result, the rhodamine derivatives containing a bridge group 14 atom show a large bathochromic shift to far-red or near infrared regions in excitation and emission spectra. The Nagono group later incorporated an alkylaminobenzene group to a Si-rhodamine dye to generate a SiR-Zn—a NIR Zn^{2+} sensor with a K_d of 1.4 nM and were able to image the Zn reporter in HeLa cells incubated with zinc or a zinc chelator, N,N,N',N'-tetrakis(2-pyridylmethyl)ethylene diamine (105). Another exciting new sensor design is a new NIR calcium probe based on Si-rhodamine which allows deeper tissue penetration with reduced photo-cytotoxicity (106). The probe, named CaSiR-1, consists of a Si-rhodamine (SiR) with excitation/emission maxima of 650 /664nm and a BAPTA ligand to chelate calcium ions. The new probe has a quantum yield of 0.20 upon binding of saturating concentrations of calcium ions with a K_d of 0.58 μM, enabling the co-imaging of sulforhodamine 101-stained astrocytes and CaSiR-1-illuminated endogenous calcium in a hippocampal slice from a Thy1-mGFP mouse. Other in cell- or *in vivo* applications include detection of HClO generation during phagocytosis of porcine neutrophil and PMA-stimulated mice (107), and visualization of tumor sites in mice intravenously injected with a NIR siR-labeled anti-tenascin-antibody (108).

Squaraine derivatives Squaraine dyes feature an electron deficient four-member ring acceptor moiety which bridges two electron donor moieties. These dyes commonly exhibit intense fluorescence at long wavelengths. The major applications of squaraine dyes have been in dye-sensitized solar cells, but their use in live cell imaging is currently under development (109-113). Oushiki *et al* developed a squarylium-based NIR probe for alkaline phosphatase and β-galactosidase (113). Upon cleavage of a dye-galactoside derivative by β-galactose expressed in LacZ-positive HEK293 cells or mice, the probe becomes brighter due to the enhanced hydrophobic environment at the probe-enzyme binding interface. The parent fluorophore has an extinction coefficient of 11,000 $cm^{-1}M^{-1}$ and a quantum yield of 0.015 in phosphate buffer. When incubated in a solution of fetal bovine serum (FBS), the dye is red-shifted from 626 nm to 645 nm in the excitation maximua and from 645 nm to 660 nm in the emission maxima. The extinction coefficient and the quantum yield values of the dye raises to 12,000 $cm^{-1}M^{-1}$ and 0.32. Another advantage of squaraine dyes is the superior photostability when compared with Cy5, a commonly used fluorophore for single molecule studies (114).

A few structures of near infrared merocyanine dyes (115, 116) have been reported. However, the current focus of most groups is to generate non-linear optical (NLO) materials, and none of these have been used for live cell imaging. While the key properties for live cell imaging of red merocyanine dyes have been carefully characterized by our group, the potential of near infrared merocyanines for multiplexed live cell imaging or *in vivo* imaging needs to be explored in more detail.

1.3 Results and Discussion

1.3.1 Design and synthesis of near infrared merocyanine dyes

The electron donor and the electron acceptor moieties of the new near infrared merocyanine dyes were selected based on red merocyanine dyes with optimized properties for live cell imaging (**Fig 1.7**). Solvent-sensitive fluorescence properties of a merocyanine dye molecule are determined by the electron donating ability of an electron donor, the electron withdrawing ability of an electron acceptor, and the conjugation length of a conjugated polymethine chain bridging the electron donor and the electron acceptor. It has been seen in many cyanine and merocyanine derivatives that polymethine dyes with hydrophobic terminal end groups tend to form dye aggregates which usually cause severe fluorescence quenching. As the conjugation system of polymethine dyes becomes more extended, the hydrophobic interactions between polymethine dye molecules increases, resulting in stronger dye-dye association. Derivatives of 2,3,3-trimethyl-3*H*-indole (**I**) used as the terminal end groups of cyanine and merocyanine dyes have been shown to greatly reduce the tendency for dye aggregation and rescue dye fluorescence in water; they contains an sp^3 hybridized carbon which provides steric hindrance to dye-dye association. For this reason derivatives such as **I** and **IS** were used to construct new merocyanine dyes (**Fig 1.7ii**). **IS** was designed to have an additional charged sulfate group for extra charge-charge repulsive forces and for improving the overall water solubility of the test dyes. In the case of merocyanine-labeled activity sensors for Src family kinases, dyes with **I** or **IS** exhibited distinct fluorescence responses to binding of the c-Src SH3 domain, indicating the importance of orientating of the charged sulfate group relative to the sensor-target binding interface. Strong electron acceptor moieties such as diketobenzothiophen-3-one (**SO**), 1,3-indanedione (**Pht**), 1,3-dimethylbarbituric acid (**BA**) and 1,3-diethyl-2-thiobarbituric acid (**TBA**) produced the best red merocyanine dyes, with balanced brightness, photostability, and solvent-sensitive fluorescence changes, when used together with the 2,3,3-trimethyl-3*H*-indole (**I**) electron donor moiety.

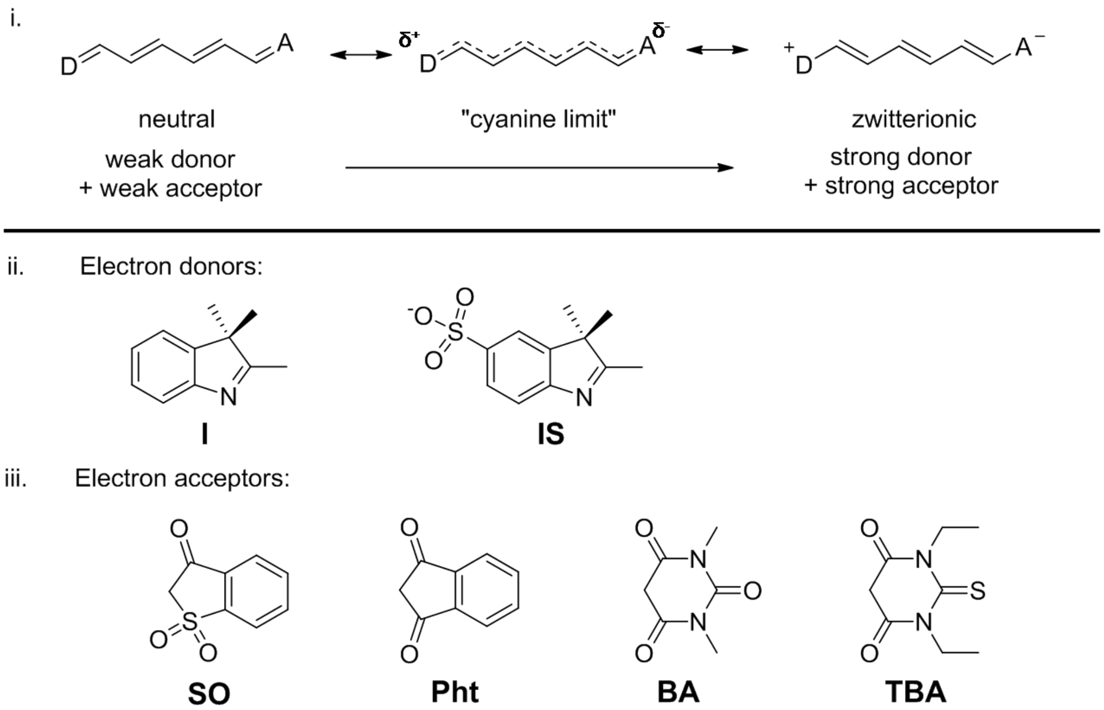

Figure 1.7 Design of red-shifted merocyanine dyes.
i. Solvatochromism of hepta-merocyanine dyes. **ii.** Structures of electron donor moieties. **I**: 2,2,3-trimethylindolenine. **IS**: 2,3,3-trimethyl-3H-indole-5-sulfonate. **iii.** Structures of electron acceptor moieties. **SO**: diketobenzothiophen-3-one. **Pht**: 1,3-indanedione. **BA**: 1,3-dimethylbarbituric acid. **TBA**: 1,3-diethyl-2-thiobarbituric acid. These end groups were previously optimized by Toutchkine *et al* (45, 56-58).

To extend the conjugation length, an extra double bond in the conjugated polymethine chain was added to each of the optimized parent red dyes. The newly synthesized red-shifted merocyanine dyes include **mero79** (**I-Pht**), **mero80** (**I-BA**), **mero81** (**I-SO**), **mero82** (**I-TBA**), **mero97** (**IS-Pht**), **mero84** (**IS-BA**), and **mero83** (**IS-SO**) as shown in **Fig 1.8**. **Mero79**, **mero80**, **mero81**, and **mero82** were designed for basic characterization of several key dye properties important in live cell imaging including brightness, photostability, and solvent-sensitive fluorescence behaviors. **Mero97**, **mero84**, **mero83**, water-soluble versions of **mero79**, **mero80**, and **mero81**, were designed to investigate dye aggregation and for studies conducted in aqueous solution including pH sensitivity and dye-protein interactions.

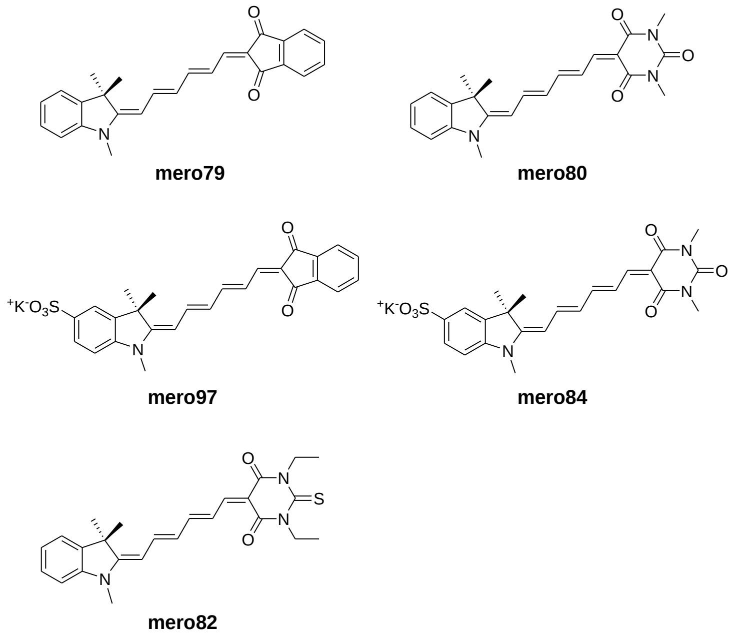
mero79 **mero80** **mero81**

mero97 **mero84** **mero83**

mero82

Figure 1.8 Structures of red-shifted merocyanine dyes.

The syntheses of the electron donor moieties **1** and **3** and electron acceptor **5** were conducted according to published procedures (**Fig 1.9**). The indolenine ring of compound **3** was synthesized from 4-hydrazinylbenzenesulfonic acid and 3,3-dimethyl-2-butanone via Fischer Indole synthesis. Methylated derivatives of **I** and **IS**, compounds **1** and **3**, were used for photophysical characterization and were prepared from indolenine intermediates through S_N2 reaction with iodomethane. The synthesis of electron acceptor **5** started with alkylation of thiosalicylic acid with chloroacetic acid. The thioether of alkylated thiosalic acid was then oxidized to sulfone with hydrogen peroxide, followed by a base-catalyzed cyclization between the aryl carboxylate group and the α-carbon between the sulfone group and the aryl carboxylate group. The sulfone group of **SO** was designed to provide additional steric hindrance to further reduce potential dye aggregation. Other electron acceptor moieties **Pht**, **BA**, and **TBA** were obtained from commercially available resources. **Pht** has the most planar structure, while **BA** and **TBA** are the least planar. **BA** and **TBA** also possess more hydrogen bonding donor and hydrogen bonding acceptor groups than **SO** and **Pht**. It would be interesting to find out how the hydrogen bonding interactions and conformations of these electron acceptor moieties affects dye aggregation in water and dye-protein interactions.

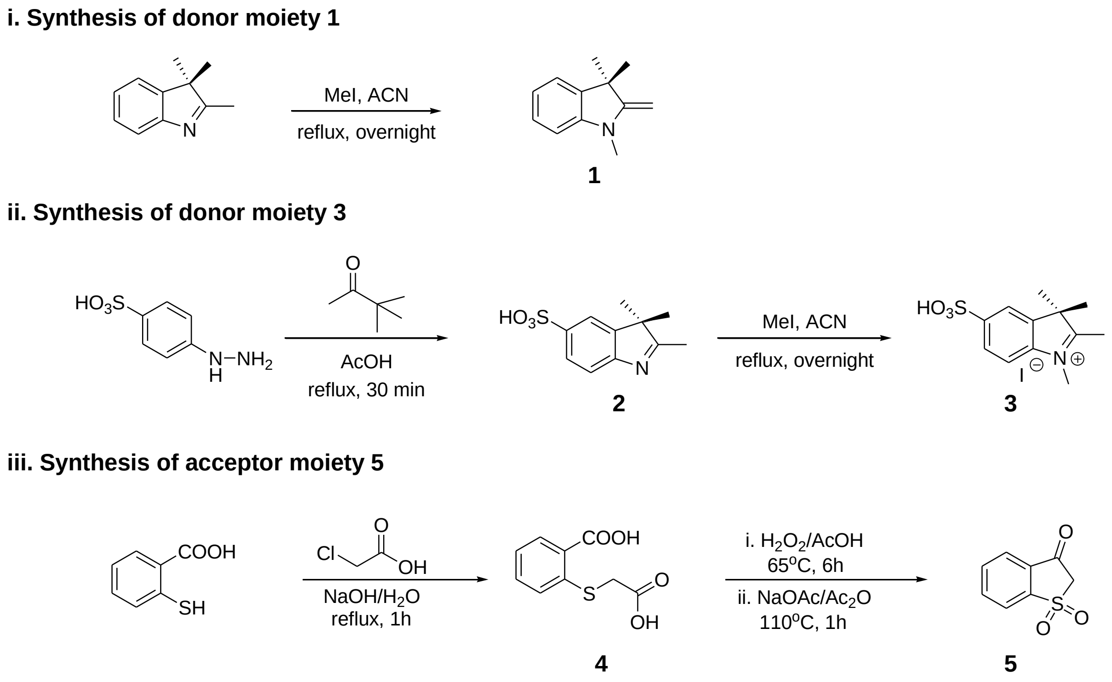

Figure 1.9 Synthesis of donor and acceptor moieties of merocyanine dyes.

The fluorophore scaffolds of red-shifted merocyanine dyes were synthesized by coupling an electron donor moiety with an activated acceptor intermediate. The α carbon adjacent to the electron withdrawing carbonyl group in an acceptor moiety can be deprotonated with sodium acetate and then react with an acetal molecule or di-anil group of an unsaturated aldehyde molecule. While the previously reported method for the preparation of red parent merocyanine dyes utilized acceptor intermediates activated by reacting acceptor moieties with malonaldehyde bis(dimethyl) acetal, the activated acceptor intermediates for red-shifted dyes were found to be highly unstable and difficult to separate by chromatography. We found that by activating the acceptor moieties via S_N2 reaction with glutacondialdehyde dianil, the resulting acceptor intermediates **6a-6d** could be easily separated by re-crystallization, filtration, or flash chromatography with reasonable yields and purities.

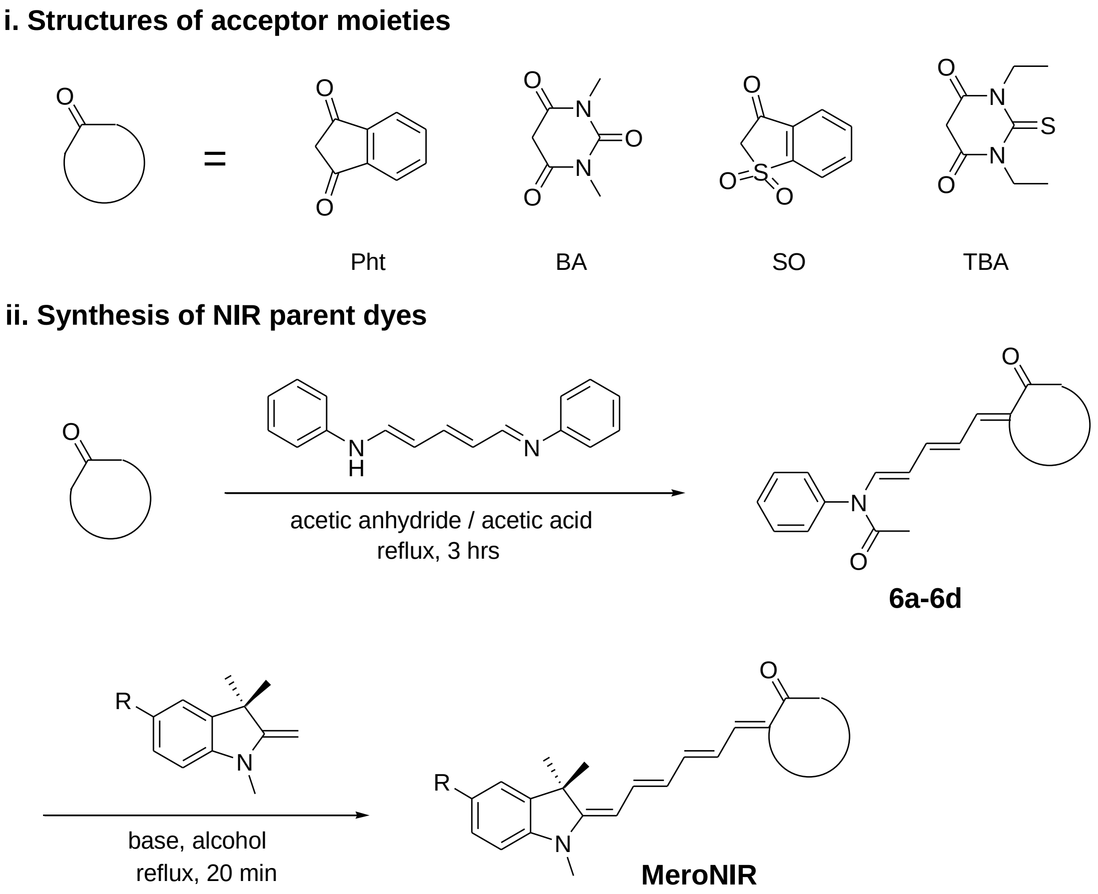

	pht	BA	SO	TBA
R = H	**mero79**	**mero80**	**mero81**	**mero82**
R = $SO_3^-K^+$	**mero97**	**mero84**	**mero83**	

Figure 1.10 Synthesis of red-shifted merocyanine dyes.
i. Structure abbreviations of electron acceptor moieties. ii. Preparation of red-shifted merocyanine dyes.

Severe compound decomposition after storage at 4 ^{o}C for three years was observed for activated **BA** and **TBA** acceptor intermediates (**6b** and **6d**). The decomposed acceptor intermediates could easily form **BA**- and **TBA**-based red fluorescent cyanine dyes in the presence of base, as characterized by nuclear magnetic resonance and mass spectrometry (data not shown). For synthesis of **mero79**, **mero80**, **mero81**, and **mero82**, compound **1**, an alkylated electron donor moiety of **I**, was dissolved in methanol and coupled with various activated electron acceptor intermediates upon addition of sodium acetate (**Fig 1.9**). Because the other electron donor moiety, compound **3,** is poorly soluble in methanol, the synthesis of **mero97**, **mero84**, and **mero83** was conducted in heated ethanol and catalyzed by triethylamine.

1.3.2 Photostability and spectral properties of NIR merocyanine dyes

Each newly synthesized merocyanine molecule has a red shift of approximately 100 nm compared to their parent red derivatives. Thus these red-shifted dyes are capable of being excited with near infrared wavelengths ranging from 650 nm to 750 nm. Dyes in various solvents were irradiated using a halogen lamp, a xenon lamp in a fluorometer, or in a plate reader. The color of the new dyes and the reference dye Cy5 faded rapidly at temperatures over 50 ^{o}C when irradiated with a halogen lamp, which produces a continuous spectrum from near ultraviolet to infrared regions; therefore the temperature for photobleaching measurement was maintained at room temperature or 18 ^{o}C and dyes were irradiated with wavelengths longer than 550 nm. Photobleaching of the new near infrared dyes at 0.1 mM resulted in significant fluorescence increase upon irradiation, indicating the presence of non-fluorescent dye aggregates (**Fig 1.11A**). The fluorescence of these dye aggregates is severely quenched due to deactivation caused by excimer formation. Once one or a few of the dye molecules in the dye aggregates is photobleached, dye-dye interactions become less significant and fluorescence of the remaining dyes are no longer quenched. **Mero79** (**I-Pht**) and **mero81** (**I-SO**) exhibited a fluorescence increase upon irradiation at 0.1 μM in n-butanol. Some dyes produced less excimer formation when placed on biosensor proteins (**Fig 1.10A**); however photobleaching rates measured on dye-labeled proteins vary from batch to batch and vary between different types of sensor proteins, making it difficult to obtain reproducible and consistent photobleaching kinetics for each dye.

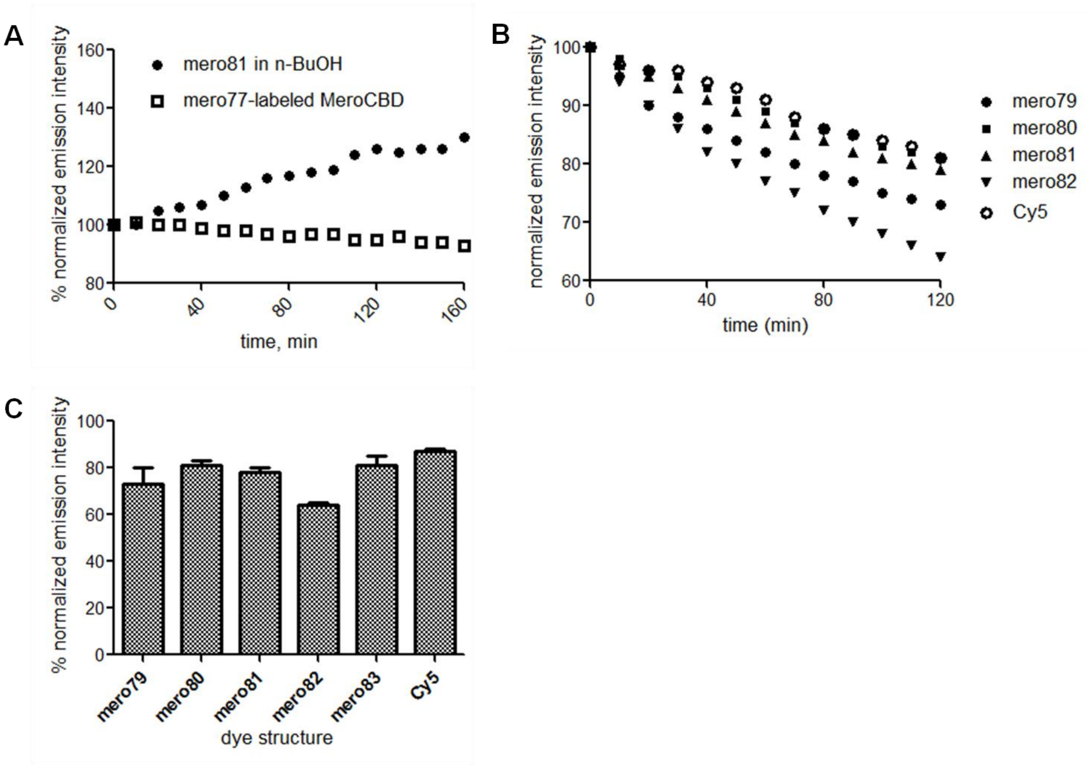

Figure 1.11 Relative photostabilities of NIR merocyanine dyes.
A. Photobleaching of 0.1 μM **mero81** in n-butanol and 1 μM **mero77**-labeled Cdc42 biosensor proteins in phosphate buffer (50 mM NaH_2PO_4, pH 7.6). **B.** Photobleaching curves of 0.1 μM near infrared merocyanine dyes and Cy5 in glycerol. **C.** Normalized remaining intensity of 0.1 μM near infrared merocyanine dyes and Cy5 in glycerol after 2 hours of irradiation.

To obtain sufficient brightness for each test dye, the optimized photobleaching protocol for the new dyes and the reference dye Cy5 was to monitor the fluorescence decay of 0.1 µM dyes in glycerol upon irradiation with a high energy xenon flashlamp (200 flashes per second) on a plate reader (**Fig 1.11B**). In general, most of the new near infrared merocyanine dyes exhibited photobleaching rates similar to the reference dye Cy5 (**Fig 1.11C**), with an exception being **mero82** (**I-TBA**). After two hours of continuous irradiation, only approximately 60% of dye emission intensity remained in the case of **mero82**. In addition, **mero62**, a red and cysteine-reactive version of **I-TBA**, suffered from the tendency of over-labeling of sensor proteins of interest probably due to the strong association between free dye and dye-labeled proteins as assessed by SDS-PAGE and fluorescence gel scanning. Based on the poor photostability and potential of over-labeling of **I-TBA** dyes, near infrared derivatives of **I-TBA** were excluded from the following studies. In summary, **mero80** (**I-BA**) is the most photostable among the new near infrared merocyanine dyes.

All new near infrared merocyanine dyes are excited and emit at long wavelengths where interference from cellular autofluorescence becomes greatly reduced. Another important criterion of ideal live cell imaging dyes is that these fluorophores need to be capable of generating fluorescence images with sufficient signal-to-noise ratios. Dye brightness is defined as the product of dye extinction coefficient ε and dye quantum yield Φ. The extinction coefficient of a molecule measures how efficiently the molecule absorbs photons while the quantum yield of a molecule reports how efficiently the molecule makes use of these photons in radiative decay processes. Among all dyes, **mero81** is brightest in DMSO while **mero82** has the best basal brightness measured in methanol (**Table 1.1**).

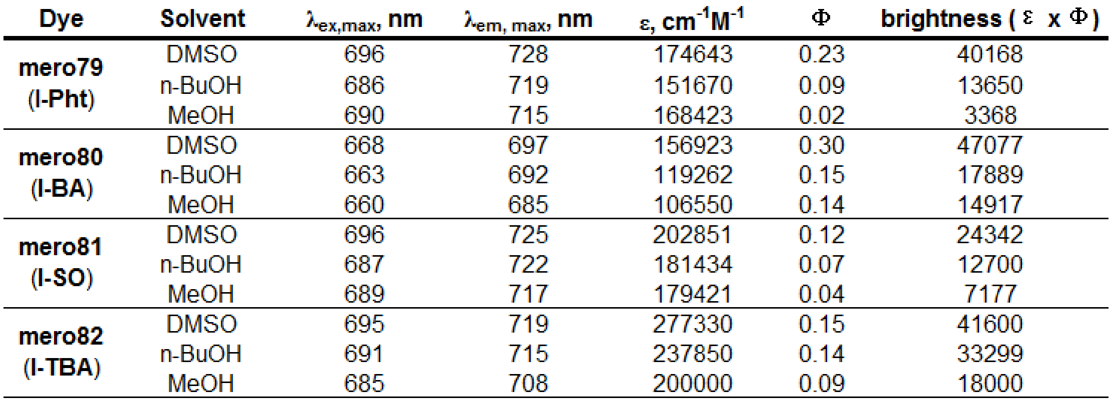

Dye	Solvent	$\lambda_{ex,max}$, nm	$\lambda_{em,\ max}$, nm	ε, cm^{-1}M^{-1}	Φ	brightness (ε x Φ)
mero79 (I-Pht)	DMSO	696	728	174643	0.23	40168
	n-BuOH	686	719	151670	0.09	13650
	MeOH	690	715	168423	0.02	3368
mero80 (I-BA)	DMSO	668	697	156923	0.30	47077
	n-BuOH	663	692	119262	0.15	17889
	MeOH	660	685	106550	0.14	14917
mero81 (I-SO)	DMSO	696	725	202851	0.12	24342
	n-BuOH	687	722	181434	0.07	12700
	MeOH	689	717	179421	0.04	7177
mero82 (I-TBA)	DMSO	695	719	277330	0.15	41600
	n-BuOH	691	715	237850	0.14	33299
	MeOH	685	708	200000	0.09	18000

Table 1.1 Spectral properties of near infrared merocyanine dyes.
Extinction coefficients were averaged with three separate preparations. Quantum yields were compared with Cy5.

Mero79 has the largest change in dye brightness with a nearly 12-fold increase from highly polar methanol to a solvent with lower hydrogen bonding such as DMSO. However the basal brightness of **mero79** is too low. Therefore this dye might be more useful for *in vitro* fluorescence screening than for ratio images in live cells which require signal-to-noise ratios of over 3.0 across whole cell regions. These near infrared merocyanine dyes not only exhibit intensity changes in excitation and emission spectra but also have wavelength shifts in various solvents (**Table 1.1** & **Fig 1.12**). For instance, **mero79**, **mero80**, and **mero81** showed similar excitation and emission intensity values in isopropanol and 1,4-dioxane, but the wavelengths of these dyes were more blue-shifted in 1,4-dioxane.

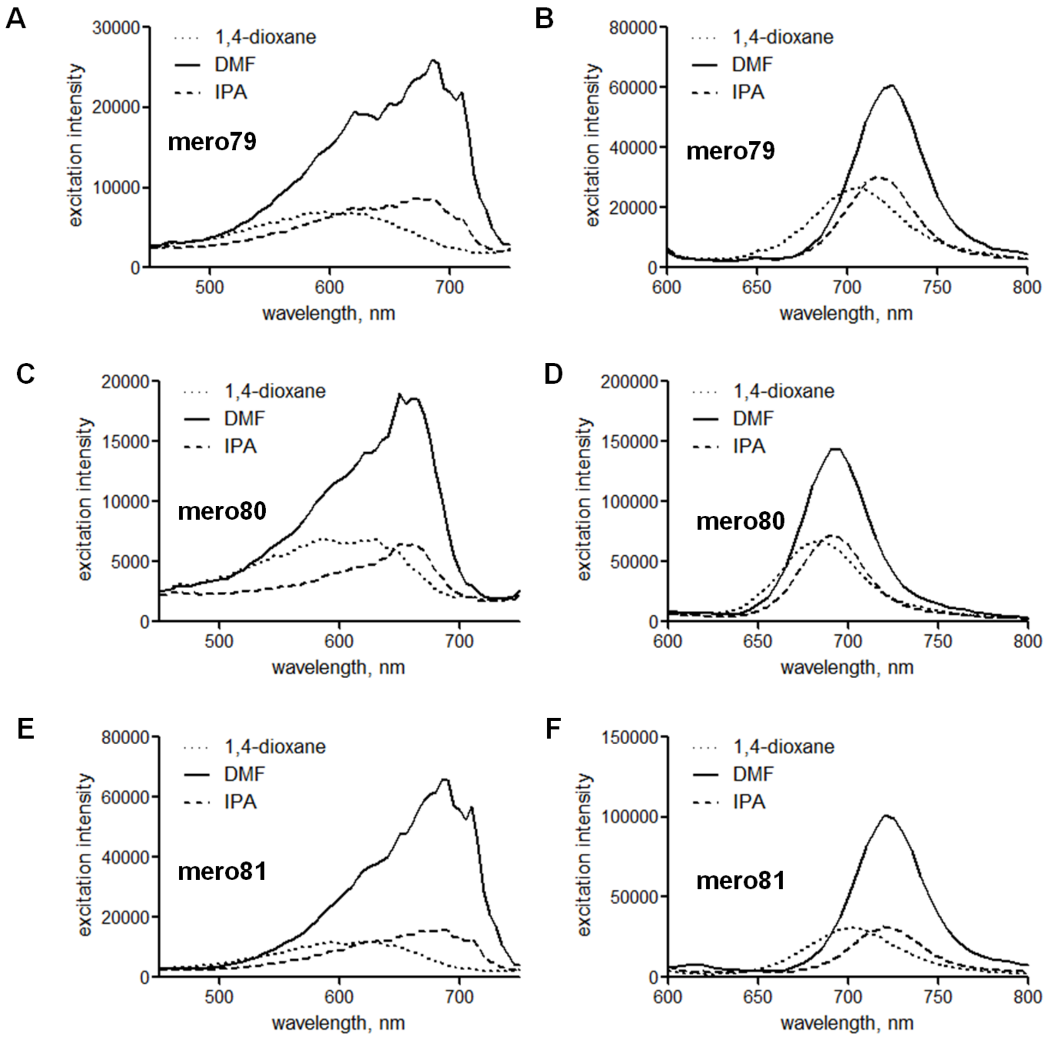

Figure 1.12 Solvent-sensitive fluorescence of NIR merocyanine dyes.
10 μM of dyes were dissolved in 1,4-dioxane, dimethyl formamide (DMF) and iso-propanol (IPA). **A.** Excitation spectra of **mero79. B.** Emission spectra of **mero79. C.** Excitation spectra of **mero80. D.** Emission spectra of **mero80. E.** Excitation spectra of mero81. **F.** Emission spectra of **mero81.**

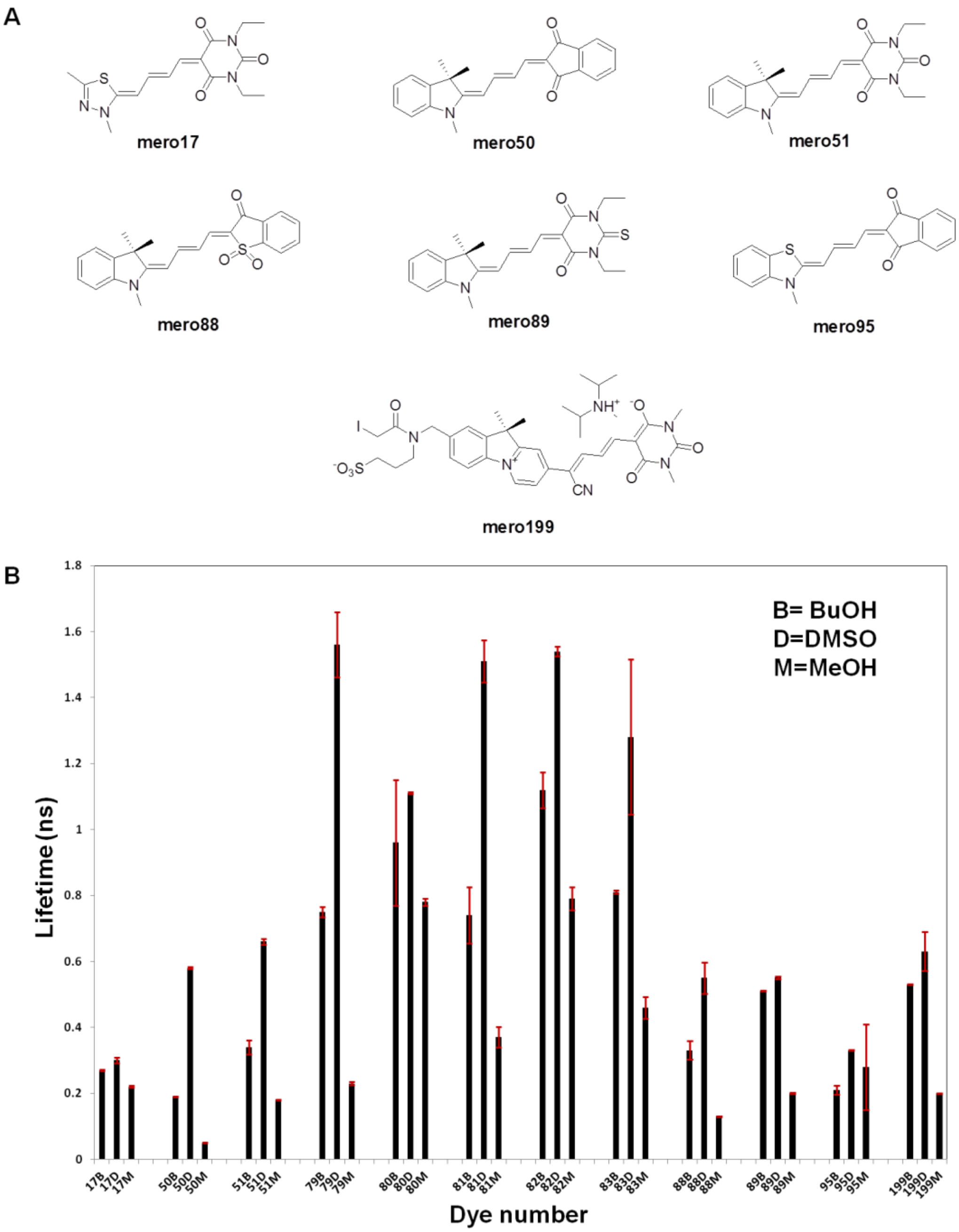

Figure 1.13 Solvent-sensitive fluorescence lifetime values of red and NIR merocyanine dyes.

A. Structures of red merocyanine dyes. Structures of tested near infrared merocyanine dyes were presented in **Fig 2.1**. **B.** Fluorescence lifetime values of merocyanine dyes in n-butanol (BuOH, abbreviated as B), dimethyl sulfoxide (DMSO, abbreviated as D) and methanol (MeOH, abbreviated as M). The measurement and data analysis was conducted by Dr. Elizabeth Hinde in the Gratton group at the University of California at Irvine.

The fluorescence lifetime of a molecule is independent of fluorophore concentrations and many other artifacts. Thus sensors based on solvatochromic dyes should not require a second insensitive fluorophore for ratio imaging in living cells using fluorescence lifetime imaging microscopy (FLIM). We set out to find near infrared dyes with the largest solvent-dependent fluorescence lifetime changes through collaborations with the laboratory of Dr. Enrico Gratton at the University of California at Irvine. The screening included seven red merocyanine dyes and five near infrared merocyanine dyes (**Fig 1.8** & **Fig 1.13A**).

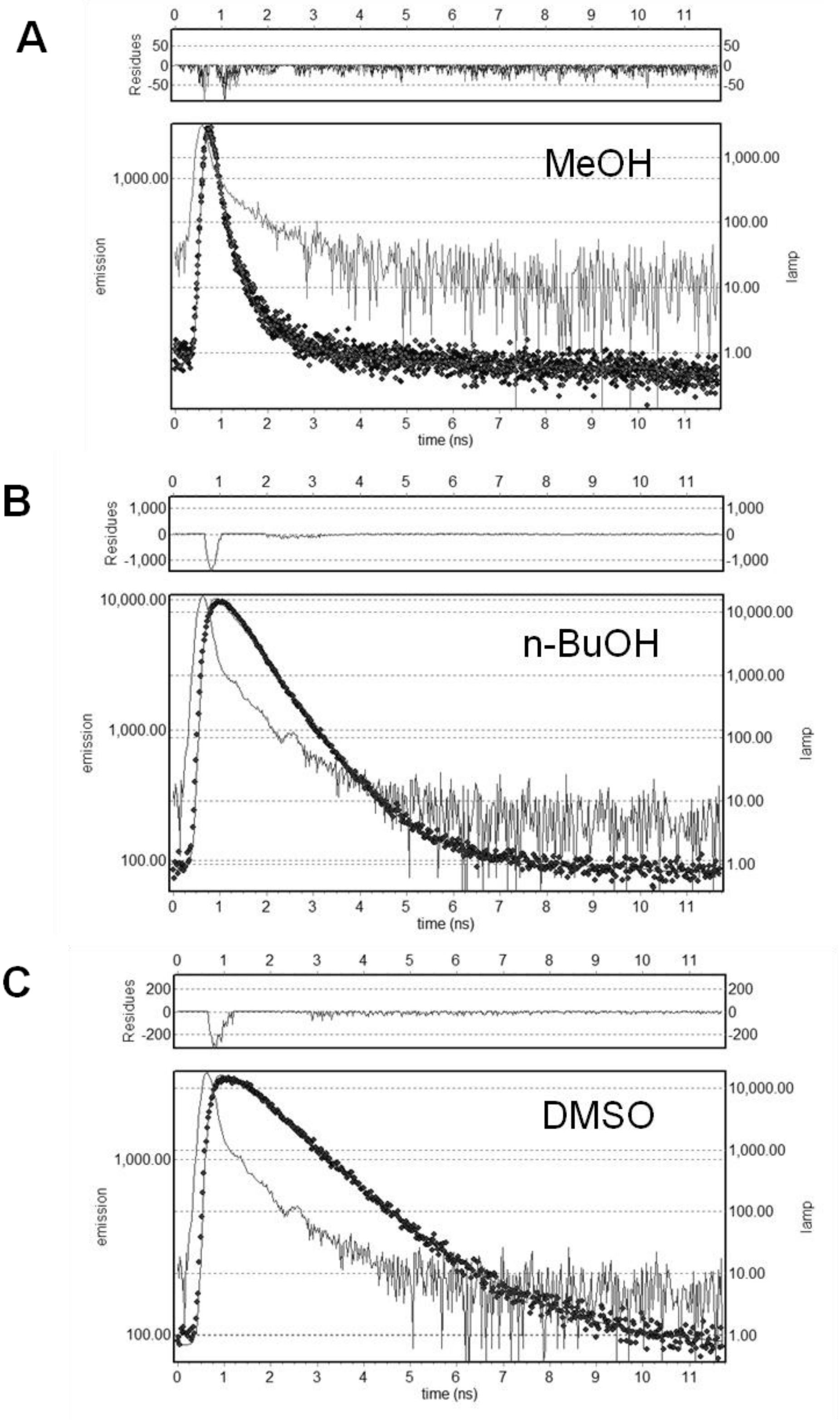

Figure 1.14 Fluorescence decays of mero79 in MeOH, BuOH, and DMSO.
The measurement was conducted by Dr. Elizabeth Hinde in the Gratton group at the University of California at Irvine.

In general, the near infrared dyes have much longer lifetime values than the tested red merocyanine dyes (**Fig 1.13B**). **Mero79**, the near infrared merocyanine dye with the largest change in dye brightness, also possesses the largest change in fluorescence lifetime with an average lifetime of 0.23 ns in methanol and an average lifetime of 1.53 ns in DMSO. All the tested dyes showed single exponential fluorescence decay kinetics as shown in the example of **mero79** (**Fig 1.14**). **Mero81** and **mero83** showed similar solvent-dependent fluorescence lifetime changes because the two dyes share the same combination of the electron donor **I** and the electron acceptor **SO**.

We next examined whether dye fluorescence responds to changes in pH and viscosity in the environment (**Fig 1.15**). Ideal solvatochromic dyes should possess constant fluorescence intensity throughout the physiological pH values ranging from pH 5.5 to pH 8.0. Water soluble derivatives of **mero79 (I-Pht)**, **mero80** (**I-BA**) and **mero81** (**I-SO**)—**mero97 (IS-Pht)**, **mero84 (IS-BA)** and **mero83 (IS-SO)** were employed here for fluorescence measurement in aqueous solution. **Mero97** was not reported because of its low emission intensity in glycerol-water mixture. We found that **mero83** is slightly brighter at lower pH while **mero84** is slightly brighter at higher pH. The pH-dependent fluorescence changes of the two dyes were regarded as insignificant as compared to polarity-dependent fluorescence changes.

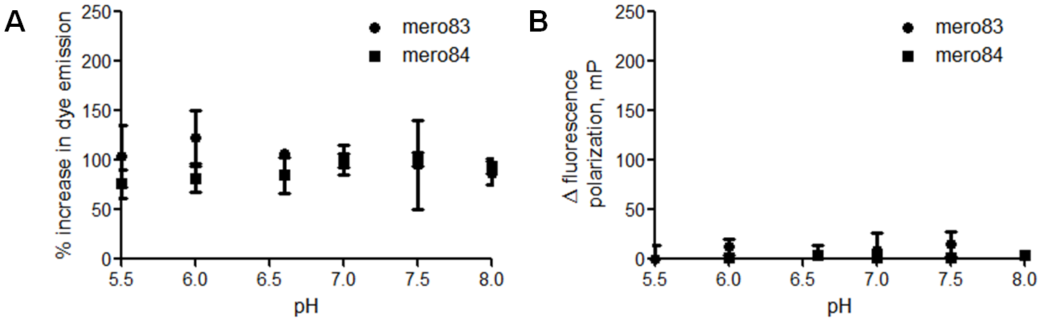

Figure 1.15 Effects of pH on the fluorescence properties of NIR merocyanine dyes

A. Relative dye emission intensity values of 10 μM **mero83** (closed squares) and **mero84** (closed squares) in phosphate buffer (50 mM NaH_2PO_4) at pH 5.5, 6.0, 6.5, 7.0, 7.5 and 8.0. Dye emission intensity values were normalized to the dye emission intensity value at pH 7.0. **B.** Relative dye fluorescence polarization values of 10 μM **mero83** and **mero84** in phosphate buffer at pH 5.5, 6.0, 6.5, 7.0, 7.5 and 8.0. Dye fluorescence polarization values were normalized to the dye fluorescence polarization values at pH 7.0

Dyes with large fluorescence response to viscosity have great potential as either membrane probes or protein activity sensors. Dye emission intensity and the fluorescence polarization values were measured in glycerol-water mixtures (**Fig 1.16**). Solvatochromic dyes usually become brighter in more viscous environments because solvent relaxation is greatly reduced. Both **mero83** (**IS-SO**) and **mero84** (**IS-BA**) exhibited limited fluorescence responses at low concentrations of glycerol molecules in water, with a maximum intensity increase of 5% for **mero83** and 13% for **mero84**. Therefore the fluorescence response of dye-labeled sensor proteins is mainly due to the solvent-sensitivity of dye molecules, rather than variations in glycerol concentrations during *in vitro* assays conducted in 0~5% glycerol-buffer mixture. In summary, **mero84** showed the most pronounced changes in fluorescence intensity and fluorescence changes in response to increased local viscosity.

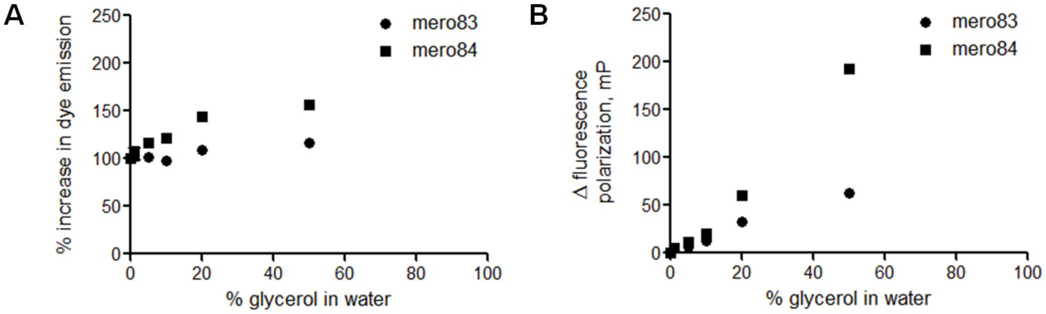

Figure 1.16 Effects of viscosity on the fluorescence properties of NIR merocyanine dyes.

A. Relative dye emission intensity of 10 μM **mero83** (closed circles) and **mero84** (closed squares) in glycerol-water mixture containing 0%, 0.5%, 5%, 10%, 20% and 50% glycerol. Dye emission intensity values were normalized to the dye emission intensity values in water. **B.** Relative dye fluorescence polarization values of 10 μM **mero83** (open circles) and **mero84** (closed squares) in glycerol-water mixture containing 0%, 0.5%, 5%, 10%, 20% and 50% glycerol. Fluorescence polarization values were normalized to the fluorescence polarization value in water.

As the length of the conjugated polymethine chain becomes more extended in near infrared merocyanine dyes as compared to their red parent dyes, association of dye molecules or dye aggregation is likely to be more pronounced because of the increased hydrophobic interactions between dye molecules. Preliminary studies of near infrared merocyanine-labeled sensor proteins revealed that the fluorescence of **I-SO**-labeled sensor proteins was much more quenched than the fluorescence of **I-BA**-labeled sensor proteins. Mutating several aromatic residues near the site for dye attachment failed to rescue dye fluorescence. While the near infrared merocyanine dyes are bright in non-polar solvents such as DMSO and DMF, the dye-labeled proteins become very dim in phosphate buffer. We reasoned that the near infrared dyes might form significant amounts of dye aggregates in water and the effects might be more pronounced when dye molecules are immobilized on bulky sensor proteins. We set to measure absorption spectra of dyes at various concentrations in water. All dyes were pre-dissolved in DMSO and then diluted to a final concentration of 5% DMSO in water. Because all near infrared merocyanine dyes have an apparent blue-shifted absorption peak from the H-type dye aggregates, the absorption spectra were normalized to the monomer absorption peak (**Fig 1.17**). The absorption of the H-type dye aggregates became stronger than the absorption of the monomeric species in the case of **mero79** (**I-Pht**) (**Fig 1.17A**). **Mero80** (**I-BA**) did not show concentration-dependent aggregation (**Fig 1.17B**). **Mero81** (**I-SO**) exhibited moderate response to concentration-dependent aggregation processes; however, the absorption of the H-type dye aggregates existed in high percentage throughout the tested dye concentrations. **Mero83**, the water soluble derivative of **mero81**, contained a smaller absorption peak of H-type aggregates and a new red-shifted absorption peak, presumably to be J-type aggregates. Since H-type and J-type aggregates are determined by the relative spatial orientations of dye molecules, the addition of a charged sulfate group in **mero83** did significantly alter dye-dye interactions. By comparing the absorption spectra of **mero81** and **mero83**, dye aggregation behaviors seemed to be dominated by contributions from hydrophobic interactions, hydrogen bonding interactions, and electrostatic interactions of dye molecules, rather than aqueous solubility issues.

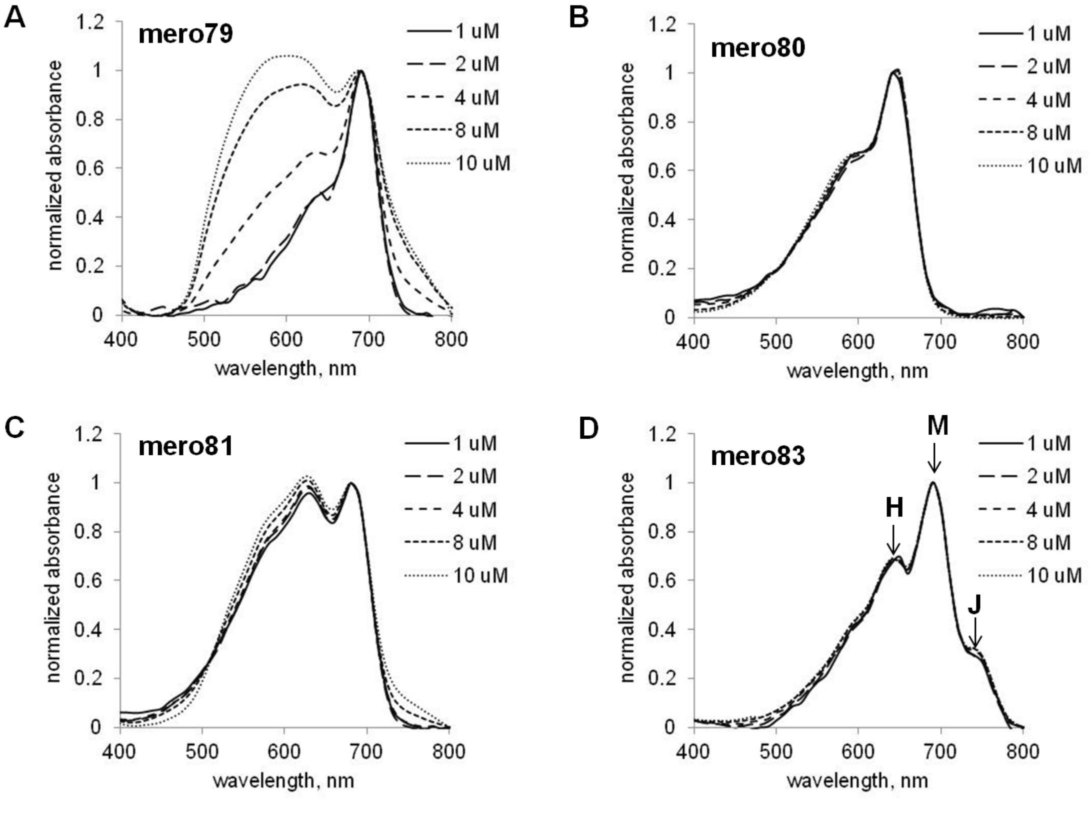

Figure 1.17 Concentration-dependent aggregation of NIR merocyanine dyes in water.

Absorption spectra of near infrared merocyanine dyes at various concentrations were measured in water and normalized to the monomeric (M) species. H and J were denoted as H-type aggregates and J-type aggregates, respectively. All dyes were pre-dissolved in DMSO and diluted to a final 5% DMSO solution in water. Dye concentrations: 1 μM ( ), 2 μM (— —), 4 μM (- - - -), 8 μM (-----) and 10 μM (·····). **A.** Absorption spectra of

mero79. B. Absorption spectra of **mero80. C**. Absorption spectra of **mero81. D**. Absorption spectra of **mero83**, a water-soluble derivative of **mero81**.

H-type aggregates of merocyanine dyes are usually non-fluorescent or weakly fluorescent. Thus the relative fluorescence changes were examined in DMSO-water mixtures (**Fig 1.18**). Both excitation and emission intensity values of **mero79**, **mero80**, and **mero81** showed large changes at various concentrations of DMSO in water. **Mero79** became nearly non-fluorescent in 1:1 DMSO-glycerol mixtures. As dye molecules covalently attached on the surface of biosensor proteins are in a very hydrophilic environment, **mero79** and its derivatives are less likely to generate bright activity sensors based on dye-labeled sensor proteins. A good correlation between the brightness of parent dyes in DMSO-water mixtures and the brightness of near infrared dye-labeled sensor proteins was found: **mero80** and **I-BA**-labeled sensor proteins are both bright in high percentages (50-75%) of water while the fluorescence intensities of **mero81** and **I-SO**-labeled sensors proteins dropped dramatically (**Fig 1.18**).

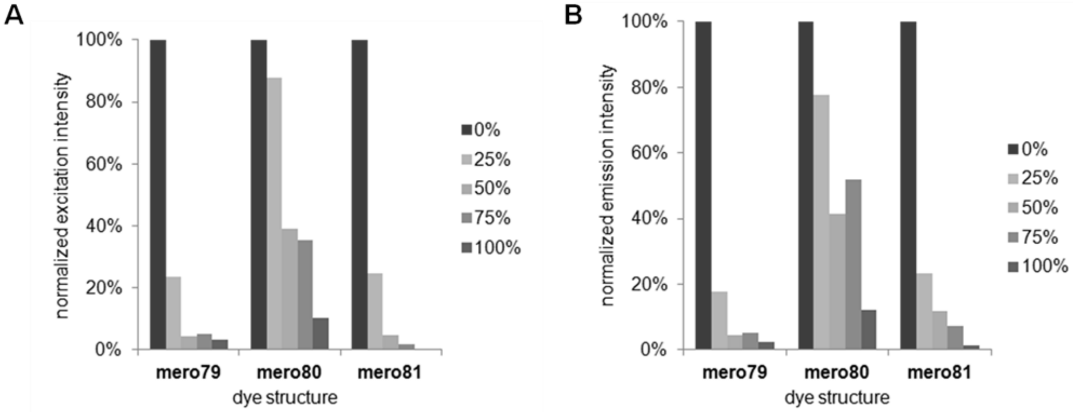

Figure 1.18 Effects of water on the excitation and emission properties of NIR merocyanine dyes.
10 μM dyes were dissolved in DMSO-water mixture containing 0%, 25%, 50%, 75% and 100% water. **A.** Maximum excitation intensity values of **mero79**, **mero80** and **mero81**. **B.** Maximum emission intensity values of **mero79**, **mero80** and **mero81**.

It was observed during the preparation of dye-labeled sensor proteins based on red merocyanine dyes that some dye structures were more prone to over-labeling due to the stronger non-covalent interactions between free dyes and dye-labeled sensor proteins. Another potential problem caused by strong association between free dyes and sensor proteins is non-specific fluorescence response to other endogenous non-target proteins or hydrophobic microdomains. We therefore sought to set up a simple screen before spending extra efforts in synthesizing thiol-reactive versions for protein labeling. Non-specific fluorescence of near infrared merocyanine dyes in response to non-target proteins was tested using bovine serum album (BSA), a commonly used reference for non-specific interactions. **Mero80** (**I-BA**) showed little response to BSA while both the absorption and emission spectra of **mero79** (**I-Pht**) showed distinct properties in the presence of 20 μM BSA in phosphate buffer (**Fig 1.19**).

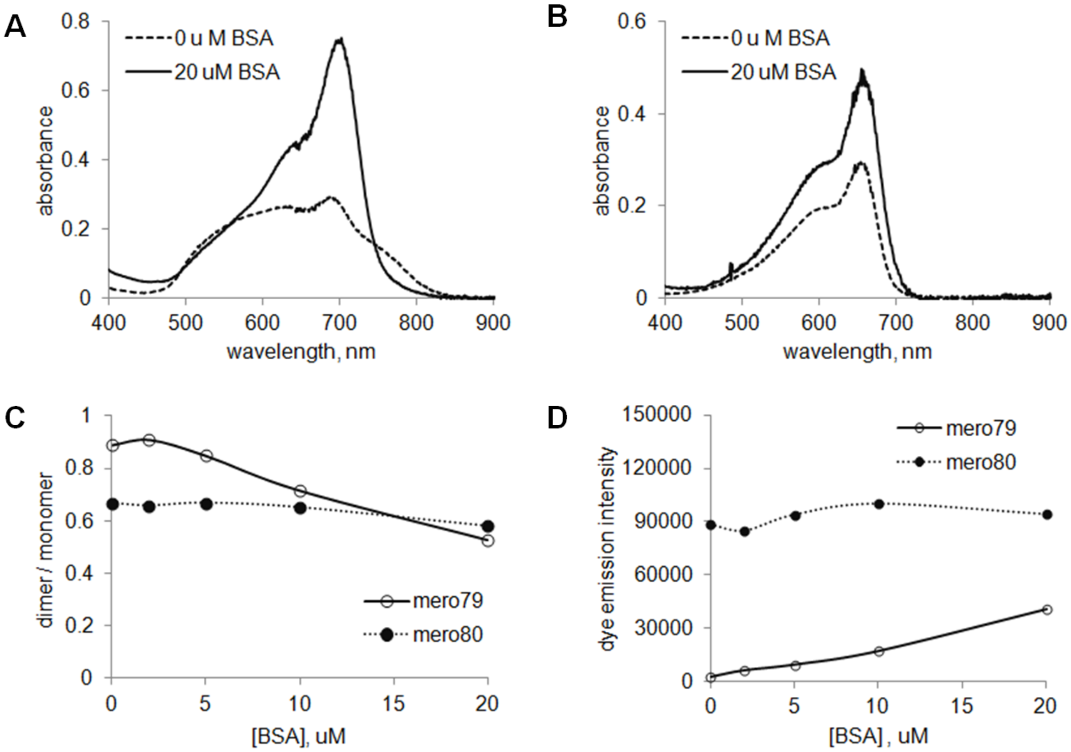

Figure 1.19 Fluorescence responses of mero79 and mero80 to BSA.

A. Absorption spectra of 10 μM **mero79** with and without 20 μM bovine serum albumin (BSA) in phosphate buffer. **B.** Absorption spectra of 10 μM **mero80** with and without 20 μM BSA in phosphate buffer. **C.** Ratio of dimer absorbance and monomer absorbance of 10 μM **mero79** and **mero80** in the presence of various amounts of BSA. **D.** Dye emission intensities of 10 μM **mero79** and **mero80** in the presence of various amounts of BSA.

In conclusion, **mero80** possesses the most ideal properties for intensity-based fluorescence imaging among the tested near infrared dyes—**mero79** (**I-Pht**), **mero80** (**I-BA**), **mero81** (**I-SO**), and **mero82** (**I-TBA**). These properties include photostability, basal brightness in water, and solvent-sensitive fluorescence intensity changes. These beneficial properties are in part due to the fact that **mero80** was the least likely dye to form non-fluorescent H-type aggregates. However, **mero80** has the smallest solvent-dependent difference in fluorescence lifetime while **mero79** (**I-Pht**) and **mero81** (**I-SO**) showed useful changes in fluorescence lifetime of 0.13 ns and 0.08 ns, respectively. **Mero79** has the best solvent-sensitive fluorescence response in intensity and lifetime but it has severe issues with aggregation in water and non-specific response to off-target proteins. Though **mero82** has the best basal and second highest maximum brightness among the new dyes, this dye is the least photostable and is prone to be spontaneously converted to blue-shifted fluorophores and other species after long term storage at 4 ^{o}C. Therefore, further development of mono-functional dyes for the generation of red-shifted sensor designs was focused on derivatives of **mero80** and **mero81**.

1.3.3 Synthesis and spectral properties of thiol-reactive NIR merocyanine dyes

Each near infared merocyanine dye molecule was functionalized with a thiol-reactive group for labeling of cysteines and a sulfate group for improving the overall water solubility. Incorporation of the charged sulfate group to the hydrophobic merocyanine dye molecule could also help reduce non-specific dye-sensor protein binding interactions and provide additional charge-charge interactions and hydrogen bonding interactions to the sensor-target binding interface.

For dye-iodoacetamde molecules **mero77 (I-SO-IAA)** and **mero99 (I-BA-IAA)**, the synthesis started with 1,3-propane sultone and 3-bromopropyl amine via a base-catalyzed ring-opening S_N2 reaction (**Fig 1.20**). The product compound **7** was then used to alklylate 2,2,3-trimethylindolenine **I** to yield compound **8**. The crystal-like compound **8** precipitated out from the reaction mixture and was filtered off, followed by immediate drying under high vacuum. Because of the highly hygroscopic character, compound **8** was used directly in the next step without further purification. The one pot procedure for the preparation of water soluble chloroacetamide derivatives was adapted from the previously described protocol for the preparation of red merocyanine derivatives. Because the same reaction led to multiple species for preparation of near infrared merocyanine derivatives, the reaction must be terminated while the majority of starting material has not yet been consumed. As monitored by absorbance spectra of reaction mixtures taken every 30 min after mixing of all reaction components, the molar ratios of product to starting material reached a plateau within the first or second hour of reaction time (data not shown). Overnight reactions usually resulted in the disappearance of blue products, as monitored by thin layer chromatography (TLC). This is consistent with previous observations in the synthesis of certain red merocyanine derivatives where the polymethine chain of dye molecules was found to be susceptible to Michael addition by the nearby free amino group of dye molecules.

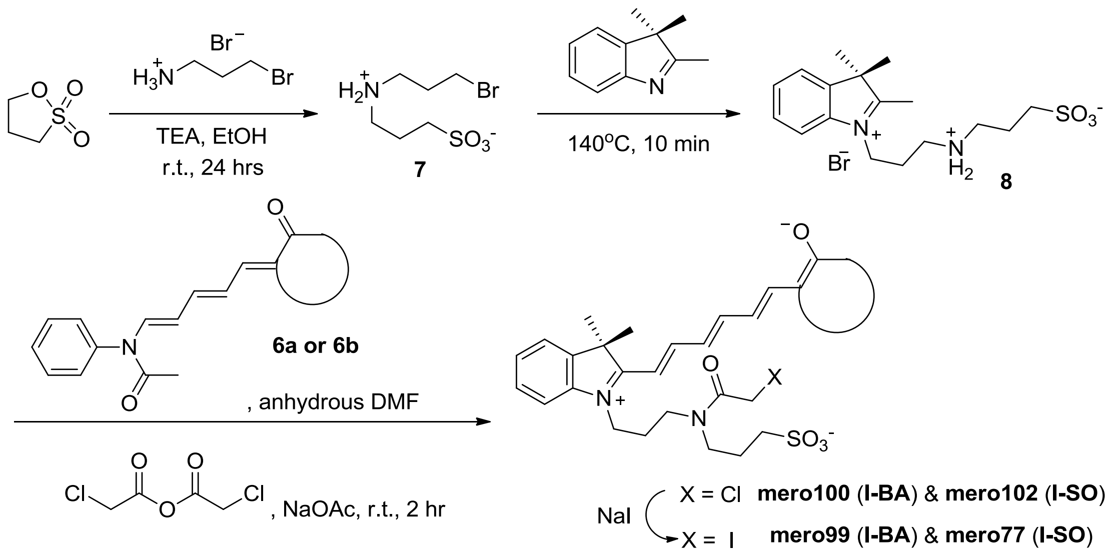

Figure 1.20 Synthesis of thiol-reactive NIR merocyanine dyes with a sulfate group on the alkyl side chain

In the synthesis of **I-BA** or **I-TBA** derivatives, the red fluorescent **BA-BA** and **TBA-TBA** side products also formed immediately after reaction. This is likely attributed to the intrinsic reactivity of barbituric acid moieties. The other distinguishable side product appeared to be blue-green or green with an absorption maximum around 750 nm as observed from TLC and HPLC. Because the use of iodoacetic anhydride led to multiple species with no product formation in the one pot reaction, near infrared merocyanine dyes were first equipped with a chloroacetamide or a bromoacetamide group, followed by halogen exchange. As bromoacetic anhydride is very toxic and carcinogenic, most dyes were prepared as chloroacetamide derivatives. Because of the low conversion of starting material and the presence of multiple side products in the reaction mixtures, the overall yields for the one pot preparation of near infrared dye-chloroacetamides were much lower than the yields for the preparation of red versions. The last step, halogen exchange, must be conducted in the dark and the product dye-iodoacetamides also need to be purified in the dark. The deep blue crude products tend to turn green immediately and completely in the presence of both iodide ions and light exposure.

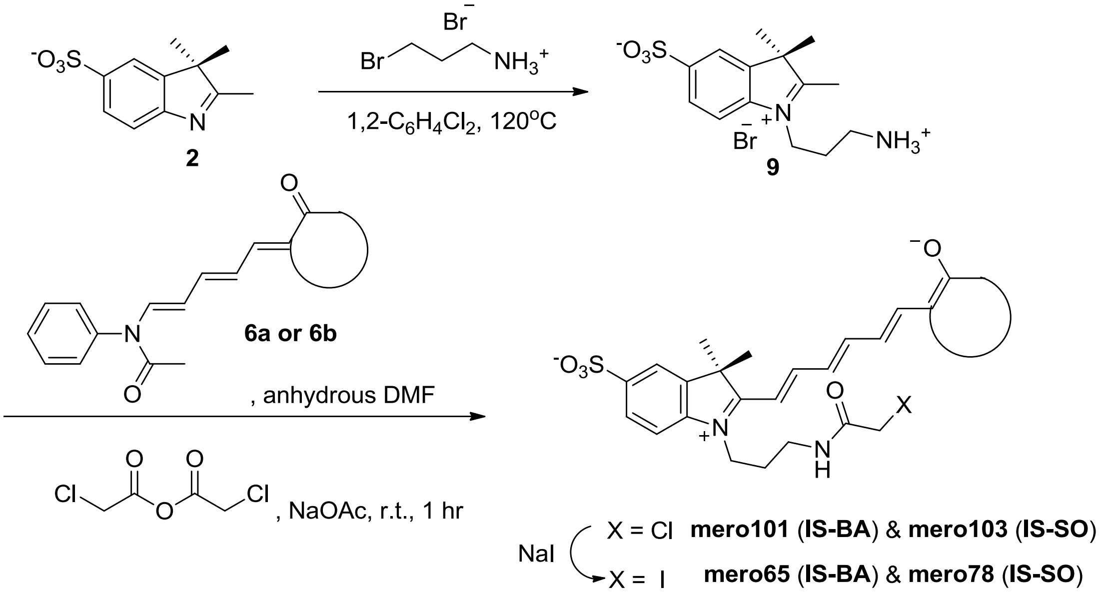

Figure 1.21 Synthesis of thiol-reactive NIR merocyanine dyes with a sulfate group on the aromatic ring of the electron donor moiety.

The synthesis of **mero65 (IS-BA-IAA)** and **mero78 (IS-SO-IAA)** started with an alkylation of compound **2** (**Fig 1.21**), followed by the one-pot preparation of dye-chloroacetamides and halogen exchange. The resulting dye-chloroacetamides, **mero101** and **mero103**, are very polar and need to be purified by reverse phase HPLC. The yields of the one pot preparation of **mero101** and **mero103** are better than the yields of **mero100** and **mero102**, probably because the donor intermediate compound **9** can be isolated in higher purity than the hygroscopic starting material compound **8**.

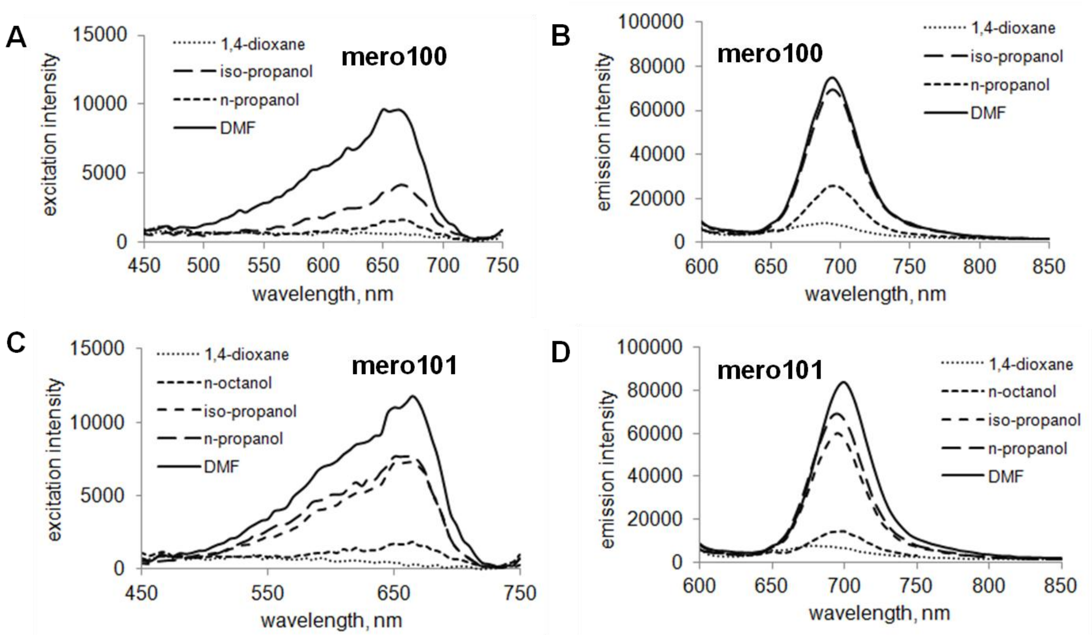

Figure 1.22 Solvent-sensitive fluorescence of thiol-reactive and water soluble NIR merocyanine dyes.
Emission spectra of 0.1 μM **mero100** (**I-BA**) and **mero101** (**IS-BA**) were measured in 1,4 dioxane, n-octanol, isopropanol, n-propanol and dimethyl foramide (DMF).

Mero100 (**I-BA-CAA**) and **mero101** (**IS-BA-CAA**), two of the dye-chloroacetamide derivatives, possess solvent-sensitive fluorescence in various solvents (**Fig 1.22**). **Mero100** exhibited better sensitivity towards hydrogen bonding interactions, as shown by the relative fluorescence intensity values in n-propanol and isopropanol (**Fig 1.22A & B**). **Mero100**, **mero101**, and **mero102** have average quantum yields of 0.14, 0.20 and 0.05 in methanol, respectively, so the first two dyes are more likely to exhibit sufficient brightness for imaging near infrared biosensors in living cells. Formation of J-type dye aggregates was seen in the absorption spectra of **mero100** but this was absent in **mero101**. Compared to **mero100**, **mero101** also has a lower percentage of H-aggregates in water. Similar to the parent dyes **mero80** (**I-BA**, **Fig 1.17B**) and **mero84** (**IS-BA**), **mero100** and **mero101** also showed no concentration-dependent aggregation in the absorption spectra (**Fig 1.23A & B**). Interestingly, **mero102** (**I-SO-CAA**) exhibited reduced absorption of the H-type aggregates and the absorbance of the aggregates was not affected by variation in dye concentrations (**Fig 1.23C**). In addition, unlike the water soluble **mero83** (**IS-SO**, **Fig 1.17D**), **mero102** did not form J-type aggregates in water. We concluded that the addition of the charged sulfate group together with the incorporation of long alkyl side chains to the near infrared merocyanine dyes help reduce dye aggregation problems.

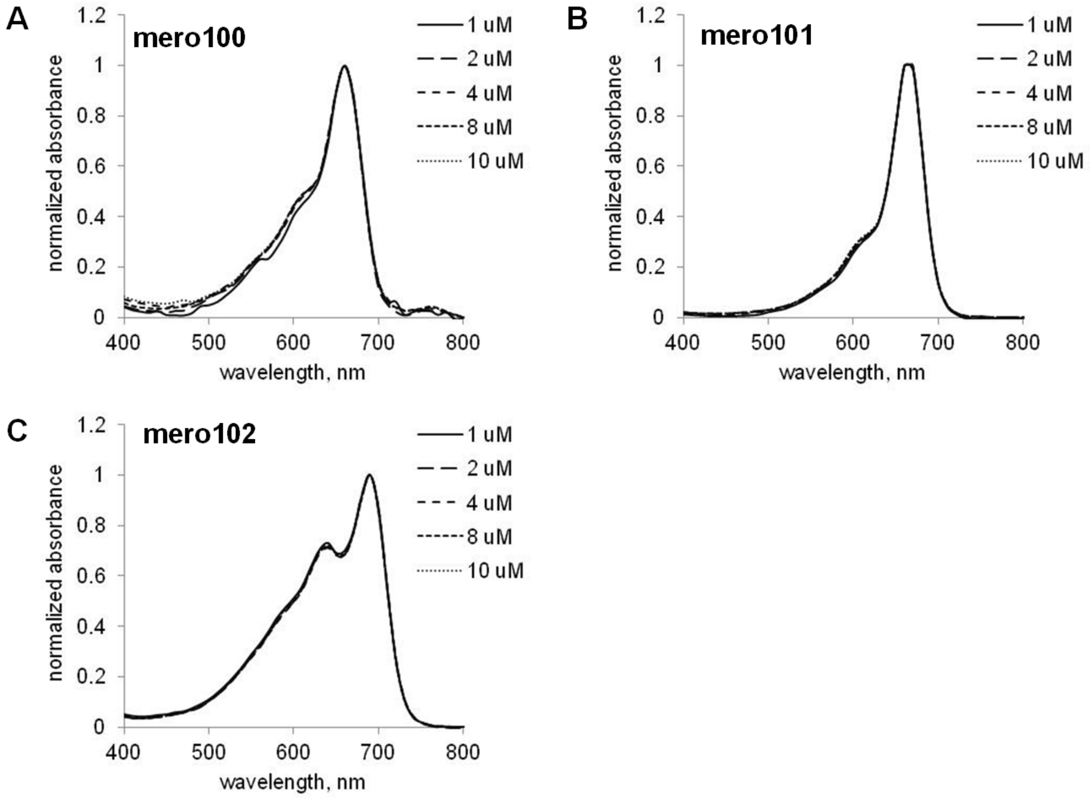

Figure 1.23 Concentration-dependent of thiol-reactive NIR merocyanine dyes in water.
Absorption spectra of **mero100** (**I-BA-CAA**), **mero101** (**IS-BA-CAA**) and **mero102** (**I-SO-CAA**) at 1, 2, 4, 8 and 10 µM in water were normalized to the monomeric species.

Because iodoacetamides are more reactive than chloroacetamides in the S_N2 reaction with deprotonated thiols, the dye-iodoacetamides—**mero65**, **mero77**, **mero78**, and

mero99 were chosen for generation of red-shifted biosensor designs in the following studies.

1.3.4 Construction of red-shifted biosensor designs using NIR merocyanine dyes

The new near infrared merocyanine dyes were first tested on the dye-based biosensor designs for active Cdc42 GTPases and Src family kinases (SFK). **Mero77** (**I-SO-IAA**) was used to generate near infrared versions of dye-labeled sensor proteins. When **mero77** was covalently attached to a cysteine residue on the biosensor protein molecules, the dye molecules became more prone to form H-type dye aggregates in phosphate buffer (50 mM NaH_2PO_4, pH 7.6) as shown in comparison with the absorption spectra of **mero77** in various solvents (**Fig 1.24**).

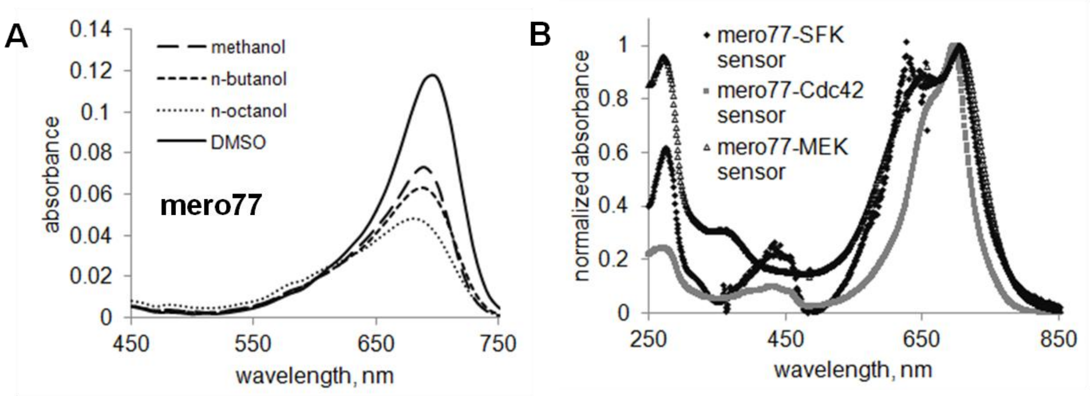

Figure 1.24 Absorption spectra of mero77 (I-SO-IAA) and mero77-labeled sensor proteins.
A. Absorption spectra of 10 μM mero77 in methanol, n-butanol, n-octanol and DMSO. **B.** Normalized absorption spectra of mero77-labeled biosensor proteins for reporting activation of Src family kinases (SFKs), Cdc42 and MEK1/2. The relative absorption of the dimeric and the monoeric species can be used to probe the local environment surrounding the dye molecule.

In general, **mero65**-labeled Cdc42 and SFK sensor proteins were brighter than other near infrared dye-labeled constructs (**Fig 1.25A & B**). Both the Cdc42 and SFK sensor proteins were fused with a monomeric Cerulean fluorescent protein molecule with a C49S mutation to avoid over-labeling.

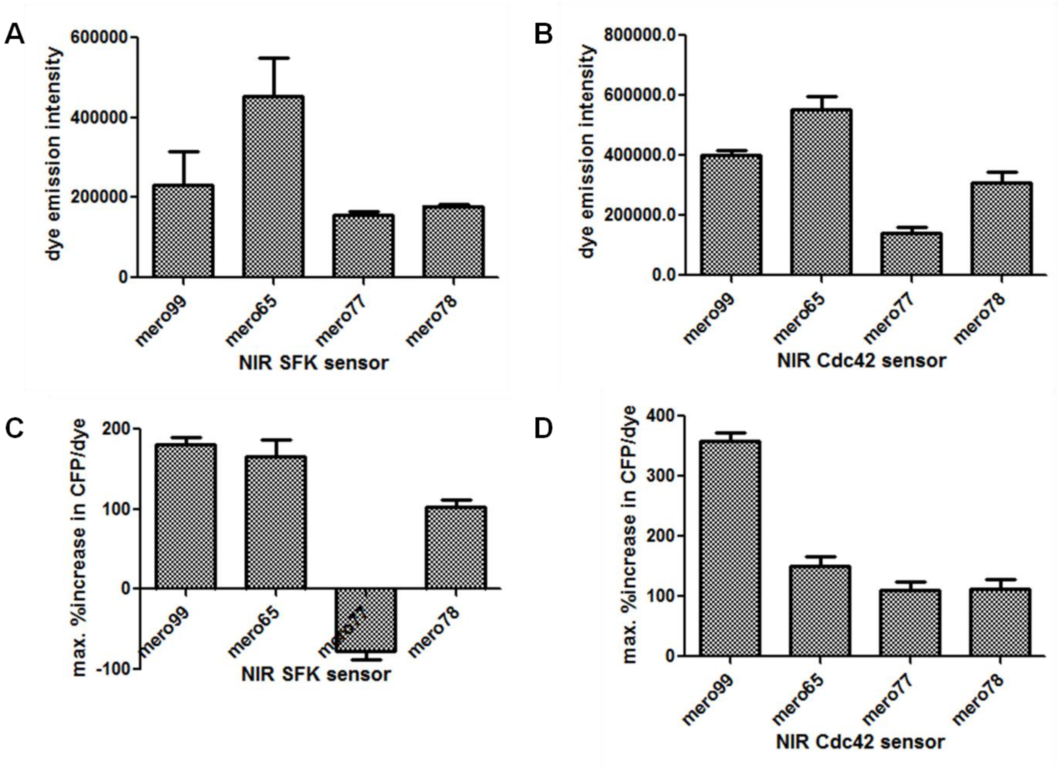

Figure 1.25 Basal brightness and maximum fluorescence change of NIR SFK and Cdc42 biosensors.
A. Average dye emission intensities of near infrared SFK sensor proteins in the absence of target proteins—active Src family kinases. **B**. Average dye emission intensities of Cdc42 sensor proteins in the absence of target proteins— active Cdc42. **C**. The maximum fluorescence response of near infrared SFK upon titration of excess c-Src SH3 domain proteins. **D.** The maximum fluorescence response of near infrared Cdc42 sensors upon titration of excess constitutively active Cdc42 Q61L proteins.

Interestingly, the Cerulean fluorescent proteins exhibited greater fluorescence change than the near infrared merocyanine dyes. For instance, both the emission intensities of the Cerulean fluorescent protein molecule and the dye molecule increased at higher concentrations of c-Src SH3 domain in the **mero78**-labeled SFK sensor design (**Fig 1.26A, C & E**). In contrast, the dye fluorescence remained steady while the Cerulean fluorescence protein first became brighter, followed by a large decrease in emission intensity at higher concentrations of c-Src SH3 domain in the **mero77**-labeled

SFK (**Fig 1.26B, D & F**). Such distinct fluorescence response was also observed in the previously described red dye-labeled SFK sensor designs based on **mero53** and **mero87** dyes. **Mero53** is the red version of **mero78**, while **mero87** is the red version of **mero77**. The main difference between **mero53** and **mero87** is the position of a charged sulfate group. Because mCerulean C49S became the major responding component, ratios for quantification of target protein activity were then defined as the CFP emission intensity divided by the dye emission intensity. Among the tested near infrared SFK sensor designs, **mero99**- and **mero65**-labeled SFK sensor proteins possesses the largest in vitro dynamic range with CFP-to-dye ratios of 180% for **mero99** and 170% for **mero65**.

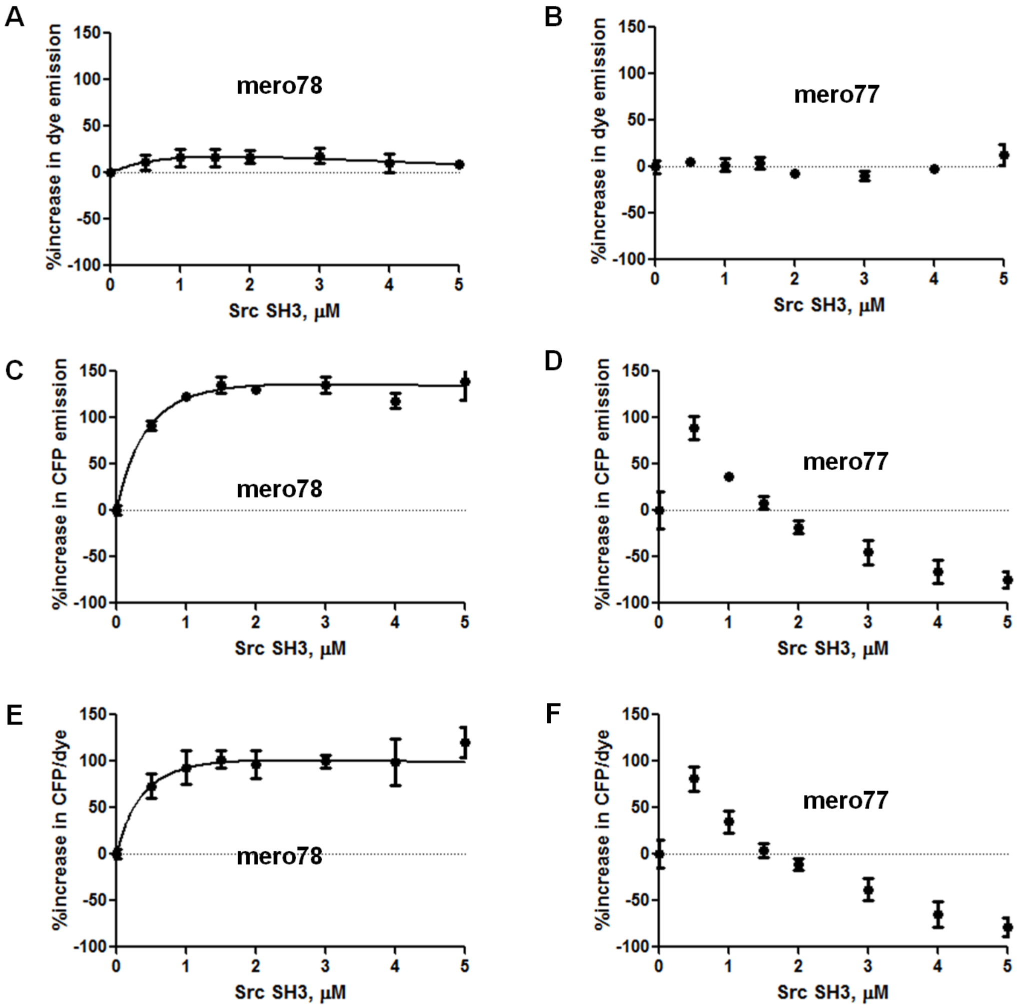

Figure 1.26 ***In vitro*** **fluorescence response of mero77- and mero78-labeled SFK biosensors.**

A. Average increase in dye emission intensity of a **mero78**-labeled SFK sensor when titrated with increasing amounts of c-Src SH3 domain proteins. **B**. Average increase in dye emission intensity of a **mero77**-labeled SFK sensor when titrated with increasing amounts of c-Src SH3 domain proteins. **C**. Average increase in CFP emission intensity of a **mero78**-labeled SFK sensor when titrated with increasing amounts of c-Src SH3 domain proteins. **D**. Average increase in CFP emission intensity of a **mero77**-labeled SFK sensor. **E**. Average increase in CFP/dye emission ratios of a **mero78**-labeled SFK sensor at various concentrations of c-Src SH3 domain proteins. **F**. Average increase in CFP/dye emission ratios of a **mero77**-labeled SFK sensor at various concentrations of c-Src SH3 domain proteins.

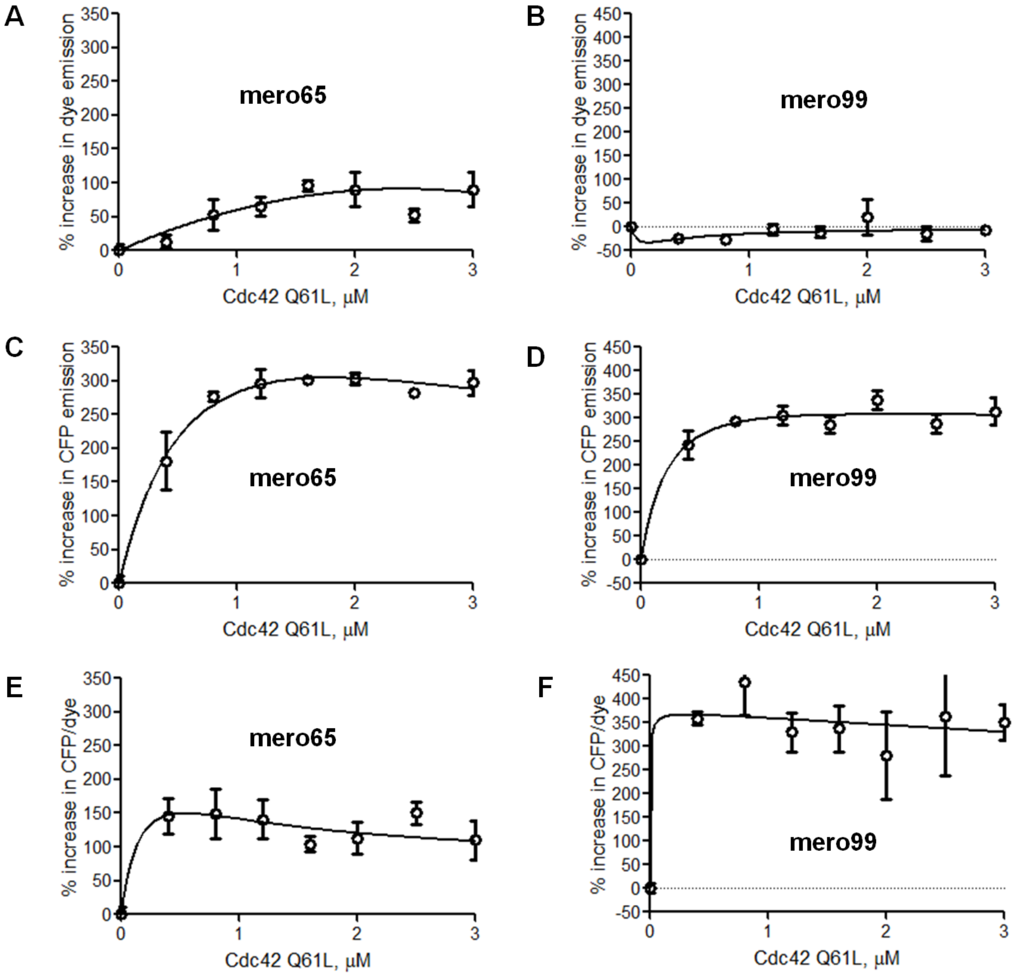

Figure 1.27 In vitro fluorescence response of NIR Cdc42 biosensors.
A. Average increase in dye emission intensity of a mero65-labeled Cdc42 sensor at various concentrations of Cdc42 Q61L. **B.** Average increase in dye emission intensity of a **mero99**-labeled Cdc42 sensor at various concentrations of Cdc42 Q61L. **C.** Average increase in CFP emission intensity of a **mero65**-labeled Cdc42 sensor at various concentrations of Cdc42 Q61L. **D.** Average increase in CFP emission intensity of a **mero99**-labeled Cdc42 sensor at various concentrations of Cdc42 Q61L. **E.** Average increase in CFP/dye emission ratios of a **mero65**-labeled Cdc42 sensor at various concentrations of Cdc42 Q61L. **F.** Average increase in CFP/dye emission ratios of a **mero99**-labeled Cdc42 sensor at various concentrations of Cdc42 Q61L.

All of the near infrared dye-labeled Cdc42 sensor designs exhibited large fluorescence increases relative to the mCerulean C49S molecule at higher concentrations of constitutively active Cdc42 Q61L (**Fig 1.27C & D**). The mCerulean C49S fluorescent protein variant seemed to undergo a fluorescence energy transfer via interactions with near infrared fluorophores or conformation change-induced fluorescence change.

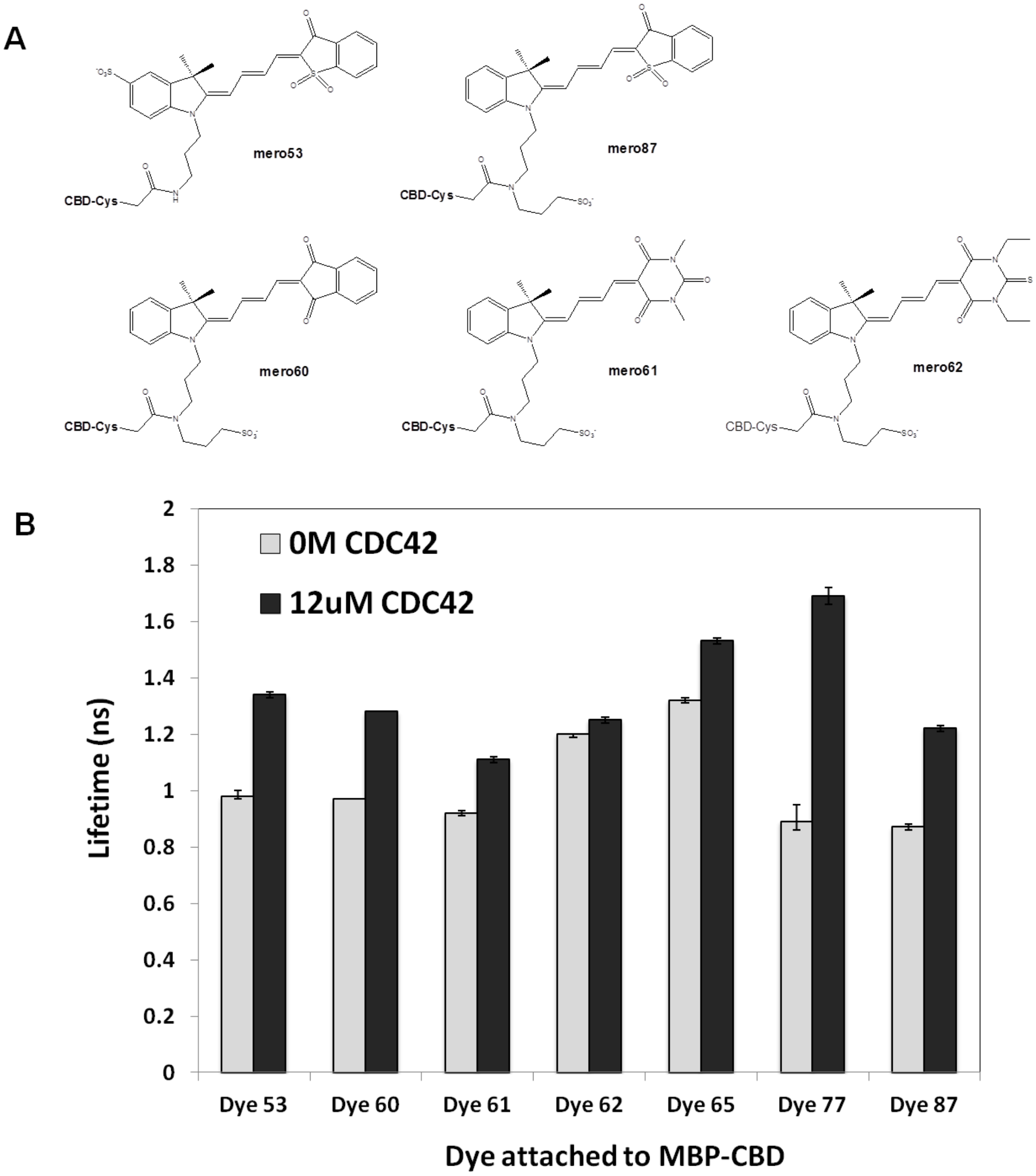

Figure 1.28 Fluorescence lifetime changes of dye-labeled Cdc42 sensor proteins titrated with constitutively active Cdc42 Q61L.

The fluorescent protein molecule of the original sensor design was replaced with a non-fluorescent maltose-binding protein (MBP) molecule. **A.** Structures of thiol-reactive red merocyanine dyes in the screening**. B.** Average fluorescence lifetime values of dye-labeled Cdc42-binding domain (CBD) in the absence and in the presence of constitutively active Cdc42 Q61L.The lifetime measurement and the data analysis were conducted by Dr. Elizabeth Hinde in the Gratton group at the University of California at Irvine.

A library of five thiol-reactive red merocyanine dyes and two thiol-reactive near infrared merocyanine dyes was tested in the established sensor designs for Cdc42. The fluorescence lifetime values of dye-based biosensors of Cdc42 were measured using a Phasor approach (117) through collaboration with the Gratton group at the University of California at Irvine (**Fig 1.28**). The **mero77**-labeled Cdc42 activity sensor has the largest difference in fluorescence lifetime upon binding of active Cdc42 (**Fig 1.29B**). The red **I-SO** versions **mero87** and **mero53** also showed superior changes in fluorescence lifetime among the red Cdc42 activity sensors. **Mero61** and **mero65**, red and near infrared derivatives of **I-BA**, both showed moderate changes in fluorescence lifetime.

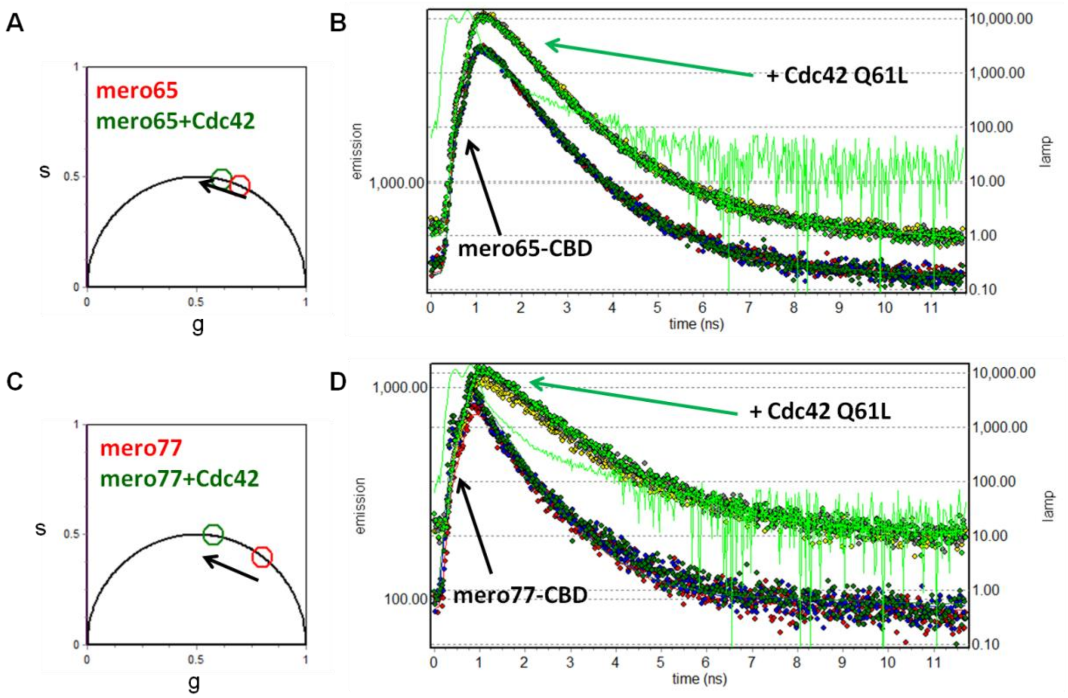

Figure 1.29 Fluorecence decays of mero65- and mero77-labeled Cdc42 biosensors. **A.** Phasor plot of a **mero65**-labeled Cdc42 activity sensor. **B.** Fluorescence decay kinetics of **mero65**-labeled Cdc42 activity sensor after irradiation. **C.** Phasor plot of a **mero77**-labeled Cdc42 activity sensor. **D.** Fluorescence decay kinetics of **mero77**-labeled Cdc42 activity sensor. The measurement was conducted by Dr. Elizabeth Hinde at the Gratton group at the University of California at Irvine.

Because the Phasor approach is based on frequency-domain analysis, a typical Phasor plot provides the information of both modulation and phase of the fluorescence signals. Each fluorescent molecule has its own modulation and phase shifts which can be reflected on a Phasor blot as a subset of g and s values. The smaller g and s values indicate longer lifetime values of the fluorophore. As the distance between (g_1, s_1) and (g_2, g_2) becomes larger, the change in fluorescence lifetime increases. In the case of the **mero77**-labeled Cdc42 activity sensor, Cdc42-bound and unbound sensor proteins have a larger difference in (g, s), as shown as a green and a red circle on the Phasor plot (**Fig 1.29C**). Faster fluorescence decay kinetics was also observed in the raw data of **mero77**-labeled Cdc42 activity sensor (**Fig 1.29D**). In summary, the near infrared **mero77**-labeled Cdc42 activity sensor possesses great potential for fluorescence lifetime biosensor imaging and for co-imaging of multiple biosensors in the same living cell.

1.3.5 Live cell imaging of a red-shifted SFK activity sensor

Spatiotemporal dynamics of endogenous Src family kinases (SFK) were visualized at near infrared wavelengths using a red-shifted sensor. The **mero65**-labeled SFK activity sensor was chosen for ratio imaging because this sensor was the brightest and the most sensitive among the tested near infrared versions of the SFK sensor design. SFK activity was defined by the ratio of CFP emission divided by dye emission. The mCerulean C49S fluorescent protein molecules were monitored with a 436/20X excitation filter and a 470/24M emission filter. **Mero65** was excited with wavelengths ranging from 620 to 660 nm and the dye emission was recorded from 669 to 741 nm. The near infrared dyes require filters with broader bandwidths than shorter wavelength fluorophores because the mercury arc lamp provides only approximately 5% light output at near infrared wavelengths as compared to CFP excitation. The near infrared **mero65**-labeled SFK activity sensor also showed ratio patterns similar to the previously reported red **mero53**-labeled SFK activity sensor (**Fig 1.30**). The dynamic range of **mero65**-labeled SFK activity (1.0-1.8) was approximately two fold greater than the original biosensor design (1.0-1.4).

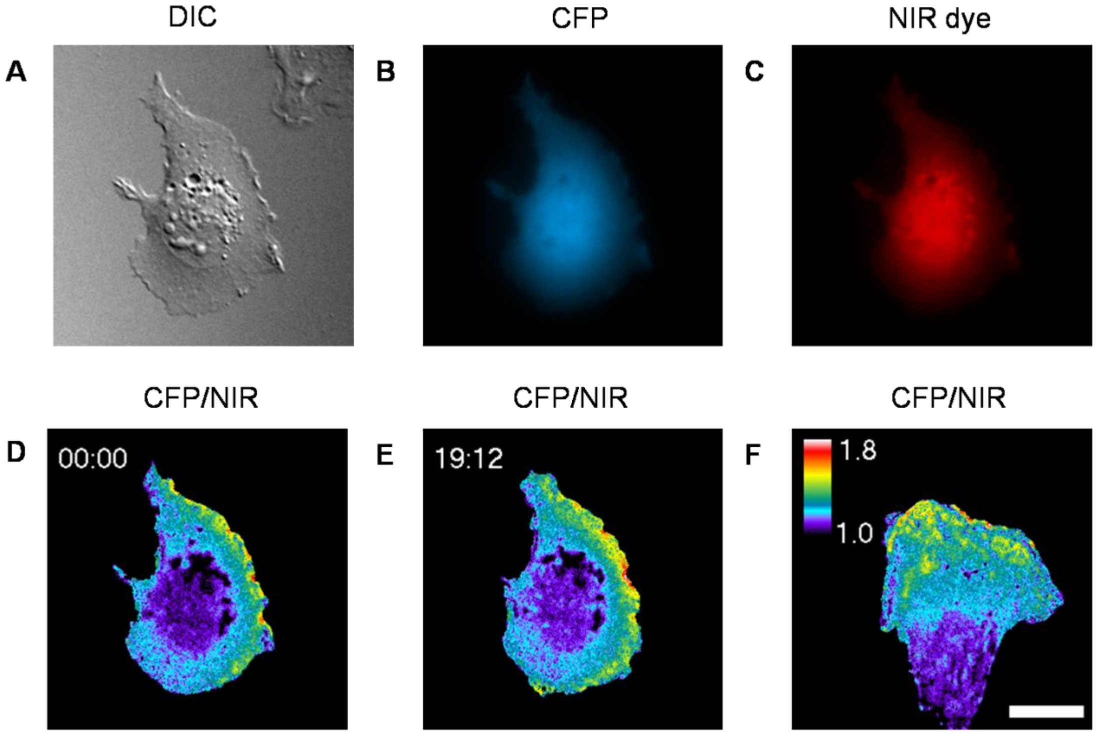

Figure 1.30 Live cell imaging of a NIR mero65-labeled SFK biosensor in NIH 3T3 MEF cells.
A. Differential interference contrast (DIC) image of a biosensor-loaded mouse embryo fibroblast (MEF). **B.** CFP emission image of a biosensor-loaded MEF cell. **C.** Dye emission image of a biosensor-loaded MEF cell. **D.** Ratio image of the biosensor-loaded MEF cell at the first time point. SFK activity was defined by the ratio of CFP to dye emissions. **E.** Ratio image of the same biosensor-loaded MEF cell imaged after 19 min and 12 sec. **F.** Ratio image of the other biosensor-loaded MEF cell.

1.3.6 Characterization of a red merocyanine dye with an intrinsic ratiometric response

Imaging two or more biosensors in the same cell remains a challenge because there are limited wavelengths in the visible region and most biosensor designs require two fluorophores of different colors to eliminate factors such as uneven illumination and varying cell thickness when recording biosensor signals in living cells. Here we describe a bright and photostable red merocyanine dye which exhibits dual fluorescence changes in both intensities and wavelength maxima for ratio imaging.

Multiplexing of current bright and photostable merocyanine dyes in live cells are limited by the need of two fluorophore for ratio imaging of a dye-based biosensor because these dyes prefer the neutral resonance form in the ground state and only show solvent-dependent changes in fluorescence intensity when placed on biosensor proteins; however the zwitterionic resonance form is the major contributor to solvent-dependent fluorescence (**Fig 1.31**). In a separate study of dye properties, we found a negative correlation between photostability and solvent-sensitive fluorescence. Dyes with large fluorescence changes in both intensities and wavelength maxima usually have a very strong electron donor moiety and the α-carbon adjacent to the electron donor moiety is more susceptible to photo-oxidation in the air because of the increased electron density. To rescue the photostability of some bright but not photostable merocyanine dyes, introduction of an electron withdrawing cyano group to the α-carbon has proven to be effective to improve the photostability of **I-SO** and **S-SO** dyes. However, the fluorescence quantum yields of the cyano-substituted merocyanine dyes were greatly reduced as compared to their parent fluorophores. In order to create new merocyanine dyes with balanced properties including brightness, photostability, and dual fluorescence changes in both intensities and wavelength maxima, we first introduced a more electron rich electron donor moiety to enhance dye brightness and solvent-dependent fluorescence properties and then added an electron withdrawing cyano group at the α-carbon adjacent to the electron donor moiety to slow down photo-oxidation rates of the tested dyes.

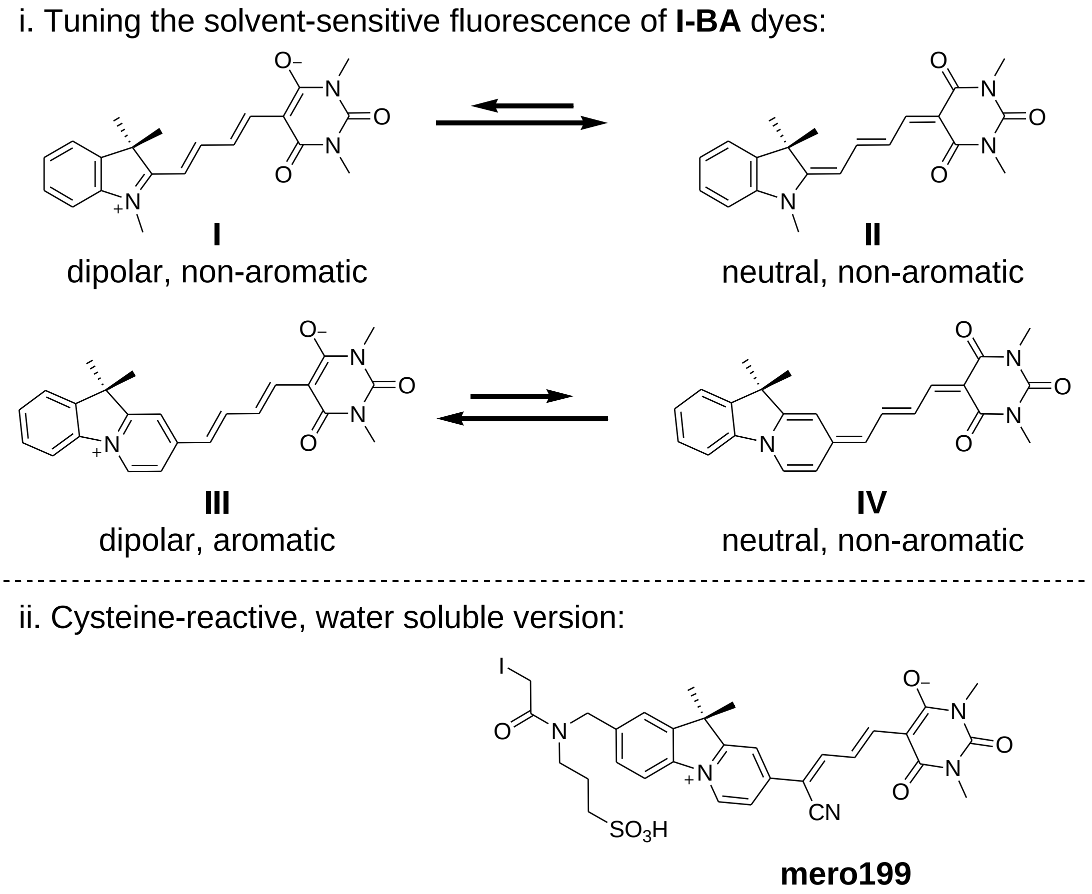
i. Tuning the solvent-sensitive fluorescence of **I-BA** dyes:

ii. Cysteine-reactive, water soluble version:

mero199

Figure 1.31 Resonance forms of merocyanine dyes.
I and **II** respresent typical merocyanine dyes. **III** and **IV** represent new merocyanine dyes. The thiol-reactive derivative mero199 was used for biosensor applications.

dye	solvent	excitation max. (nm)	emission max. (nm)	extinction coefficient (x 10-5, cm-1M-1)	quantum yield	relative photostability
I-SO	MeOH	582	614	1.6	0.03	3.19
	BuOH	582	616	1.4	0.50	
I-BA	MeOH	560	582	0.6	0.10	5.15
	BuOH	564	586	0.8	0.19	
AI-BA	MeOH	585	618	0.8	0.52	0.03
	BuOH	615	654	1.5	0.29	
AI-BA-CN	MeOH	589	613	3.7	0.05	1.25
	BuOH	600	620	2.8	0.25	

Table 1.2 Spectral properties of ratiometric merocyanine derivatives. Quantum yields were measured using merocyanine 540 as an internal standard (quantum yield of merocyanine 540 = 0.39 in methanol, excited at 530 nm). Cy5 was used to measure relative photostability (rel. photostability of Cy5 = 1.0). These properties were measured by Dr. Alexei Toutchkine.

Increased aromaticity was introduced to 2,3,3-trimethylindolenine (**I**) to stabilize the more solvent-sensitive resonance form in the ground state (**Fig 1.31**). Derivatives of **I-BA**, **I-SO**, and **I-TBA** were synthesized and characterized by Dr. Alexei Toutchkine. The resulting dyes have larger Stokes' shifts and solvent-dependent wavelengths than the parent dyes (**Table 1 .2**). For instance, the new dye **AI-BA** has a red shift of 30 nm in excitation spectra and a red shift of 36 nm in emission spectra when transitioning from methanol to n-butanol, while the parent dye **I-BA** only has red shifts of 4 nm in both excitation and emission spectra under the same conditions. **AI-TBA** decomposed easily, probably due to the poor photostability and chemical instability. The extinction coefficients and quantum yields of **AI-BA** were also larger than **I-BA**. However, the photobleaching rate of **AI-BA** was approximately 100 fold faster than **I-BA** and 33 fold faster than the Cy5 dye reference. An electron withdrawing cyano group was added at the α-carbon of **AI-BA** to yield **AI-BA-CN**. **AI-BA-CN** was 42 fold more photostable than **AI-BA** and 1.25 fold more photostable than the Cy5 dye reference. Therefore, the thiol-reactive derivative **mero199** (**Fig 1.31**) was designed based on **AI-BA-CN**.

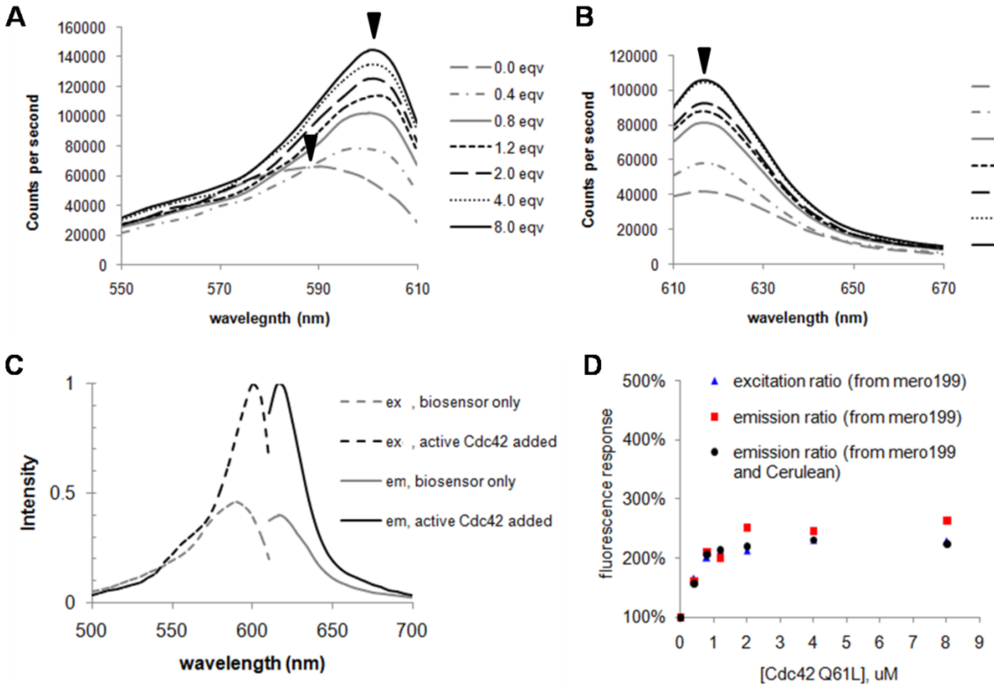

Figure 1.32 Fluorescence response of a mero199-labeled Cdc42 biosensor. Biosensor proteins were titrated with 0, 0.4, 0.8, 1.2, 2.0, 4.0 and 8.0 µM constitutively active Cdc42 Q61L. Each sensor molecule was composed of a **mero199** dye molecule and a mCerulean C49S molecule. **A.** Excitation spectra of the **mero199**-labeled Cdc42 activity sensor at various concentrations of active Cdc42. **B.** Emission spectra of the **mero199**-labeled Cdc42 activity sensor at various concentrations of active Cdc42. **C.** Excitation and emission spectra of the **mero199**-labeled Cdc42 activity sensor in the absence and in the presence of Cdc42 Q61L. **D.** Ratiometric response from a dye/CFP pair and from a single dye **mero199** at increasing concentrations of active Cdc42.

Mero199 was tested on the established biosensor designs for Cdc42 and Src family kinases (SFK). **Mero199**-labeled sensor proteins exhibited ratiometric response in the Cdc42 sensor design but not the SFK sensor design (data not shown). The introduction of the electron withdrawing cyano group to the **AI-BA** dye greatly improved the photostability but also caused a reduction in solvent-dependent wavelength shifts and dye brightness of approximately 50%. **AI-BA-CN** has a red shift of only 11 nm in excitation spectra and a red shift of 7 nm in emission spectra when going from methanol to n-butanol. In the case of the SFK sensor design, the sensor-SH3 binding interactions produced less of a change to the environmental properties surrounding the site of dye attachment when compared to the Cdc42 sensor design. For example, the most sensitive red SFK sensor has a narrower dynamic range of 1.0 to 1.4 while the most sensitive Cdc42 sensor showed a 14.7 fold maximum fluorescence change upon binding of active Cdc42 (data not shown).

Mero199 showed ratiometric response in the excitation spectra of the **mero199**-labeled Cdc42 sensor designs (**Fig 1.32A**) while the dye alone also showed intensity change in the emission spectra (**Fig 1.32B & C**). The biosensor design consisted of a **mero199** dye molecule, a Cdc42-binding domain, and a non-fluorescent maltose-binding protein (MBP) molecule. Upon binding of constitutively active Cdc42 Q61L, a blue shift of 10 nm in excitation spectra and a 2.5 fold enhancement in emission intensity were observed. On the contrary, **I-BA** or **I-SO**-labeled Cdc42 sensor designs did not show any wavelength shifts in either excitation or emission spectra (data not shown) although their parent dyes showed dual fluorescence changes in wavelengths and intensities in various solvents. One possible explanation is that the dye-protein interactions help stabilize the dipolar resonance form of dye molecules in the ground state. Only dyes with greatly enhanced solvent sensitivity such as **AI-BA-CN** are capable of retaining partial ratiometric response even on the protein surface.

We speculate that the 10 nm wavelength shift of the **mero199**-labeled Cdc42 activity sensor is still sufficient for it to be used alone to quantify Cdc42 activity, negating the need of a second fluorophore for ratio imaging. For comparison, the **mero199**-labeled Cdc42 sensor was fused with a monomeric Cerulean fluorescent protein molecule with a C49S mutation to prevent over-labeling. Since most fluorescence microscopes measure fluorescence emission images, protein activity values are usually quantified by ratiometric response in emission spectra of the fluorescence reporter. Based on the Frank-Condon principle, electronic transitions in excitation should be similar to electronic transitions in emission. Ratiometric response in the excitation spectra of the **mero199**-labeled Cdc42 activity sensor should also be reflected in emission ratios with the proper settings. We determined that the best ratiometric response was achieved when collecting emission intensity at 620 nm, using 570 nm and 600 nm as the two excitation wavelengths. Thus we developed three methods to quantify Cdc42 activity in *vitro* (*Method A-C*).

Method A: Using Dye/CFP ratio

$$biosensor\ response\ = \frac{I_{em,620\ nm,mero199}}{I_{em,476\ nm,Cerulean}}$$

I_{em} stands for emission intensity. **Mero199** is the protein activity indicator and mCerulean C49S serves as a volume indicator for normalization. **Mero199** was excited at 600 nm and the dye emission intensity at 620 nm was collected. mCerulean C49S was excited at 435 nm and the CFP emission intensity at 476 nm was recorded.

Method B: Using Dye/Dye excitation ratio

$$biosensor\ response\ = \frac{I_{ex,600\ nm,mero199}}{I_{ex,570\ nm,mero199}}$$

I_{ex} stands for excitation intensity. A second excitation wavelength of **mero199** was used for normalization. Dye emission was set at 620 nm and the excitation intensities were collected at 600 nm (I_{ex}, 600 nm) and 570 nm (I_{ex}, 570 nm).

Method C: Using Dye/Dye emission ratio:

$$biosensor\ response\ = \frac{I_{em,620\ nm,mero199\ (excited\ at\ 600\ nm)}}{I_{em,620\ nm,mero199\ (excited\ at\ 570\ nm)}}$$

This method measures dye emission ratios by using two excitation wavelengths of **mero199**. **Mero199** was excited at 570 nm or 600 nm. The resulting dye emission intensity values at 620 nm were recorded.

For comparison, the intrinsic ratiometric response of **mero199** and the ratiometric response of a pair of **mero199** and mCerulean C49S were recorded at increasing concentration of constitutively active Cdc42 (**Fig 1.32D**). The large correlation coefficient of 0.99 between the two quantification methods confirmed that we could generate a ratiometric response from a single fluorophore using **mero199**. The excitation and emission ratios from a single fluorophore, **mero199**, also exhibited a large correlation coefficient of 0.91.

Mero199-labeled CBD-MBP was used to quantify activation of endogenous activated Cdc42 in living NIH 3T3 mouse embryo fibroblasts (MEF) (**Fig 1.33**). To obtain ratio images from **mero199**, one fluorescence channel was collected by an excitation filter of 577/10X and an emission filter of 645/30M, and the second fluorescence channel was collected using the same emission filter but with an excitation filter of 600/20X. As compared to the conventional Cdc42 activity sensor design based on a typical merocyanine dye **mero87** (**Fig 1.33A**), **mero199**-labeled sensor proteins report similar activation patterns of endogenous Cdc42 (**Fig 1.33B**). The **mero199**-labeled non-binding control biosensor CBD H246D/H249D also showed weak fluorescence response to endogenous activated Cdc42 under the same cell culture and imaging conditions (**Fig 1.34**).

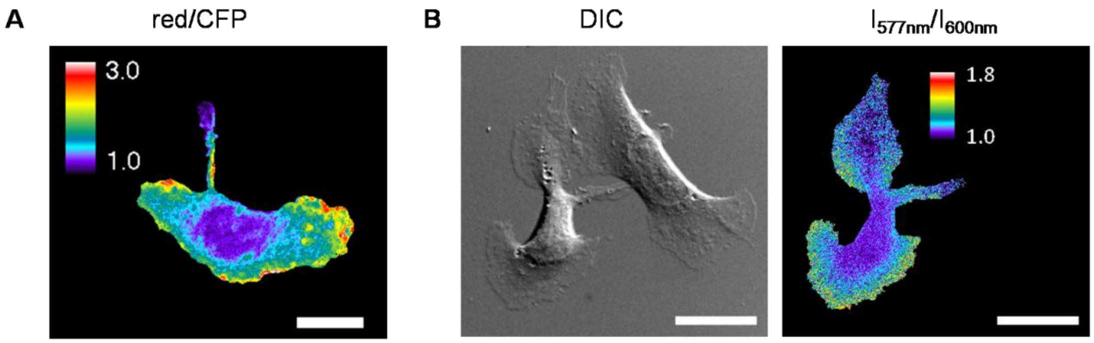

Figure 1.33 Activation of endogenous Cdc42 revealed by mero87- and mero199-labeled sensor designs in MEF cells.

Biosensors were imaed in NIH 3T3 mouse embryo fibroblasts (MEF). Scale bar: 20 μM for all images. **A.** Ratio image of a **mero87**-labeled Cdc42 activity sensor. Cdc42 activity was quantified by the relative emission ratios of **mero87** and mCerulean C49S. **B.** *Left*: Differential interference contrast (DIC) image of one biosensor-loaded cell and one biosensor-free cell. *Right*: Ratio image of **mero199**-labeled Cdc42 activity sensor of the biosensor-loaded cell. Cdc42 activity was quantified by the relative emission intensity ratios recorded at 577 nm and 600 nm excitation wavelengths.

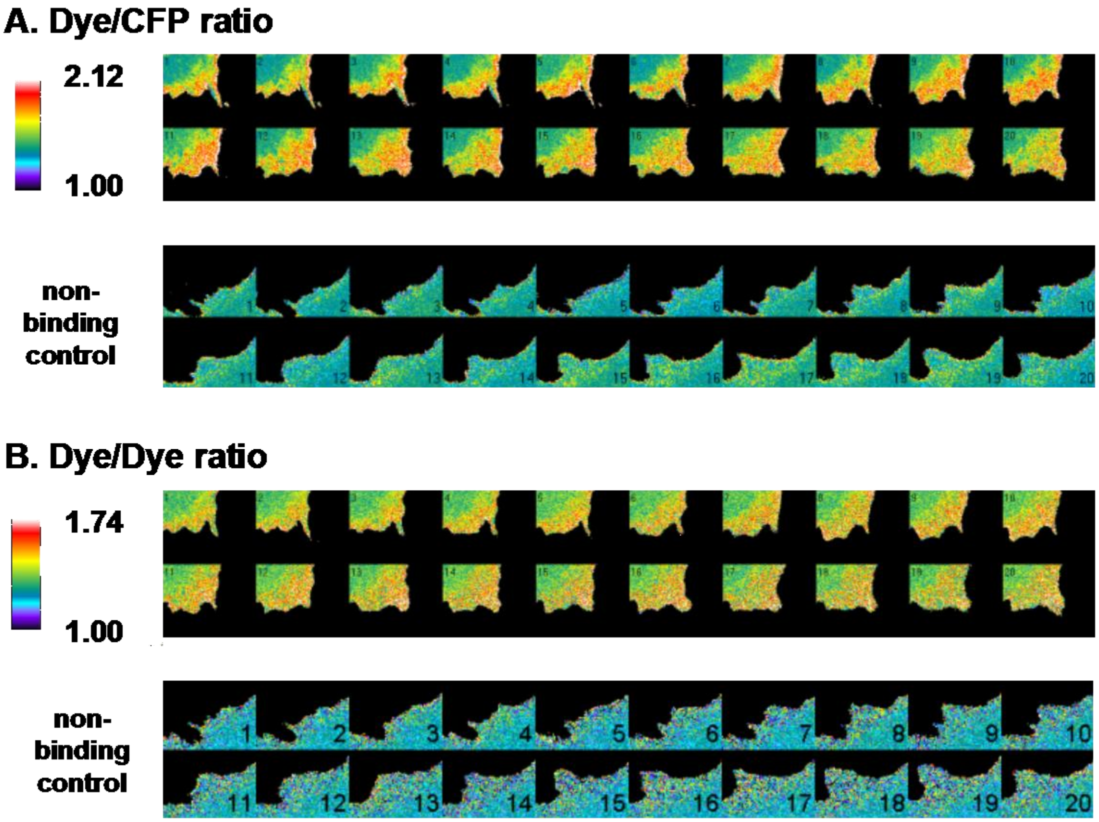

Figure 1.34 Cdc42 biosensor ratios at the protrusion sites of MEF cells.

Cells were loaded with **mero199**-labeled CBD-mCerulean C49S via microinjection. Each image was acquired using a 30 second increment. **A.** *Top*: Cdc42 activation was quantified by dye-to-CFP emission ratios. *Bottom*: Dye-to-CFP emission ratios of a non-binding mutant sensor. **B.** *Top*: Cdc42 activation was quantified by the intrinsic ratiometric response of **mero199**. *Bottom*: Dye-to-dye emission ratios of a non-binding mutant sensor.

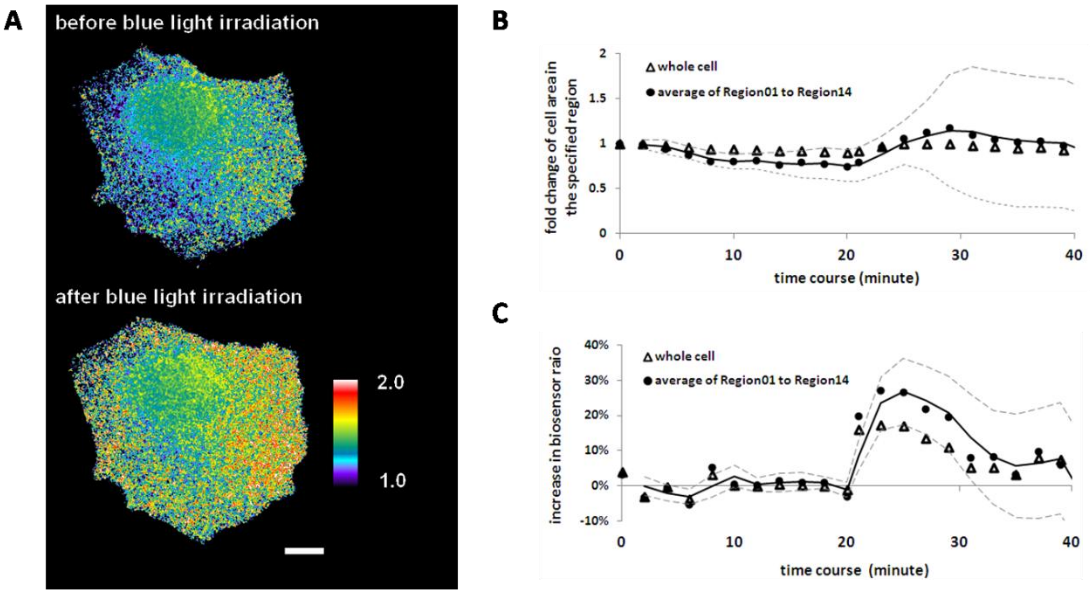

Figure 1.35 Endogenous Cdc42 became more activated during cell spreading as initiated by a photoactivatable Rac Rho GTPase.
NIH 3T3 mouse embryo fibroblasts (MEF) stably expressing photoactivatable mVenus-LOV2-Rac1 Q61L (PA-Rac) were loaded with **mero199**-labeled Cdc42 activity sensor (CBD-MBP). Fourteen regions with an identical size at the cell edges were used for comparison of Cdc42 activation in the whole cell level and specifically at the cell edge. At the 20th min, cells were irradiated with 5 sec of GFP excitation per 10 sec cycle. Dye fluorescence images were acquired at every 2 min intervals. **A**. Ratio images of Cdc42 activity before and after photoactivation of PA-Rac. **B**. Change in total cell area and in the fourteen regions at the leading edge in response to photoactivation of PA-Rac. **C**. Change in biosensor ratios in the entire cell and in the fourteen regions at the leading edge in response to photoactivation of Rac1 Q61L.

The **mero199**-labeled Cdc42 activity sensor doesn't require a second fluorophore for ratio imaging. Thus this new red fluorescent sensor can be easily used together with a second biosensor or a protein manipulation tool with orthogonal wavelengths. It is extremely difficult to characterize dye-based biosensors using the traditional starvation-stimulation protocols because starved cells respond poorly to microinjection or bead loading. Therefore protein manipulation tools that selectively activate a known upstream activator in non-starved conditions would be valuable for not only studying cross-talk of multiple signaling molecules in the same living cell but also for characterization of non-cell permeable and non-genetically-encodable sensor designs. For instance, Rac and Cdc42 GTPases are both important regulators of cell motility. There is no direct evidence regarding the possible role of Rac in regulating Cdc42 during cell migration. Here we imaged the **mero199**-labeled Cdc42 activity sensor molecules in MEF cells stably expressing photoactivatable Rac1 Q61L (PA-Rac) (**Fig 1.35**). This photoactivatable Rac is composed of an mVenus fluorescent protein molecule as an indicator of protein expression levels, a photosensory LOV2 domain for light regulation, and a constitutively active Rac1 Q61L molecule for effector activation (118). Upon blue light irradiation, the photosensory LOV2 domain undergoes a large conformational change and the constitutively active Rac Q61L protein molecule fused at the C-terminal of the LOV2 domain becomes accessible for activating the downstream effectors such as p21-activated protein kinase, resulting in protrusions and lamellipodia. Because cells are highly dynamic and heterogenous, not every Rac-activated cell produces huge cell spreading and protrusions upon light irradiation. In the preliminary studies, the **mero199**-labeled Cdc42 activity sensor only showed fluorescence increase in cells with large increases in cell area upon blue light irradiation and the biosensor signals remained steady in cells with no cell area change (**Fig 1.35B & C**). Increase in Cdc42 activity was more pronounced at the leading edge than the entire cell. This is consistent with the EGF-stimulation experiment of **mero199**-labeled Cdc42 activity sensor in MEF cells where the biosensor ratios also increased during cell spreading induced by EGF. A good correlation between cell area and total Cdc42 activity was consistently seen in these two types of experiments. It would be interesting to dissect the underlying mechanism of cell spreading and activation of endogenous Cdc42 at the cell edge.

1.3.7 Co-imaging the spatiotemporal dynamics of endogenous Cdc42 and SFK activation in the same living cell

Next we tried to co-image two dye-based biosensors in the same living cell. It has been challenging to image multiple protein activity sensors in the same cell because both the FRET type sensors and the typical dye-based sensors require two colors for ratio imaging and there are a limited number of wavelengths in the visible region for generation of orthogonal sensor designs. With the new near infrared merocyanine dyes and the new red ratiometric merocyanine dye **mero199**, we sought to co-image the spatiotemporal dynamics of endogenous Cdc42 and SFK in the same living cell using a **mero199**-labeled Cdc42 activity sensor and a **mero65**-labeled SFK activity sensor. We were able to begin by using a set of excitation filters, emission filters and a dichroic available in the Hahn laboratory (**Fig 1.36**). Though these were not optimal for all fluorophores, they were sufficient for preliminary studies.

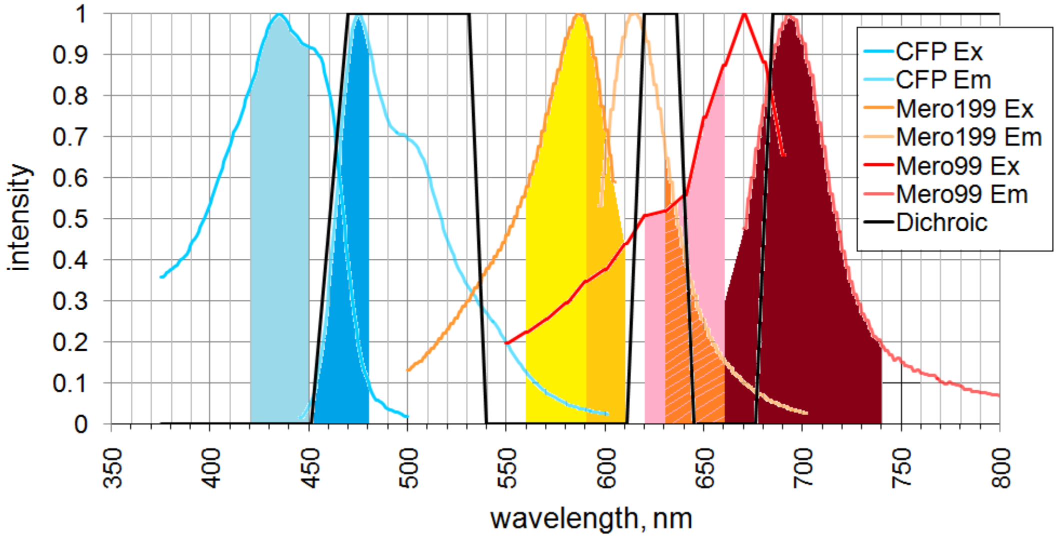

Figure 1.36 Filter and dichroic setting for co-imaging CFP, mero199 and mero65 channels in the same cell.

The transmittance of the dichroic is presented as a black line.

The first issue we encountered was in the simultaneous delivery of the two types of dye-labeled sensor proteins. As the total amount of sensor proteins doubled for multiplexing, the protein solution containing the two sensors was more prone to cause severe clogging in micropipettes during microinjection. The best solution to this problem was found to be the use of bead loading methods to deliver these dye-labeled sensor proteins. Unlike microinjection that usually uses 50 µM or higher concentrations for loading, the loading concentrations for bead loading were limited to 10~30 µM. At higher loading concentrations, severe fluorescence backgrounds and low numbers of biosensor-loaded cells were observed. Very bright cells usually rounded up because of the dominant negative effects from elevated total sensor concentrations of SFK and Cdc42 sensor proteins. Therefore all fluorescent channels required longer exposure time to accumulate sufficient signal-to-ratios to enable the imaging of healthy biosensor-loaded cells. The lack of optimal microscope settings, together with the increasing biological perturbation at higher total biosensor concentrations, made it difficult to rapidly acquire biosensor signals.

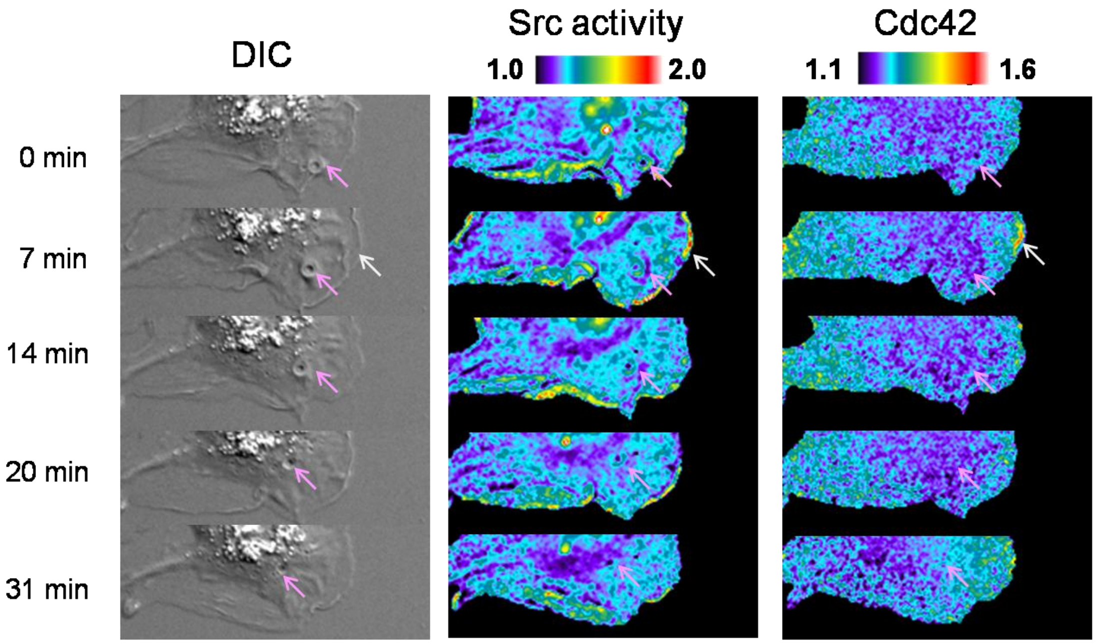

Figure 1.37 Co-imaging of spatiotemporal dynamics of endogenous SFKs and Cdc42 in the same living cell.
COS7 cells were loaded with a near infrared mero65-labeled SFK activity sensor and a red **mero199**-labeled Cdc42 activity sensor. Images were taken every 60 sec in the acquisition sequence of DIC, CFP, **mero65**, **mero199**-577 nm and **mero199**-600 nm. SFK activity was defined by the ratios of CFP emissions divided by dye emissions. Cdc42 activity was defined by the emission ratios of **mero199** excited with 577 nm and 600 nm.

Despite the difficulty of rapid acquisition of two biosensor signals at millisecond's level which makes it impossible to study how Cdc42 and Src coordinate at the cell leading edge during cell motility with seconds and submicrons resolutions, the multiplexable sensors were still capable of monitoring cellular events with subminute resolution. For instance, both Cdc42 and Src are involved in pinocytosis (11, 119-125). Co-imaging of a SFK activity sensor and a Cdc42 activity in the same living cell revealed that both SFK and Cdc42 were activated at the cell edge (23, 44, 126-132) while only SFK activity peaked at the pinocytolic vesicles (122, 124, 125) but not Cdc42 (**Fig 1.37**). The result is consistent with the earlier findings that Cdc42 mainly participates in the beginning of pinocytosis at the plasma membrane regions (119, 120, 123). At the current stage, the major application of multiplexing two dye-based protein activity sensors in the same cell is to study spontaneous cellular events. Because Src is an upstream regulator of Rho GDP-dissociation factors (RhoGDI) (119, 133-136) and several guanidine nucleotide exchange factors (GEF) including vav2 (136, 137), cool-2/α-pix (138), and FRG (137, 139), it would be interesting to investigate how the spatiotemporal dynamics of Src and Cdc42 are altered in response to selective knock-outs or activation of one of the regulators.

1.3.8 Fluorescence lifetime imaging of dye-based biosensors

The first dye-based biosensor tested for fluorescence lifetime imaging was the **mero87**-labeled ERK activity sensor characterized in part 2. **Mero87**-labeled ERK activity sensor was loaded into NIH 3T3 mouse embryo fibroblasts (MEF) stably expressing YPet fluorescent protein molecule. Because the **mero87**-labeled ERK activity sensor photobleached very rapidly upon continuous laser irradiation on a confocal fluorescence scope, we were only able to capture one fluorescent biosensor-loaded cell with sufficient brightness for lifetime imaging. Intensity-based ratio analysis was not conducted because **mero87** became too dim after the lifetime acquisition. Both the phase lifetime values (τ_P) and the modulation lifetime values (τ_M) were recorded at the three cell regions of interest—nucleus, cytosol, and cell edge. In the nucleus, the ERK activity sensor showed a largest average τ_P of 1.654 ns and a smallest average τ_M of 1.817 ns (**Fig 1.38A**). In the cytosol, the ERK activity sensor has a moderate average τ_P of 1.572 ns and a greatly increased average τ_M of 3.790 ns (**Fig 1.38B**). At the cell edge, the sensor exhibited the smallest average τ_P of 1.522 ns and the largest average τ_M of 4.790 ns (**Fig 1.38C**). The lifetime values at the cell edge was the least confident as the background noise became higher at the thinner cell edge. The modulation lifetime and the phase lifetime values showed a perfect negative correlation in the three regions (**Fig 1.38D**). In summary, we have demonstrated that we could quantify biosensor response based on the fluorescence lifetime change of a single solvatochromic fluorophore.

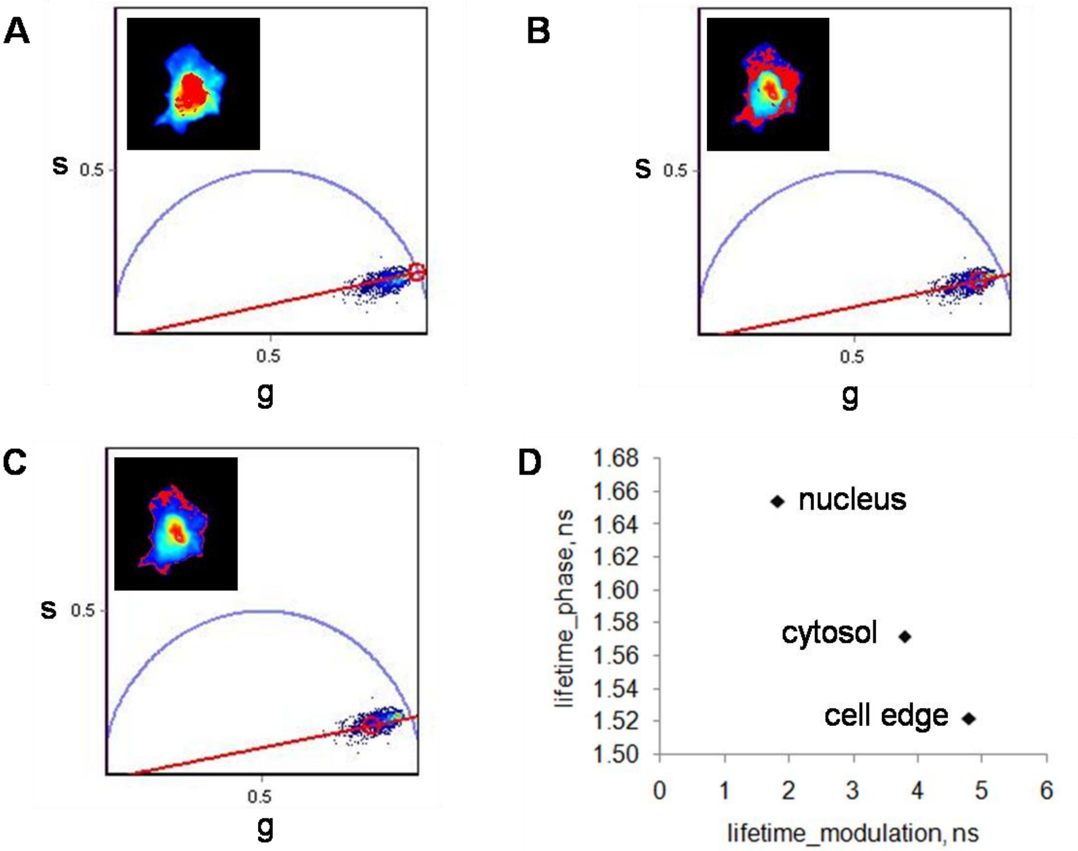

Figure 1.38 Fluorescence lifetime imaging of mero87-labeled ERK biosensor in MEF cells.

Mero87-labeled ERK activity sensor was imaged in NIH 3T3 mouse embryo fibroblasts (MEF) stably expressing YPet fluorescent protein molecules. The phase lifetime and the modulation lifetime values were measured on a confocal fluorescence microscope equipped with lifetime acquisition settings and quantified using Phasor analysis. **A.** Phasor plot of nuclear ERK sensor signals. **B.** Phasor plot of cytosolic ERK sensor signals. **C.** Phasor plot of ERK sensor signals at the cell edge. **D.** Plot of phase lifetime and modulation lifetime values of the three regions. Lifetime values were normalized to a lifetime standard—fluorescein prior to acquisition.

1.4 Conclusions

We have developed a series of new near infrared merocyanine dyes and demonstrated the potential of the new dyes for multiplexed live cell imaging. The new near infrared dyes were designed based on the best set of red merocyanine dyes with optimized properties for live cell imaging. These key properties include brightness, photostability, solvent-dependent fluorescence, and optimal dye-protein interactions. These new near infrared merocyanine dyes have superior maximum brightness as compared to current near infrared fluorescent proteins and are able to use direct excitation for reporting protein conformation changes *in vitro* and in live cell imaging. The best dye has a maximum brightness value similar to the commonly used enhanced green fluorescent protein (EGFP) molecules and the near infrared dyes can be excited at long wavelengths where cellular autofluorescence is greatly reduced. However, the dye brightness of near infrared merocyanine dyes was greatly diminished when located on the surface of sensor protein molecules in phosphate buffer. This fluorescence quenching effect was later found to be correlated with the tendency of the new dyes to form H-type aggregates in water. Near infrared merocyanine dyes consisting of **I-BA** structures showed no concentration-dependent dye aggregation and their fluorescence intensities also exhibited the smallest decreases in aqueous solution. **I-BA**-labeled sensor proteins for active Src family kinases (SFK) and for active Cdc42 were the brightest among the near infrared sensor designs. The resulting **I-BA**-labeled SFK activity sensor displayed sufficient brightness for ratio imaging and its dynamic range was approximately two-fold larger than the previously reported red SFK activity sensor design.

In collaboration with Dr. Alexcei Toutchkine, I also developed a new red merocyanine dye with an intrinsic ratiometric response. Because we found a negative correlation between photostability and solvent-dependent fluorescence in a series of red merocyanine dyes, we introduced aromaticity into the electron donor moiety to shift the equilibrium towards the more solvent-sensitive zwitterionic resonance form in the ground state, followed by addition of an electron withdrawing group to the polymethine chain to minimize photo-oxidation. The resulting dye, **mero199**, possesses balanced properties in brightness, photostability, and solvent-dependent dual fluorescence changes in intensity and wavelength maximum. We also demonstrated that activation of endogenous Cdc42 could be quantified by the intrinsic ratiometric response of a **mero199**-labeled Cdc42 activity sensor in living cells.

Next we showed that the spatiotemporal dynamics of endogenous Src and Cdc42 could be monitored in the same living cell by using a new near infrared SFK activity sensor and a new red ratiometric Cdc42 activity sensor. By co-imaging the two sensors in the same cell, we found that both active Cdc42 and SFK are enriched at the cell edge while only Src is activated throughout pinocytosis. The observations were consistent with the literature. The main difference is that we can now provide more precise information regarding the relative timing and subcellular localization of Cdc42 and Src activation in each pinocytolic vesicle. Multiplexing of Cdc42 and Src in the same cell also has great potential to be used together with protein manipulation tools and knock-outs of specific regulators.

In the future it will be possible to multiplex two or more dye-based biosensors using the lifetime changes of the solvatochromic dyes. Because the fluorescence lifetime of a molecule is independent of varying biosensor concentrations and uneven illumination settings, protein activity sensors based on solvatochromic dyes could be quantified by the average fluorescence lifetime values of target-bound and unbound sensors. Among all of the red and near infrared merocyanine dyes tested, the near infrared **I-Pht** and **I-SO** dyes displayed the largest solvent-dependent fluorescence lifetime changes. The **I-SO**-labeled Cdc42 activity sensor also showed decent response in fluorescence lifetime when titrated with active Cdc42 *in vitro*. The preliminary study on a red **I-SO**-labeled ERK activity sensor revealed distinct fluorescence lifetime values in the nucleus, in the cytosol, and at the cell edge, which was consistent with the earlier observations of elevated ERK activity in the nucleus. The study also pointed out the problem of rapid photobleaching of these merocyanine dyes under continuous laser irradiation. Current efforts are focused on adjustment of the microscope settings to enable time-course studies of dye-FLIM.

In summary, the newly developed near infrared and red merocyanine dyes exhibit great potential for imaging multiple biosensors in the same living cell via intensity-based and lifetime-based imaging. The current capacities of these new multiplexable sensors are for studying cellular events that occur on the minutes timescale and also for still images of samples pre-treated with various environmental stimuli. Faster acquisition and higher quality ratio images will require significant work in upgrading current microscope settings, including improved light sources for near infrared dyes, more sensitive cameras for making good use of photons, and optimal filters for each multiplexable fluorophore.

1.5 Materials and Methods

General materials and methods All reagents were purchased from Sigma Aldrich, Acros Organics, Alfa Aesar, or TCI America. UV-Visible spectra were recorded on a Hewlett-Packard 8453 diode array spectrophotometer. Fluorescence spectra were obtained on a Spex Fluorolog 2 spectrofluorometer. Reverse phase high performance liquid chromatography was performed on a Shimadzu module with a Phenomenex C18 preparative column using elution systems composed of acetonitrile/water/0.5% trifluoroacetic acid (TFA). Fluorescence screening was conducted on a PHERAstar HTS microplate reader equipped with a 430EX/480EM optical filter module for CFP acquisition and a 590EX/675EM optical filter module for near infrared dye acquisition. NMR spectra were taken on a Varian Mercury-300 or Inova-400 spectrometers using deuterated solvents purchased from Cambridge Isotope Laboratories. Low resolution mass spectra were collected on an Agilent MSD-trap Ion trap mass spectrometer with direct infusion. High resolution mass spectra were obtained on an Agilent 6520 Accurate-Mass Q-TOF LC-MS.

Synthesis of intermediate **1**:

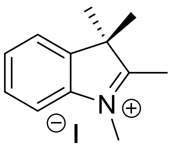

1,2,3,3-tetramethyl-3*H*-indolium iodide (1) 2,3,3-trimethylindolenine (7.998 g, 50.27 mmol) and iodomethane (3.3 ml, 53.01 mmol) in 500 ml of ethanol was heated to reflux under argon for 20 hours and cooled down to room temperature. The precipitate was washed with ethyl acetate, diethyl ether and methanol, followed by drying under high vacuum overnight to give the product as a red powder (10.71 g, 71%). ^{1}H NMR (400 MHz, d_6-DMSO) δ 7.91 (d, 1H, J = 7.4 Hz), 7.82 (d, 1H, J = 7.0 Hz), 7.62 (t, 2H, J = 3.5 Hz), 3.97 (s, 3H), 1.52 (s, 6H). Cal. Mw for $C_{12}H_{16}N^+$: 174.1; LRMS (ESI) for [M+]: 174.2.

Synthesis of intermediate **2**:

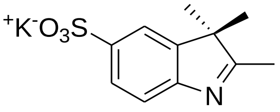

Potassium 2,3,3-trimethyl-3*H*-indole-5-sulfonate (2) 3-methyl-2-butanone (17 ml, 158.69 mmol) was added to a stirring solution of p-hydrazinobenzenesulfonic acid (10.0010 g, 53.14 mmol) in 30 ml of acetic acid at room temperature. The resulting mixture was heated to reflux for 4 hours and then cooled down to room temperature. The precipitate was filtered off, washed with ethyl acetate, and dried under reduced pressure to give a pink solid intermediate. The intermediate was dissolved in 35 ml of methanol and added dropwise to a stirring solution of potassium hydroxide (3.0 g, 53 mmol) in 35 ml of n-propanol. The resulting solution was then stirred at room temperature for 24 hours. The precipitate was filtered off, washed with hexane and dried under high vacuum as a yellow powder (8 g, 56% yield). ^{1}H NMR (400 MHz, D_2O) δ 7.61 (s, 1H), 7.59 (d, 1H, J = 8.2 Hz), 7.34 (d, 1H, J = 8.0 Hz), 2.06 (s, 3H), 1.06 (s, 6H). Cal. Mw for $C_{11}H_{12}NO_3S^-$: 238.1; LRMS (ESI) for [M$^-$]: 238.0.

Synthesis of intermediate **3**:

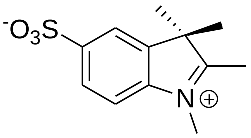

1,2,3,3-tetramethyl-3*H*-indolium-5-sulfonate (**3**) To compound **4** (4.513 g, 16.22 mmol) in 100 ml of ethanol was added iodomethane (5 ml, 81.09 mmol). The resulting mixture was heated to reflux under argon for 24 hours. The precipitate was filtered off, washed with hexane and dried under high vacuum as a pink power (4.733 g, quant.). ^{1}H NMR (d_6-DMSO, 400 MHz) δ 7.32-7.38 (m, 2H), 6.57-6.67 (m, 1H), 3.87 (s, 2H), 2.47 (s, 3H), 1.25 (s, 6H). Cal. Mw for $C_{12}H_{14}NO_3S^-$: 252.1; LRMS (ESI) for [M-H]: 252.2.

Synthesis of intermediate **4**:

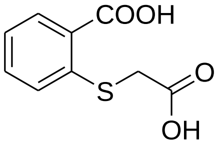

2-(carboxymethylthio)benzoic acid (4) Thiosalicilic acid (15.737 g, 102.06 mmol) was dissolved in 100 ml of stirred 10% NaOH aqueous solution at 0 ^{o}C, followed by dropwise addition of chloroacetic acid (12.128 g, 128.34 mmol) in 50 ml of 10% NaOH aqueous solution over 30 min . The mixture was heated at reflux under argon with stirring for 3 hours, cooled to room temperature, and acidified with 22 ml of HCl aqueous solution. The acidified mixture was then heated to boiling and cooled down again. The precipitate was filtered off, washed with water, and dried under high vacuum overnight to give the product as a pink solid (27.9408 g, 85% yield). ^{1}H NMR (400 MHz, d_6-DMSO) δ 7.63 (d, 1H, J = 7.4 Hz), 7.38-7.47 (m, 2H), 7.24 (t, 1H, J = 7.0 Hz), 3.61 (s, 2H). Cal. Mw for $C_9H_7O_4S$: 211.0; LRMS (ESI) for [M-H]: 211.1.

Synthesis of intermediate **5**:

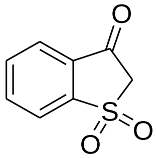

Benzo[*b*]thiophen-3(2*H*)-one 1,1-dioxide (5) A suspension of compound **4** (20.352 g, 95.90 mmol) in 120 ml acetic acid was added 25 ml of 35% hydrogen peroxide aqueous solution. The mixture was heated to 60 ^{o}C and stirred for 4 hours, cooled to room temperature, and concentrated via rotary evaporation. The residue was dissolved in 50 ml of acetic anhydride, followed by addition of sodium acetate (1.0001 g, 12.19 mmol). The resulting mixture was stirred at 110 ^{o}C under argon for 1 hour. Acetic anhydride was removed via rotary evaporation and the residue was treated with 50 ml of 5% HCl aqueous solution. The precipitate was filtered off, washed with water, and dried under high vacuum overnight to give the product as a light yellow solid (16.521 g, 95% yield for two steps). R_f: 0.15 (hexane: EA = 4:1). ^{1}H NMR ($CDCl_3$, 300 MHz), 7.93-8.02 (2H, m), 7.91 (1H, d, J = 1.2 Hz), 7.78-7.85 (m, 1H), 4.09 (2H, s). ^{13}C NMR ($CDCl_3$, 300 MHz) δ187.2, 148.2, 137.7, 134.7, 133.9, 125.2, 122.2, 57.7. Cal. Mw for $C_8H_6O_3S$: 182.0; LRMS (ESI) for [M-H]: 181.3.

General procedures for the synthesis of acceptor intermediates A mixture of 15.0 mmol of the acceptor precursor and 21.00 mmol of N-(5-anilino-2,4-pentadienylidene)aniline hydrochloride in 25 ml of acetic anhydride was heated to reflux under argon for 2 hours and cooled down to room temperature. The precipitate was washed with ethyl acetate and dried under vacuum. The product was re-crystalized from isopropanol or purified by silica gel chromatography using dichlromethane and ethyl acetate as the eluents.

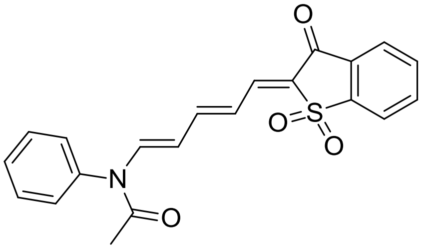

***N*-((1*E*,3*E*,5*E*)-5-(1,1-dioxido-3-oxobenzo(*b*)thiophen-2(3*H*)-ylidene)penta-1,3-dien-1-yl)-*N*-phenylacetamide (6a)** Yield: 73%. R$_f$: 0.26 (hexane: EA = 2 : 1). ^{1}H NMR (400 MHz, CDCl$_3$) δ 8.14 (d, 1H, J = 13.84 Hz), 8.01 (d, 1H, J = 7.6 Hz), 7.92 (d, 1H, J = 7.7 Hz), 7.82 (t, 1H, J = 7.4 Hz), 7.75 (t, 1H, J = 7.6 Hz), 7.53-7.64 (m, 4H), 7.19 (d, 2H, J = 7.7 Hz), 7.12 (d, 1H, J = 11.2 Hz), 6.79 (t, 1H, J = 13.6 Hz), 5.34 (t, 1H, J = 13.6 Hz), 1.96 (s, 3H). Cal. Mw for $C_{21}H_{17}NNaO_4S$: 402.1; LRMS (ESI) for [M+Na]: 402.0.

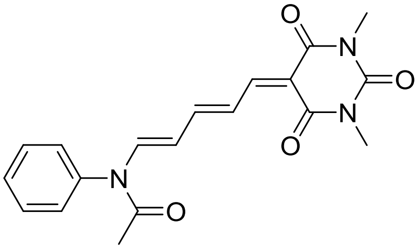

***N*-((1*E*,3*E*)-5-(1,3-dimethyl-2,4,6-trioxo-tetrahydropyrimidin-5(6*H*)-ylidene) penta-1,3-dienyl)-*N*-phenylacetamide (6b)** Yield: 66%. ^{1}H NMR (CDCl$_3$, 300 MHz), 8.16 (1H, d, J = 13.5 Hz), 8.04 (1H, d, J = 12.3 Hz), 7.70 (1H, t, J = 14.4 Hz), 7.52-7.66 (3H, m), 7.16-7.29 (3H, m), 5.36 (1H, t, J = 12.8 Hz), 3.29-3.35 (6H, m), 1.98 (3H, s). ^{13}C (CDCl$_3$, 300 MHz), 169.2, 162.5, 161.9, 157.1, 154.9, 151.5, 140.7, 138.2, 130.5, 129.7, 128.2, 126.7, 113.7, 111.5, 28.5, 27.8, 23.3. Cal. Mw. for $C_{19}H_{19}N_3NaO_4$: 376.1; LRMS (ESI) for [M+Na]: 376.1.

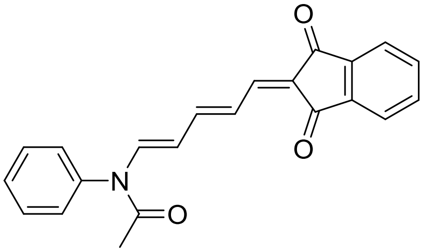

***N*-((1*E*,3*E*)-5-(1,3-dioxo-1*H*-inden-2(3*H*)-ylidene)penta-1,3-dienyl)-*N*-phenylacetamide (6c)** Yield: 48%. R_f: 0.11 (hexane: EA = 4:1). ^{1}H NMR (400 MHz, d_6-DMSO) δ8.18 (d, 1H, J = 13.6 Hz), 7.83-7.86 (m, 4H), 7.55-7.64(m, 4H), 7.34-7.49 (m, 4H), 5.28 (t, 1H, J = 13.4 Hz), 1.95 (s, 3H). Cal. Mw for $C_{22}H_{17}NNaO_3$: 366.1; LRMS (ESI) for [M+Na]: 366.2.

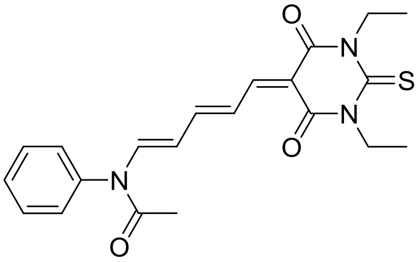

***N*-((1*E*,3*E*)-5-(1,3-diethyl-4,6-dioxo-2-thioxo-tetrahydropyrimidin-5(6*H*)-ylidene)penta-1,3-dienyl)-*N*-phenylacetamide (6d)** Yield: 19%. R_f: 0.45 (hexane: EA = 5:1). 1H NMR (CDCl3, 300 MHz), 8.20 (1H, d, J = 13.5 Hz), 8.06 (1H, d, J = 12.6 Hz), 7.74 (1H, t, J = 14.1 Hz), 7.54-7.58 (3H, m), 7.18-7.30 (3H, m), 5.38 (1H, t, J = 13.5 Hz), 4.43-4.55 (4H, m), 1.98 (3H, s), 1.21-1.30 (6H, m). Cal. Mw for $C_{21}H_{23}N_3NaO_3S$: 420.1; LRMS (ESI) for [M+Na]: 420.2.

General procedure for the synthesis of parent dyes without an aryl sulfate. A mixture of compound **2**, acceptor intermediate and sodium acetate in methanol was heated at reflux for 10 min with stirring and then cooled down to room temperature. The mixture was concentrated via rotary evaporation and purified by silica gel chromatography using dichloromethane and ethyl acetate as the eluent. The blue fractions were combined, concentrated, and dried under high vacuum to give the product as a blue-olive solid.

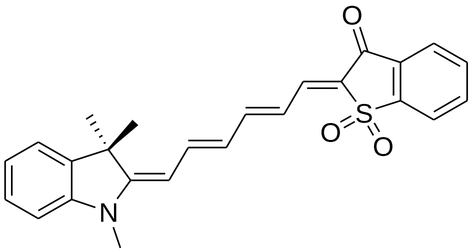

(*E*)-2-((2*E*,4*E*,6*E*)-6-(1,3,3-trimethylindolin-2-ylidene)hexa-2,4-dien-1-ylidene) benzo(*b*)thiophen-3(2*H*)-one 1,1-dioxide (mero81) Yield: 65%. R_f: 0.31 (CH_2Cl_2: EA = 100:1). ^{1}H NMR (400 MHz, $CDCl_3$) δ 8.00 (d, 1H, J = 7.6 Hz), 7.94 (d, 1H, J = 7.5 Hz), 7.66-7.81 (m, 3H), 7.38-7.47 (m, 1H), 7.21-7.28 (m, 3H), 7.03 (t, 1H, J = 7.4 Hz), 6.93 (t, 1H, J = 13.32 Jz), 6.82 (d, 1H, J = 6.8 Hz), 6.38 (t, 1H, J = 12.7 Hz), 5.64 (d, 1H, J = 12.8 Hz), 3.31 (s, 3H), 1.63 (s, 6H). Cal. Mw for $C_{25}H_{24}NO_3S$: 418.1; LRMS (ESI): 418.3.

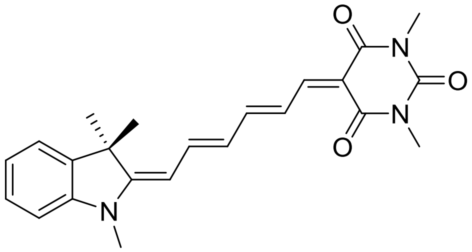

1,3-dimethyl-5-((2*E*,4*E*,6*E*)-6-(1,3,3-trimethylindolin-2-ylidene)hexa-2,4-dienylidene)pyrimidine-2,4,6(1*H*,3*H*,5*H*)-trione (mero80) Yield: 33%. R_f: 0.15 in pure CH_2Cl_2. ^{1}H NMR ($CDCl_3$, 300 MHz) 8.04 (d, 1H, J = 12.9 Hz), 7.81 (t, 1H, J = 13.5 Hz), 7.42 (t, 1H, J = 13.2 Hz), 7.29 (t, 1H, J = 12.0 Hz), 7.19-7.29 (m, 1H), 7.00 (t, 1H, J

= 7.2 Hz), 6.79 (d, 1H, J = 8.1 Hz), 6.35 (t, 1H, J = 12.0 Hz), 5.63 (d, 1H, J = 12.6 Hz), 5.27 (s, 1H), 3.33 (d, 6H, J = 3.3 Hz), 3.28 (s, 3H), 1.57-1.60 (m, 6H)

^{13}C NMR (CDCl3, 100 MHz) 165.8, 163.3, 159.3, 156.8, 152.0, 145.6, 139.6, 136.1, 128.1, 124.7, 123.9, 122.3, 121.8, 101.9, 88.0, 47.2, 29.7, 28.3, 28.2, 27.7. Cal. Mw for $C_{23}H_{25}N_3O_3$: 391.2; LRMS (ESI): 392.2 [M+H] and 413.3 [M-H+Na].

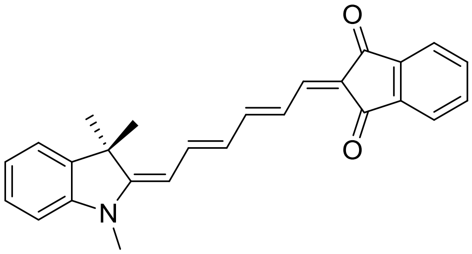

2-((2*E*,4*E*,6*E*)-6-(1,3,3-trimethylindolin-2-ylidene)hexa-2,4-dienylidene)-2*H*-indene-1,3-dione (mero79) Yield: 61%. R_f: 0.49 (CH_2Cl_2: EA = 100:1). ^{1}H NMR (400 MHz, $CDCl_3$) δ7.82-7.90 (m, 2H), 7.64-7.76 (m, 3H), 7.54 (d, 1H, J = 12.7 Hz), 7.35 (t, 1H, J = 13.08 Hz), 7.16-7.24 (m, 3H), 6.99 (t, 1H, J = 7.2 Hz), 6.77 (d, 1H, J = 7.7 Hz), 6.40 (t, 1H, J = 12.6 Hz), 5.60 (d, 1H, J = 12.6 Hz), 3.27 (s, 3H), 1.63 (s, 6H). Cal. Mw for $C_{26}H_{24}NO_2$: 382.2; LRMS (ESI): 382.2.

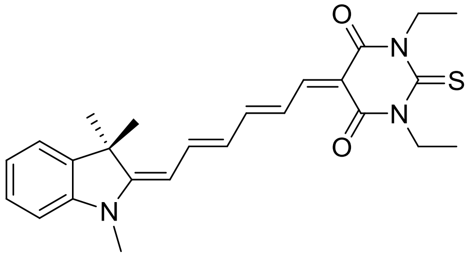

1,3-diethyl-2-thioxo-5-((2*E*,4*E*,6*E*)-6-(1,3,3-trimethylindolin-2-ylidene)hexa-2,4-dienylidene)-dihydropyrimidine-4,6(1*H*,5*H*)-dione (mero82) Yield: 19%. ^{1}H NMR ($CDCl_3$, 300 MHz) 8.05 (d, 1H, J = 13.2 Hz), 7.89 (t, 1H, J = 7.2 Hz), 7.55 (t, 1H, J =

13.2 Hz), 7.37 (t, 1H, J = 12.6 Hz), 7.26-7.30 (m, 2H), 7.09 (t, 1H, J = 7.5 Hz), 6.90 (d, 1H, J = 7.8 Hz), 7.75 (d, 1H, J = 13.2 Hz), 5.30 (s, 1H), 4.56 (q, 4H, J = 7.2 Hz), 3.38 (s, 3H), 1.64 (s, 6H), 1.25-1.33 (m, 6H). ^{13}C NMR ($CDCl_3$, 100 MHz) 178.3, 162.5, 160.5, 160.42, 156.9, 147.8, 128.2, 125.1, 124.5, 123.1, 121.9, 108.5, 106.9, 100.1, 47.7, 43.3, 42.8, 28.1, 12.5. Cal. Mw for $C_{25}H_{29}N_3O_2S$: 435.2; LRMS [ESI]: 435.3 for [M-H], 437.6 for [M+H].

General procedure for the synthesis of parent dyes with an aryl sulfate. Compound **3** (0.50 mmol) and an acceptor intermediate compound **6a-6c** were suspended in ethanol (5 ml), followed by addition of triethylamine (60 μl, 0.51 mmol). The resulting mixture was stirred at reflux for 30 min. The solvent was removed by evaporation at reduced pressure. Unreacted starting material was removed by passing the mixture through a short plug of silica gel and the acetone-eluted fractions were concentrated. The residue was re-dissolved in acetonitrile-water co-solvents and subjected to reverse phase HPLC purification. The blue fractions were confirmed by mass spectrometry and dried by lyophilization.

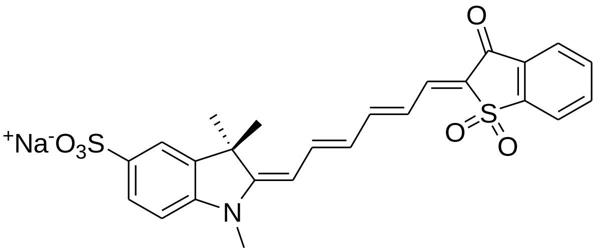

Sodium (E)-2-((2E,4E,6E)-6-(1,1-dioxido-3-oxobenzo(b)thiophen-2(3H)-ylidene) hexa-2,4-dien-1-ylidene)-1,3,3-trimethylindoline-5-sulfonate (mero83) Yield: 80%. R_f: 0.09 (CH_2Cl_2: MeOH = 10:1). ^{1}H NMR (d_6-DMSO, 400 MHz) δ 8.01 (d, 1H, J = 7.2 Hz), 7.69-7.92 (m, 5H), 7.66 (s, 1H), 7.57 (d, 1H, J = 8.2 Hz), 7.52 (d, 1H, J = 13.4 Hz), 7.07-7.21 (m, 2H), 6.51 (t, 1H, J = 12.5 Hz), 6.06 (d, 1H, J = 13.3 Hz), 3.43 (s, 3H), 1.61 (s, 6H).Cal. Mw for $C_{25}H_{22}NO_6S_2^-$: 496.08940; LRMS (ESI) for [M-H]: 495.9; HRMS (Q-TOF) for [M-H]: 496.09090.

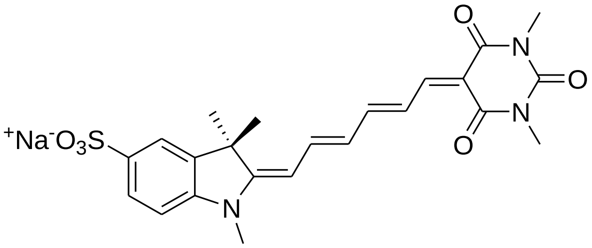

sodium (*E*)-2-((2*E*,4*E*)-6-(1,3-dimethyl-2,4,6-trioxo-tetrahydropyrimidin-5(6*H*)-ylidene)hexa-2,4-dienylidene)-1,3,3-trimethylindoline-5-sulfonate (mero84) Yield: 55%. ^1H NMR (d_6-DMSO, 400 MHz) δ 8.03 (d, 1H, J = 12.6 Hz), 7.82 (t, 1H, J = 13.2 Hz), 7.40 (t, 1H, J = 13.3 Hz), 7.17-7.27 (m, 2H), 6.82 (d, 1H, J = 7.8 Hz), 6.37 (t, 1H, J = 12.1 Hz), 5.70 (d, 1H, J = 12.5 Hz), 5.30 (s, 1H), 3.29 (s, 3H), 1.55-1.58 (m, 6H). Cal. Mw for $C_{23}H_{24}N_3O_6S^-$: 470.1; LRMS (ESI) for [M-H]: 470.7.

Synthesis of intermediate **7**:

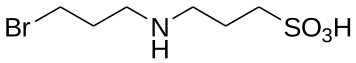

3-(3-bromopropylamino)propane-1-sulfonic acid (7) Triethylamine (14 ml, 50 mmol) was added to a solution of bromopropylamine (11.0224 g, 50.35 mmol) and 1,3-propane sultone (12.2138 g, 100.00 mmol) in 250 ml of ethanol. The reaction mixture was stirred at room temperature for 24 hours and precipitation was induced by cooling in an ice bath. The precipitate was filtered, washed with hexane, dried under high vacuum, and the product was isolated as white flakes (7.5226 g, 57% yield). ^1H NMR (400 MHz, d_6-DMSO) δ3.59 (t, 2H, J = 6.6 Hz), 2.96-3.12 (m, 4H), 2.63 (t, 2H, J = 6.8 Hz), 2.08-2.18

(m, 2H), 1.88-1.98 (m, 2H). Cal. Mw for $C_6H_{14}BrNNaO_3S$: 282.0; LRMS (ESI): 260.0/262.0 for [M+H], 280.0/282.0 for [M-H+Na].

Synthesis of intermediate **8**:

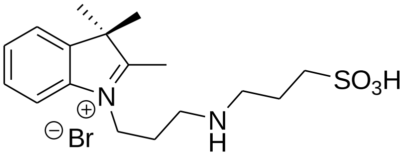

2,3,3-trimethyl-1-(3-(3-sulfopropylamino)propyl)-3*H*-indolium bromide (8) To compound **1** (1.5031 g, 5.78 mmol) in a microwave tube was added 2,3,3-trimethyl indolenine (1.3572g, 8.52 mmol). The sealed microwave tube was stirred and heated at 180 °C for 30 min and then cooled down to room temperature. The excess starting material was removed by pipetting while new diethyl ether was added to wash and protect the hygroscopic product crystals. The crystals in diethyl ether were transferred to a 20 ml vial and the solvent was removed by rotary evaporation. The product crystals were then dried under high vacuum overnight to yield red crystals (1.5697 g, 80% yield). Dried compound **8** was used directly in the next step without further purification. Cal. Mw for $C_{17}H_{27}N_2O_3S^+$: 339.2; LRMS (ESI) for [M^+]: 339.3.

Synthesis of intermediate **9**:

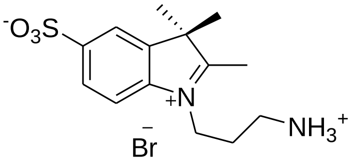

1-(3-ammoniopropyl)-2,3,3-trimethyl-3*H*-indolium-5-sulfonate bromide (9) Compound **2** (2.7760 g, 10.01 mmol) and 2-bromopropylamine (2.1898 g, 10.00 mmol) were suspended in 10 ml of α-dichlorobenzene. The resulting mixture was heated at reflux under argon for 16 hours. Precipitation was induced by cooling on an ice bath. The precipitates were filtered, washed with ethyl acetate, and dried under vacuum to give the product as a pink solid (2.4749 g, 60% yield). Because compound **9** is highly hygroscopic, the solid was used without further purifications. Cal. Mw for $C_{14}H_{19}N_2O_3S^-$: 295.1; LRMS (ESI) for [M-H]: 295.2.

General procedures for synthesis of dye-chloroacetamides with an alkyl sulfate. Compound **8** (0.5 mmol) in 10 ml of anhydrous DMF was added 2.5 mmol of chloroacetic anhydride and 1.5 mmol of sodium acetate. The solution was stirred at room temperature for 15 min, followed by addition of an acceptor intermediate **6a-c** (0.6 mmol, 1.2 eq). For compounds **12a** and **12b**, the reaction mixture was stirred at room temperature under argon for 2 hours. For compound **12c**, the mixture was heated to 60^{o}C with stirring under argon for 2 hours and cooled to room temperature. The majority of DMF was removed via azeotropic distillation with toluene under reduced pressure. The residue was purified by gradient elution on a silica gel column using dichloromethane and methanol as the elutants (0 to 10% MeOH in CH_2Cl_2). The blue fractions were combined, concentrated via rotary evaporation, and dried under high vacuum to yield blue solid products.

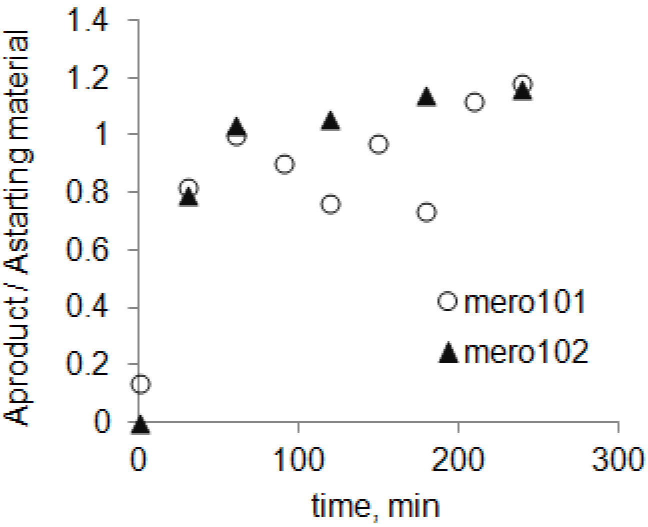

Figure 1.39 Reaction tracking of the formation of dye-chloroacetamide conjugates. The product/starting material ratios were obtained by the relative absorbance at 450 nm ($A_{\text{starting material}}$) for the starting material and at 695 nm (A_{product}) for the product. Prolonged reaction times resulted in the disappearance of the blue products and the increasing amount of red and green side products.

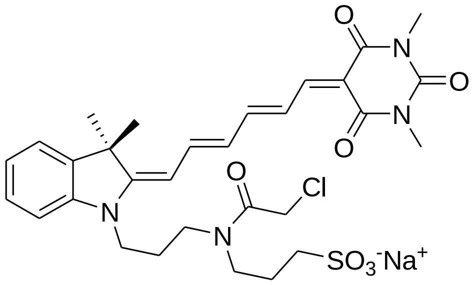

Sodium 3-(2-chloro-*N*-(3-((*E*)-2-((2*E*,4*E*)-6-(1,3-dimethyl-2,4,6-trioxo-tetrahydro-pyrimidin-5(6*H*)-ylidene) hexa-2,4-dienylidene)-3,3-dimethylindolin-1-yl)propyl) acetamido)propane-1-sulfonate (mero100) Yield: 28%. R_f: 0.16 (CH_2Cl_2: MeOH = 10 : 1). ^1H NMR (d_6-DMSO, 400 MHz) δ 7.85-8.02 (m, 1H), 7.80-7.85 (m, 1H), 7.54-7.68 (m, 1H), 7.46 (d, 1H, J = 7.2 Hz), 7.27-7.34 (m, 1H), 7.15-7.27 (m, 1H), 7.08 (t, 1H, J = 7.2 Hz), 6.78-7.03 (m, 1H), 6.38-6.50 (m, 1H), 6.03 (t, 1H, J = 13.3 Hz), 4.07 (s, 2H), 3.37-3.70 (m, 4H), 3.17 (s, 6H), 3.08-3.13 (m, 2H), 2.32-2.44 (m, 2H), 1.68-1.83 (m, 2H), 1.54 (s, 6H). Cal. Mw for $C_{30}H_{36}ClN_4O_7S$: 631.2; LRMS (ESI) for [M-H]: 631.7.

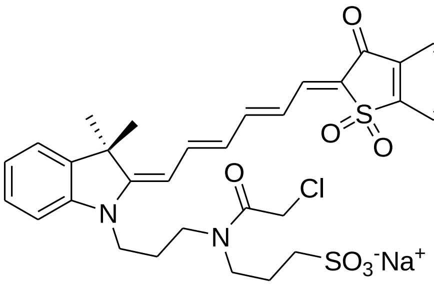

sodium-3-(2-chloro-*N*-(3-((*E*)—((2*E*,4*E*,6*E*)-6-(1,1-dioxido-3-oxobenzo(*b*) thiophen-2(3*H*)-ylidene)hexa-2,4-dien-1-ylidene)-3,3-dimethylindolin-1-yl) propyl)acetamido)propane-1-sulfonate (mero102) Yield: 15%. R_f: 0.11 (CH_2Cl_2: MeOH = 10 : 1). ^1H NMR (400 MHz, d_6-DMSO) δ8.01 (d, 1H, J = 7.2 Hz), 7.49 (d, 1H, J = 7.4 Hz), 7.26-7.36 (m, 1H), 7.21 (d, 1H, J = 7.8 Hz), 7.11 (t, 1H, J = 7.3 Hz), 6.46-6.58 (m, 1H), 6.04-6.20 (m, 1H), 4.39 (s, 2H), 4.26-4.32 (m, 2H), 3.90-4.00 (s, 2H), 2.30-2.50 (m, 4H), 1.80-1.95 (m, 2H), 1.61 (s, 6H). Cal. Mw for $C_{32}H_{34}ClN_2O_7S_2^-$: 657.15014; LRMS (ESI): 657.2; HRMS (Q-TOF): 657.14900.

General procedures for synthesis of dye-chloroacetamides with an aryl sulfate. Compound **9** (0.50 mmol) was dissolved in 10 ml of anhydrous DMF, followed by addition of chloroacetic anhydride (2.5 mmol) and sodium acetate (1.5 mmol). The solution was stirred at room temperature for 15 min, followed by addition of an acceptor intermediate **6a-c** (0.55 mmol). For compound **13a** and **13b**, the reaction mixture was stirred at room temperature under argon for 2 hours. For compound **13c**, the stirred mixture was heated at 60 ^oC under argon for 2 hours, cooled to room temperature, and concentrated via azeotropic distillation with toluene under reduced pressure. The residue was first passed through a short plug of silica and eluted with acetone. The purple, blue, or green fractions were combined, concentrated via rotary evaporation and separated by reverse HPLC using acetonitrile/water/0.5%TFA as the eluents. Fractions with an absorption peak around 660 nm (for **13b**) or 690 nm (for **13a** and **13c**) were concentrated via rotary evaporation and dried by lyophilization.

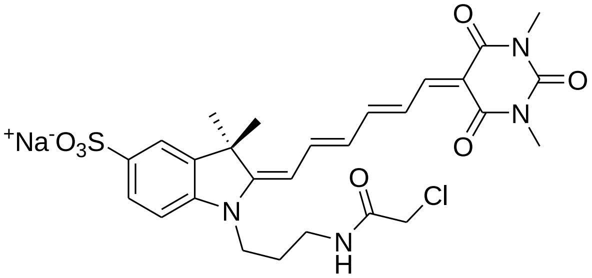

Sodium (*E*)-1-(3-(2-chloroacetamido)propyl)-2-((2*E*,4*E*)-6-(1,3-dimethyl-2,4,6-trioxo-tetrahydropyrimidin-5(6*H*)-ylidene)hexa-2,4-dienylidene)-3,3-dimethyl indoline-5-sulfonate (mero101) Yield: 29%. R_f: 0.23 (CH_2Cl_2: MeOH: NH_4OH = 10 : 1:0.01) 1H NMR (d6-DMSO, 400 MHz) δ 8.36 (m, 1H), 7.83-7.92 (m, 1H), 7.70-7.83 (m, 1H), 7.60-7.70 (m, 2H), 7.48-7.57 (m, 1H), 6.97-7.12 (m, 1H), 6.42 (t, 1H, J = 10.6 Hz), 5.98 (t, 1H, J = 5.6 Hz), 4.07 (s, 2H), 3.03-3.36 (m, 10H), 1.72-1.88 (m, 2H), 1.59 (s, 6H).

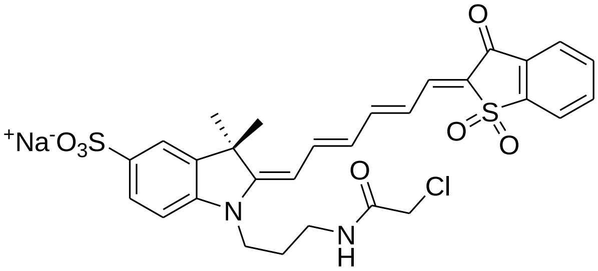

Sodium (*E*)-1-(3-(2-chloroacetamido)propyl)-2-((2*E*,4*E*,6*E*)-6-(1,1-dioxido-3-oxobenzo(*b*)thiophen-2(3*H*)-ylidene)hexa-2,4-dien-1-ylidene)-3,3-dimethyl-indoline-5-sulfonate (mero103) Yield: 23%. R_f: 0.26 (CH_2Cl_2: MeOH: NH_4OH = 10 : 1:0.01). Cal. Mw for $C_{29}H_{28}ClN_2O_7S_2$: 615.1; LRMS (ESI) for [M-H]: 615.1.

General procedures for synthesis of dye-iodoacetamides. The dye-chloroacetamides (0.036 mmol) and sodium iodide (0.18 mmol) in anhydrous methanol (10 ml) was refluxed for 3 hrs under nitrogen and then concentrated by evaporation at reduced pressure in the dark. The product was purified by reverse phase HPLC, using acetonitrile and water as the eluents.

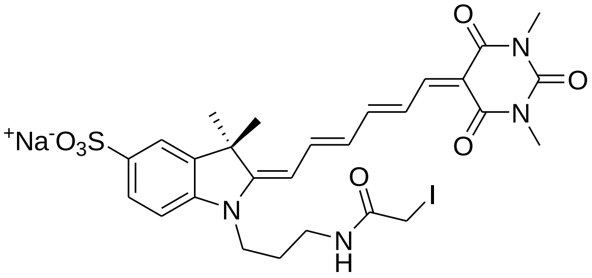

Sodium (*E*)-2-((2*E*,4*E*)-6-(1,3-dimethyl-2,4,6-trioxo-tetrahydropyrimidin-5(6*H*)-ylidene)hexa-2,4-dienylidene)-1-(3-(2-iodoacetamido)propyl)-3,3-dimethyl indoline-5-sulfonate (mero65) Yield: 20%. ^{1}H NMR (DMSO, 400 MHz) δ 8.40 (t, 1H, J = 5.0 Hz), 7.72-7.87 (m, 2H), 7.60-7.69 (m, 2H), 7.54 (d, 1H, J = 8.0 Hz), 7.10 (d, 1H, J = 2.0 Hz), 6.45 (t, 1H, J = 12.0 Hz), 6.01 (d, 1H, J = 13.0 Hz), 3.89 (s, 2H), 3.66 (s, 2H), 3.17 (s, 6H), 3.01 (s, 2H), 1.75-1.80 (m, 2H), 1.59 (s, 6H). Cal. Mw for $C_{27}H_{30}IN_4O_7S^-$: 681.08854; LRMS (ESI): 680.9; HRMS (Q-TOF): 681.08818.

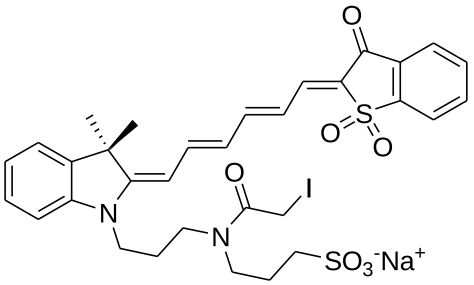

sodium 3-(N-(3-((E)-2-((2E,4E,6E)-6-(1,1-dioxido-3-oxobenzo(b)thiophen-2(3H)-ylidene)hexa-2,4-dien-1-ylidene)-3,3-dimethylindolin-1-yl)propyl)-2-iodo acetamido)propane-1-sulfonate (mero77) Yield: 12%. R$_f$: 0.50 (CH_2Cl_2: MeOH = 5: 1). ^{1}H NMR (d$_6$-DMF, 7.87-8.08 (m, 4H), 7.80 (t, 1H, J = 12.9 Hz), 7.62-7.64 (m, 1H), 7.58-7.60 (m, 1H), 7.53 (d, 1H, J = 7.8 Hz), 7.32-7.45 (m, 2H), 7.16 (t, 1H, J = 7.2 Hz), 6.96 (t, 1H, J = 13.5 Hz), 6.53-6.65 (m, 1H), 6.29 (d, 1H, J = 13.5 Hz), 4.07-4.25 (m, 4H), 3.45-3.3.70 (m, 4H), 2.71 (t, 2H, J = 6.6 Hz), 2.01-2.16 (m, 4H), 1.69-1.71 (m, 8H). Cal. Mw. for $C_{32}H_{35}IN_2O_7S_2$: 750.1; LRMS (ESI) for [M+H]: 751.1.

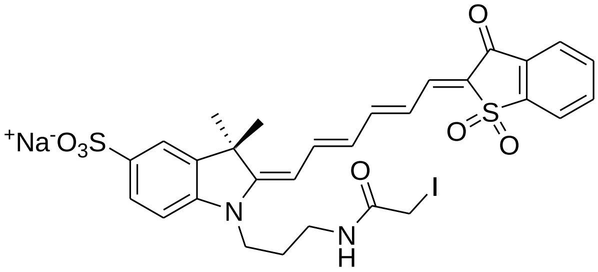

Sodium (*E*)-2-((2*E*,4*E*,6*E*)-6-(1,1-dioxido-3-oxobenzo(*b*)thiophen-2(3*H*)-ylidene) hexa-2,4-dien-1-ylidene)-1-(3-(2-iodoacetamido)propyl)-3,3-dimethylindoline-5-sulfonate (mero78) Yield: 21%. R_f: 0.29 (CH_2Cl_2: MeOH = 5: 1). ^1H NMR (d_6-DMSO, 400 MHz) δ 8.36 (t, 1H, J = 5.2 Hz), 8.02 (d, 1H, J = 7.4 Hz), 7.81-7.95 (m, 2H), 7.68-7.81 (m, 2H), 7.65 (s, 1H), 7.52-7.58 (m, 2H), 7.13 (d, 1H, J = 8.2 Hz), 6.50 (t, 1H, J = 12.3 Hz), 6.07 (d, 1H, J = 13.0 Hz), 4.09 (s, 2H), 3.87-3.97 (m, 2H), 3.18-3.27 (m, 2H), 1.78-1.87 (m, 2H), 1.61 (s, 6H). Cal. Mw. for $C_{29}H_{28}IN_2O_7S_2$: 708.0; LRMS (ESI) for [M-H]: 707.0.

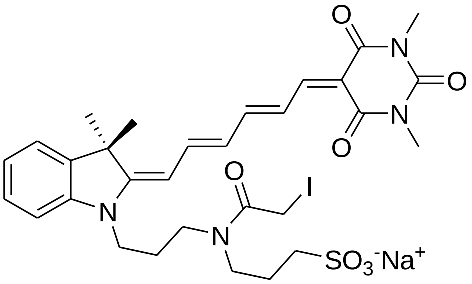

Sodium 3-(*N*-(3-((*E*)-2-((2*E*,4*E*)-6-(1,3-dimethyl-2,4,6-trioxo-tetrahydro

pyrimidin-5(6*H*)-ylidene)hexa-2,4-dienylidene)-3,3-dimethylindolin-1-yl)propyl)-2-iodoacetamido)propane-1-sulfonate (mero99) Yield: 9%. R_f: 0.07 (CH_2Cl_2: MeOH = 10: 1). Cal. Mw for $C_{30}H_{38}IN_4O_7S$: 752.2; LRMS (ESI): 725.4.

Quantum yield measurements Spectrometric grade solvents were degassed on a sonicator for 1 hour prior to measurement. The absorbance at the excitation wavelength was kept below 0.1 to avoid inner filter effects. Each quantum yield value was calculated as the average of three separate preparations. Dye quantum yields were calculated using the following formula:

$$QY_{dye} = QY_{std.} \times \frac{Area_{em,dye}}{Area_{em,std.}} \times \frac{Abs_{std.}}{Abs_{dye}} \times \frac{n_{dye}^2}{n_{std}^2}$$

$Area_{em,dye}$ and $Area_{em,std.}$ are the integrated area of the emission peak of the dye molecule and the QY standard, respectively. The references include Cy5 (QY = 0.27 in MeOH) and 3,3'-diethylthiadicarbocyanine iodide (QY = 0.36 in MeOH).

Photobleaching experiments Time-based fluorescence decays of 1 μM of parent dye in glycerol in a 96-well black bottom plate (Costar) was measured on a PHERAstar microplate reader (BMG Labtech) equipped with an optical module with a 590/50 excitation filer and a 675/50 emission filter. Dye solutions were illuminated with 200 flashes per well and per cycle and the fluorescence intensity values were recorded for every 30 sec.

Protein expression and purification Plasmids encoding for CBD, SFK Fn, and Cdc42 were transformed into BL21 (DE3) *E.coli* strain and cultured at 37 ^{o}C on LB-agar plates containing 100 μg/ml carbencillin. Plasmids encoding for the SFK SH3 domain were transformed into NEB *Express Iq E.coli* strain and cultured at 37^{o}C on LB-agar plates containing 100 μg/ml kanamycin. Bacteria were cultured at 37 ^{o}C untill the cultures reached an optical density at 600 nm of 0.8. Protein expression was conducted at 32 ^{o}C overnight in the presence of 0.5 mM isopropyl β-D-1-thiogalactopyranoside (IPTG) and 100 μg/ml antibiotics. Frozen bacteria pellets were warmed up on ice and re-suspended in equilibration buffer (50 mM NaH_2PO_4, 300 mM NaCl, pH 7.0). The bacterial suspension was homogenized by sonication and the insoluble bacterial debris was removed by centrifugation (Sorvall, model T21). The supernatant was incubated with pre-equilibrated Talon Metal Affinity Resin (Clontech) at 4 ^{o}C for 1 hour on a nutator (BD Clay Adams, model 1105). Protein-bound resins were washed with equilibrium buffer by centrifugation, loaded onto a polypropylene column, and washed with wash buffer (50 mM NaH_2PO_4, pH 7.5). The 6xHis-tagged proteins were eluted by gravity using elution buffer (300 mM imidazole, pH 7.0) and concentrated by centrifugation (VivaSpin 20 MWCO 10K; Eppendorf, model 5810). Protein solutions for labeling were added 1 μl of β-mercaptoethanol (BioRad) to reduce cysteines prior to concentration. The concentrated proteins were passed through a dextran desalting column (Pierce) using protein labeling buffer (50 mM NaH_2PO_4, pH 7.5) as the eluent. Protein solutions for labeling were adjusted to 100 μM and all proteins were stored as aliquots at -80 ^{o}C.

SDS-PAGE and fluorescence gel scanning Protein samples were loaded to a 4-12% Bis-Tris NuPAGE gel (Invitrogen) and separated according to manufacturer's protocol. Dye-labeled proteins were imaged on a fluorescence imager (Typhoon 9410) equipped with 520BP40, 610 BP30 and 670 BP30 emission filters. Relative fluorescence intensity of dye-labeled proteins and free dyes were quantified using imageJ software.

Protein labeling with thiol-reactive dyes 100 μM Cdc42 or SFK sensor protein solution was incubated with 5 fold excess dye-iodoacetamide at room temperature in the dark for 1 hour on a rotary shaker. The reaction was terminated by adding 1 μl of β-mercaptoethanol per 100 μl protein solution at room temperature for 5 min. Excess dyes and dye-labeled proteins were separated on a Sephadex G-15 size exclusion column (GE Healthcare Life Sciences) using protein labeling buffer as the eluent. Labeling efficiency of dye-labeled proteins was calculated by the following formula:

$$labeling\ efficiency = \frac{[dye]_{DMSO}}{[protein]_{buffer}} = \frac{Abs_{dye}}{Abs_{protein}} \times \frac{\epsilon_{protein}}{\epsilon_{dye}}$$

The biosensor solution was concentrated to 20 to 60 μM by centrifuge at 12000 rpm at 4 ^{o}C (Millipore, Amicon Ultra-0.5mL, MWCO 10K). Insoluble dye-protein aggregates were removed prior to microinjection.

Fluorescence titration assays of MeroCBD GTP-bound wild type Cdc42 was prepared by incubating 10 μM 6xHis-tagged wild type Cdc42, 100 μM non-hydrolyzable GTPγS, and 1 mM EDTA in protein labeling buffer 37 ^{o}C for 5 min. To compare relative response of wild type GTP-bound Cdc42 and constitutively active Cdc42 Q61L, 300 nM mero53-labeled CBD-mCerulean was mixed with 0 or 2 μM of active Cdc42 at room temperature for 5 min in assay buffer (50 mM Tris, 50 mM NaCl, 5 mM $MgCl_2$, 1 mM dithiothreitol, 1.2 mM EDTA, pH 7.5). To compare relative response of near infrared MeroCBD, 100 nM MeroCBD was incubated with 0, 0.5, 2.5, 5.0, 7.5, 10.0, 12.5 and 15.0 μM Cdc42 Q61L at room temperature for 5 min. For **mero199**, 100 μl of 300 nM dye-labeled CBD fusion proteins in assay buffer (50 mM NaH_2PO_4, 150 mM NaCl, pH 7.6) was added 100 μl of 0 to 40 μM constitutively active Cdc42 Q61L. Fluorescence spectra were recorded at room temperature on a SPEX Fluorolog 1681 fluorometer. To obtain maximum excitation intensity, emission was set at 611 nm in the absence of Cdc42 Q61Lor 615 nm in the presence of Cdc42 Q61 for excitation spectra. To obtain maximum emission intensity, excitation was set at 581 nm in the absence of Cdc42 Q61L and 599 nm in the presence of Cdc42 Q61L.

Fluorescence titration assays of SFK Merobody 50 nM SFK Merobody was incubated with 0, 0.5, 1.0, 1.5, 2.0, 2.5, 3.0 and 3.5 μM of Src SH3 domain in assay buffer (50 mM NaH_2PO_4, 150 mM NaCl, pH 7.6) at room temperature for 10 min.

Live cell imaging and image analysis The NIH 3T3 mouse embryonic fibroblasts (MEF), COS7 cells, and MEF cells expressing YPet or PA-Rac were maintained in 10% CO_2 at 37 ^{o}C in Dulbecco’s modified Eagle’s medium (DMEM, Cellgro) with 10% fetal bovine serum (HyClone, Thermo Scientific) and 2 mM GlutaMax (Gibco, Life Technologies). The cells were plated on fibronectin (Sigma-Aldrich) coated coverslips overnight. Micropipettes were freshly made with a flaming/brown micropipette puller (Sutter Instrument Co., Model P-97) and thin-walled glass capillary tubes (World Precision Instruments, 1.2 O.D./ 0.9 I.D., TW120F-4). Biosensor proteins were delivered into cells via microinjection or bead loading. Microinjection was executed on an inverted microscope (Ziess Axiovert S100 TV) with a 20x objective (LD Achrostigmat, 0.30 N.A., Ph1), followed by recovery in the cell incubator in Ham’s F-12K medium without phenol red (Gibco) with 5% fetal bovine serum, 15 mM HEPES, and 2mM GlutaMax for at least 30 min prior to imaging. All fluorescence images were shade-corrected, background substracted, photobleaching-corrected, and processed according to routine protocols using MetaMorph and Matlab software.

Chapter 2

Dye-based biosensors to quantify the spatiotemporal dynamics of MAPKKs and MAPKs in living cells

2.1 Summary

Mitogen-activated protein kinase (MAPK) signaling cascades govern numerous cellular processes. Subtle differences in the relative timing and the sub-cellular location of activation of different MAPK pathways can lead to highly divergent cell responses such as apoptosis versus cellular proliferation. Despite the importance of MAPK signaling, very few biosensors for the detection of MAPK kinase (MAPKK) or MAPK activation in live cells are currently available. We describe here a generic strategy to create MAPKK activity sensors based on MAPK binding scaffolds. A solvent-sensitive dye that is covalently attached at a position within the MAPKK-MAPK binding interface can report binding interactions through associated fluorescence changes. Multiple solvent-accessible intrinsic cysteines of ERK2 and p38α were mutated to serines to prevent over-labeling while the phosphorylation site of MAPKs remained unaltered. Dye-labeled ERK2 and dye-labeled p38α showed maximum fluorescence increases upon binding to active MEK1/2 and MKK3/6 of 77% and 30%, respectively. Several dye-labeled ERK2 constructs specifically responded to active MEK1, and not to other tested ERK-interacting proteins. Preliminary imaging studies of a MEK1/2 activity sensor in NIH 3T3 mouse embryo fibroblasts revealed that endogenous activated MEK1/2 is abundant in the cytoplasm but absent in the nucleus. Unusually high biosensor signals at

the cell periphery were also observed. Protein stability predictions suggested that most of the new MAPK binding scaffolds were highly destabilized due to the multiple cysteine-to-serine mutations and the extent of protein destabilization is likely to play important roles in sensor specificity and lifetime in cells. Collaborative efforts to develop a new ERK activity sensor based on designed ankyrin repeat protein (DAPRin) are also reported in this chapter.

2.2 Introduction and Background

2.2.1 Overview of MAPK signaling

Mitogen-activated protein kinase (MAPK) signaling regulates diverse cell functions including proliferation, growth, survival, differentiation, development, inflammation, stress/osmotic response and cell motility. Complex MAPK signaling responds to a wide array of extracellular stimuli via the coordination of several parallel MAPK cascades in space and in time. A typical MAPK cascade consists of a MAP kinase kinase kinase (MAPKKK), a MAP kinase kinase (MAPKK), and a MAP kinase (MAPK) (**Fig 2.1**). Each component is an ultrasensitive switch in which the activity of these molecules can be turned on and off through phosphorylation and dephosphorylation by the corresponding upstream regulators. Growth factors or mechanical stimulation lead to activation of subsets of small GTPases including Ras, Rac, Cdc42, and RhoA by regulating the binding of a guanosine triphosphate (GTP) molecule or a guanosine diphosphate (GDP) molecule. These small GTPases activate one or multiple downstream protein kinases such as MAPKKKKs, MAPKKKs, and p21-activated protein kinases (PAKs). The mammalian MAPKs can be categorized into the following four classes: extracellular signal-regulated kinases (ERK1 and ERK2), isozymes of p38 (p38α, p38β, p38γ and p38δ), Jun N-terminal kinases (JNK1, JNK2 and JNK3), and ERK5. Each pathway is tightly regulated at various levels including specific kinase-substrate interactions, kinase-scaffold protein interactions, duration and strength of upstream signals, feedback mechanisms, and sub-cellular location of each component during individual transient signaling events.

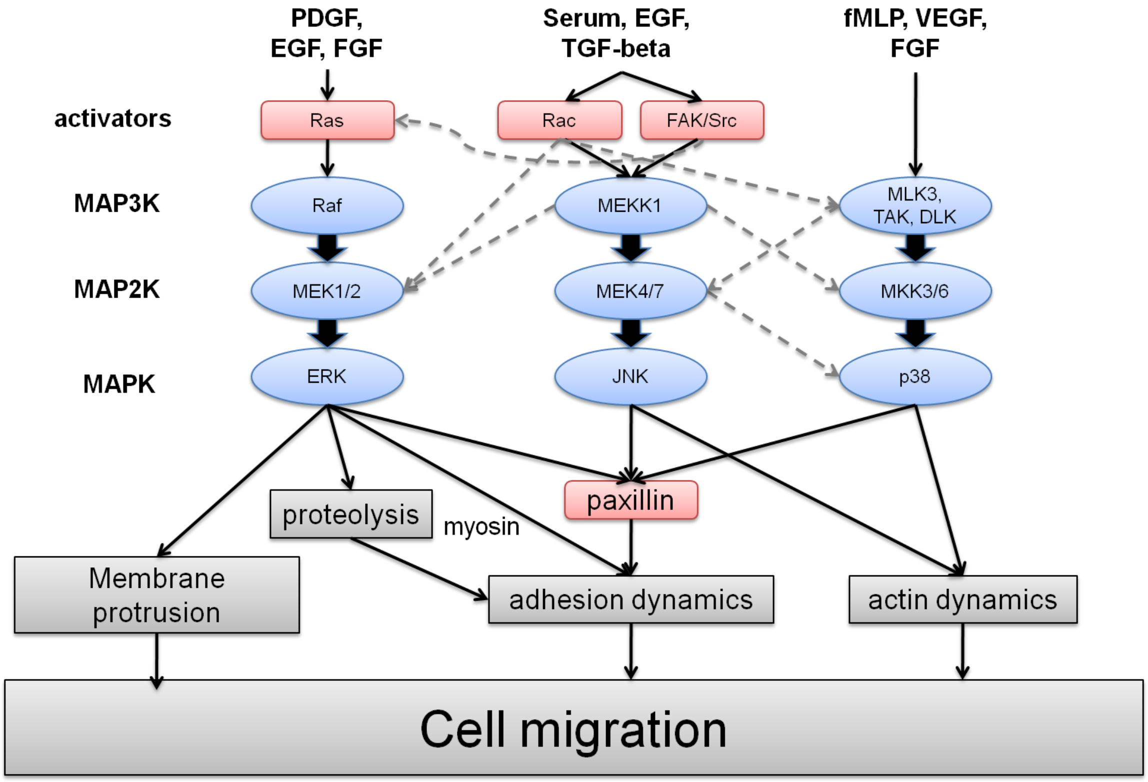

Figure 2.1 Overview of MAPK signaling in cell motility.
A typical MAPK cascade is composed of MAPKKKs, MAPKKs and MAPKs. Upstream activators of MAPK signaling include Rho GTPases and protein kinases such as Ras, Rac, Src and FAK. In response to growth factors or mechanical forces, ERK, JNK, and p38 coordinate to regulate cell motility by activating distinct subsets of effectors involved in protrusion, adhesion and actin dynamics.

Origins of signaling specificity of MAPK signaling MAPKKs show great specificity towards the downstream MAPKs, but these MAPKKs are regulated by a large number of upstream MAPKKKs through phosphorylation of dual sites on the activation loop of MAPKKs (**Fig 2.2**). MAPKs also undergo a dual phosphorylation of the T-X-Y sequence in their activation loop by the corresponding upstream MAPKKs. Activated MAPKs become capable of phosphorylating thousands of MAPK substrates containing the P-X-S/T-P motif. The duration and strength of each MAPK signal is specifically controlled by a variety of dual-specificity MAPK phosphatases (MKPs) (140), Thr/Ser phosphatases and tyrosine phosphatases in both the nucleus and cytoplasm. The bipartite binding mechanism might account for the signaling specificity of each MAPK pathway (141). MAPK proteins contain a common docking (CD) site for all MAPK-interacting proteins and a MAP kinase insert region which is absent in other protein kinase families (142-146).

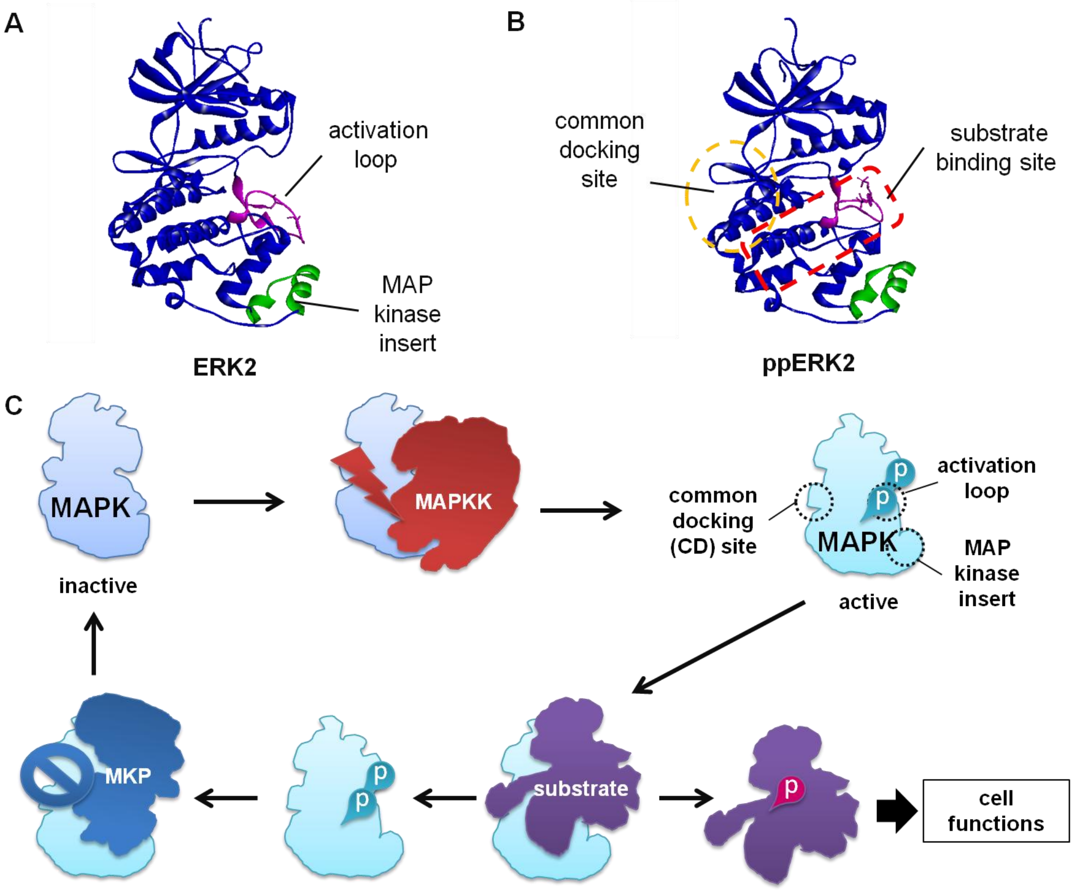

Figure 2.2 Structures and regulation of MAPKs.
A. Structure of unphosphorylated/ inactive ERK2 (PDB: 1ERK) (147). The MAP kinase insert and the activation loop are colored in green and magenta, respectively. **B.** Structure of phosphorylated/active ERK2 (PDB: 2ERK) (147). The common docking (CD) site and the substrate-binding site are circled in yellow and red, respectively. **C.** Regulation of MAPKs. All MAPK-interacting proteins dock to the CD site. Inactive MAPK is phosphorylated by MAPKKs. Phosphorylated MAPKs phosphorylate and activate downstream substrates of distinct cell functions. Activated MAPKs are also inactivated by phosphatases such as MAP phosphatases (MKPs) through dephosphorylation.

MAPKs and cell motility The ERK, JNK, and p38 MAPK pathways coordinate to regulate cell motility (**Fig 2.1**) (148). During lamellipodial protrusions, Rac GTPase activates p21-activated protein kinase (PAK), and then PAK phosphorylates and activates MEK1/2 MAPKK, followed by phosphorylation/activation of ERK1/2 by MEK1/2; active ERK1/2 phosphorylates multiple sites in the WASP-family verprolin homologous protein-2, thus promoting binding of Arp2/3 to the WAVE2 regulatory complex (WRC) (149-152). Rac GTPase also activates the JNK pathway through PAK to control collective cell migration (153). ERK, p38, and JNK are all capable of phosphorylating and regulating paxillin, a signal transduction adaptor protein that anchors at focal adhesions (129). During cell adhesion and detachment, recruitment of Src tyrosine protein kinase, focal adhesion kinase (FAK), and ERK to paxillin has been observed (128, 132, 154-156). ERK also mediates the phosphorylation and activation of calpain, a cysteine protease that cleaves and degrades focal adhesion kinase to facilitate cell detachment during motility (155, 157). JNK and p38 MAPK regulate actin dynamics through phosphorylation of MARCKSL1 and heat shock protein 27 (HSP27) (158, 159), respectively.

Disease relevance to aberrant activation of MAPK pathways Potential new therapeutics targeting the ERK, JNK, and p38-mediated pathways are currently under development because of the direct relevance of these pathways in several clinical conditions, including inflammatory diseases, neurological disorders, and cancer (128, 160-167). For instance, hyper-activation of the MEK-ERK pathways frequently occurs in various types of human cancer including pancreatic cancer, papillary thymus cancer, colon cancer, ovary cancer, and breast cancer (**Fig 2.3A**) (168). There are at least seven MAPKKs for regulating ERK, p38, JNK or ERK5. Each MAPKK consists of a kinases domain and short N-terminal and C-terminal sequences (**Fig 2.3B**). Both the active and inactive MEK1 and MEK2 are retained in the cytoplasm because the two MAPKKs feature a nuclear export signal (NES) in the N-terminal sequence (169). Preclinical studies indicate that blocking ERK activation by MEK1/2 inhibitors is effective in inhibiting proliferation of various cancer cells through regulation of the cell cycle and apoptosis (170-172). However, targeting either one of the MAPK pathways has been difficult because these parallel pathways can not only compete with each other but can also develop compensatory effects under certain circumstances. Acquired resistance to Raf inhibitors and MEK1/2 inhibitors has been observed in melanoma cells (161, 173-176).

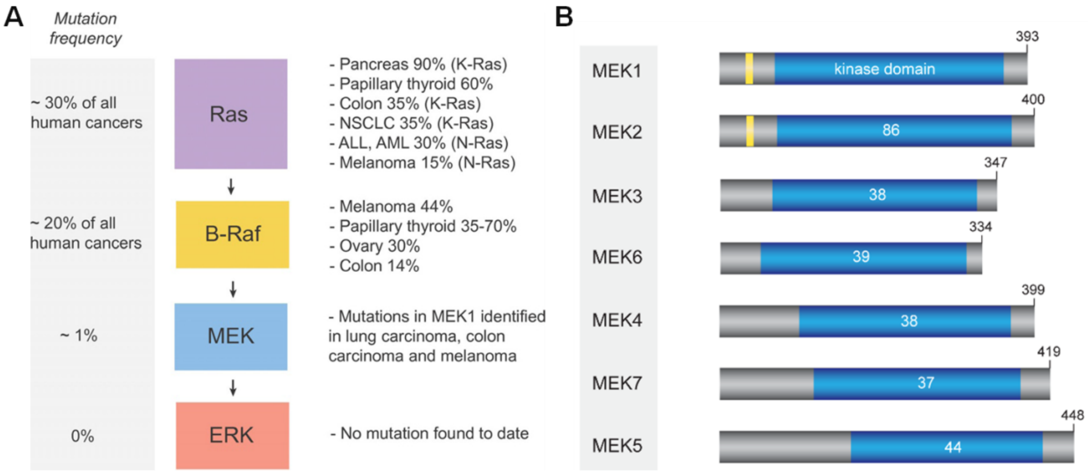

Figure 2.3 Cancer-relevance of mutations in the ERK pathway and structures of human MAPKKs.
A. High occurrence of mutations in Ras and B-Raf in cancer patients. **B.**MAPKKs have a kinase domain (colored in blue) and short N-terminal and C-terminal sequences. The N-terminal sequences of MEK1 and MEK2 contain a nuclear export signal (NES) as indicated in yellow. The two figures were reprinted from the reference (168) with permissions: Frêmin *et al* (2010), *J. Hematol. Oncol.*, 3, 1-11.

Understanding the cross-talk between individual MAPK pathways with improved spatial and temporal resolutions is therefore of great importance. Traditional methods such as *in vitro* biochemical assays and fixed cell experiments (128, 169, 177-181) are limited in their ability to reveal MAPK dynamics with submicron and seconds resolution.

While several versions of fluorescent protein-based reporters of ERK phosphorylation for live cell experiments (15, 17, 20) and a dye-based p38 phosphorylation sensor (182, 183) for use in unfractionated cell lysate (49) have been reported, activity sensors for their activators—MEK1/2 for ERK and MKK3/6 for p38 are not yet available.

2.2.2 Structures and regulation of MAPKs and MAPKKs

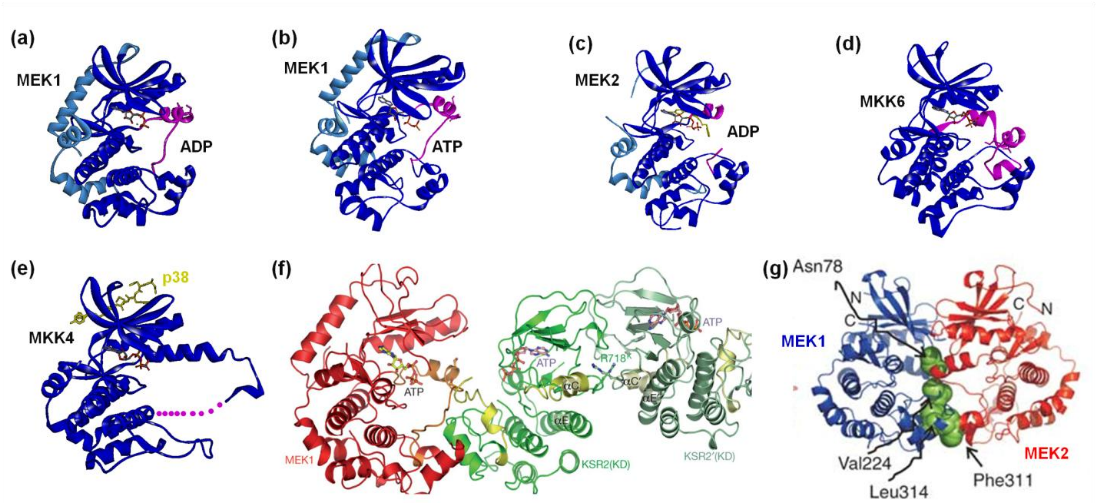

Figure 2.4 Structures of MAPKKs and MAPKK complexes, and a model of a MEK1-MEK2 heterodimer.

The kinase domain, activation loop and other regions are colored in blue, magenta and cyan, respectively. The synthetic peptide of p38 is colored in yellow. **(a)** Unphosphorylated Homo sapiens MEK1 [39-382] in complex with ADP, Mg^{2+}, Ca^{2+} and Na^{+} at 1.90 Å resolutions (PDB: 3EQI) (184). **(b)** Unphosphorylated Homo sapiens MEK1 [39-382] in complex with Mg^{2+}, Ca^{2+}, Na^{+} and a non-hydrolyzable ATP analog, ATP-γS, at 2.1 Å resolutions (3EQD) (184). **(c)** Unphosphorylated Homo sapiens MEK2 [60-393] in complex with ATP, Mg^{2+} and an inhibitor at 3.2 Å resolutions (PDB: 1S9I) (185). **(d)** Homo sapiens MKK6 [44-334] in complex with Mg^{2+} and a non-hydrolyzable ATP analog, AMP-PNP, at 2.60 Å resolutions. (PDB: 3VN9) (186). **(e)** Homo sapiens MKK4 [5-389] in complex with a mono-phosphorylated synthetic peptide of p38α [3-10], AMP-PNP and Mg^{2+} at 2.60 Å resolutions (PDB: 3ALO) (187). **(f)** Unphosphorylated Oryctolagus cuniculus MEK1 [37-381] in complex with Homo Sapiens KSR [653-931], ATP, Mg^{2+} and Cl^{-} at 3.46 Å resolutions (PDB: 2Y4I) (188). The figure was reprinted with permissions. **(g)** A computation model of a MEK1-MEK2 heterodimer (188). The figure was reprinted with permissions.

Structures of MAPKKs Structures of wild type MAPKKs have been solved for MEK1, MEK2, MKK4, and MKK6 (**Fig 2.4**). A co-crystal structure of MKK4 in complex with a mono-phosphorylated synthetic peptide derived from p38 suggested that MKK4 is likely to be auto-inhibited by the binding of a substrate molecule at an allosteric site on the N-terminal lobe of MKK4, which leads to extension of an α-helix and blockage of substrate access to the ATP-binding pocket of MKK4 (187). A recently reported co-crystal structure of MEK1 in complex with truncated KSR scaffold protein molecules shed new light on the regulation of Raf-MEK-ERK signaling (**Fig 2.4f**) (188). MEK1 and KSR interact with each other through their catalytic sites and some regions at the C-terminal lobes near the catalytic sites. MEK1 and MEK2 form both homodimers and hetereodimers. The formation of a MEK1-MEK2 heterodimer is found to be responsible for modulating the duration and strength of MEK/ERK signaling by affecting the ERK-mediated phosphorylation of Thr292 of MEK1 (189). The computational model of a MEK1-MEK2 heterodimer revealed that the dimerization interface occurs at the activation loops of MEK1 and MEK2 (**Fig 2.4g**). The heterodimer was predicted to have a free energy of dimerzation of -15.1 kcal/mol and dissociation constants of 1.1 x 10^{-11} M^{-1}, which are similar to the calculated values for the MEK1 homodimer. There is no clear structural information showing how the activator MAPKKs, the substrate MAPKs, or the phosphatases bind MAPKKs.

Upstream signaling of MEKs Upstream activators of MEK include PAK1 and several MAPKKKs including Raf, MOS, TPL2, and MEKK2 (164). Both MEK1 and MEK2 have dual phosphorylation sites for activation: Ser218 and Ser222 in MEK1, Ser222 and Ser226 in MEK2. The dual phosphorylation sites of MEK1/2 are mainly phosphorylated by Raf family MAPKKK. Raf isoforms exhibit differential regulation of MEK1/2. A-Raf weakly activates MEK1/2. B-Raf prefers to activate MEK1 while Raf-1 is capable of activating both. Upon activation by GTP-bound activated GTPases, Rafs are recruited to the plasma membrane, the outer membrane of the Golgi apparatus, or other putative cellular compartments such as mitochondria and endoplasmic reticulum (ER). Constitutively active forms of MEK1 and MEK2 have been obtained by mutating the dual phosphorylation sites to charged amino acids. For instance, S218D or S222D mutations to MEK1 increase MEK activity by 10-50 fold, and S218D/S222D or S218D/S222 E double mutations activate MEK1 about 6000 fold (190). Other phosphorylation sites of MEK1 include Ser212, Thr 286, Thr292, Ser298, and Thr386. PAK1 phosphorylates Ser218 and/or Ser222 of MEK1 but does not phosphorylate MEK2 (191). Phosphorylation on Ser212 of MEK1 was found to result in inhibition of MEK activity both *in vitro* and *in vivo* but the upstream regulator has not yet been identified. Thr286 and Thr386 of MEK1 can be phosphorylated by Cdk5 (192, 193). When Ser218, Ser222, and Ser298 of MEK1 are all phosphorylated, the association of phosphorylated MEK1 and its substrate ERK is enhanced. In contrast, phosphorylation of Thr292 of MEK1 by activated ERK not only decreases the phosphorylation levels of Ser298 of MEK1 but also greatly reduces the binding affinity between phosphorylated MEK1 and phosphorylated ERK (194).

Subcellular localization of MEKs Expression of CFP-tagged wild type MEK1 in HEK293 cells showed that CFP-MEK1 localizes homogeneously and exclusively in the cytoplasm throughout growth factor-induced stimulation (195), which is consistent with immune-staining of total MEK in epidermal growth factor (EGF)-stimulated and phorbol 12-myristate 13-acetate (PMA)-stimulated Swiss 3T3 cells (196). The observed localization is due to the fact that both MEK1 and MEK2 contain a nuclear export signal

(NES) in the N-terminal sequence of MEKs. Seger group reasoned that active MEK massively translocates to the nucleus and is then rapidly exported to the cytoplasm because of the NES signal (197). When they deleted the NES region of MEK, they observed substantial accumulation of the MEK mutant in the nucleus in both COS7 and HEK 293T cells. The NES-deleted MEK mutant proteins were also found in the cytoplasm, cell periphery, and possibly in the lamellipodia regions. Interestingly, Tolwinski *et al* showed that wild type dual-phosphorylated MEKs localized mainly in the cytoplasm in resting cells and were enriched in the nucleus in mitotic cells, as visualized by immunostaining (198).

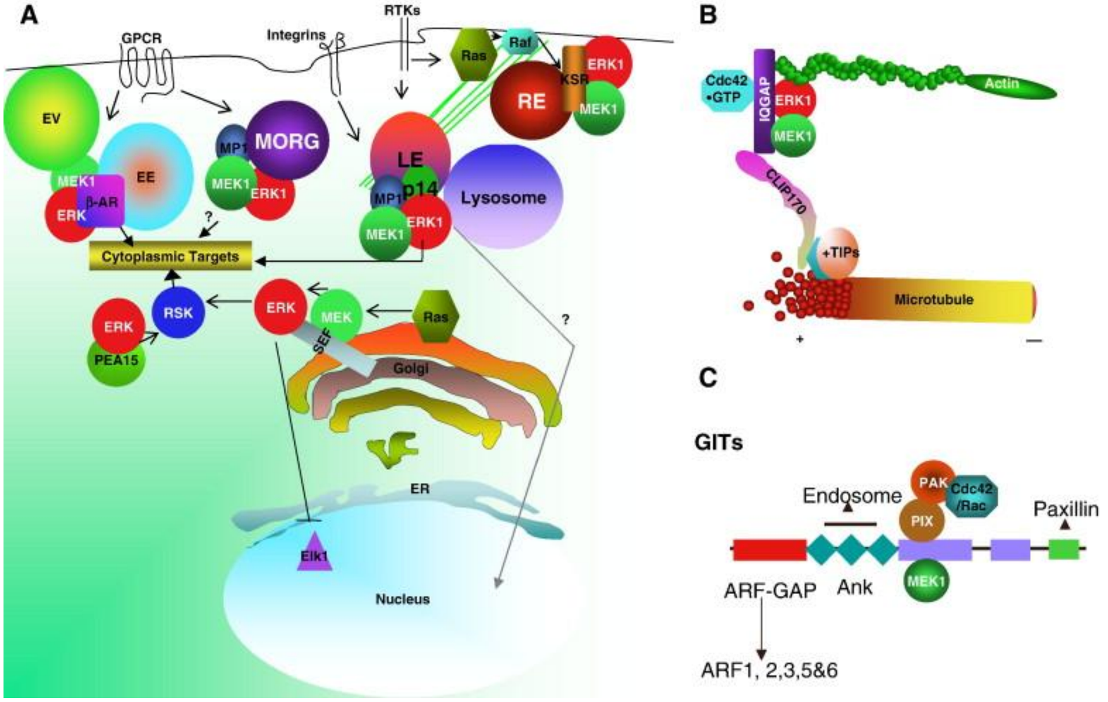

Figure 2.5 Signal specificity of MEKs and ERKs is regulated by subsets of scaffold proteins.

A. GPCRs modulate the Raf-MEK-ERK signaling activity in the cytoplasm through β-arrestin and MORG. MEKs constitutively associate with KSR to respond to various growth factors. MP1/p14 is responsible for growth factor-stimulated MEK-ERK signaling in the later endosomes. PEA-15 regulates the Ras-mediated MEK-ERK signaling to inhibit apoptosis. Sef sequesters MEK and ERK in the Golgi apparatus. EV: endocytic vesicles. EE: early endosomes. RE: recycling endosomes. LE: late endosomes. **B.** IQGAP is an actin-binding molecule that renders Cdc42 and Rac in GTP-bound conformations. MEKs and ERKs are likely to be localized at the tips of microtubes through binding of IQGAP and interactions with CLIP170/+TIPs. **C.** GRK interacting GIT molecules interact with multiple proteins, coordinating MEK and ERK to membrane trafficking through the action of ARF-GAPs. Paxillin is both the scaffold and the substrate of ERKs at peripheral adhesion complexes. This figure was reprinted from the reference (199) with permission: A.K. Pullikuth *et al* (2007), *Cellular Signaling* **19**, 1621-1632.

Another plausible mechanism contributing to why MEKs are mainly localized in the cytoplasm is their association with distinct scaffold proteins in various cellular compartments (199-209). These known scaffold proteins include kinase suppressor of Ras (KSR) (188, 210, 211), MEK partner 1 (MP1) (212-215), similar expression to FGF genes (sef) (216-218), MAP kinase organizer 1 (MORG-1) (219), phosphoprotein enriched in astrocytes 15 (PEA-15) (220-222), GRK-interacting protein (GIT1) (223-225), IQGAP1 (226-230), paxillin (132, 231-234), and β-arrestins (235-237) (**Fig 2.5**). KSR enhances ERK activation by anchoring Rafs, MEKs, and ERKs at the plasma membrane. MP1 brings MEKs and ERKs to p14 and endosomes to fully activate ERKs, thus MP1 determines how long ERK activation is sustained. In contrast, Sef is important for suppression of ERK signaling. Sef has a transmembrane segment and tethers MEK and ERK to the Golgi apparatus. Sef preferentially binds to activated MEK and inhibits the dissociation of the MEK-ERK complex. As a result, the activated ERKs cannot enter the nucleus and mainly activate downstream effectors in the cytoplasm. ERKs have been found to co-localize with paxillin (**Fig 2.5C**) and IQGAP1 (**Fig 2.5B**). IQGAP1, an actin-binding protein important for cell-cell adhesion, is also a scaffold protein for EGF-stimulated activation of the BRAF-MEK-ERK pathway. Paxillin is an important cytoskeletal protein that anchors to focal adhesions. Upon stimulation by hepatocyte growth factor (HGF), Raf1, MEK, and ERK associate with paxillin (131, 238). The HGFstimulated ERK activation is also promoted by Src-mediated phosphorylation of Tyr118 of paxillin. Activated ERK then phosphorylates Ser83 of paxillin to enhance recruitment of focal adhesion kinase (FAK) to paxillin, resulting in turnover of focal adhesions and lamellipodia via the FAK-PI3K-Rac pathaway (239). The use of biosensors for simultaneous imaging of MAPKK and MAPK sensors at specific time and subcellular localization will greatly improve the understanding of the complex regulation and signaling specificity of MAPK pathways.

Structures of MAPKs All MAPK-binding proteins bind MAPKs through the common docking (CD) site of the corresponding MAPK and a second docking site on the MAPK surface. Most available structures are complexes of a full length MAPK molecule in complex with one or two synthetic peptides derived from the binding partners (**Fig 2.6**). Fus3, ste7, ste5, far1, and Msg5 are a MAPK, a MAPKK, a scaffold protein, a MAPK substrate, and a MAPK phosphatase in yeast. The co-crystal structures of unphosphorylated p38α in complex with the full length MAPK-activated protein kinase-2 (MK2), a substrate of p38α (**Fig 2.6j**, PDB: 2OZA (240) , 2OKR (241) and 2ONL (241)), provide a clear picture of how MAPK susbstrates bind MAPKs; p38α interacts with MK2 through the CD site and the substrate binding site near the catalytic site of p38α. It has been determined that unphosphorylated and activated p38α binds inactive MK2 with a K_d of 2.5 nM and 6.5 nM, respectively (242). The binding interaction between unphosphorylated p38 and MK2 has a proposed role in regulating the transport of the p38-MK2 complex from the nucleus to the cytoplasm because the NLS signal of MK2 becomes inaccessible when MK2 binds p38, as shown in the co-crystal structures (241). *In vitro* binding assays of unphosphorylated ERK2 with several ERK2 substrates also showed that some ERK2 substrates preferentially bind unphosphorylated ERK2 over phosphorylated ERK2 (243). Although there is no direct evidence showing that the binding interactions between inactive MAPKs and MAPK substrate proteins do exist *in vivo*, we cannot exclude the possibility that some MAPK substrates might constitutively associate with inactive MAPK and compete with the activator MAPKKs. Interestingly, the MAP kinase insert region of unphosphorylated p38α showed minimal contacts with MK2. Together with the fact that deletions or some mutations in the MAP kinase insert region of ERK2 abolished the formation of stable MEK-ERK complex but only caused slight to moderate influences on the stability of the ERK-substrate or ERK-phosphatase complexes (244), a small environment sensitive fluorophore attached at the MAP kinase insert region of MAPK proteins is likely to exhibit fluorescence change specifically to MAPKK-MAPK binding interactions, despite the fact that the unphosphorylated dye-labeled MAPK proteins might still bind to diverse substrates *in vivo*.

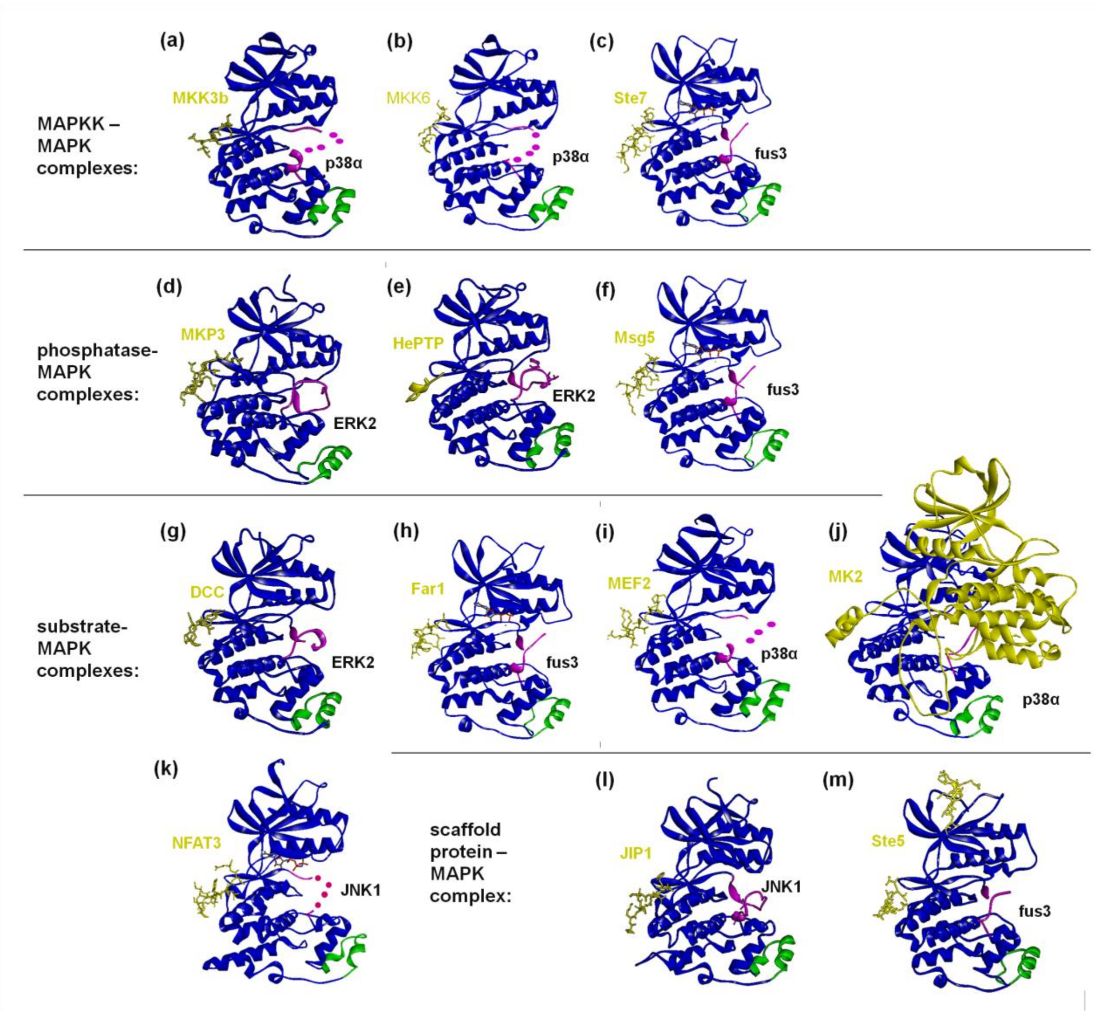

Figure 2.6 Structures of MAPKs in complex with full length proteins or synthetic peptides derived from ERK-interacting proteins.

MAPKs and MAPK-interacting proteins are colored in blue and yellow, respectively. The MAP kinase insert of MAPKs is highlighted in green and the missing residues are represented as magenta spheres. **(a)** Mus musculus p38α [4-353] in complex with a synthetic peptide of MKK3b [97-104] at 2.3 Å resolutions (PDB: 1LEZ) (245) . **(b)** Homo sapiens p38α [4-353] in complex of a synthetic peptide of MKK6 [10-17] at 1.95 Å resolutions (PDB: 2Y8O, to be published by Barkal *et al*). **(c)** Saccharomyces cerevisiae fus3 [1-353] in complex with ADP, Mg^{2+} and a synthetic peptide derived from Saccharomyces cerevisiae Ste7 [9-20] at 1.55 Å resolutions (PDB: 2B9H) (246) . **(d)** Unphosphorylated Rattus norvegicus ERK2 [8-356] in complex with a synthetic peptide derived from MKP-3 [64-74] at 2.5 Å resolutions (PDB: 2FYS) (247) . **(e)** Unphosphorylated Rattus norvegicus ERK2 [10-354] in complex with a synthetic peptide derived from the D motif of HePTP [16-31] at 1.90 Å resolutions (PDB: 2GPH) (248) . **(f)** Saccharomyces cerevisiae fus3 [1-353] in complex with a synthetic peptide derived from Saccharomyces cervisiae Msg5 [25-38] at 2.5 Å resolutions (PDB: 2B9I) (246) . **(g)** Unphosphorylated Rattus norvegicus ERK2 [9-354] in complex with a synthetic peptide derived from a netrin acceptor DCC [148-155] at 1.95 Å resolutions (PDB: 3O71) (249). **(h)** Saccharomyces cerevisiae fus3 [1-353] in complex with a synthetic peptide derived from Saccharomyces cerevisiae Far1 [72-82] at 2.3 Å resolutions (PDB: 2B9J) (246) . **(i)** Mus musculus p38α [5-354] in complex of a synthetic peptide of MEF2 [2-11] at 2.30 Å resolutions (PDB: 1LEW) (245) . **(j)** Homo sapiens p38α [6-353] in complex with Homo sapiens MK2 [51-390] at 2.70 Å resolutions (PDB: 2OZA) (240) . **(k)** Homo sapiens JNK1 [6-365] in complex of a synthetic peptide derived from Homo sapiens NFAT3 [143-154] at resolutions (PDB: 2XS0, to be published by Barkai *et al*). **(l)** Unphosphorylated Homo sapiens JNK1 [7-363] in complex of a synthetic peptide derived from Homo sapiens JIP1 [54-63] at 3.00 Å resolutions (PDB: 3O17, to be published by Comess *et al*). **(m)** Saccharomyces cerevisiae fus3 [3-353] in complex with two synthetic peptides derived from Saccharomyces cerevisiae Ste5 [288-297] and [306-314] at 1.90 Å resolutions (PDB: 2F49) (246) .

Putative binding sites of ERK-interacting proteins by computational analysis The putative binding sites of several known ERK-interacting proteins on the ERK protein (**Fig 2.7**) were recently predicted by the Nussinov group using PRISM, a motif-based protein-protein interaction (PPI) prediction method (250) . The target set of ERK-interacting proteins included an activator MEK1, a scaffold protein—MP1, two phosphatases—MKP and PTP, and four substrates—c-Myc, cPLA2, Rsk2, and Mnk1/2. These known protein-protein interactions, obtained through the KEGG database, were clustered and the potential binding motifs were extracted based on the structural similarity of the target proteins using Multiprot. All of the available ERK structures with and without binding partners were used as a template set. Hot spots responsible for binding affinity and stabilization of the protein complexes were identified by the HotPoint webserver. Protein-protein interaction prediction by structural matching (PRISM) then generated several potential ERK-target protein complexes through comparing the structural and sequence similarities of the target proteins with the known binding interactions in the template set. Bad predictions indicating severe steric clashes in the putative binding interface were excluded. The flexibility of the complexes was refined using FiberDock. According to the predictions, the activator MEK1 and the substrate cPLA2 possibly bind ERK at the same time (**Fig 2.7a**), while the phosphatase MKP3 and the substrate Rsk2 are unlikely to bind ERK simultaneously, owing to the large steric clashes of these protein-protein interactions (**Fig 2.7b**). The generated model suggested that MEK1 binds ERK throught the MAP kinase insert. The truncated MEK1 with a deletion in the N-terminal sequence abolishes the binding between MEK and ERK (251). The model also predicted that MEK2 and the scaffold protein MP1 cannot bind MEK simultaneously because they share the identical binding site (**Fig 2.7c**). Although the predictions collectively provide a big picture of how the activators, the substrates, the phosphatases, and the scaffold proteins could possibly interact with ERK, all the models of the ERK-target complexes only contain one binding site on ERK, whereas numerous biochemical and structural studies suggest that most ERK-interacting proteins should bind ERK in a bipartite manner (141, 145, 252-256).

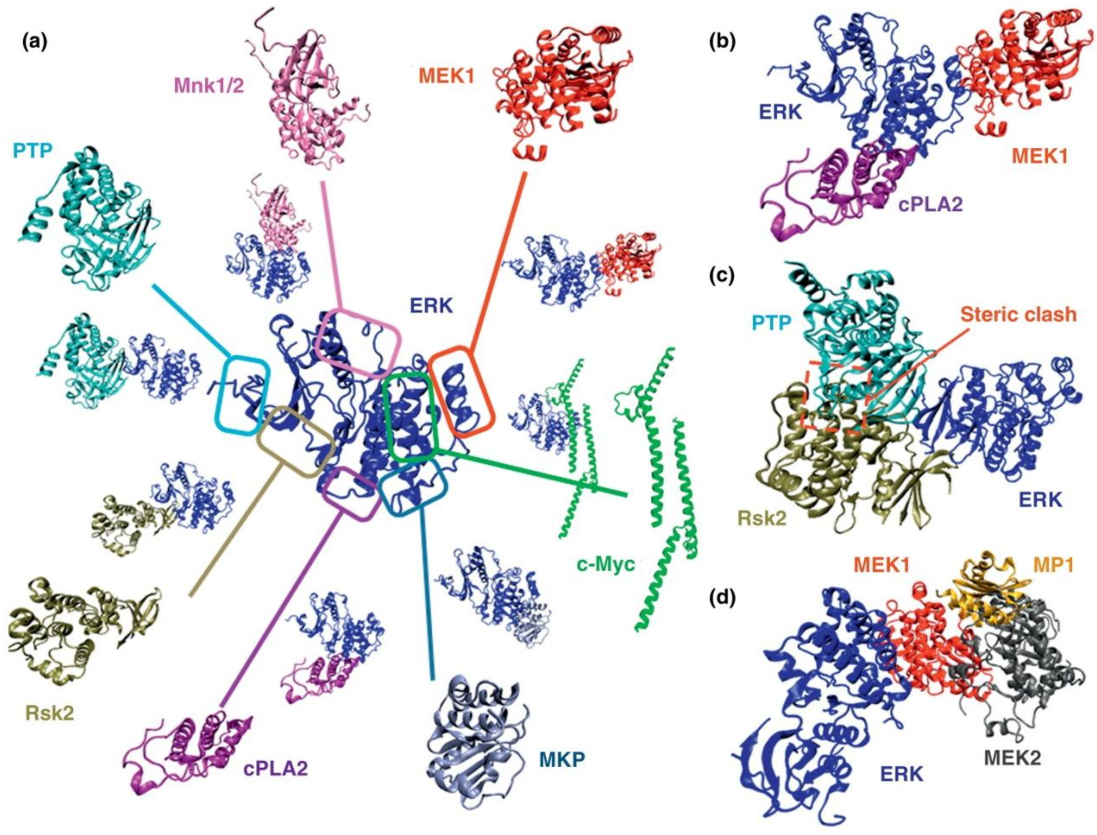

Current Opinion in Structural Biology

Figure 2.7 Putative binding interfaces of ERK and ERK-interacting proteins predicted by PRISM.
(a) Potential binding sites of individual ERK-interacting proteins mapped on an ERK molecule (blue). **(b)** Model of simultaneous binding interactions of ERK-MEK1 and ERK-cPLA2**.** ERK, MEK1 and cPLA2 were colored in blue, red and magenta, respectively **(c)** Steric clash in the model of simultaneous binding interactions of ERK-PTP and ERK-Rsk2. ERK, PTP and Rsk2 ware colored in blue, cyan, and brown, respectively. **(d)** Model of complex formation between ERK (blue), MEK1 (red), MEK2 (grey), and the MP1 scaffold (yellow). This figure was reprinted from the reference (250) with permission: G. Kuzu *et al* (2012), *Current Opinion in Structural Biology* **22**, 367-377.

Regulation of ERKs Active MEK1/2 first phosphorylate Tyr185 of ERK2. The resulting phosphorylated ERK2 dissociates from MEK1/2 and then associates with MEK1/2 again for the second phosphorylation on Thr187 of ERK2 (32, 257, 258). The two residues of ERK2 must be both phosphorylated to become fully activated. The dual phosphorylation sites of ERK1/2 are dephosphorylated by dual specificity phosphatases (DUSPs) (259-265). There are at least 10 DUSPs known to dephosphorylate ERK in mammalian cells and these DUSPs are so-called MAPK phosphatases (MKPs). ERKs are also inactivated by protein phosphatase-2 (PP2A) (266) and hematopoietic protein-tyrosine phosphatase (HePTP) (248, 267), indicating the importance of these phosphatases in determining the duration and strength of ERK activation at a specific time and place (265, 268, 269). ERK signaling is compartmented inside cells as regulated by various scaffold proteins molecules for MEK and ERK (270-272).

Downstream of ERKs The majority of ERK substrates are nuclear targets (178, 273, 274). Upon phosphorylation in the cytoplasm, activated ERKs rapidly translocate to the nucleus and regulate gene expression (177, 178, 275-281). For instance ERK phosphorylates E twenty-six (ETS)-like transcription factor 1 (Elk1) (180, 243, 259, 282-285) and mitogen- and stress-activated protein kinases (MSKs) (286-288) at multiple sites. Two products of proto-oncogenes important for growth control are c-fos and v-myc myelocytomatosis viral oncogene homolog (c-Myc) (289-291) transcription factors. To regulate cell growth and proliferation, ERKs phosphorylate Pol III-specific transcription factor B (TFIIIB) (292, 293) which is in charge of the synthesis of 5S rRNA and tRNA during protein synthesis. Other key transcription factors that are activated by ERKs in the nucleus include activator protein 1 (AP-1) for stimuli-induced gene expression (294-297), NFκB for inflammation (200, 273), and B cell lymphoma 2 (Bcl-2) for apoptosis (266, 298). Cytoplasmic targets of ERKs are crucial for negative feedback regulation of ERK signaling. For instance, once SOS is phosphorylated by ERK in the cytoplasm, the SOS-GRB2 complex becomes destabilized for membrane recruitment, which in turn leads to down regulation of the Ras-dependent ERK activation pathway (299). ERK-mediated cell motility relies on the phopshorylation of paxillin (131, 132, 232, 234, 300) and myosin light chain kinases (MLCKs) (128, 301, 302) in the cytoplasm. Another important cytoplasmic target of RSKs (286, 303), activated RSKs translocate to the nucleus and phosphorylate many transcription factors, including Ser103 of serum response factor (SRF), Ser133 of cyclic AMP response element-binding protein (CREB), and Ser 362 of c-fos (288, 304). ERKs also directly phosphorylate MAPK-interacting kinases (MNKs) at Thr197 and Thr202 in the cytoplasm (305, 306). Activated MNKs then activate CREB or eukaryotic initiation factor-4E (eIF-4E) to regulate translation (306-309). RSKs, MSKs, and MNKs can be group together as MAPK activated protein kinases (MAPKAPKs) which work together with ERK to phosphorylate hundreds of downstream substrates that regulate distinct cell functions including proliferation, growth, survival, differentiation, and cell motility (143, 305, 310). Tanimura *et al* showed that sustained duration of ERK activity in the nucleus is responsible for hepatocyte growth factor (HGF)-induced cell motility in MDCK cells (311). They observed abolished activation of Elk-1, c-fos, and matrix metalloproteinase 9 (MMP-9) when cells were transfected with MKP3, which anchored ERKs in the cytoplasm.

2.2.3 Current biosensor designs for reporting spatiotemporal dynamics of MAPK signaling in live cells

Several biosensor designs that report activation of ERK and JNK in live cells have been developed by various groups (**Fig 2.8**). All the biosensor designs were based on genetically targetable fluorescent proteins and Förster resonance energy transfer (FRET).

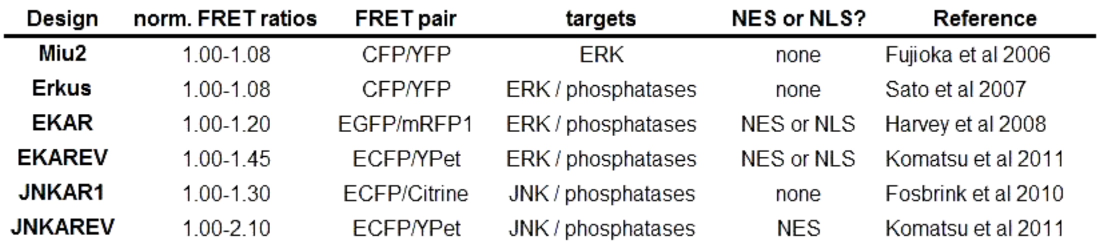

Design	norm. FRET ratios	FRET pair	targets	NES or NLS?	Reference
Miu2	1.00-1.08	CFP/YFP	ERK	none	Fujioka et al 2006
Erkus	1.00-1.08	CFP/YFP	ERK / phosphatases	none	Sato et al 2007
EKAR	1.00-1.20	EGFP/mRFP1	ERK / phosphatases	NES or NLS	Harvey et al 2008
EKAREV	1.00-1.45	ECFP/YPet	ERK / phosphatases	NES or NLS	Komatsu et al 2011
JNKAR1	1.00-1.30	ECFP/Citrine	JNK / phosphatases	none	Fosbrink et al 2010
JNKAREV	1.00-2.10	ECFP/YPet	JNK / phosphatases	NES	Komatsu et al 2011

Table 2.1 Comparison of the reported biosensors for ERK and JNK MAPKs.

Miu2 (**Fig 2.8a**), the first biosensor design for visualizing ERK activity in live cells, consists of a wild type ERK molecule, a CFP molecule, and a YFP molecule (32). Upon phosphorylation by endogenous MEK or dephosphorylation by endogenous phosphatases, the CFP-ERK-YFP molecules undergo conformational changes that affect the relative orientations and distance between the CFP and the YFP molecules. Ideal probes for live cell imaging should exhibit at least a 20% change in FRET/donor ratios between the active state and the inactive state, so the small dynamic range of the Miu2 probe limits its further application (**Table 2.1**). Other biosensor designs are based on substrates of ERK or JNK (15-17, 32, 312). A phosphor-binding domain that binds the phosphorylated region and/or a docking domain for recruitment of specific MAPK was incorporated into the sensor designs. EKAR **(Fig 2.8c)**, an ERK biosensor based on FRET between EGFP and mRFP1, showed a 20% maximum change in FRET ratios and a maximum change in fluorescence lifetime of 0.08 ns in two-photon fluorescence lifetime imaging microcopy (2p-FLIM) (17). EKAR has also been used to image ERK activity in hippocampal neurons. EKAREV, an optimized version of EKAR with a maximum change of about 45%, was applied in a high content screen of nuclear ERK activity change in response to growth factors or inhibitors (312). In general, the JNK biosensors have superior dynamic ranges relative to the currently available ERK biosensors (16, 312).

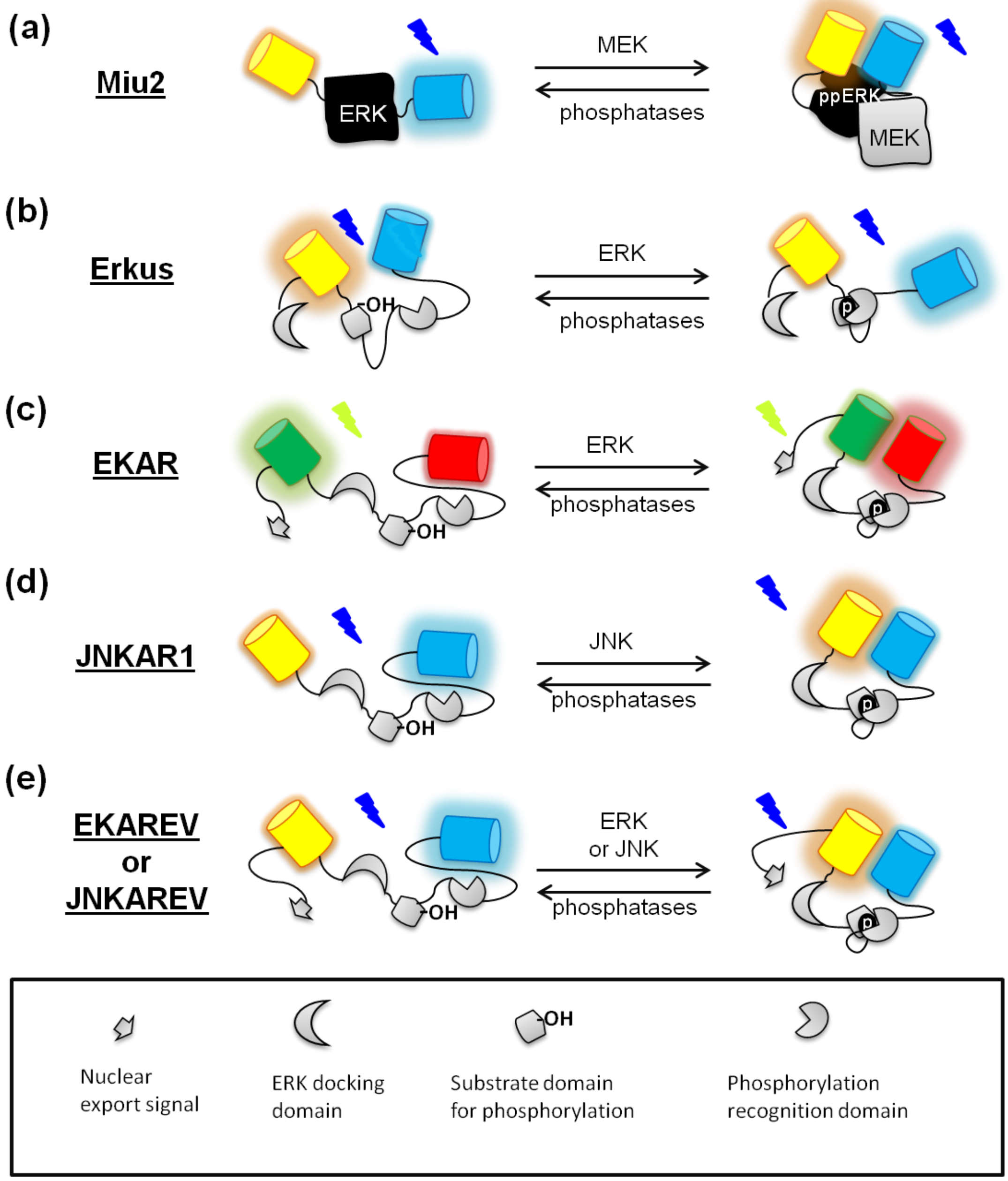

Figure 2.8 Existing biosensor designs for ERK and JNK.

The biosensor design (**a**) relies on the conformational changes of the ERK fusion proteins upon phosphorylation and dephosphorylation. Other designs (b)-(e) use MAPK substrates and the binding interactions between phosphorylated substrates and a motif which preferentially binds the phosphorylation sites of biosensor proteins.

Except in the case of Miu2, these sensor designs not only respond to endogenous ERK activation but also sense fluctuation from endogenous phosphatases. Without directly sensing the target, accurate measurements of spatial and temporal resolution were hampered by phosphorylation kinetics and the diffusion rate of the biosensor proteins. The other two major issues are the use of nuclear export signals (NES)/ nuclear localization signals (NLS), and the bulky size of the FRET cassette. The cytoplasmic-retained versions still have insufficient sensitivity for studying MAPK dynamics in the cytoplasm. NES or NLS tags are usually added to the biosensor designs to enhance the dynamic range of these biosensor designs in specific subcellular compartments. Since the activation of MAPKs by MAPKKs is mainly regulated by scaffold proteins, the appended fluorescent proteins in the sensor designs likely limit the access of the biosensor proteins to endogenous MAPKs in such multi-protein complexes. Despite the importance of MAPKKs, there is currently no way to accurately monitor the signaling dynamics of MAPKKs *in vivo* due to the lack of available biosensors.

2.3 Results and Discussion

2.3.1 Biosensor designs based on dye-labeled ERK2

ERK2 activity sensors and MEK1/2 activity sensors were both designed based on dye-labeled ERK2 with two distinct mechanisms of fluorescence response (**Fig 2.9**). According to previous studies, the measured dissociation constant of the ppMEK1/ERK2 complex is approximately 0.1 μM while the association constant of ppMEK1 and ppERK2 cannot be measured by current experimental methods (32). The inability to measure this constant is likely due to a feedback mechanism in which ppERK2 phosphorylates T292 of ppMEK1 to initiate fast dissociation of the ppMEK1-ppERK2 complex (164, 313). Based on these facts, new ERK2 activity sensors were designed based on a dye-labeled ERK2 molecule that would maintain the capacities of endogenous wild type ERK2, including that it is phosphorylated by active upstream MAPK kinase MEK1/2, is dephosphorylated by active MAPK phosphatases, and phosphorylates substrates of wild type ERK2. Upon activation/phosphorylation by active MEK1/2, an ERK2 protein molecule undergoes a large conformational change. To report a phosphorylation-induced conformational change of ERK2, a solvent-sensitive dye was covalently attached to a solvent-accessible cysteine of ERK2 in a region where major conformational changes occur after phosphorylation. The dye molecule exhibited changes in fluorescence in response to the altered hydrophobicity around the dye-attachment site, resulting from phosphorylation-induced conformational changes. In contrast, MEK1/2 activity sensors require a “dead” dye-labeled ERK2 protein molecule as an affinity scaffold that specifically binds activated MEK1/2 but not other ERK-interacting proteins. In this case a solvent-sensitive dye molecule was covalently attached to an engineered cysteine at or near the MEK-ERK binding interface. Upon binding, the dye became brighter when hydrophobicity at the MEK-ERK binding interface increased. Since MEK1 and MEK2 MAPKK are the only known upstream activators of ERK2, inactivated dye-labeled ERK2 molecules possess great potential of being specific reporters of MEK activation.

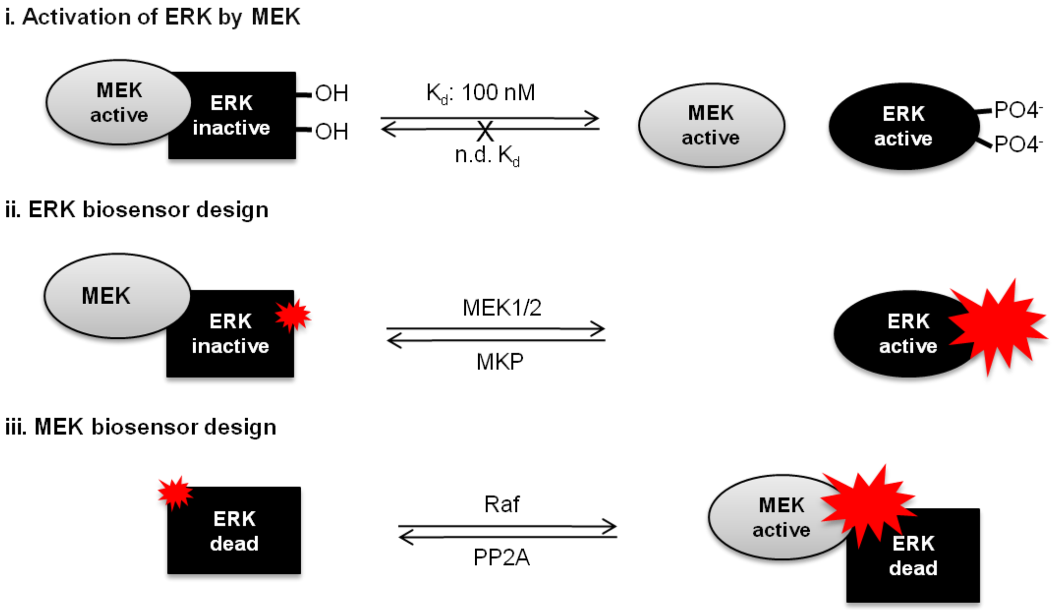

Figure 2.9 Rational designs of ERK biosensors and MEK1/2 biosensors based on dye-labeled ERK2.
i. Phosphorylated MEK1/2 binds unphosphorylated ERK2 with a K_d of 100 nM; phosphorylated ERK2 dissociates from phosphorylated MEK1/2. **ii.** A dye-labeled ERK mimic reports phosphorylation-induced conformation changes by changing fluorescence properties of the attached dye molecule. **iii.** A dye-labeled dead ERK reports binding with activated MEK1/2 through a fluorescence change of the attached dye molecule.

Strategies for selection of the best dye-labeled ERK2 molecules as ERK2 activity sensors or as MEK1/2 activity sensors are depicted as a workflow (**Fig 2.10**). Because it is prohibitively labor-intensive to sample all 358 amino acids in *Rattus norvegicus* ERK2 for dye attachment, the first step was to determine suitable sites for dye attachment through computational approaches. Each of the predicted sites from this initial set was then mutated to a cysteine residue and reacted with an iodoacetamide-containing dye to form a stable covalent linkage. The next step was to construct a library of dye-labeled ERK2 from combinations of an ERK2 mutant protein molecule and one of several solvent-sensitive dyes. Each dye-labeled ERK2 construct was then titrated with various amounts of active MEK1, both in the absence and in the presence of ATP, to identify whether the biosensor candidate senses phosphorylation-induced conformational changes of dye-labeled ERK, MEK-ERK binding interactions, or both mechanisms. For MEK1/2 activity sensor designs, biosensor candidates with more than 20% *in vitro* fluorescence response to MEK binding were then titrated with several test proteins representative of the wide array of over 500 known ERK-interacting proteins. Subcellular localization and response to known stimuli of the best biosensor candidates were examined in live cells to determine whether the biosensor could be useful for investigating biological questions, or if further modification of the design was required.

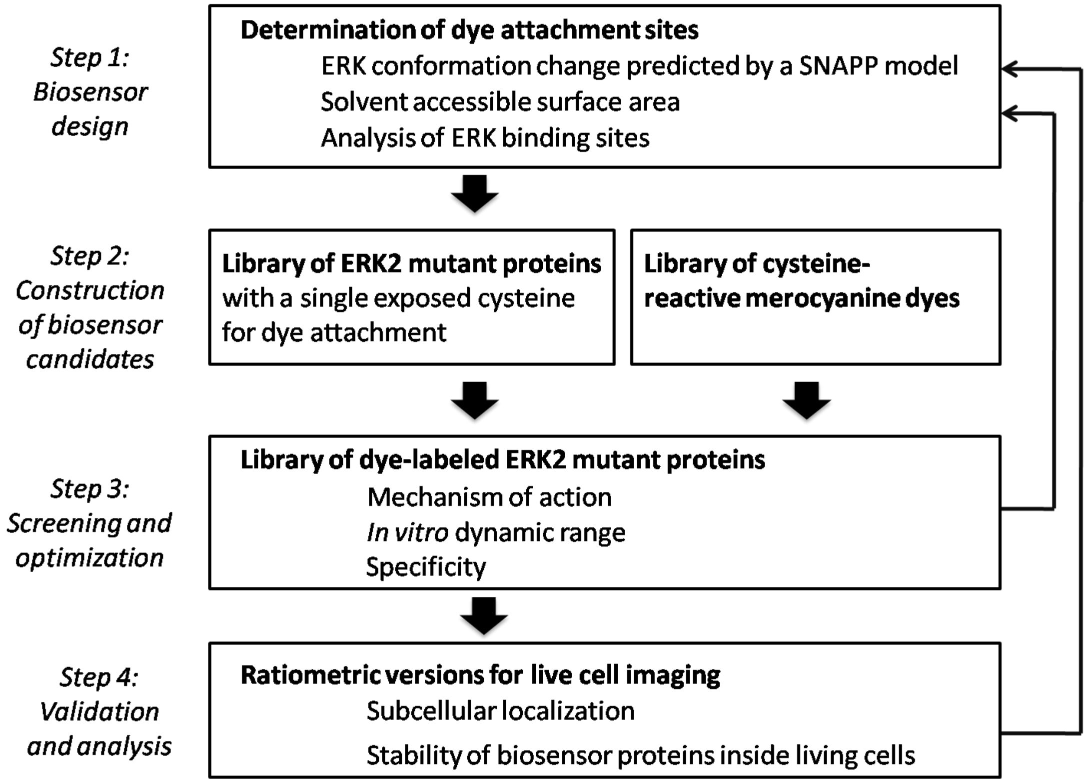

Figure 2.10 Work flow for developing ERK biosensor and MEK biosensors based on dye-labeled ERK2.
Step 1: Identification of i) solvent-accessible residues which might undergo large conformation changes upon phosphorylation in the case of ERK2 activity sensors and ii) solvent-accessible residues located on MEK-ERK binding interface but away from docking sites of other ERK-interacting proteins. **Step 2:** Preparation of ERK mutants with a solely exposed cysteine residue for dye attachment and a paint box of cysteine-reactive solvent-sensitive dyes. **Step 3**: Screening, characterization and optimization of dye-labeled ERK. **Step 4:** Validation and redesign of dye-labeled ERK2.

As a proof of principle, a library of nine solvent-sensitive merocyanine dyes was used to construct biosensors based on dye-labeled ERK2. According to previous work in the Hahn laboratory to optimize red merocyanine dyes for live cell biosensor applications (45, 56, 57, 314), **mero60** (**Fig. 2.11**) was found to be more solvent-sensitive than all other dyes in the library. A biosensor using this dye was therefore most likely to exhibit the largest dynamic range, but its maximum brightness was known to be lower than other red dyes. **Mero61** is the least solvent-sensitive but the most photostable among the red merocyanine dyes, so it might be more useful for time-lapse imaging experiments.

Another red dye, **mero62**, with balanced properties in brightness, photostability, and solvent-sensitivity, could serve as an alternative fluorophore to tune dye-protein interactions depending on the type of protein interactions encountered. **Mero77** and **mero99**, two near infrared merocyanine dyes previously described (see Part 1) were employed to generate red-shifted sensor designs that could enable co-imaging of multiple dye-based biosensors in the same cell. **Mero199**, a unique red merocyanine dye which can produce an intrinsic ratiometric response, was also tested on dye-labeled ERK with the aim of generating MEK1/2 biosensors with intrinsic ratiometric responses for the purpose of multiplex imaging. **Mero87** has shown well-balanced photophysical properties in biosensor designs for activated endogenous Cdc42 and Src family kinases. Two other structurally similar derivatives, **mero53** and **mero221**, share the identical electron donor, electron acceptor, and conjugation length as **mero87** but differ in the position of a thiol-reactive iodoacetamide group and the position of a charged sulfate group. These differences can potentially have profound effects on dye-protein interactions. Therefore **mero87**, **mero53**, and **mero221** were chosen as the primary set of test dyes for construction and screening of bright and sensitive biosensors based on dye-labeled ERK2.

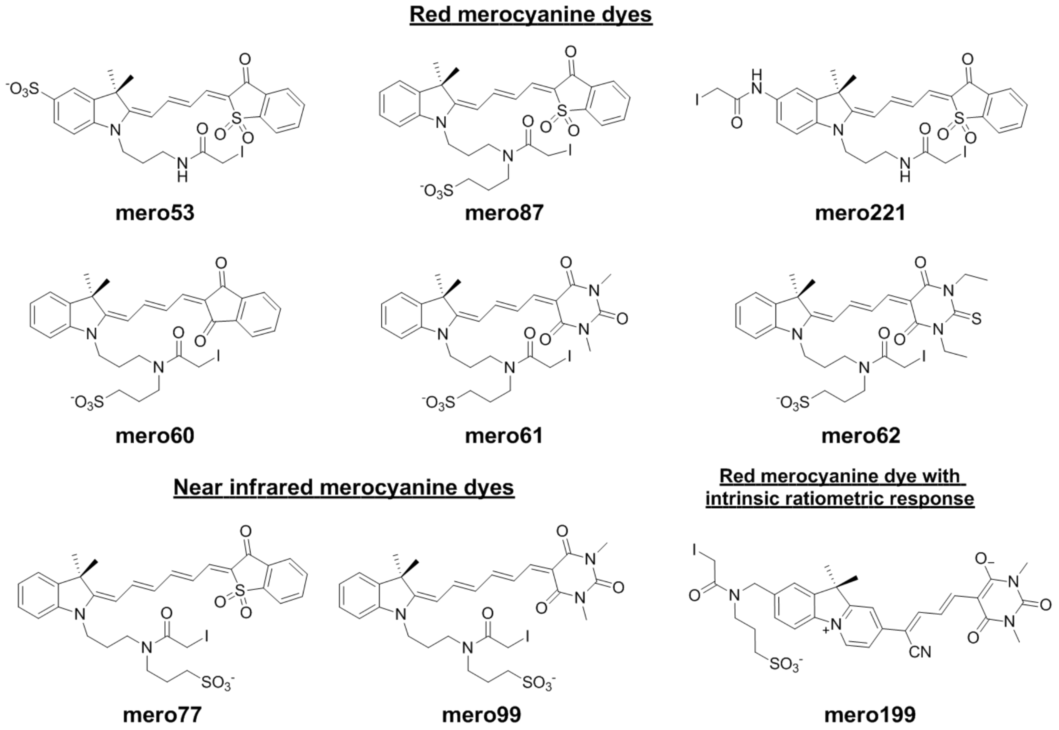

Figure 2.11 Cysteine-reactive merocyanine dyes used in this study.
These dyesin the composition of electron donor, electron acceptor, and conjugation lengths which determine brightness, labeling efficiency, dynamic range and protein stability of biosensor conjugates.

2.3.2 Selection of sites for dye attachment in ERK2

Robust biosensors require reproducible one-way reactions in which a dye molecule only forms a covalent linkage with the most reactive engineered cysteine residue but not with other exposed intrinsic cysteines in the biosensor protein of interest. Over-labeling of other exposed cysteines in biosensor proteins usually results in non-reproducible biosensor response as observed in a preliminary study of dye-labeled wild type ERK2, which suffered from over-labeling of multiple solvent-accessible intrinsic cysteines. To ensure that only the desired cysteine residue is covalently labeled with the solvent-sensitive dye molecule, all other solvent-accessible intrinsic cysteines in ERK2 must be mutated to non-cysteine amino acids.

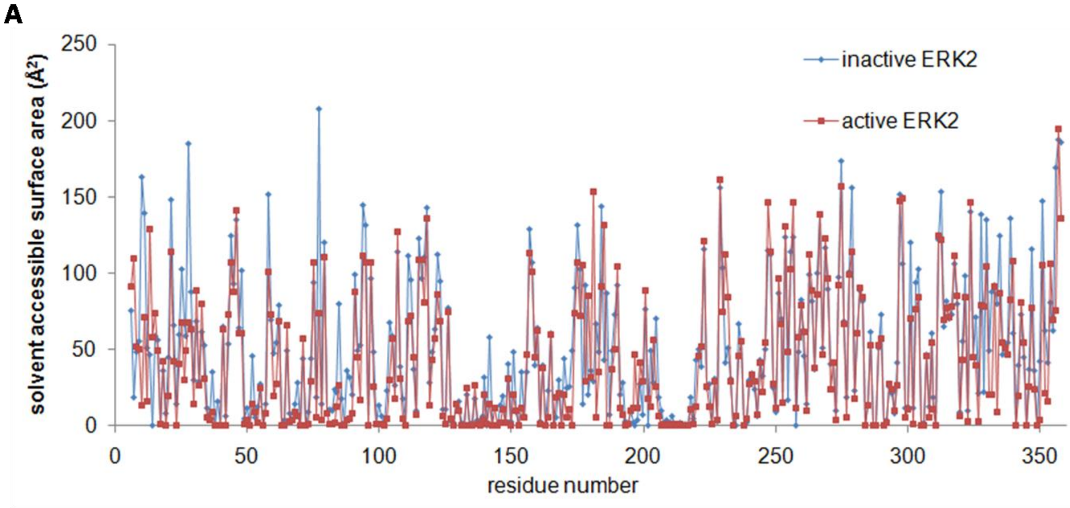

B

ERK2 Residue	SASA (Å²) inactive	 active
Cys38	0.0	0.0
Cys63	0.0	0.0
Cys125	11.0	1.3
Cys159	39.8	44.9
Cys164	23.2	5.4
Cys214	1.7	0.9
Cys252	70.1	66.9

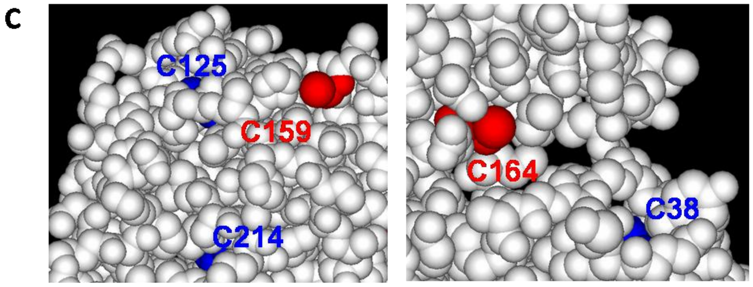

Figure 2.12 Solvent accessible surface area (SASA) analysis of each residue in ERK2.

SASA values were calculated by VMD using the published structures of inactive ERK2 (PDB: 1ERK) and active ERK2 (PDB: 2ERK). **A.** Comparison of SASA values at each residue in active and inactive conformations of ERK2. **B.** List of SASA values of intrinsic cysteines. **C**. Location of exposed (colored in red) and buried (colored in blue) intrinsic cysteines mapped in the crystal structure of inactive ERK2 (1ERK).

Residues with sufficient solvent accessibility and minimal steric hindrance for dye labeling reactions were identified using computational models including Visual Molecular Dynamics (VMD), GetArea and ASAView with the input protein structures of inactive/unphosphorylated ERK2 (PDB: 1ERK) and active/dual-phosphorylated ERK2 (PDB: 2ERK). The estimated solvent accessible surface area (SASA) values of each residue in active and inactive conformations of wild type ERK2 were plotted (**Fig 2.12A)**. Higher SASA values indicate higher accessibility to solvent or dye molecules at the residue of interest. Residues with SASA values smaller than 50 Å^2 are considered to be buried residues in the protein of study. According to the model generated by VMD, Cys252 is the most solvent-accessible. Cys159 and Cys164 are partially exposed while Cys38, Cys63, Cys125 and Cys214 are essentially buried intrinsic cysteines in both active and inactive conformations of wild type ERK2 (**Fig 2.12B**, **Fig 2.12C**). Because Cys63 was thought to be responsible for sensing ERK conformation changes in the case of dye-labeled wild type ERK2 in preliminary studies, C63S, C159S, C164S and C252S mutations were introduced into all biosensor constructs.

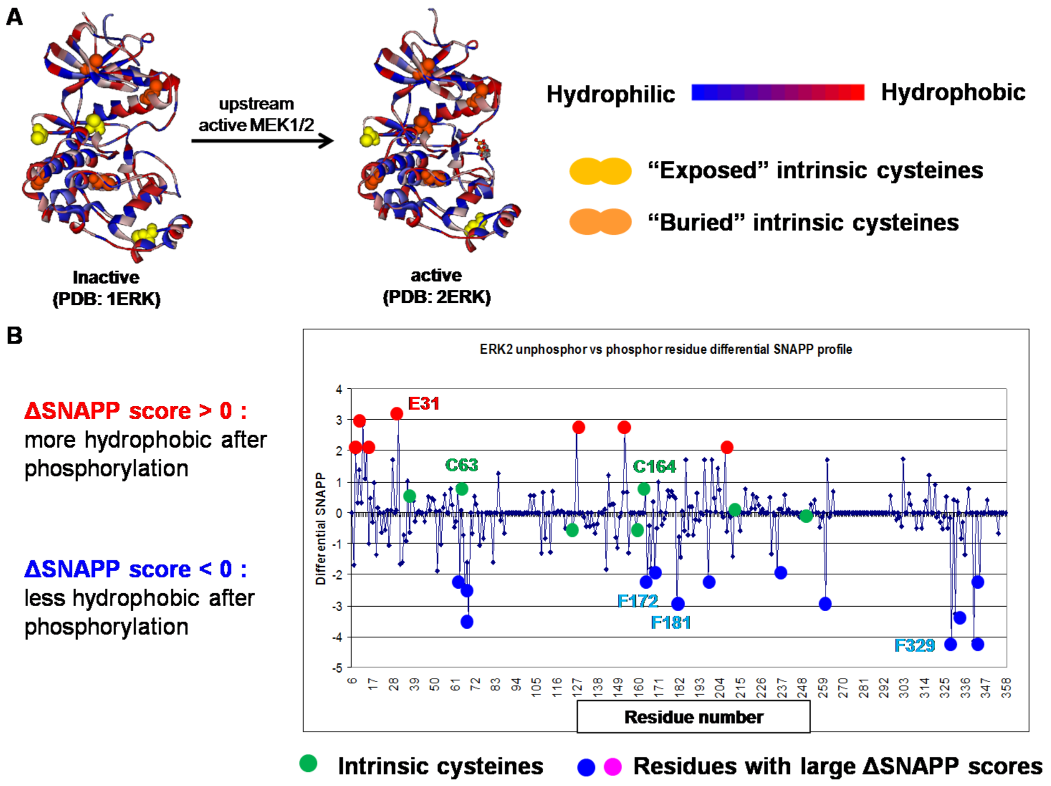

C

Residue	$SASA_{inactive\ ERK2}$ (Å^2)	$SASA_{active\ ERK2}$ (Å^2)	ΔSNAPP
Ile29	87.2	63.2	0
Glu31	68.4	88.6	3.2
Ser151	48.6	20.5	0
Cys164	23.2	5.4	0.7
Ala172	25.1	10.7	0
Phe181	29.2	153.1	-2.8
Cys252	70.1	66.9	0
Ile254	123.5	130.9	0
Asn255	16.7	47.9	0.5
Phe329	21.7	78.0	-4.2
Leu333	92.1	91.0	0

Figure 2.13 Local hydrophobic property of each residue in ERK2.
A. Hydrophobicity maps of inactive ERK2 (PDB: 1ERK) and active ERK2 (PDB: 2ERK) created by Discovery Studio Visualizer. **B**. ΔSNAPP scores of each residue in ERK2 calculated by Yetian Chen. **C**. Solvent-accessible surface area (SASA) values and ΔSNAPP scores of selected residues for dye attachment in ERK2.

The initial attempt was to design dye-labeled ERK2 which acts like the wild type ERK2 in living cells and shows fluorescence change upon activation/inactivation of the dye-labeled ERK2. In this design the solvent-sensitive dye molecule needs to be placed at a region where the dye is able to sense large changes in local hydrophobicity upon phosphorylation-induced conformation changes of the dye-labeled ERK molecule itself. Structural alignment of the published protein structures of active/phosphorylated ERK2 (PDB: 2ERK) and inactive/unphosphorylated ERK2 (PDB: 1ERK) (**Fig 2.13A**) indicated that the conformational change mainly occurs around the activation loop of ERK2. With the high resolution structures of inactive and active ERK2, residues that undergo large conformational changes upon phosphorylation were identified by a model generated by Simplicial Neighborhood Analysis of Protein Packing (SNAPP) (315-318) through collaboration with Yetain Chen in the Tropsha group at the University of North Carolina at Chapel Hill (**Fig 2.13B**). The SNAPP score of a residue reflects the extent of hydrophobicity surrounding the residue, thus the difference of SNAPP scores of a residue in inactive and active conformations was used here to predict whether a residue of interest will be in a more hydrophobic or in a less hydrophobic environment after phosphorylation-induced conformational changes. The SNAPP model was first validated using the published biosensor design for Cdc42; Phe271 in the Cdc42-binding domain (CBD), the optimized site for dye attachment, was also predicted to be the residue with the largest SNAPP score in the model of Cdc42-WASP complex (data not shown). Because it is necessary to retain the function of dye-labeled ERK in our designed ERK activity sensor, candidate residues located at or near the ATP-binding pocket, the activation loop, and the common docking (CD) sites were excluded from the list. Glu31 in ERK2 was predicted to be in a more hydrophobic environment after phosphorylation while Ala172, Phe181, and Phe329 in ERK2 were predicted to be in a less hydrophobic environment after phosphorylation. Ile29, Ser151, Gly228 and Leu333 in ERK2, with

ΔSNAPP scores close to zero, were chosen as negative controls to validate the predictive power of this model. The intrinsic cysteine Cys164 in ERK2, partially solvent-accessible and with a moderate ΔSNAPP score of 0.7, was also chosen for dye attachment. The solvent-accessible surface area values of these predicted sites for dye attachment are listed in **Fig. 2.13C**.

The biosensor designs of MEK1/2 activity sensors rely on inactivated ERK2 mutant proteins as affinity reagents which specifically bind to activated MEK1 and MEK2 MAPKK. The dye molecule needs to be placed at the MEK-ERK binding interface and at a distance from the docking sites of other ERK-interacting proteins to ensure specific fluorescence response of the designed biosensor constructs. Inactive/unphosphorylated ERK2 is known to bind active MEK1/2 and scaffold proteins while active/phosphorylated ERK2 interacts with a tremendous number of ERK2 substrates and several MAPK phosphatases (203). Additionally, phosphorylated ERK2 is able to form a homodimer in the cytoplasm that promotes nuclear translocation of activated ERK2 (319, 320). Due to the lack of co-crystal structures of ERK and its interacting proteins, the alternative approach here was to build a model to map the possible ERK2 binding interactions on the crystal structures of active ERK2 (PDB: 2ERK) and inactive ERK2 (PDB: 1ERK) based on correlation of biochemical and structural studies of known ERK mutations (**Fig 2.14A**). Criteria used to define relevant and irrelevant ERK mutations included binding affinity values and phosphorylation rates of ERK mutants, wild type ERK regulators, and wild type ERK effectors (141, 146, 253, 282, 320-333). In summary, it seems that all ERK-interacting proteins bind ERK in a bipartite manner involving the common docking (CD) domain as well as a second region on the protein surface of ERK;

active MEK1/2 MAPKKs bind the CD domain, the MAP kinase insert domain, and some regions near the activation loop of inactive ERK2.

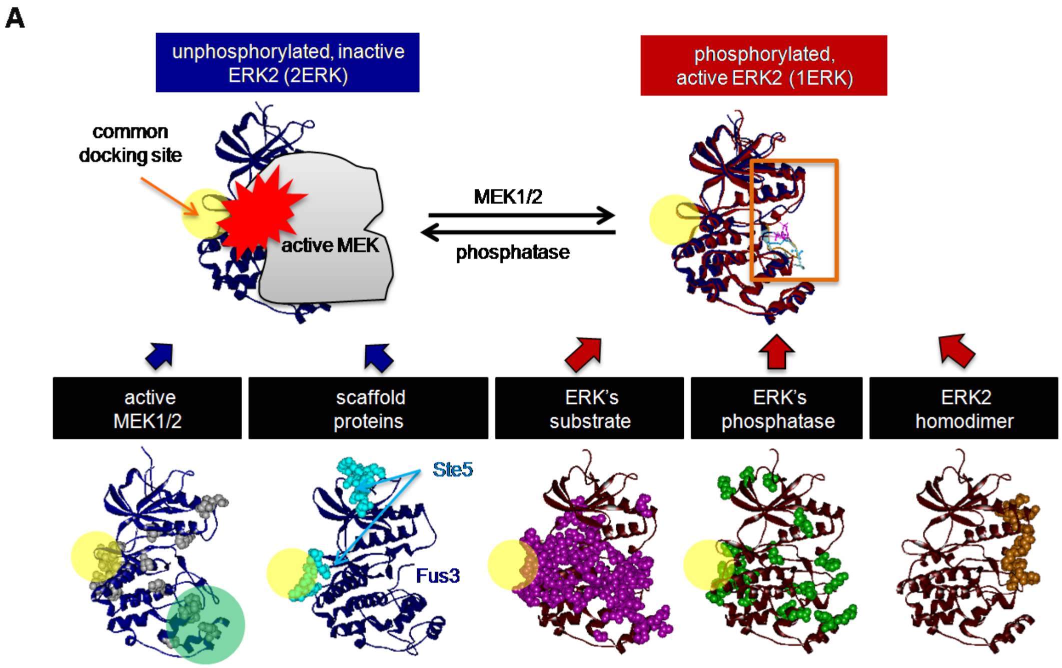

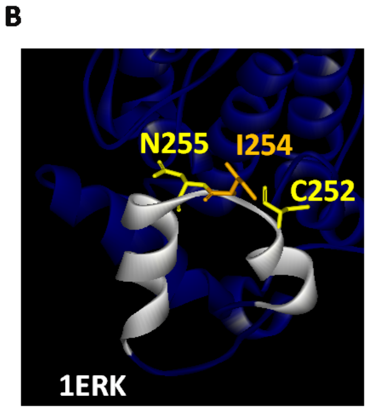

C

Residue	$SASA_{inactive\ ERK2}$ (Å^2)	$SASA_{active\ ERK2}$ (Å^2)	Secondary structure
Ser246	112.0	66.9	loop
Gln247	24.9	15.2	α-helix
Glu248	9.2	130.9	α-helix
Asp249	86.5	47.9	α-helix
Leu250	70.1	102.8	α-helix
Asn251	14.7	146.2	α-helix
Cys252	123.5	11.5	loop
Ile253	16.7	57.8	loop
Ile254	113.6	79.1	loop
Asn254	123.4	61.6	loop
leu256	0.0	10.1	α-helix
Lys257	47.9	112.4	α-helix
Ala258	82.4	88.7	α-helix
Arg259	45.2	37.7	α-helix
Asn260	13.8	85.9	α-helix
Tyr261	99.0	138.1	α-helix
Leu262	81.1	46.6	α-helix
Leu263	37.2	122.4	α-helix
Ser264	99.7	96.3	α-helix
Leu265	138.8	23.9	loop
Pro266	50.7	41.3	loop

Figure 2.14 Potential docking sites of ERK-interacting proteins.

A. Known ERK mutations with corresponding altered ERK function are shown in spheres on the structures of inactive ERK2 (blue, PDB: 1ERK) and phosphorylated ERK2 (red, PDB: 2ERK). The activation loop is shown in magenta in 1ERK and cyan in 2ERK. The common docking (CD) site for all ERK-interacing proteins is highlighted in yellow. The MAP kinase insert region is highlighted in green. Mutations in ERK which alter binding affinity between ERK and MEK were shown as white spheres. Residues of

ERK responsible for Ste5-fus3 binding interactions were shown as cyan spheres (PDB: 2F49). Ste5 and fus3 are homologs of KSR and ERK in yeast. Mutations in ERK which alter ERK-substrate binding interactions or phosphorylation kinetics of ERK substrates were shown in magenta spheres. Mutations in ERK which alter the ERK-phosphatase binding interactions or dephosphorylation kinetics of ERK mutants were shown as green spheres. Residues forming homodimerization interface of phosphorylated ERK were shown in orange spheres. **B.** A magnified view of the MAP kinase insert region with inactive ERK2 colored in white. **C.** Solvent accessible surface area (SASA) values of residues at the MAP kinase insert region.

According to a previous study, deletion of the MAP kinase insert of ERK2 (ERK2-Δ242-271) and single point mutations at Tyr261 or Ser264 of ERK2 were found to severely disrupt MEK-ERK binding interactions (244). The same truncation and single point mutations in ERK2 showed a slight decrease in ERK-substrate binding interactions and ERK-phosphatase binding interactions, indicating that the docking interactions of ERK substrates and ERK phosphatases are less dependent on the MAP kinase insert. Scaffold proteins are likely to interact with the CD domain and the N-lobe of ERK2 as shown in the co-crystal structure of fus3 and two peptides derived from ste5 (PDB: 2F49) (334); fus3 and ste5 are homologs of ERK2 and a scaffold protein KSR1 in yeast, respectively. There are more than seven existing scaffold proteins for MEK and ERK (204, 206, 207, 335); it remains unclear whether all these scaffold proteins bind ERK and MEK in the same manner. The docking sites of ERK substrates and MAPK phosphatases overlap extensively on active ERK2. In addition, some ERK substrates including c-fos, RSK-1 and ELK-1 have a preference to bind unphosphorylated ERK2 with binding affinities in the sub-micromolar range (243). An important finding here was the extensive overlap between the ERK homodimerization interface, ERK's substrate binding sites, and the sites with large ΔSNAPP scores. Thus the majority of dye-labeled ERK sensor proteins would be likely to exhibit fluorescence changes not only in response to phosphorylation-induced conformational changes of dye-labeled ERK but also due to binding interactions with the ERK homodimer or sensor-ERK interacting proteins.

Based on these facts, the working hypothesis was that ERK mutant proteins with a dye attached at or near the MAP kinase insert are more likely to produce specific fluorescence changes in response to activated MEK1/2. The solvent accessibility values of residues 246-266 in the MAP kinase insert of ERK2 are compared in **Fig 2.14C**. Except for Cys252, Ile254 and Asn255 in ERK2, other residues are located away from the insert or in the α-helical structures which might be easily disrupted by mutagenesis. Thus Cys252, Ile254, and Asn255 in ERK2 were chosen as the sites for dye attachment to generate MEK1/2 activity sensors.

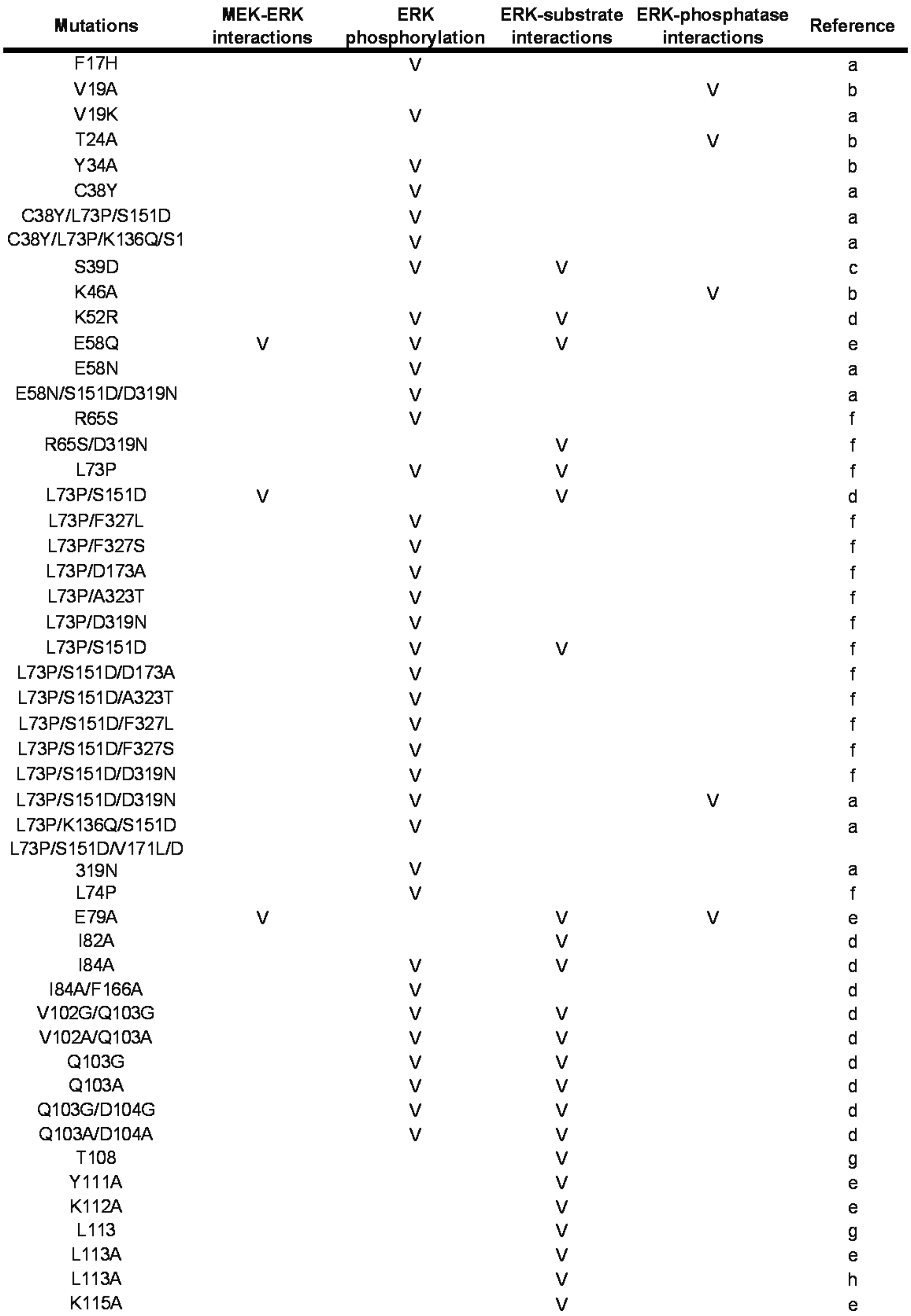

Mutations	MEK-ERK interactions	ERK phosphorylation	ERK-substrate interactions	ERK-phosphatase interactions	Reference
F17H		V			a
V19A				V	b
V19K		V			a
T24A				V	b
Y34A		V			b
C38Y		V			a
C38Y/L73P/S151D		V			a
C38Y/L73P/K136Q/S1		V			a
S39D		V	V		c
K46A				V	b
K52R		V	V		d
E58Q	V	V	V		e
E58N		V			a
E58N/S151D/D319N		V			a
R65S		V			f
R65S/D319N			V		f
L73P		V	V		f
L73P/S151D	V		V		d
L73P/F327L		V			f
L73P/F327S		V			f
L73P/D173A		V			f
L73P/A323T		V			f
L73P/D319N		V			f
L73P/S151D		V	V		f
L73P/S151D/D173A		V			f
L73P/S151D/A323T		V			f
L73P/S151D/F327L		V			f
L73P/S151D/F327S		V			f
L73P/S151D/D319N		V			f
L73P/S151D/D319N		V		V	a
L73P/K136Q/S151D		V			a
L73P/S151D/V171L/D319N		V			a
L74P		V			f
E79A	V		V	V	e
I82A			V		d
I84A		V	V		d
I84A/F166A		V			d
V102G/Q103G		V	V		d
V102A/Q103A		V	V		d
Q103G		V	V		d
Q103A		V	V		d
Q103G/D104G		V	V		d
Q103A/D104A		V	V		d
T108			V		g
Y111A			V		e
K112A			V		e
L113			V		g
L113A			V		e
L113A			V		h
K115A			V		e

Table 2.2 Summary of known mutations in ERK2 that cause altered binding affinity and/or phosphorylation kinetics of ERK2.

Mutations	MEK-ERK interactions	ERK phosphorylation	ERK-substrate interactions	ERK-phosphatase interactions	Reference
T116A			V		e
Q117			V		g
Q117A			V		e
Q117A			V		h
H118A			V		e
L119A			V		e
S120A					f
N121A			V		e
D122A			V		e
H123			V		g
H123A			V		h
Y126			V		g
Y126A			V	V	e
F127			V		g
Y129			V		g
R133			V		g
R133A	V		V	V	e
K136Q		V			a
K149A			V		e
S151A		V	V		e
S151D		V	V		f
S151D/F327L		V			f
S151D/F327S		V			f
S151D/D173A		V			f
S151D/D319N		V	V		f
S151D/A323T		V			f
S151D/V171L/D319N		V			a
S151D/H230N/D319N		V			a
N152A			V		e
L154A			V		e
L155			V		g
T157A			V		e
T158A			V		e
C159			V		g
D160N	V		V	V	e
D160E	V			V	i
F166A		V			d
L168A		V			d
V171L		V			a
D173A		V			f
D173A/A323T		V			f
D173A/F327S		V			f
D173A/F327L		V			f
D173A/D319N		V			f
H176E		V			j
H176E, E343A		V			j
H176E/L333E/L336E/ E343A		V			j
H176A/F181A/L333A/ L336A/L341A/L344A		V			j
T179A		V	V		e
T183E		V			a

Table 2.2 (Continued) Summary of known mutations in ERK2.

Mutations	MEK-ERK interactions	ERK phosphorylation	ERK-substrate interactions	ERK-phosphatase interactions	Reference
E184G			V		e
Y185F		V			k
V186S		V			d
T188A			V		e
T188A		V			d
R189A			V		e
W190A			V		e
V191L	V			V	i
Y191F		V	V		k
I196A/M197A				V	l
M197A			V	V	g
M197A/L198A			V		m
M197A/L198A/Y261A			V		m
L198A			V	V	
N199A/S200A				V	l
K201A				V	o
Y203C		V	V	V	f
K205A				V	o
E218A			V		e
S221A			V		e
N222A			V		e
R223A			V		e
I225A			V		e
P227A			V		e
K229A			V		e
H230A			V		e
H230N	V	V	V	V	e
H230R			V	V	p
Y231A				V	g
Y231A/L232A				V	l
Y231A/L232A/Y261A			V		m
L232A			V	V	g
D233A			V		e
L235A	V		V	V	g
L235P	V		V		n
L235P/N236I			V		n
N236A			V	V	o
N236K			V		p
G243R	V		V		n
N266K	V		V		p
K257A				V	o
Y261A		V	V	V	
Y261C	V		V	V	f
Y261N	V		V	V	p
S264A			V		e
S264P			V		p
R299A				V	o
L306A				V	o
Q313E			V	V	e
Y314			V		g

Table 2.2 (Continued) Summary of known mutations in ERK2 that cause altered binding affinity and/or phosphorylation kinetics of ERK.

Mutations	MEK-ERK interactions	ERK phosphorylation	ERK-substrate interactions	ERK-phosphatase interactions	Reference
Y314A	V		V	V	e
Y314A/Y315A	V		V		q
Y314A/Y315A/D316A/ D319A/D320A	V		V		q
D316N	V		V	V	e
D316A/D319A	V		V	V	p
D316A/D319A/E320A	V		V		q
S318D			V	V	e
D319N	V	V	V	V	e
D319A			V	V	e
D319E	V			V	e
D319R	V			V	e
E320A	V			V	i
E320Q	V			V	i
E322K			V		r
A323T		V			f
E324A			V	V	e
E324Q				V	e
F327S		V			f
F327L		V			f
F329L			V	V	e
F329A	V	V			j
L333A/L336A		V			j
L333A/L336A/L341A/L 344A		V			j
L333E/L336E/K340A/ L344E		V			j
E339A	V				j
K340A	V				j

Table 2.2 (Continued) Summary of known mutations in ERK2 that cause altered binding affinity and/or phosphorylation kinetics of ERK. Sources: (a) M.A. Emrick *et al*, 2001; (b) B. Zhou *et al*, 2006; (c) D.J. Robbins *et al*, 1993; (d) Emrick *et al*, 2006; (e) J. Zhang *et al*, 2003; (f) V. Levin-Salomon *et al*, 2008; (g) T. Zhou *et al*, 2006; (h) O. Abramczyk *et al*, 2007; (i) C. Tarrega *et al*, 2005; (j) J.L.Wilsbacher *et al*, 2006; (k) D. J. Robbins *et al*, 1993; (l) M.N. Yazicioglu *et al*, 2007; (m) S. Polychronopoulos *et al*, 2006; (n) A.W. Whitehurst *et al*, 2004; (o) B. Zhou *et al* 2006; (p) A.M. Delaney *et al*, 2002; (q) B. Xu *et al*, 2001; (r) M. Mahalingam *et al*, 2008.

2.3.3 Generation of ERK2 mutants

Full length *rat* ERK2 with an additional hexa-histidine tag at the N-terminus for affinity purification was cloned into a pET23 vector for bacterial expression. Over-expression of ERK2 mutant proteins in growing bacteria was observed in crude bacteria lysate, with an approximate fivefold increase in protein yields induced by 1.0 mM IPTG

(**Fig 2.14B**). IPTG-induced expression in the BL21 (DE3) *E.coli* strain yielded from 0.02 to 15 mg of soluble ERK2 mutant proteins per 1 L culture, likely depending on the stability of the ERK2 mutant proteins (**Fig 2.14A**). 6xHis-tagged ERK2 mutant proteins with a molecular weight of 42 kDa (theoretical Mw: 42236.48) were prepared in 90-95% purity using cobalt-NTA resins (**Fig 2.14C**).

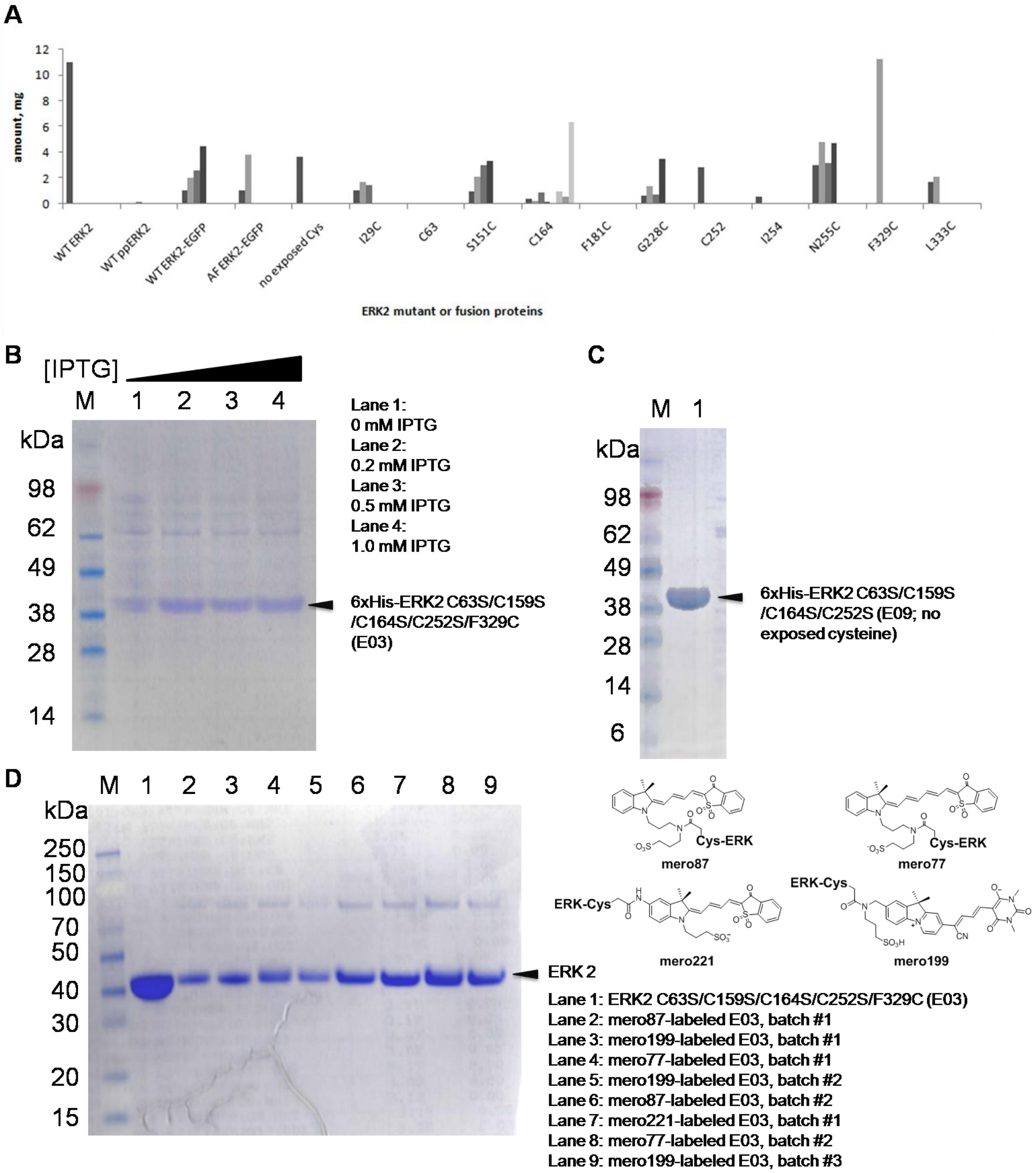

Figure 2.15 Expression and purification of ERK mutant proteins.

A. Weight of soluble ERK2 mutant proteins purified from 1 L culture. **B.** ERK2 C63S/C159S/C164S/C252S/F329C was cultured at 32 °C untill OD600 reached 0.8, followed by IPTG-induced protein expression at 28 °C. Lane 1: 0.0 mM IPTG. Lane 2: 0.2 mM IPTG. Lane 3: 0.5 mM IPTG. Lane 4: 1.0 mM IPTG. **C**. Purified hexa-histidine tagged ERK2 C63S/C159S/C164S/C252S protein. **D**. Purified dye-labeled ERK2 C63S/C159S/C164S/C252S/F329C proteins. Lane 1: unlabeled ERK mutant protein. Lane 2 & 6: different batches of **mero87**-labeled ERK mutant proteins. Lane 3, 5 & 9: different batches of **mero199**-labeled ERK mutant proteins. Lane 4 & 8: different batches of **mero77**-labeled ERK mutant proteins. Lane 7: **mero221**-labeled ERK mutant proteins.

In general, 6xHis-tagged ERK2-EGFP constructs produce a lower amount of soluble proteins compared with wild type 6xHis-tagged ERK2, and the purity of ERK2-EGFP drops to 70% after affinity purification (date not shown). Both of these findings indicate decreased stability of the ERK2-EGFP fusion proteins. Dye-labeled ERK2 mutant proteins were purified by size-exclusion chromatography. After dye labeling reactions the products contained the dye-labeled ERK2 protein and a side product of a molecular weight of approximately 90 kDa (**Fig 2.15D**). The side product is likely to be a cross-linked adduct between the iodoacetamide dye and nucleophiles present in ERK2. Dye concentrations of dye-labeled ERK2 were used to calculate biosensor concentrations for the following fluorescence titration and live cell imaging experiments.

2.3.4 Preparation of test MEK proteins for fluorescence screening

Each biosensor candidate requires at least 30 µg of active MEK1 protein for fluorescence screening. Therefore the development of protocols for large scale production of active MEK1 and other test proteins were necessary to reduce production costs. Expression levels and protein purity after affinity chromatography of the two constructs of constitutively active MEK1, 6xHis-tagged MEK1 R4F (MEK1 ΔN3/S218D/S222D), and GST-tagged MEK1DD (MEK1 S218D/S222D) are compared in **Fig 2.16**. The 6xHis-tagged human MEK1 R4F was expressed in large quantity with an average yield of 8 mg protein per 1 L culture. In contrast, all of the GST-tagged human MEK1DD constructs were poorly expressed and severely contaminated with degradation products containing GST tags (**Fig 2.16C, Fig 2.16D**). The kinase activity of 6xHis-tagged MEK1 R4F was however found to be greatly reduced after freeze-thaw cycles whereas the GST-tagged MEK1DD remained active to phosphorylate ERK2 under the same conditions. Therefore fresh-made 6xHis-tagged MEK1 R4F was used for fluorescence titration experiments. Commercially available active MEK1 or GST-tagged MEK1DD proteins were used for Western blot analysis.

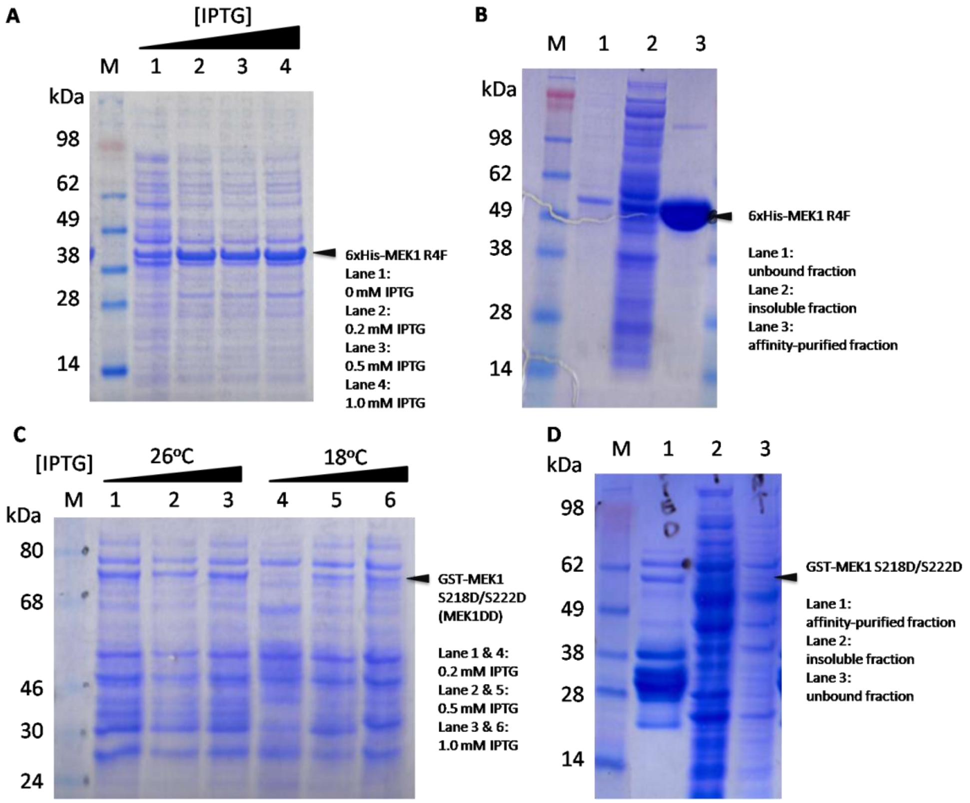

Figure 2.16 Expression and purifcation of active MEK proteins.
A. IPTG-induced expression of 6xHis-tagged MEK1 R4F (MEK1 ΔN3/S218D/S222D). Cultures were grown at 32 ^{o}C untill OD_{600} reached 0.8 and protein expression was conducted at 28 ^{o}C in the presence of IPTG. Lane 1: 0 mM IPTG. Lane 2: 0.2 mM IPTG. Lane 3: 0.5 mM IPTG. Lane 4: 1.0 mM IPTG. **B.** Purified 6xHis-tagged MEK1 R4F. Lane 1: Excess MEK proteins in the supernatant after incubation with resins. Lane 2:

Insoluble proteins in bacterial lysate. Lane 3: Eluted MEK proteins after affinity chromatography. C. IPTG-induced expression of GST-tagged MEK1DD (MEK1 S218D/S222D). Cultures were grown at 32 ^{o}C untill OD600 reached 0.8 and protein expression was conducted at 26 ^{o}C or 18 ^{o}C at various concentrations of IPTG. Lane 1: 0.2 mM IPTG, 26^{o}C. Lane 2: 0.5 mM IPTG, 26^{o}C. Lane 3: 1.0 mM IPTG, 26^{o}C. Lane 4: 0.2 mM IPTG, 18^{o}C. Lane 5: 0.5 mM IPTG, 18^{o}C. Lane 6: 1.0 mM IPTG, 18^{o}C. **D**. Purification of GST-tagged MEK1 DD using immobilized glutathione. Lane 1: Eluted MEK proteins after affinity chromatography. Lane 2: Insoluble proteins in bacterial lysate. Lane 3: Unbound fractions in the supernatant after incubation with resins.

2.3.5 Preparation of test proteins for specificity screening

The purified test proteins included 6xHis-tagged wild type E twenty-six-like transcription factor-1 (ELK-1), 6xHis-tagged MAPK phosphatase-3 (MKP3), GST-tagged truncated murine wild type kinase-suppressor of Ras 1 (KSR1) 383-619, GST-tagged truncated non-binding mutant of KSR1 383-619 FSF471-473AAA, GST-tagged truncated murine paxillin α (PXNα) 1-338, 6xHis-tagged wild type ERK1 and 6xHis-tagged wild type MKK3. GST-tagged KSR1 proteins, with a molecular weight of 41 kDa (theoretical Mw: 41338.91), were well expressed with an average yield of 10 mg proteins per 1 L culture and were isolated in 50% purity after affinity purification by immobilized glutathione (**Fig 2.17B**). GST-paxillin α 1-338 requires further optimization because of the low expression levels in both BL21(DE3) and NEB *Express I^q* competent *E.coli* strains at various concentrations of IPTG and at temperatures ranging from 18 ^{o}C to 37 ^{o}C (data not shown). The 6xHis-tagged ELK-1, MKK3, MKP3, ERK1 proteins, prepared in moderate yields and purity (**Fig 2.17A**), were used directly after affinity chromatography to prevent activity loss over the course of multiple purification steps.

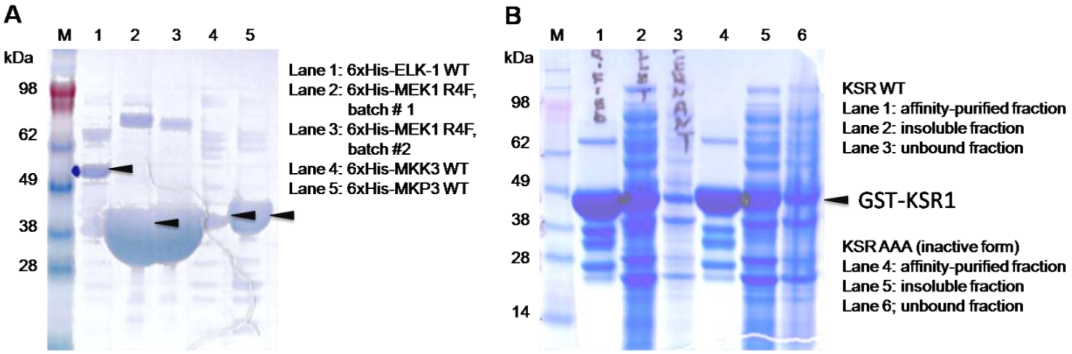

Figure 2.17 Purified ERK-interacting proteins and controls for specificity test.
A. Lane 1: 6xHis-tagged wild type ELK-1 proteins. Lane 2: The first batch of 6xHis-tagged MEK1 R4F proteins. Lane 3: The second batch of 6xHis-tagged MEK1 R4F proteins. Lane 4: 6xHis-tagged wild type MKK3 proteins. Lane 5: 6xHis-tagged wild type MAPK phosphatase-3 (MKP3). **B.** Lane 1: Eluted GST-tagged wild type [383-589] KSR-1 from immobilized glutathione. Lane 2: Insoluble proteins in bacteria lysate of

GST-tagged wild type [383-589] KSR-1. Lane 3: Unbound fractions in the supernatant of GST-tagged wild type [383-589] KSR-1 after incubation with resins. Lane 4: Eluted GST-tagged [383-589] KSR-1 FSF471-473AAA from immobilized glutathione. Lane 5: Insoluble proteins in bacteria lysate of GST-tagged [383-589] KSR-1 FSF471-473AAA. Lane 6: Unbound fractions in the supernatant of GST-tagged [383-589] KSR-1 FSF471-473AAA after incubation with resins.

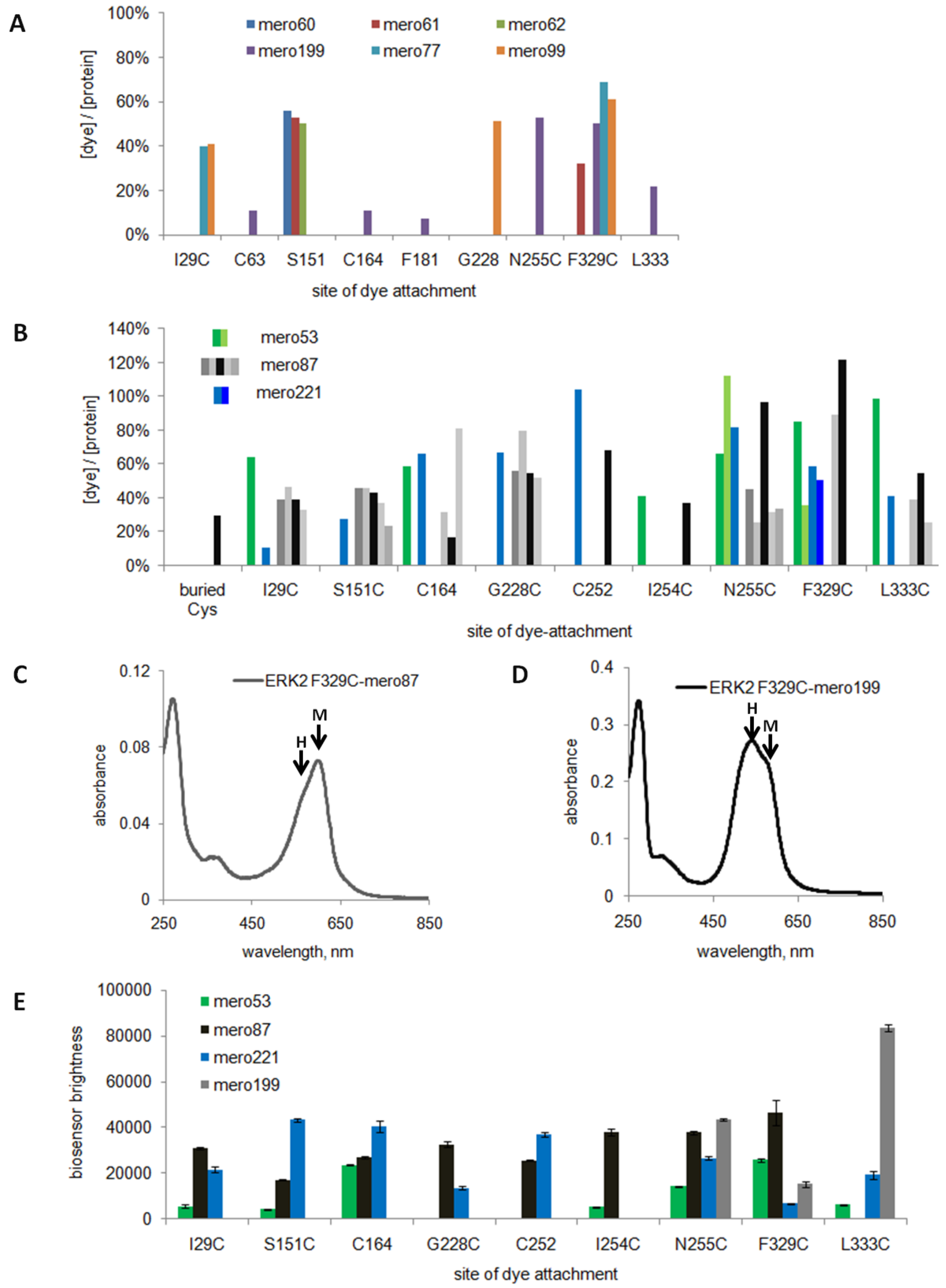

Figure 2.18 Spectral properties of dye-labeled ERK2 conjugates.

A, B. Labeling efficiency of dye-labeled ERK2. **C**. Absorption spectra of **mero87**-labeled ERK2 C63S/C159S/C164S/C252S/F329C and **mero199**-labeled ERK2

C63S/C159S/C164S/C252S/F329C in phosphate buffer. H and M are denoted for the H-type aggregates and the monomers, respectively. **D.** Dye emission intensity of dye-labeled ERK2.

2.3.6 Properties of dye-labeled ERK2

Labeling efficiency, brightness, and absorption spectra of several dye-labeled ERK2 samples are summarized in **Fig 2.18**. Labeling efficiency, or dye-to-protein ratio, can be affected by the relative solvent accessibility and nucleophilicity of the desired site for dye attachment, the degree to which over-labeling of other potentially reactive residues may occur, and the residual association of free dyes with the dye-labeled protein molecules. Unusually low labeling efficiency at residues with high predicted solvent accessibility implies unfavorable dye-protein interactions at the site of dye attachment or severe structural destabilization caused by mutations. For example, **mero199** was able to label ERK2 N255C and ERK2 F329C mutant proteins with moderate dye-to-protein ratios but only produced poorly-labeled ERK2 C63, ERK2 C164, and ERK2 F181C (**Fig 2.18A**). Importantly, the labeling control, an ERK2 mutant with no exposed intrinsic cysteines (ERK2 C63S/C159S/C159S/C252S), was labeled with a 30% dye-to-protein ratio (**Fig 2.18B**). One possible explanation is that the "buried" cysteines—C38S, C125S, and C214S in ERK2 become partially solvent accessible because the ERK protein is strongly destabilized by the C63S/C159S/C164S/C252S mutations. Methionines, histidines, aspartates, glutamates, and N-terminal lysines are also likely to become the major species reacting with excess iodoacetamide in the absence of solvent-accessible cysteines. In certain cases, free dye may remain associated with the dye-labeled protein throughout the purification process, depending on the hydrophobicity of both the dye and the labeled protein. As a result, the primary site for dye attachment in the optimized biosensor construct for biological applications must be confirmed by MALDI analysis. Unlike **mero87**-labeled MeroCBD and **mero87**-labeled SFK Merobody in which the dye absorption peaks were mainly composed of monomeric (M) dye species, all **mero87**-labeled ERK2 mutant proteins showed broadening in the absorption peak. This can be attributed to the spectral overlap between the monomeric species and H-aggregates (H) of dye molecules (**Fig 2.18C** *Left*). Formation of H-aggregates deactivates the excitation pathways of the monomeric species and usually causes severe fluorescence quenching. In the case of some **mero199**-labeled ERK2 mutant proteins, absorption from H-aggregates was more pronounced than absorption from the monomeric species (**Fig 2.17C** *Right*). In general observations, the basal brightness of **mero87**-labeled ERK mutant proteins is more constant than **mero53**-labeled or **mero221**-labeled ERK mutant proteins. For instance, **mero53**-labeled ERK2 F329C and **mero53**-labeled ERK2 S151C exhibited similar ratios of H-aggregates and monomers in phosphate buffer (data not shown). However, **mero53**-labeled ERK2 F329C was 1.5 fold brighter than **mero53**-labeled ERK2 S151C. In the case of **mero199**-labeled ERK2 F329C, in which its H-aggregate absorption peak was significantly higher than the monomer absorption peak, the sensor protein showed dramatically reduced dye emission intensity, indicating severe fluorescence quenching due to dye aggregation. In conclusion, brightness of dye-labeled ERK was influenced by both the hydrophobicity of the site of dye attachment and the tendency of the conjugates to form non-fluorescent dye aggregates.

2.3.7 Mechanisms of action of dye-labeled ERK

ERK2 activity sensors require a functional dye-labeled ERK2 molecule that can undergo conformational changes upon activation/inactivation. The MEK1/2 activity sensors are instead based on dye-labeled dead ERK2 that only binds active MEK1/2 and no other ERK-interacting proteins. Because it was unclear how the introduction of C63S, C159S, C164S, and C252S mutations might affect the structural flexibility of ERK2, the dual phosphorylation sites Thr183 and Tyr185 of the initial set of ERK mutants were not mutated. According to Western blot analysis (**Fig 2.19A**), the labeling control, an ERK2 mutant with no exposed intrinsic cysteines (ERK2 C63S/C159S/C164S/C252S), cannot be efficiently phosphorylated by active MEK1. This mutant also failed to phosphorylate ELK-1, a substrate of wild type ERK2. Since the four cysteine-to-serine mutations were sufficient to generate inactivated ERK, no additional mutations at the ERK phosphorylation sites were required. The representative biosensor candidate ERK2 N255C (ERK2 C63S/C159S/C164S/C252S/N255C) also showed behavior similar to ERK2 T183A/Y185F-EGFP (**Fig 2.19B**). Western blot analysis of several other ERK2 mutant proteins all showed much slower or abolished phosphorylation kinetics. The strategy of using dye-labeled ERK containing the four cysteine mutations is more likely to generate MEK1/2 activity sensors, rather than ERK2 activity sensors.

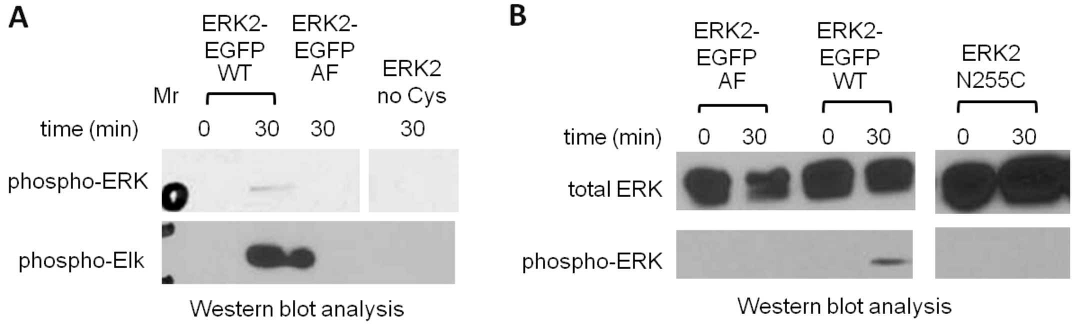

Figure 2.19 Assessment of phosphorylation kinetics of ERK2 mutants.

A. Phosphorylation of wild type ERK2-EGFP, control ERK2 T183A/Y185F-EGFP, and ERK2 C63S/C159S/C164S/C252S (ERK2 no Cys) by activator MEK1 was blotted with anti-phosphoERK antibody. Phosphorylation of ELK1, an ERK substrate, by wild type ERK2-EGFP, ERK2 T183A/Y185F-EGFP and ERK2 C63S/C159S/C164S/C252S was blotted with anti-phoshpoELK antibody. **B.** Phosphorylation of wild type ERK2-EGFP, ERK2 T183A/Y185F-EGFP and a biosensor candidate ERK2 C63S/C159S/C164S/C252S/N255C was blotted with anti-phosphoERK antibody and anti-ERK antibody.

Fluorescence response of dye-labeled ERK towards binding of active MEK1 and/or phosphorylation by MEK1 was recorded at various concentrations of 6xHis-tagged MEK1 R4F and at multiple time points following addition of ATP in order to monitor MEK1-mediated phosphorylation of dye-labeled ERK. **Mero87**-labeled ERK2 was chosen for mechanistic studies because this dye has demonstrated good biosensor response when used in other biosensors such as MeroCBD and the SFK Merobody. According to the results of fluorescence titration assays, the affinity between the biosensor proteins and the target—active MEK1, although weaker than the reported binding affinity of unphosphorylated ERK2 and phosphorylated MEK1, was still within a useful range to construct biosensors for live cell experiments. All **mero87**-labeled ERK2 mutants showed a dose-dependent fluorescence increase at increasing concentrations of constitutively active MEK1 R4F (**Fig 2.20**). **Mero87**-labeled ERK2 L333C (ERK2 C63S/C159S/C164S/C252S/L333C) had the largest dynamic range of 77% maximum fluorescence increase upon addition of active MEK1. However no significant fluorescence change was observed after addition of ATP to active MEK1. This result is consistent with a previous finding that these ERK2 mutants cannot be phosphorylated by active MEK1 as efficiently as wild type ERK2. A significant drop of emission intensity at 2.6 μM of constitutively active MEK1 R4F was observed in the fluorescence titration experiments of all dye-labeled ERK2. Signal drops were also seen in the titration experiments of MeroCBD when using very high concentrations of constitutively active Cdc42 Q61L. In both cases, constitutively active kinases or GTPases are less thermostable than wild type enzymes. Thus when dye-based biosensors have reached the maximum response, higher target concentrations are likely to induce aggregation of target proteins or biosensor proteins. Biosensor signals can therefore be greatly reduced due to decreased amounts of soluble target proteins or formation of non-fluorescent dye-aggregates.

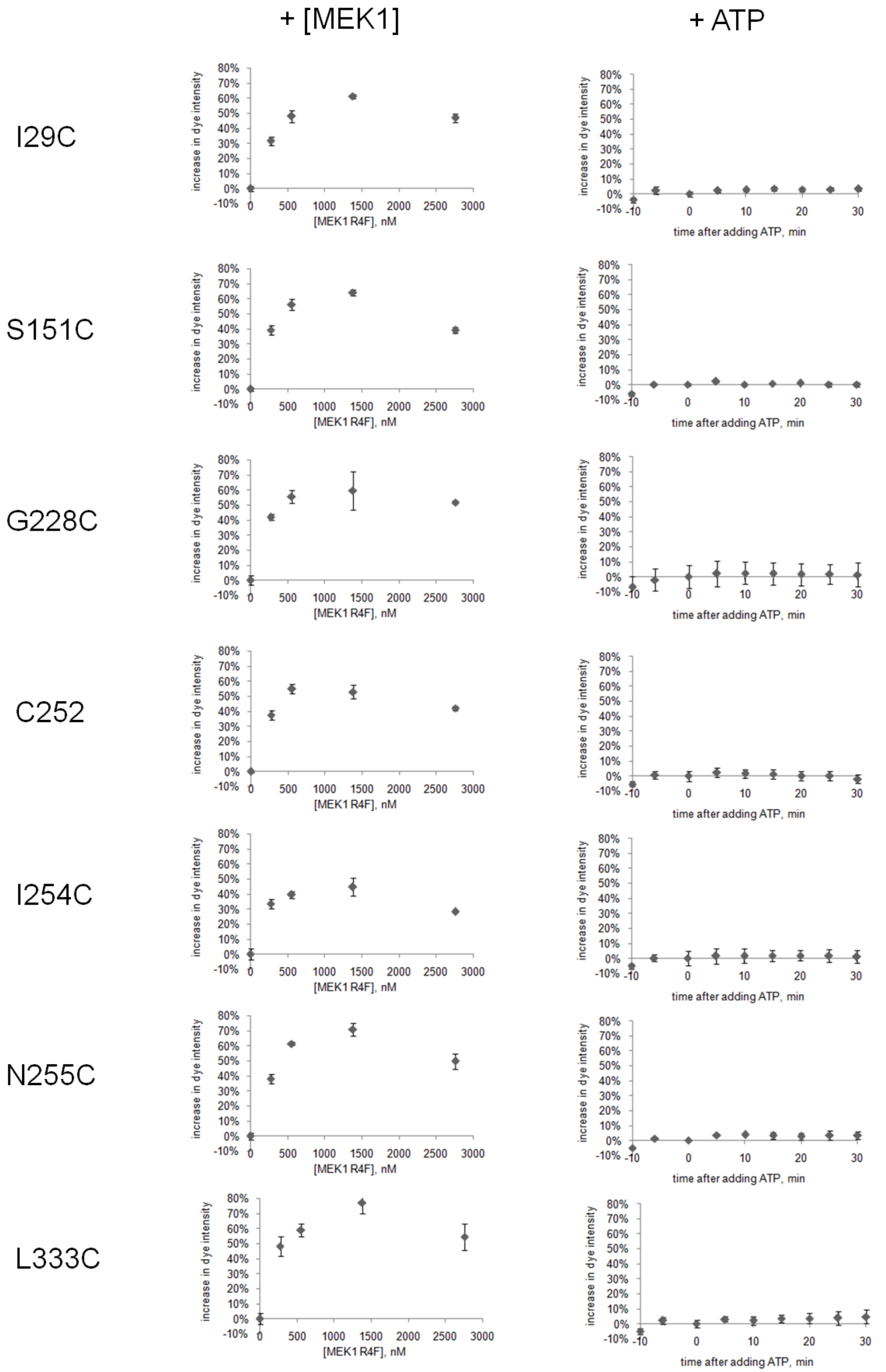
+ [MEK1]
+ ATP
I29C
S151C
G228C
C252
I254C
N255C
L333C
increase in dye intensity
80%
70%
60%
50%
40%
30%
20%
10%
0%
-10%
0
500
1000
1500
2000
2500
3000
[MEK1 R4F], nM
-10
0
10
20
30
time after adding ATP, min

Figure 2.20 Fluorescence titration of 50 nM dye-labeled ERK2.
Dye emission intensity of **mero87**-labeled ERK mutants in the presence of 0, 0.25, 0.55, 1.4, and 2.8 µM constitutively active MEK1 without (left) and with (right) addition of ATP.

ERK2 F329C (ERK2 C63S/C159S/C164S/C252S/F329), expressed in large quantity and highly accessible for labeling, was first tested with the following dyes: **mero53**, **mero60**, **mero87**, **mero199**, and **mero221** (**Fig 2.21**). Among all biosensor candidates, the **mero87**-labeled ERK2 F329C is brighter and has greater dynamic range than other versions (**Fig 2.21C**). Unlike **mero199-**labeled MeroCBD, which exhibits an intrinsic ratiometric response in the excitation spectra upon binding to GTP-bound Cdc42, **mero199**-labeled ERK2 F329C did not produce a ratiometric response in either the excitation or emission spectra (**Fig 2.21D**). Together with the fact that all **mero87**-labeled ERK2 have much smaller dynamic ranges as compared with **mero87**-labeled MeroCBD (9-fold change in dye emission intensity), the change in local hydrophobicity of MEK-ERK binding interactions is likely also smaller than the binding interactions between Cdc42 and WASP, as probed by these solvent-sensitive fluorophores. Interestingly, ERK2 F329C possesses residual ERK activity towards MEK1-mediated phosphorylation and phosphorylation of ELK-1, an ERK2 substrate (**Fig 2.21E**), while its fluorescence intensity remains constant after MEK1-mediated phosphorylation (**Fig 2.21B**). The possible explanation is that this type of ERK2 mutant can be phosphorylated but the phosphorylation-induced conformational changes were undetectable by solvent-sensitive fluorophores. Western blot analysis of some other unlabeled or dye-labeled ERK2 mutant proteins also showed that some versions become more prone to undergo MEK1-mediated phosphorylation than the labeling control mutant which has no exposed intrinsic cysteines. It is plausible that both the combination of multiple mutations in

ERK2 and the degree of dye labeling of ERK2 mutants have strong influences on the stability of these biosensor proteins

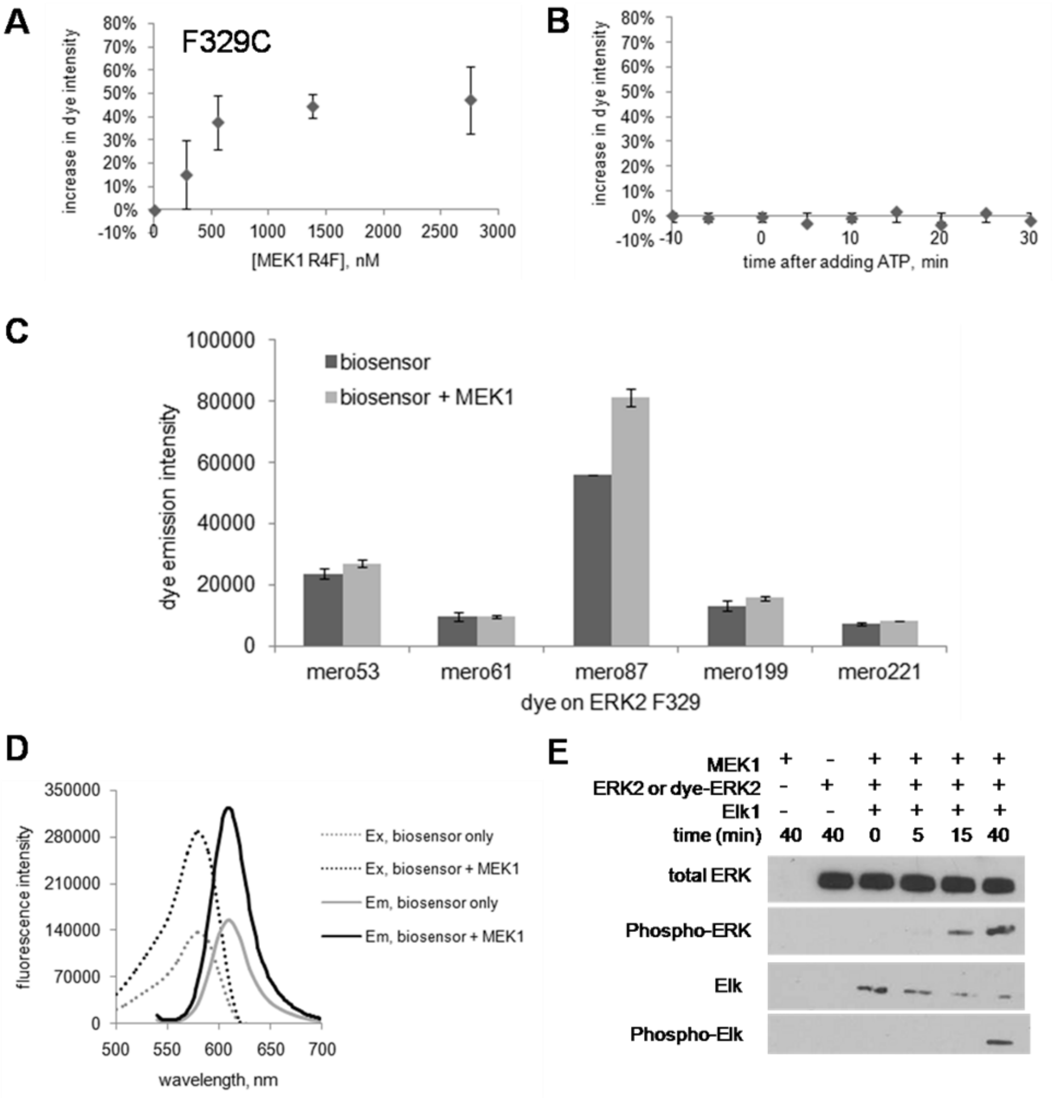

Figure 2.21 Characterizaiton of dye-labeled ERk2 F329C.
A. Fluorescence titration of **mero87**-labeled ERK2 F329 (ERK2 C63S/C159S/C164S/C252S/F329C) with 0, 276, 552, 1380 and 2760 nM constitutively active MEK1 R4F. **B**. Fluorescence response of **mero87**-labeled ERK2 F329 before and after phosphorylation by MEK1 R4F. **C**. Maximum fluorescence change of dye-labeled ERK2 F329 in the absence and in the presence of MEK1 R4F. **D**. Excitation and emission spectra of **mero199**-labeled ERK2 F329 in the absence and in the presence of MEK1 R4F. **E**. Western blot analysis of **mero87**-labeled ERK2 F329. Phosphorylation of **mero87**-labeled ERK2 F329 by MEK1 was blotted by anti-ERK and anti-phosphoERK antibodies. Phosphorylation of ELK-1 by **mero87**-labeled ERK2 F329 was blotted by anti-ELK and anti-phosphoELK antibodies.

2.3.8 Fluorescence screening of MEK1/2 activity sensors

A library of 24 dye-labeled ERK2 mutant proteins was freshly prepared and average dye emission intensity values were compared in both the absence and presence of 1000 nM constitutively active MEK1 R4F proteins. The **mero53** version of ERK2 G228C (ERK2 C63S/C159S/C164S/G228C/C252C), the **mero53** version of ERK2 C252 (ERK2 C63S/C159S/C164S), and the **mero221** version of ERK2 I254C (ERK2 C63S/C159S/C164S) were not included in the screening because these ERK2 mutant proteins precipitated on ice during the freeze-thaw process. All other test biosensor proteins either remained soluble after a freeze-thaw cycle or were freshly purified from bacteria without freeze-thaw cycles. In general, **mero87**-labeled ERK2 mutants have greater dynamic range while **mero53**-labeled ERK2 have less favorable dye-protein interactions in this biosensor design (**Fig 2.22**).

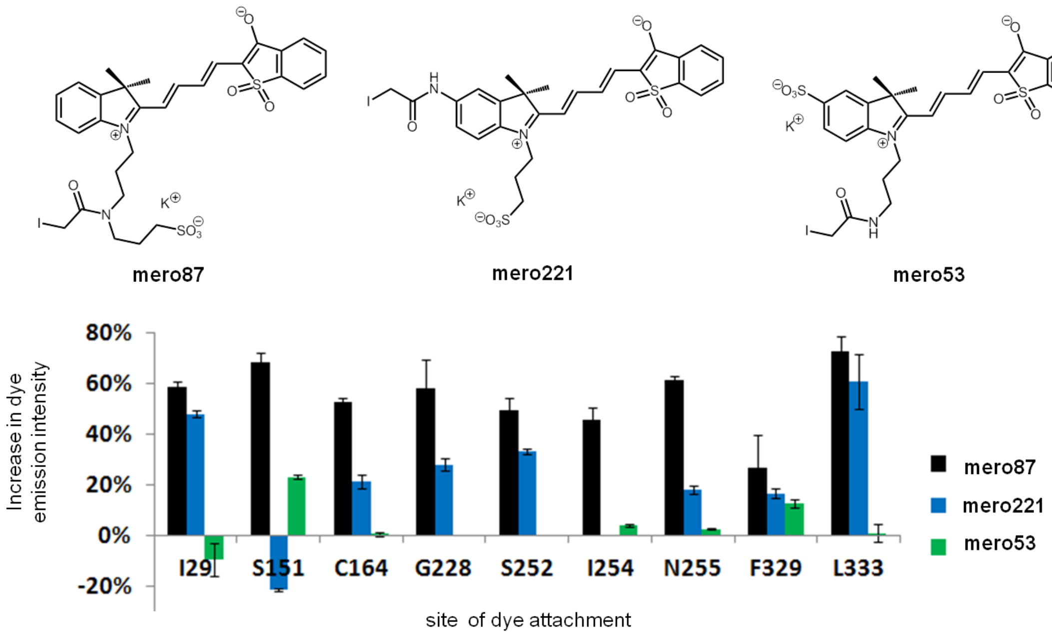

Figure 2.22 Maximum fluorescence change of dye-labeled ERK2.
Mero53, **mero87**, and **mero221** differ in the positions of iodoacetamide and sulfate group attachment. Dye-labeled ERK mutant proteins (50 nM) were titrated with constitutively active MEK1 R4F.

In the case of ERK2 S151C (ERK2 C63S/S151C/C159S/C164S/C252S), **mero87**-labeled and **mero53**-labeled ERK2 S151C became brighter with increasing concentration of MEK1 R4F while the fluorescence of **mero221**-labeled ERK2 became quenched upon addition of active MEK1. The orientation of charge-charge interactions of the dye molecule appeared to be the most important factor at this residue in proximity to the ATP binding site. In the case of ERK2 I29C (ERK2 I29C/C63S/C159S/C164S/C252S), both **mero87**-labeled and **mero221**-labeled ERK2 I29C showed increases in dye emission intensity in the presence of active MEK1, while the dye emission intensity of **mero53**-labeled ERK2 I29C was slightly decreased upon binding to active MEK1. All **mero87**-labeled ERK2 mutants tested in the screening have sufficient sensitivity for live cell imaging, because all of the selected sites for dye attachment are near the activation loop and/or near the MAPK kinase insert. It seems that most ERK-binding interactions and ERK conformational changes mainly occur near the activity loop. A good negative control will be to place a solvent sensitive dye at a residue distant from these regions.

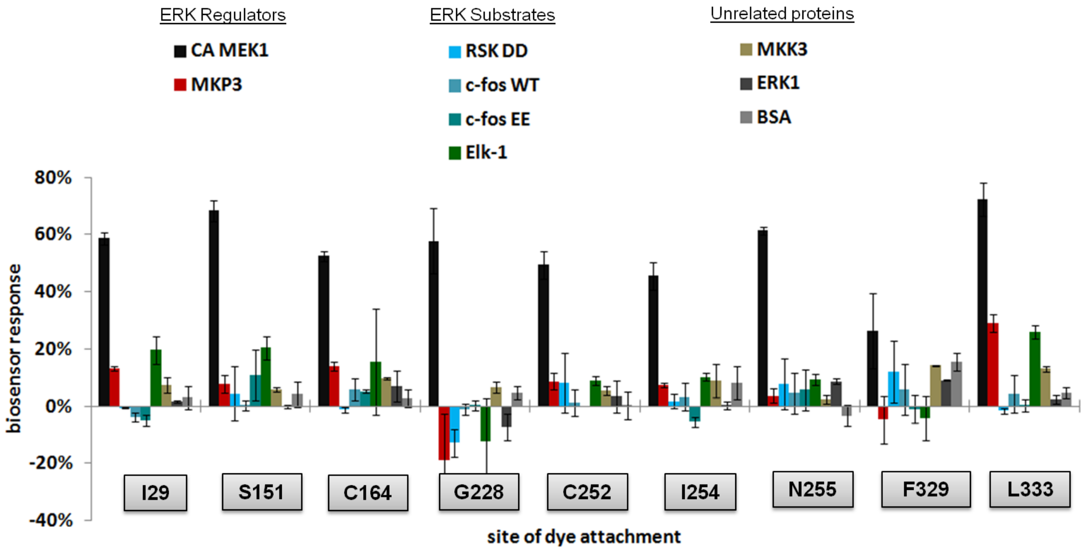

Figure 2.23 Fluorescence response of mero87-labeled ERK2 against ERK regulators, ERK substrates, and control proteins.

Biosensor response is defined as the increase in dye emission intensity of 50 nM dye-labeled ERK2 mutant proteins upon addition of 1µM test proteins. ERK regulators include constitutively active MEK1 R4F (CA MEK) and wild type MAPK phosphatase-3 (MKP3). ERK substrates include constitutively active RSK1DD, wild type c-fos, constitutively active c-fos, and wild type ELK1. Unrelated test proteins include wild type MKK3, wild type ERK1, and BSA.

Mero87-labeled ERK2 mutants with sufficient dynamic range were titrated with the same amount of test proteins (**Fig 2.23**). The initial pool of representative ERK-interacting proteins chosen for specificity testing included three types of ERK2 substrates, two scaffold proteins, one MAPK phosphatase and three un-related proteins. c-Fos, a substrate for both ERK and p38, is known to bind unphosphorylated ERK2 with a dissociation constant of 0.97 µM through a DEF motif (243). The second representative ERK substrate, ribosomal S6 kinase-1 (RSK-1), uses a DEJL motif to bind unphosphorylated ERK2 with a dissociation constant of 0.15 µM (243). E twenty-six (ETS)-like transcription factor 1 (ELK-1), another shared substrate of ERK and p38, binds unphosphorylated ERK2 with a dissociation constant of 0.25 µM using both the DEF and DEJL motifs (243). Constitutively active RSK1 DD, wild type c-fos, and constitutively active c-fos EE were dialyzed in assay buffer prior to the screening to remove glycerol contained in the storage buffer which if left in the sample may influence the fluorescence readout of the solvent-sensitive dye **mero87**. ERK2 L333C (ERK2 C63S/C159S/C164S/C252S/L333C) not only exhibited the best response against active MEK1 but also showed the maximum increase to wild type MKP3 and wild type ELK-1. The dirty specificity profile of ERK2 F329C (ERK2 C63S/C159S/C164S/C252S/F329C) likely indicates the exposure of hydrophobic regions due to destabilization of the ERK2 mutant. Among the library, **mero87**-labeled ERK2 C252 (ERK2 C63S/C159S/C164S), **mero87**-labeled ERK2 I254C (ERK2 C63S/C159S/C164S/C252S/I254C), and **mero87**-

labeled ERK2 N255C (ERK2 C63S/C159S/C164S/C252S/N255C) yielded relatively cleaner specificity profiles; these three sites of dye attachment are located at the MAP kinase insert region of ERK2. Ile29, Ser151, Cys164 and Gly228 in ERK2 are located closer to the substrate binding sites in ERK2. Dyes labeled at these residues have higher fluorescence response to ELK-1. The use of solvent-sensitive fluorophores also revealed that wild type ELK-1 still binds ERK2 mutants with a lower affinity than active MEK1. Thus the reversibility of MEK-biosensor and ELK-biosensor binding interactions should be examined in greater detail in further studies. In practice, non-specific fluorescence response from endogenous ELK-1 may be trivial in live cell imaging experiments since the MEK1/2 activity sensor and endogenous ELK-1 are likely to be in different cellular compartments. This difference in localization is due to the fact that an ideal MEK1/2 activity sensor is based on dead ERK, which hardly shuffles into the nucleus due to the lack of a phosphorylation-promoted nuclear transport mechanism, while ELK-1 is only found inside the nucleus, except in the case of a second function in the cytoplasm of neurons (336, 337). The results of biosensor candidate titrations with both constitutively active and dominant negative versions of MEK1 and MEK2 MAPK kinase proteins, GST-tagged MEK1DD, GST-tagged MEK1AA, GST-tagged MEK2DD, and GST-tagged MEK2AA, are not reported due to significant non-specific response from impurities present in the preparations. GST-tagged KSR proteins were also not tested in this screening because scaffold proteins are likely to only bind ERK in multi-protein complexes, and it remains challenging to reconstruct such protein complexes *in vitro*. The **mero87**-labeled ERK2 constructs other than ERK2 F329C and ERK2 L333C were qualified for further validation in cell experiments.

2.3.9 Construction of dye-labeled ERK-EGFP for ratio imaging

When quantifying protein activity levels using a dye-based biosensor in live cell microscopy, dye fluorescence intensity is not only determined by activation of target proteins but is also influenced by illumination settings, biosensor concentrations, and cell thickness. It is therefore necessary to normalize dye fluorescence with a second fluorophore with an orthogonal emission wavelength. A second fluorophore, usually enhanced green fluorescent protein (EGFP) or monomeric Cerulean fluorescent protein (mCerulean), was fused to the N-terminus of ERK2 mutants through a Gly-Ser-Gly-Ser linker (**Fig 2.24A**). MEK1/2 activity could then be defined by the relative emission ratio of the solvent sensitive dye relative to the fluorescence protein molecule. Fusion of ERK2 mutants with mCerulean was not successful due to difficulties in cloning the mCerulean fragments from the available constructs. EGFP fusions of ERK2 C252, ERK2 N255C and ERK2 G228C were successfully cloned into a pET23 bacterial expression vector, but all three constructs could not be expressed as full length proteins in BL21(DE3) and NEB *Express* I^q *E.coli* strains. Instead, yellow-to-green colored truncated proteins were expressed in these constructs with good yields (>10 mg per 1 L culture). The molecular weight of these truncated proteins corresponds to the molecular weight of a GFP molecule; the identity of the truncated proteins was later confirmed to contain EGFP fragments by Western blotting (**Fig 2.24C**). As was seen during expression and purification of the full length proteins of 6xHis-tagged wild type ERK2-EGFP and 6xHis-tagged ERK2-EGFP T183A/Y185F, the yields of soluble proteins are much lower than the yields of wild type 6xHis-tagged ERK2. Protein degradation products were observed as shown in the SDS PAGE gel (**Fig 2.24B**). The translational artifacts of expressing these EGFP versions of ERK2 mutants in bacteria were likely due to the dual destabilization effects from multiple mutations and from ERK-EGFP fusions. Fusion of bulky protein molecules at either the N-terminus or the C-terminus of ERK2 might easily disrupt MEK-ERK binding interactions or the overall stability of ERK mutant proteins. It has been reported that the C-terminus of wild type ERK2 interacts with the N-terminus of MEK1 and the N-terminus of ERK2 is spatially very close to the C-terminus of ERK2. An alternative approach would be to insert a circularly permuted fluorescent protein molecule into one of the loops in ERK2 to generate more stable biosensor proteins for cell experiments. The other option is to modify the N-terminus of ERK2 so that a cysteine-reactive dye and a second organic dye with an orthogonal wavelength could be used to generate dual-labeled ERK2 through thiol-modification and native chemical ligation.

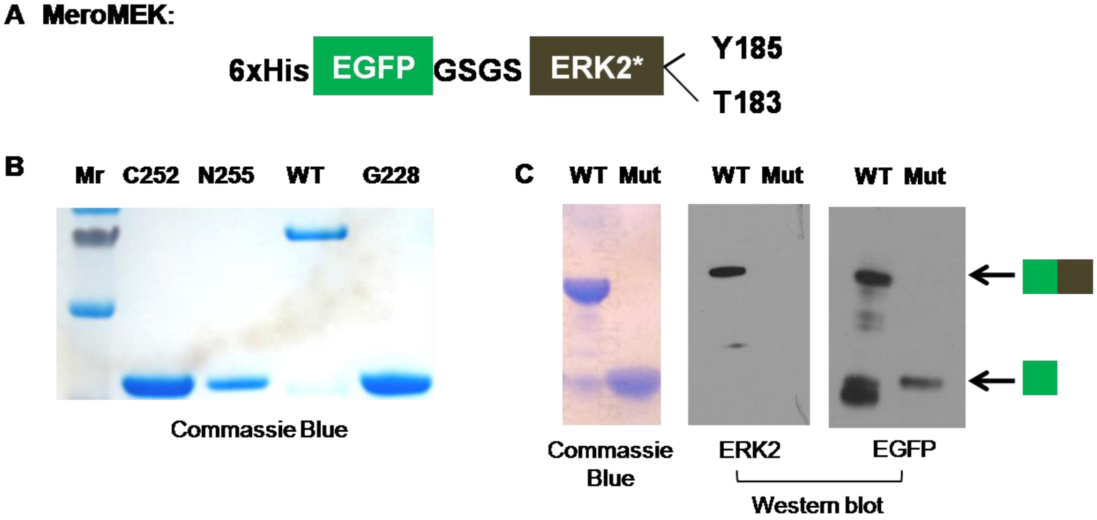

Figure 2.24 Construction of ERK-EGFP fusion proteins for ratio imaging.
A. Design of ERK-EGFP fusion proteins. T183 and Y185 in ERK2 are the phosphophoryltion sites for MEK1/2. **B.** Purified 6xHis-tagged wild type ERK-EGFP and truncated protein products from bacteria expressing ERK2 C63S/C159S/C164S EGFP, ERK2 C63S/C159S/C164S/C252S/N255C, or ERK2 C63S/C159S/C164S/ G228C/C252S. **C.** Identity of truncated protein products was confirmed by anti-ERK and anti-GFP antibodies.

2.3.10 Live cell imaging of dye-labeled ERK2

Mero87-labeled ERK2 S151C was successfully loaded into mouse embryo fibroblasts stably expressing YPet fluorescent proteins (**Fig 2.25**) through bead loading. Freshly prepared **mero87**-labeled ERK2 N255C and **mero87**-labeled G228C failed to enter cells via bead loading and produced high fluorescence backgrounds. Biosensor ratios were obtained by dividing a dye fluorescence image with a YPet fluorescence image. The biosensor ratios were close to zero in the nuclear region and moderate in the cytoplasm, with peaks at the cell periphery and at the leading edge. The subcellular localization of **mero87**-labeled ERK2 S151C was in good correlation with the known biology of MEK1 and MEK2. The N-terminus of MEK1 contains a nuclear export sequence (NES) and the only known role of MEK1 is to phosphorylate/activate ERK1/2 in the cytoplasm (164, 169, 194, 195, 338). MEK2 also phosphorylates/activates ERK1/2; the other role of MEK2 is to form a heterodimer with MEK1 to regulate MEK1 activation in the cytoplasm (189). In contrast, ERK2 is activated in the cytoplasm and is believed to rapidly translocate into the nucleus through formation of homodimers of phosphorylated ERK2 (279, 319, 320, 339). Therefore, under serum-stimulated conditions, the total ERK and active ERK are more abundant in the nucleus (**Fig 2.25**). Significantly, elevated biosensor ratios were observed at the leading edge, which is consistent with the fact that MEK and ERK are downstream effectors of both Rac GTPases and Src family kinases during protrusion and adhesion dynamics (127-130, 156, 191, 300, 340-342). In all cells loaded with dye-labeled ERK2 or dye-labeled wild type ERK2-EGFP, high biosensor ratios were seen at the cell periphery. More controls are required to identify whether the elevated sensor signals at the cell periphery reveal an abundance of active MEK at this region or are artifacts arising from degradation products of sensor proteins in cells. Since aggregates of merocyanine dyes are essentially non-fluorescent, and **mero87** is very dim in water, one possible explanation is that the biosensor protein molecules were rapidly recognized and degraded by endogenous proteases or proteasomes within 30 minutes after biosensor loading and the cleaved dye molecules then became brighter when they were recruited to more hydrophobic microdomains inside cells. The best way to distinguish the two mechanisms will be to create a non-binding mutant biosensor and compare the fluorescence images. According to the literature, mutations in the common docking (CD) sites of ERK2 are insufficient to remove all ERK-interactions because these ERK2-interacting proteins bind ERK2 in a bipartite manner (330). Deletion or mutation of the MAPK insert in ERK2 was effective to block MEK-ERK interactions in yeast two hybrid screening; however, it is uncertain whether these proteins could be expressed and purified as stable proteins.

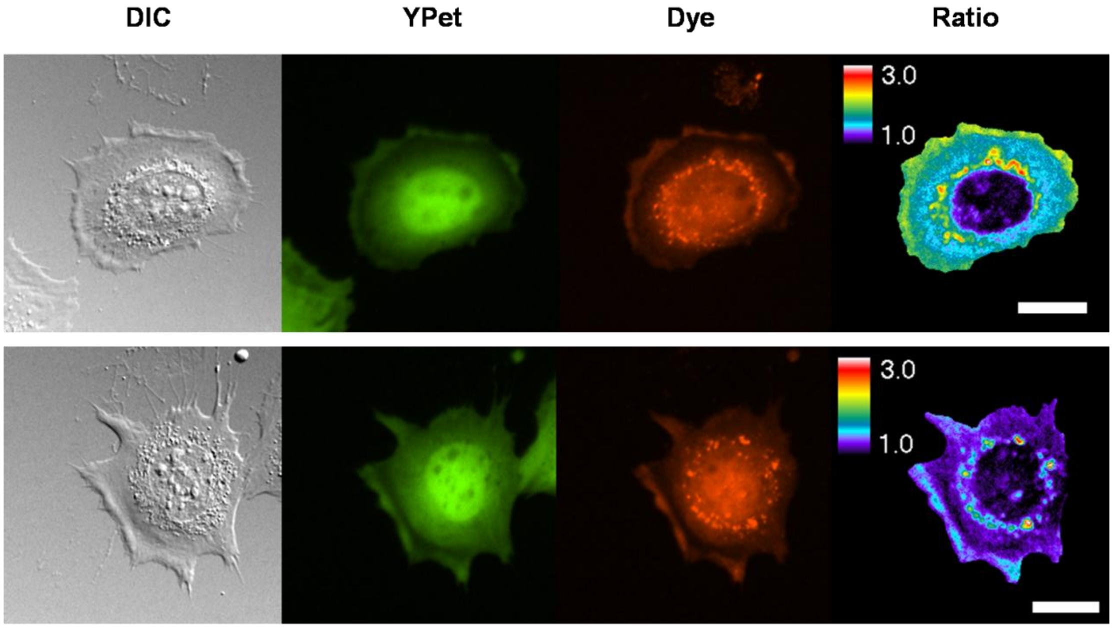

Figure 2.25 Live cell images of a MEK1/2 activity sensor.
Scale bar: 20 µm. ERK2 C63S/S151C/C159S/C164S/C252S was delivered into NIH 3T3 mouse embro fibroblasts (MEF) stably expressing YPet fluorescent protein. From left to

right: differential interference contrast (DIC) image, YPet fluorescence image, dye fluorescence image, and ratio image. Biosensor ratio is generated by normalizing dye emission intensity with YPet emission intensity.

The other important observation related to the cell morphology differences in these brighter biosensor-loaded cells when compared to neighboring biosensor-free cells. Cell thickness at the cell edge in biosensor-loaded cells was usually greater than that of biosensor-free cells, despite the fact that these biosensor-loaded cells were still capable of forming protrusions and filopodia. The use of lower amounts of biosensor proteins will be necessary to diminish such dominant negative effects, while the basal brightness of biosensor proteins at this concentration must still be sufficient to produce ratioed images with signal-to-noise ratios greater than 3.0. Because the basal brightness of the **mero87**-labeled ERK2 S151C test construct exhibited only 50% of the average brightness of all dye-labeled ERK2 constructs *in vitro* (**Fig 2.18**), several other brighter constructs should be tested before deciding to replace **mero87** with a brighter dye such as **mero61** or **mero199**.

2.3.11 Correlation of biosensor properties with protein stability predictions

Eris (343, 344), a protein stability prediction server, was used to estimate the change in protein stability caused by the sum of multiple mutations (**Fig 2.26**). The crystal structures of active ERK2 (PDB: 2ERK) and inactive ERK2 (PDB: 1ERK) were used as the input protein structures. Backbone structure pre-relaxation prior to simulations and the backbone flexibility was modeled in most cases. The Medusa force field was used to model the structures and the free energy of the input protein computed by Eris was the result of a combination of van der Waals (VDW) interactions, solvation effects, hydrogen-bonding interactions, and backbone-dependent statistical energies . The last term is of great importance because it detects the strain on the backbone induced by multiple mutations and these effects are taken into consideration by Eris. Positive changes in the free energy $\Delta\Delta G$ ($\Delta\Delta G = \Delta G^{mutant} - \Delta G^{wild\text{-}type}$) of the mutant of interest indicates that destabilization effects are introduced by the mutations. Strong stabilization by mutations might also cause malfunction of the mutant proteins, thus the ideal $\Delta\Delta G$ values should be close to zero. It is clear that the labeling control, the ERK2 mutant with no exposed intrinsic cysteines (ERK2 Cys-free, ERK2 C63S/C159S/C164S/C252S), was strongly destabilized as compared to wild type ERK2; $\Delta\Delta G$ between inactive wild type ERK2 and inactive mutant is 2.42 kcal/mol and $\Delta\Delta G$ between active wild type ERK2 and active mutant is 4.22 kcal/mol. Only the ERK2 I254C (ERK2 C63S/ C159S/C164S/C252S/I254S) construct has a slightly lower $\Delta\Delta G_{inactive}$ of 2.04 kcal/mol and $\Delta\Delta G_{active}$ of 2.14 kcal/mol. However these values still imply strong destabilization effects. ERK2 F181C (ERK2 C63S/C159S/C164S/F181C/C252S), ERK2 G228C (ERK2 C63S/C159S/C164S/G228C/C252S), ERK2 C252 (ERK2 C63S/C159S/C164S), and ERK2 F329C (C63S/C159S/C164S/C252S/F329C) were predicted to have more than 10 kcal/mol destabilization in free energy as compared to inactive wild type ERK2. Compared to wild type ERK2, these strongly destabilized ERK mutants still retained the same features in secondary structures but the orientation of individual residues was very distinct as indicated by structural alignment of wild type ERK2 and computed models (data not shown). In conclusion, protein stability of dye-labeled ERK2 needs to be improved through the computer-aided selection of mutations. Effects of dye attachment on the stability of biosensor proteins should also be modeled and compared using models compatible with unnatural amino acids.

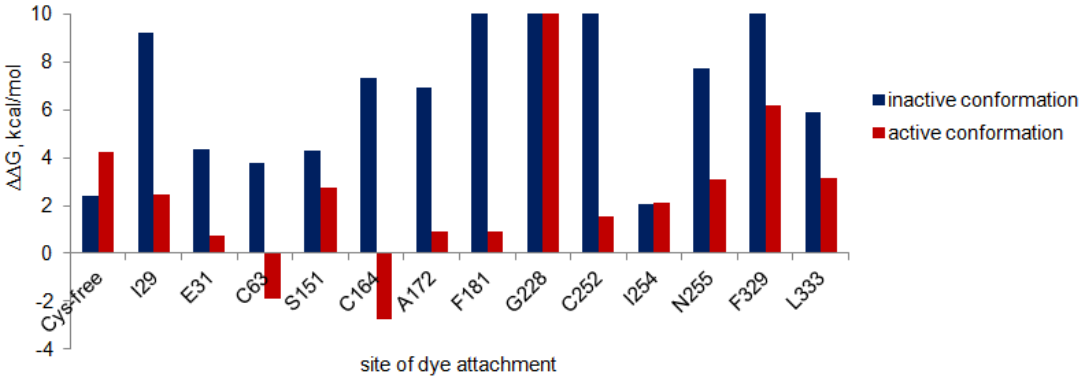

Figure 2.26 Calculated ΔΔG for all tested biosensor constructs.
Results were obtained from the Eris protein stability predictor using pre-relaxation of flexible backbones of protein structures of inactive ERK2 (PDB: 1ERK) and active ERK2 (PDB: 2ERK). The change in free energy difference was calculated as: $\Delta\Delta G = \Delta G^{mutant} - \Delta G^{wild\text{-}type}$. Except ERK2 C63, ERK2 C164, and ERK2 C252, all other mutants contain C63S, C159S, C164S, C252C mutations.

Correlation between estimated protein stability change ($\Delta\Delta G_{inactive}$) versus average protein yields, average labeling efficiency, average biosensor brightness, average biosensor response to MEK binding, and average biosensor specificity of ERK2 cysteine mutants are plotted in **Fig 2.27**. $\Delta\Delta G_{inactive}$, the change in protein stability between inactive conformations of wild type ERK2 and an ERK2 mutant, was used for correlation because these purified ERK2 proteins are mainly unphosphorylated, as confirmed by Western blotting. The experimental values of ERK2 I29C, ERK2 S151C, ERK2 C164, ERK2 G228C, ERK2 C252, ERK2 I254C, ERK2 N255C, ERK2 F329C, and ERK2 L333C were used for correlation analysis. Average protein yields were measured as amounts of soluble proteins purified from a 1 L culture using similar expression and purification procedures. A low correlation coefficient was found between $\Delta\Delta G_{inactive}$ and average protein yields because many samples were expressed with sufficient amounts for assays only once (**Fig 2.18**). Multiple smaller-scale protein productions or the use of ratios of soluble and insoluble fractions as assessed by SDS PAGE and Coomassie blue staining should yield more consistent data points for correlation analysis. Average labeling efficiency of each ERK2 cysteine mutant was obtained using the dye-to-protein ratios of **mero53**-labeled, **mero87**-labeled, and **mero221**-labeled ERK2 sensor proteins. A correlation coefficient of 0.49 was found between labeling efficiency and relative stability of inactive biosensor proteins. Since dye concentrations for calculation of labeling efficiency include contributions from both dye-labeled proteins and free dye that may be non-covalently associated with the surface of biosensor proteins, one possible explanation of low correlation between labeling efficiency and protein stability may be that, due to misfolding, the surface of some destabilized mutant proteins becomes more hydrophobic than that of wild type ERK2, which results in increased association of free dye through hydrophobic interactions. These low-molecular weight non-covalently associated free dyes would dissociate from dye-labeled proteins upon denaturing, thus ratios of free dyes and dye-labeled proteins could be quantified by SDS PAGE and fluorescence gel scanning. Average brightness and average biosensor response of these dye-labeled proteins showed no correlation with predicted protein stability of biosensor proteins because dyes were attached to different regions on the ERK surface. The correlation value would be useful when comparing ERK mutants with an identical site of dye attachment, but different combinations of cysteine mutations for removal of intrinsic exposed cysteines. Incorporation of protein stability predictions and measurements of biosensor proteins into the design of MAPKK activity sensors will be very helpful for understanding how these sensor proteins behave and whether they are truly able to report events of interest.

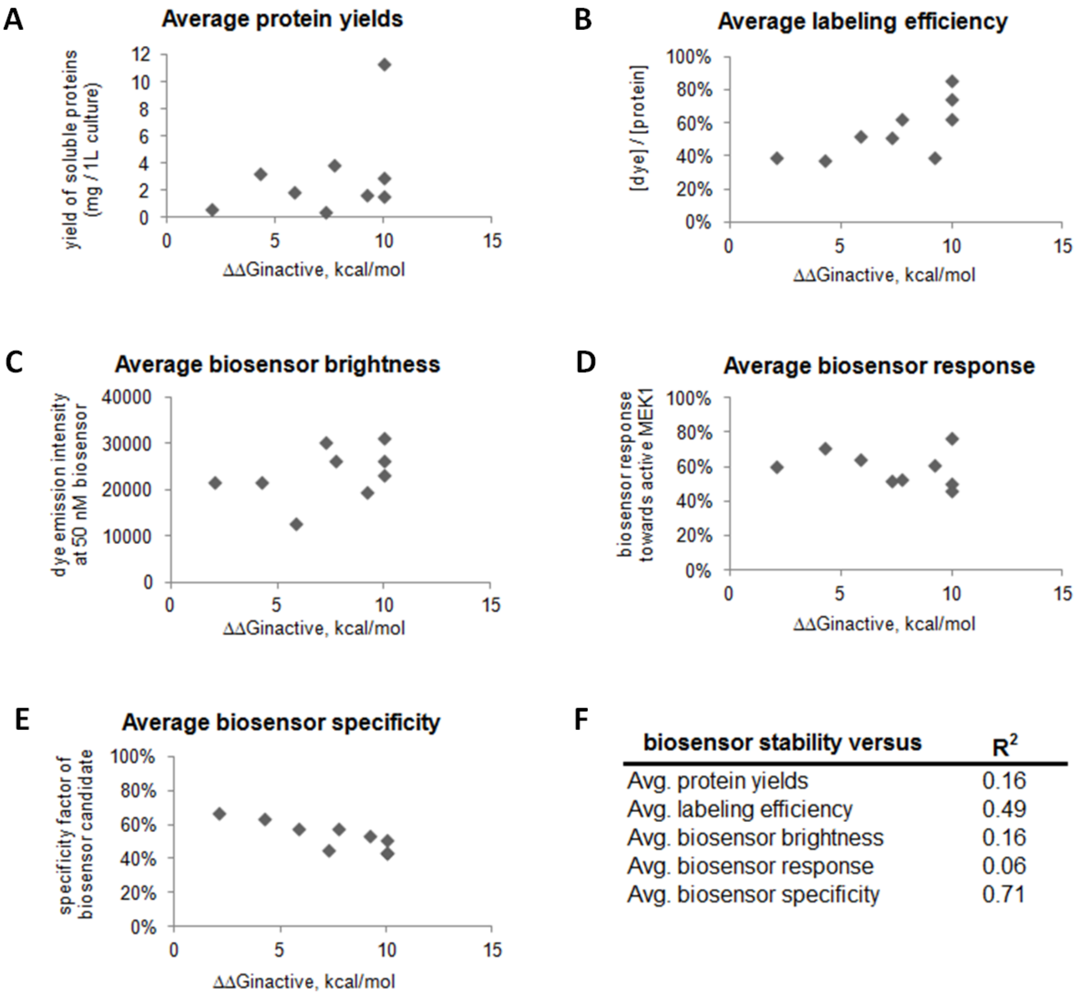

biosensor stability versus	R^2
Avg. protein yields	0.16
Avg. labeling efficiency	0.49
Avg. biosensor brightness	0.16
Avg. biosensor response	0.06
Avg. biosensor specificity	0.71

Figure 2.27 Correlation of experimental data with predicted protein stability of biosensor proteins.
$\Delta\Delta G^{inactive}$, the change of free energy difference after mutations calculated by Eris, represents the predicted protein stability value of ERK mutants. **A.** Correlation between average protein yields and predicted protein stability. Amounts of purified soluble proteins from a 1 L culture were used to calculate average protein yields. **B**. Correlation between average labeling efficiency and predicted protein stability. Labeling efficiency was defined as the relative concentrations of dyes and proteins of dye-labeled ERK measured in phosphate buffer. **C.** Correlation between average biosensor brightness and predicted protein stability. Average biosensor brightness values measured the average dye emission intensity values of **mero53-**, **mero87-**, or **mero221**-labeled ERK. **D.** Correlation between average biosensor response and predicted protein stability. Average biosensor response was defined as the maximum fluorescence change upon addition of constitutively active MEK1. **E.** Correlation between average biosensor specificity and predicted protein stability. Average biosensor specificity is defined as the ratio of

fluorescence response towards active MEK1 versus the total amounts of fluorescence response against all test proteins. **F.** A table of correlation coefficients of the above comparison.

2.3.12 Future directions: Designing more stable MEK1/2 activity sensors

Mutating cysteines to serines might not be the best choice to increase protein stability in the case of ERK2, as calculated by i-Mutant and Site-directed Mutator (SDM), predictors of protein stability change upon single point mutation. ΔΔG values of single point mutations of cysteine-to-serine, cysteine-to-alanine, and cysteine-to-methionine at Cys63, Cys159, Cys164, and Cys252 in inactive ERK2 (PDB: 1ERK) and active ERK2 (PDB: 2ERK) are compared in **Fig 2.28**. Both i-Mutant and SDM are in general agreement that cysteine-to-serine mutations tend to cause much more destabilization on ERK protein structures as compared to cysteine-to-alanine and cysteine-to-methionine mutations. In fact, the Cys63 residue remains buried in both inactive conformations of wild type ERK2 (SASA at C63 = 0 Å^2) and ERK2 Cys-free mutant (ERK2 C63S/C159S/C164S/C252S, SASA at C63 = 6.0 Å^2) as calculated by Eris and VMD; therefore C63S, C63A and C63M mutations in ERK2 result in higher degrees of protein destabilization compared to mutations at the more solvent-accessible Cys159, Cys164, and Cys252 residues of ERK2. According to predictions by i-Mutant and SDM, ERK2 C159M/C164M/C252M and ERK2 C63M/C159M/C164M/C252M were superior affinity scaffolds with greater stability then the original construct, ERK2 C63S/C159S/C164S/ C252S.

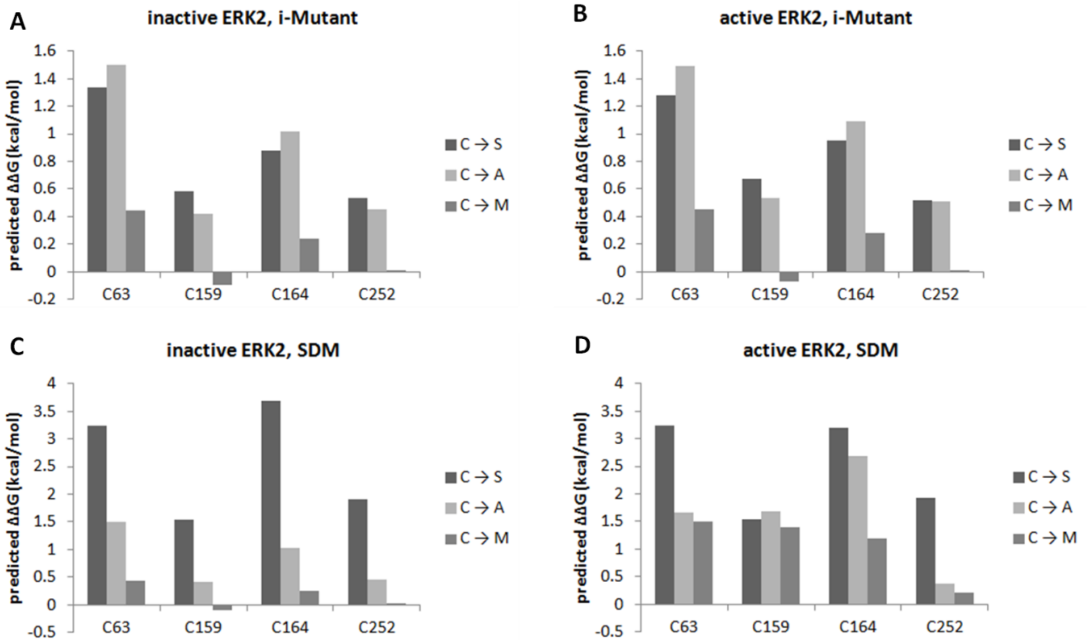

Figure 2.28 Estimated ΔΔG of cysteine mutations in ERK2.
The three types of mutations to remove intrinsic solvent-accessible cysteines include Cys to Ser, Cys to Ala, and Cys to Met of inactive ERK2 (PDB: 1ERK) and active ERK2 (PDB: 2ERK), predicted using i-Mutant and Site-Directed Mutator (SDM). **A**. ΔΔG values of cysteine mutations in inactive ERK2 predicted by i-Mutant. **B**. ΔΔG values of cysteine mutations in active ERK2 predicted by i-Mutant. **C**. ΔΔG values of cysteine mutations in active ERK2 predicted by SDM. **D.** ΔΔG values of cysteine mutations in inactive ERK2 predicted by SDM.

A good rule in designing dye-labeled ERK2 as MEK1/2 activity sensors is to introduce the fewest possible mutations so the generated biosensor proteins can have better stability in living cells. Estimated $\Delta\Delta G_{inactive}$ and $\Delta\Delta G_{active}$ values of twenty combinations of mutations in ERK2 were predicted by Eris (**Table 2.3**). Combinations of multiple cysteine-to-methionine mutations stabilize the ERK structure while combinations of multiple cysteine-to-alanine or cysteine-to-serine alanine mutations introduce slight to severe structural destabilization effects to wild type ERK2. Because stable ERK2 mutant constructs may undergo phosphoryation-induced conformational changes, while ideal MEK1/2 activity sensors require inactivated ERK2 as the affinity reagent, mutations at the dual phosphorylation sites of ERK2 might need to be incorporated to abolish the remaining kinase activity of sensor proteins. The computed data predicted by Eris collectively indicate that introduction of the phosphorylation site mutations-T183A/Y185F are likely to dramatically decrease the stability of sensor proteins. Therefore an alternative, although potentially risky approach is to look for constructs that might be stabilized in the inactive conformation and be strongly destabilized in the active conformation. For example, the construct ERK2 C159M/C164M/C252M/I254 was predicted to be stabilized in the inactive form ($\Delta\Delta G$ of -7.76 kcal/mol) and destabilized in active form ($\Delta\Delta G$ of +6.31 kcal/mol). Such constructs could be the next starting point for screening and could also be useful to test the predictive power of various protein stability prediction models. It would also be interesting to compare the conformations of final unphosphorylated and phosphorylated ERK2 biosensor constructs via circular dichroism (CD) spectroscopy or amide hydrogen-exchange NMR (HX-NMR).

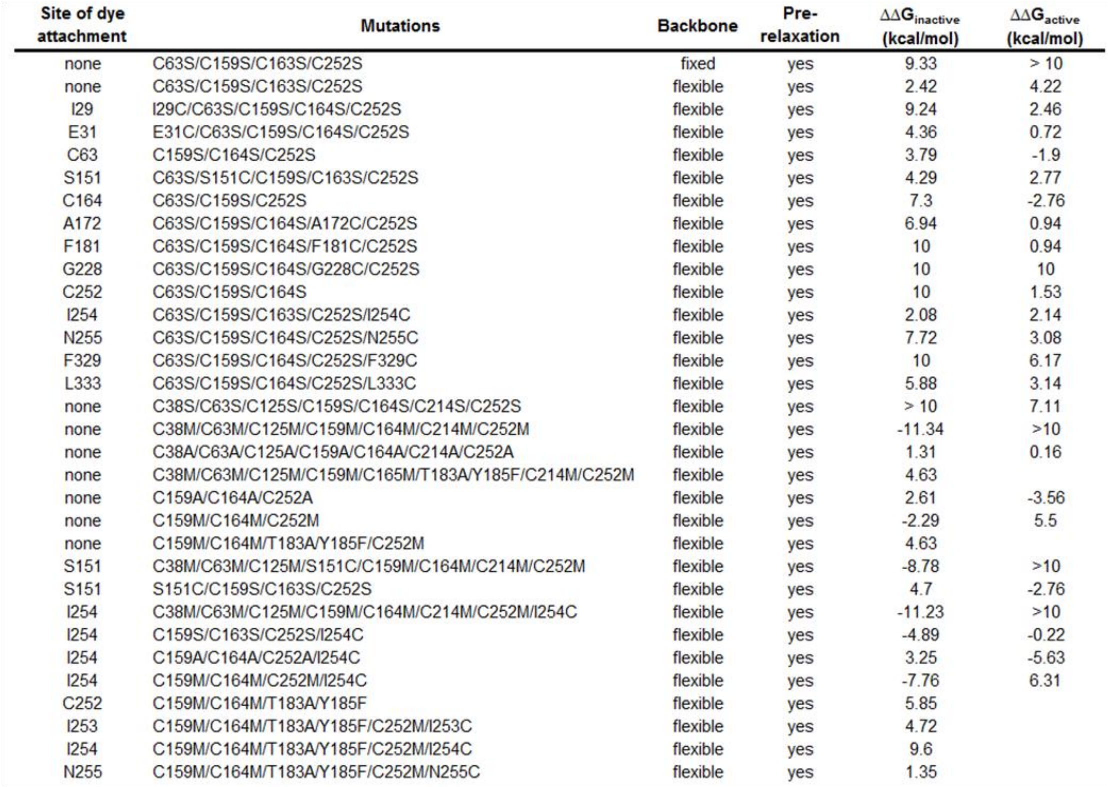

Site of dye attachment	Mutations	Backbone	Pre-relaxation	$\Delta\Delta G_{inactive}$ (kcal/mol)	$\Delta\Delta G_{active}$ (kcal/mol)
none	C63S/C159S/C163S/C252S	fixed	yes	9.33	> 10
none	C63S/C159S/C163S/C252S	flexible	yes	2.42	4.22
I29	I29C/C63S/C159S/C164S/C252S	flexible	yes	9.24	2.46
E31	E31C/C63S/C159S/C164S/C252S	flexible	yes	4.36	0.72
C63	C159S/C164S/C252S	flexible	yes	3.79	-1.9
S151	C63S/S151C/C159S/C163S/C252S	flexible	yes	4.29	2.77
C164	C63S/C159S/C252S	flexible	yes	7.3	-2.76
A172	C63S/C159S/C164S/A172C/C252S	flexible	yes	6.94	0.94
F181	C63S/C159S/C164S/F181C/C252S	flexible	yes	10	0.94
G228	C63S/C159S/C164S/G228C/C252S	flexible	yes	10	10
C252	C63S/C159S/C164S	flexible	yes	10	1.53
I254	C63S/C159S/C163S/C252S/I254C	flexible	yes	2.08	2.14
N255	C63S/C159S/C164S/C252S/N255C	flexible	yes	7.72	3.08
F329	C63S/C159S/C164S/C252S/F329C	flexible	yes	10	6.17
L333	C63S/C159S/C164S/C252S/L333C	flexible	yes	5.88	3.14
none	C38S/C63S/C125S/C159S/C164S/C214S/C252S	flexible	yes	> 10	7.11
none	C38M/C63M/C125M/C159M/C164M/C214M/C252M	flexible	yes	-11.34	>10
none	C38A/C63A/C125A/C159A/C164A/C214A/C252A	flexible	yes	1.31	0.16
none	C38M/C63M/C125M/C159M/C165M/T183A/Y185F/C214M/C252M	flexible	yes	4.63	
none	C159A/C164A/C252A	flexible	yes	2.61	-3.56
none	C159M/C164M/C252M	flexible	yes	-2.29	5.5
none	C159M/C164M/T183A/Y185F/C252M	flexible	yes	4.63	
S151	C38M/C63M/C125M/S151C/C159M/C164M/C214M/C252M	flexible	yes	-8.78	>10
S151	S151C/C159S/C163S/C252S	flexible	yes	4.7	-2.76
I254	C38M/C63M/C125M/C159M/C164M/C214M/C252M/I254C	flexible	yes	-11.23	>10
I254	C159S/C163S/C252S/I254C	flexible	yes	-4.89	-0.22
I254	C159A/C164A/C252A/I254C	flexible	yes	3.25	-5.63
I254	C159M/C164M/C252M/I254C	flexible	yes	-7.76	6.31
C252	C159M/C164M/T183A/Y185F	flexible	yes	5.85	
I253	C159M/C164M/T183A/Y185F/C252M/I253C	flexible	yes	4.72	
I254	C159M/C164M/T183A/Y185F/C252M/I254C	flexible	yes	9.6	
N255	C159M/C164M/T183A/Y185F/C252M/N255C	flexible	yes	1.35	

Table 2.3 Predicted ΔΔG values of tested biosensor proteins and newly designed constructs.

2.3.13 Generation of MKK3/6 activity sensors based on dye-labeled p38α

Simultaneous monitoring of parallel MAPK pathways in the same living cell will greatly improve the understanding of when, where, and how these complex and parallel pathways coordinate to regulate cell function. Here this approach was explored through the generation of MKK3/6 activity sensors as a proof of concept. MKK3 and MKK6 MAPKKs are the upstream activators of p38 MAPK; no activity sensors for MKK3 and MKK6 have been reported yet. The design of MKK3/6 activity sensors relied on a solvent sensitive dye covalently attached to the MAPK insert region of dead p38 (**Fig 2.29A**). Unlike ERK2, which has seven intrinsic cysteines, p38α has four intrinsic cysteines and only Cys119 and Cys162 are solvent accessible. A published crystal structure of p38β C119S/C162S (PDB: 3GC9) was used to estimate the solvent accessible surface area (SASA) at each residue in p38α C119S/C162S. Ser252 in p38 is the sole solvent accessible residue at the loop region of the MAP kinase insert in p38, so several other residues near the MAPK insert were also taken into consideration (**Fig 2.29B & C**). Residues in proximity to the substrate binding region in p38 were excluded in accordance with the published co-crystal structures (PDB: 2ONL and 2OZA)(240, 345) of the complex of unphosphorylated p38α and MAPK activated kinase-2 (MK2). Based on these criteria, the primary set of sites for dye attachment included Ala172, Asn196, Met198, His199, Tyr200, and Ser252 in p38α. The dual phosphorylation sites of p38α remained unaltered in this preliminary study; therefore, all p38-based biosensor proteins carried C119S/C162S double mutations and a third point mutation as the site for dye attachment.

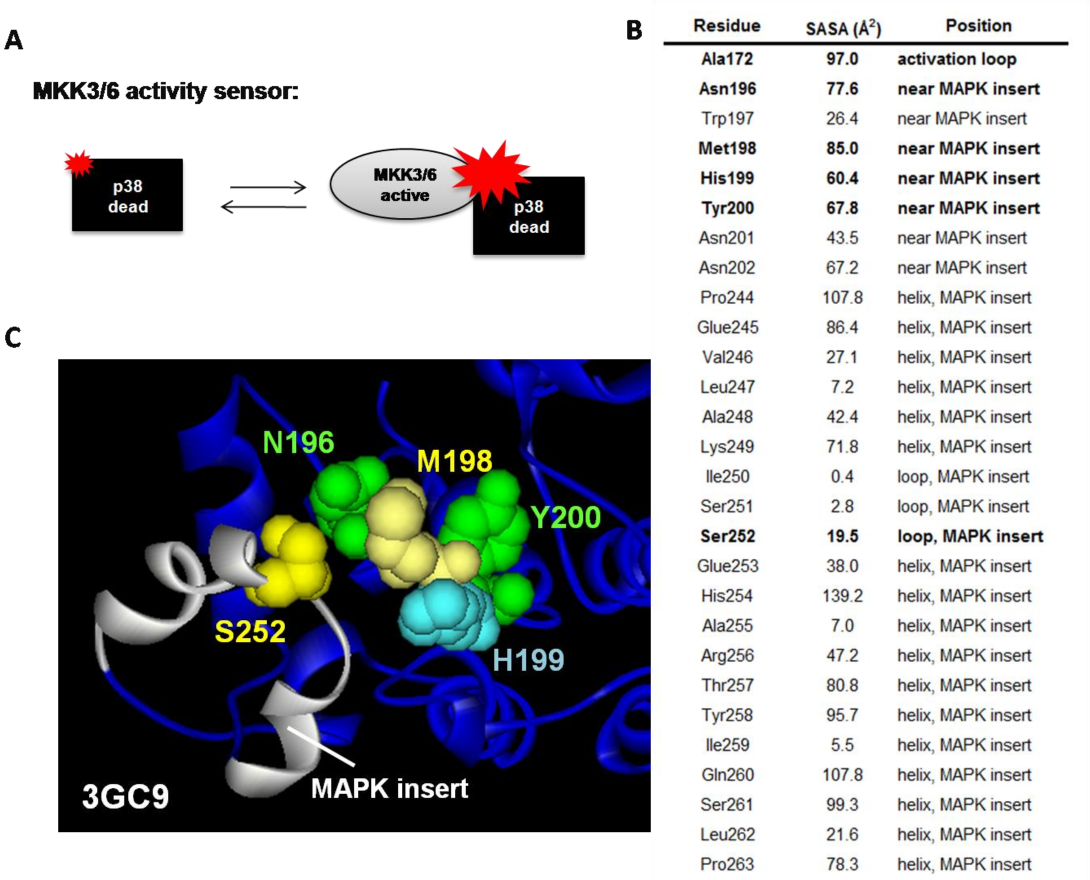

Residue	SASA (Å^2)	Position
Ala172	**97.0**	**activation loop**
Asn196	**77.6**	**near MAPK insert**
Trp197	26.4	near MAPK insert
Met198	**85.0**	**near MAPK insert**
His199	**60.4**	**near MAPK insert**
Tyr200	**67.8**	**near MAPK insert**
Asn201	43.5	near MAPK insert
Asn202	67.2	near MAPK insert
Pro244	107.8	helix, MAPK insert
Glue245	86.4	helix, MAPK insert
Val246	27.1	helix, MAPK insert
Leu247	7.2	helix, MAPK insert
Ala248	42.4	helix, MAPK insert
Lys249	71.8	helix, MAPK insert
Ile250	0.4	loop, MAPK insert
Ser251	2.8	loop, MAPK insert
Ser252	**19.5**	**loop, MAPK insert**
Glue253	38.0	helix, MAPK insert
His254	139.2	helix, MAPK insert
Ala255	7.0	helix, MAPK insert
Arg256	47.2	helix, MAPK insert
Thr257	80.8	helix, MAPK insert
Tyr258	95.7	helix, MAPK insert
Ile259	5.5	helix, MAPK insert
Gln260	107.8	helix, MAPK insert
Ser261	99.3	helix, MAPK insert
Leu262	21.6	helix, MAPK insert
Pro263	78.3	helix, MAPK insert

Figure 2.29 Rational designs of MKK3/6 activity sensors based on dye-labeled p38α. A. Mechanism of action of a MKK3/6 activity sensor. A "dead" p38 MAPK which cannot be phosphorylated by MKK3/6 was designed as the affinity reagent for MKK3 and MKK6. A solvent-sensitive fluorophore was covalently attached to the MKK-p38 binding interface and became brighter upon binding to activated MKK3 or MKK6. **B.** Calculated solvent-accessible surface area (SASA) values of some residues at or near the MAP kinase insert region of p38β C119S/C162S (PDB: 3GC9). The structure was used to mimic the mutation-induced backbone change in p38α C119S/C162S. **C.** A magnified view of the sites chosen for dye attachment.

Most dye-labeled p38α mutant proteins retain the ability to be phosphorylated by MKK6 because the two cysteine-to-serine mutations at Cys119 and Cys162 of p38 have limited destabilization effects on protein structures (**Fig 2.30B**). **Mero87**-labeled p38α N196C (p38α C119S/C162S/N196C), **mero221**-labeled p38α N196C, **mero87**-labeled p38α H199C (p38α C119S/C162S/N196C), and **mero87**-labeled p38α Y200C (p38α C119S/C162S/Y200C) were 1.2 fold brighter than the brightest **mero87**-labeled or

mero221-labeled ERK2 mutant proteins (**Fig 2.30A**). The basal phosphorylation level of **mero87**-labeled p38α Y200C was higher than wild type p38α, while other dye-labeled p38α proteins exhibited slower phosphorylation kinetics (**Fig 2.30B**). This finding was consistent with the result of fluorescence titrations of biosensor proteins with increasing amounts of active MKK6; the dye emission intensity of **mero221**-labeled p38α Y200C continuously increased over time in the presence of both active MKK6 and ATP (**Fig 2.30D**). Such apparent fluorescence change caused by phosphorylation-dependent conformational changes was also seen in the case of **mero87**-labeled p38α S252 (p38α C119S/C162S/S252C) (**Fig 2.30E**). Interestingly, **mero87**-labeled p38α Y200C did not show a fluorescence increase after addition of ATP (**Fig 2.30C**) despite the fact that the conjugate could be phosphorylated by MKK6, as quantified by Western blot analysis (**Fig 2.30B**). The main difference between **mero87** and **mero221** is the position of the thiol-reactive iodoacetamide group. Thus the relative spatial orientation of the electron donor, the electron acceptor, and the sulfate group differ at the binding surface of biosensor proteins and activated targets. Most of the **mero87**-labeled p38α and **mero221**-labeled p38α proteins also exhibited distinct fluorescence response upon phosphorylation (**Fig 2.30C & D**), indicating the importance of the orientation of dye-attachment. **Mero87**-labeled p38α A172C (p38α C119S/C162S/A172C) and **mero221**-labeled p38α N196C (p38α C119S/C162S/N196C), which did not show significant fluorescence response towards phosphorylation, have relatively low dynamic ranges of 20% maximum fluorescence change upon MKK6 binding (**Fig 2.30F**). **Mero87**-labeled p38α S252C and **mero221**-labeled p38α Y200C possess the largest *in vitro* dynamic range among all **mero87**-labeled and **mero221**-labeled p38α conjugates. However, the two biosensor candidates respond to both MKK6 binding and phosphorylation-dependent conformational changes. Therefore these two sensors require further modification, including mutation of the dual phosphorylation sites-Thr180 and Tyr182 to other unphosphorylable amino acids.

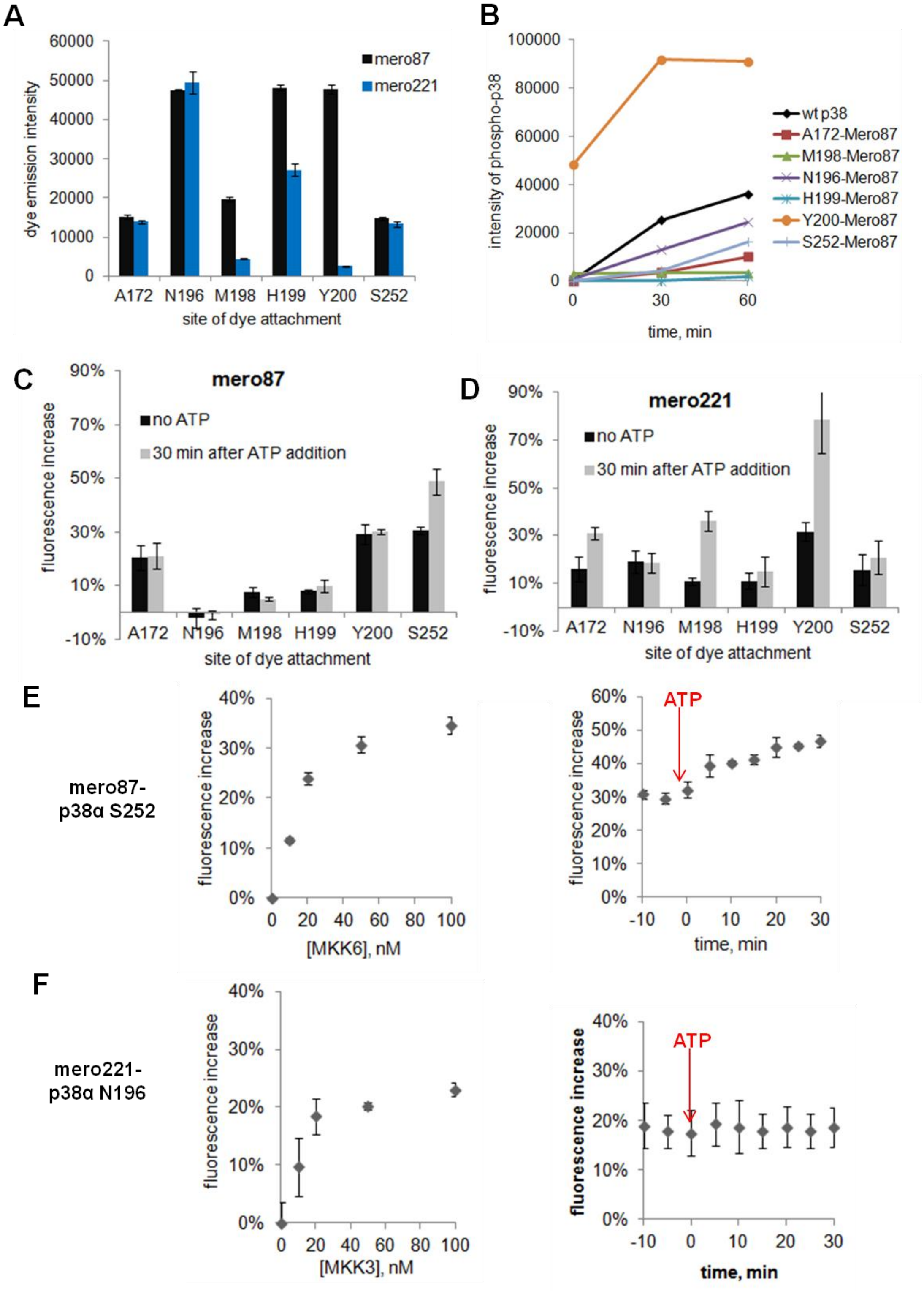

Figure 2.30 Characterization of dye-labeled p38α mutants.

A. Brightness of 50 nM **mero87**- or **mero221**-labeled p38α in phosphate buffer. **B**. *In vitro* kinase assay of **mero87**-labeled p38α. Biosensor proteins were phosphorylated by constitutively active MKK3 S218E/T222D and analyzed by Western blotting using antiphospho p38 antibody. **C**. Maximum fluorescence change of **mero87**-labeled p38α upon addition of active MKK6 and upon phosphorylation by MKK6. **D**. Maximum fluorescence change of **mero221**-labeled p38α upon addition of active MKK6 and upon phosphorylation by MKK6. **E.** Fluorescence response of **mero87**-labeled p38α S252 (p38α C119S/C162S/S252C) versus MKK binding or phosphorylation-dependent conformational changes. Biosensor proteins were titrated with 0, 12.5, 25, 50, and 100 nM active MKK6. **F**. Fluorescence response of **mero221**-labeled p38α N196 (p38α C119S/C162S/N196C) versus MKK binding or phosphorylation-dependent conformational changes. Biosensor proteins were titrated with 0, 12.5, 25, 50, and 100 nM active MKK6.

In conclusion, the new library of dye-labeled p38α mutants should contain mutations at Cys119, Cys162, Thr180 and Tyr182 positions. In addition, since many crystallographic structures of phosphorylated p38, unphosphorylated p38, and p38 in complex with substrates or small molecule inhibitors have been published, the selection of mutations could be guided by protein stability prediction and protein-protein docking models.

2.3.14 Characterization of an ERK activity biosensor based on artificial binders

A new dye-based biosensor for endogenous activated ERK—pE59RFD was characterized in living cells. pE59, the affinity reagent specific to phosphorylated ERK2 based on designed ankyrin repeat proteins (DARPins) (346, 347), was recently obtained from ribosome display through collaboration with Dr. Lutz Kummer at the laboratory of Andreas Plückthun at the University of Zurich. The co-crystal structure of pE59 in complex with phosphorylated ERK2 (PDB: 3ZUV) (347) aided in the selection of the optimal sites for dye attachment and these sensor candidates were characterized by biochemical assays prior to live cell experiments. The N123C residue of the pE59 binder was covalently labeled with **mero87** and the resulting **mero87**-labeled pE59—pE59RFD produced a fluorescence increase in response to binding of phosphorylated ERK2 (**Fig**

2.31A). When **mero87** was covalently attached at an engineered cysteine at the N-terminus, a region away from the pE59-pERK binding interface, the resulting control biosensor did not show dose-dependent fluorescence change against purified phosphorylated ERK2 (**Fig 2.31B**). The pE59RFD biosensor construct was tested in NIH 3T3 cells stably expressing YPet, a yellow fluorescent protein variant. The emission of YPet enabled ratiometric imaging of ERK activity to correct for dye fluorescence change caused by uneven illumination or varying cell thickness. The pE59RFD sensor can be easily loaded into cells via microinjection or bead loading methods due to the small size of the sensor proteins. The sensor proteins remain stable in living cells for at least six hours after biosensor loading. No significant dominant negative effects were observed throughout a wide range of bright and dim biosensor-loaded cells (**Fig 2.31D**). The raw fluorescence images in the dye channel showed apparent nuclear localization of dye signals (**Fig 2.31C**). ERK activity as defined by the ratios of dye to YPet images revealed high ERK activity in the nucleus and cell periphery because the majority of ERK substrates are transcription factors and regulators of transcription factors. To confirm that the elevated biosensor ratios in the nucleolus were real signals, and not artifacts due to non-uniform distribution of biosensor proteins and YPet fluorescent protein molecules, a single chain biosensor designs based on a solvent sensitive dye and a fluorescent protein molecule was constructed. A monomeric Cerulean fluorescent protein molecule was fused to the N-terminus of the DARPin fragment through a Gly-Ser-Gly-Ser-Gly-Ser-Gly-Ser linker or a Gly-Ser-Gly-Ser-Gly-Ser-Gly-Ser-Gly-Ser-Gly-Ser-Gly-Ser-Gly-Ser linker. The biosensor ratio images of DARPin pE59-mCerulean also confirmed the elevated ERK activity in the nucleolus (**Fig 2.31E**).

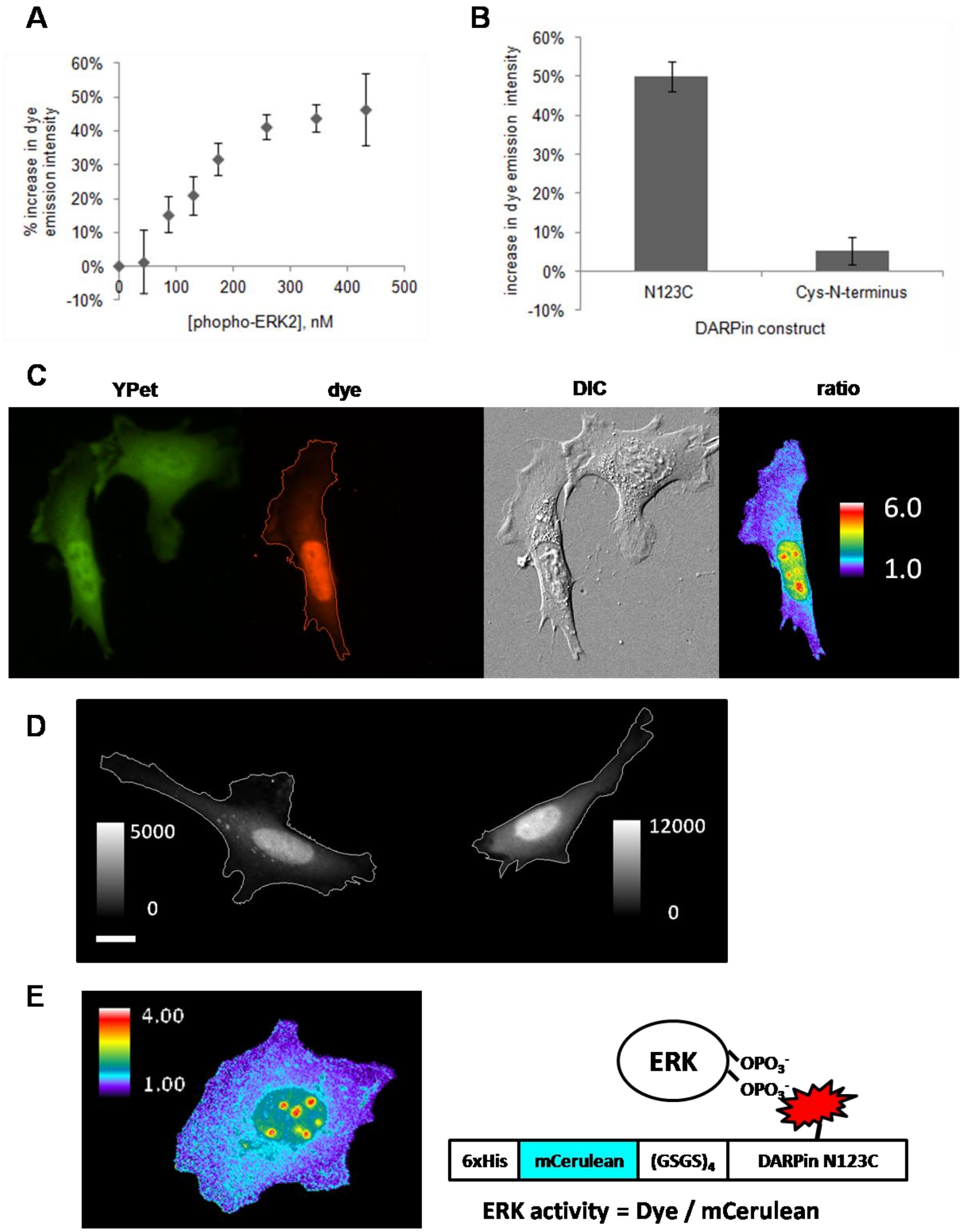

Figure 2.31 Characterization of pE59RFD, an ERK activity sensor.

A, **B**. Fluorescence titration of **mero87**-labeled pE59 N123C with various amounts of phosphorylated ERK2. Cys-N-terminus served as a negative control as **mero87** was attached away from the pE59-pERK binding interface. **C**. pET59RFD was imaged in NIH 3T3 mouse embryo fibroblasts (MEF) stably expressing YPet fluorescence protein. From left to right: YPet fluorescence image, dye fluorescence image, differential interference contrast (DIC) image and dye/YPet ratio image. **D**. Cell health of biosensor-loaded MEFs with different concentrations of pE59RFD. Retraction is indicative of perturbation. **E**. Ratio image of a YPet-MEF loaded with a single chain ERK activity sensor containing the red solvent-sensitive dye **mero87** and a fluorescent protein molecule Cerulean.

The image analysis of ERK activity patterns was conducted using MetaMorph software. The average ratios of ERK activity in the cytoplasm, in the nucleus, or in the nucleolus were measured using the region statistics function (**Fig 2.32A**). Regions used to segment the ERK ratios into the cytoplasm, the nucleus, and the nucleolus were created by manual thresholding. Signals outside or inside the thresholded regions were assigned to zero depending on the region being studied. The ratio values were normalized against the lowest 5% value to compare ratio images obtained from different image acquisition settings. It has been well characterized that phosphorylated ERK1/2 can translocate from the cytoplasm to the nucleus and activate numerous nuclear targets, including several families of transcription factors, the mitogen- and stress-activated protein kinases (MSKs), and RSK-related kinases. The biosensor showed a higher abundance of nuclear phosphorylated ERK1/2 in non-starved MEF cells relative to cells serum-starved or pre-incubated with a MEK1/2 inhibitor U0126 prior to biosensor loading (**Fig 2.32B & C**). Some cells exhibited an extremely high concentration of phosphorylated ERK1/2 in the nucleolus, implying higher transcriptional activity in these cells (285, 288, 292, 303, 348). Greatly reduced biosensor response was observed in the weak-binding control biosensor where the D46A/R90A mutations in pE59RFD prevent the formation of two essential hydrogen bonds in the DARPin/pERK binding interface (Asp46 to K229 in pERK2 and Arg90 to pTyr185 in pERK). More importantly, unlike the current ERK biosensors that only illuminate ERK activity in the nucleus or in the cytoplasm, the fluctuation of the cytoplasmic ERK phosphorylation recorded by the DARPin biosensor is easily visualized by saturating the biosensor ratios in the nucleus region. In the cytoplasm, the trafficking and spatiotemporal regulation of ERK1/2 have been shown to be governed by MEK1, MEK2, several scaffold proteins, and the MAP kinase phosphatase (MKP). In addition to the cytoplasmic targets of ERK1/2 that activate certain transcription factors, such as MAPK-interacting kinase 1 (MNK1), MNK2 (291, 305-309), and ribosomal protein S6 kinases (RSKs) (286, 303, 305, 349, 350), several other cytoplasmic substrates of ERK1/2 have been indicated to regulate the feedback mechanism of ERK1/2 phosphorylation (351, 352) or to mediate cell movement (129, 234, 342, 353). While the spatiotemporal regulation of ERK1/2 in the cytoplasm remains poorly characterized due to the lack of sensitive ERK biosensors, this DARPin-based ERK biosensor could be very useful, particularly for studying the cross-talk of MEK and ERK dynamics during cell motility.

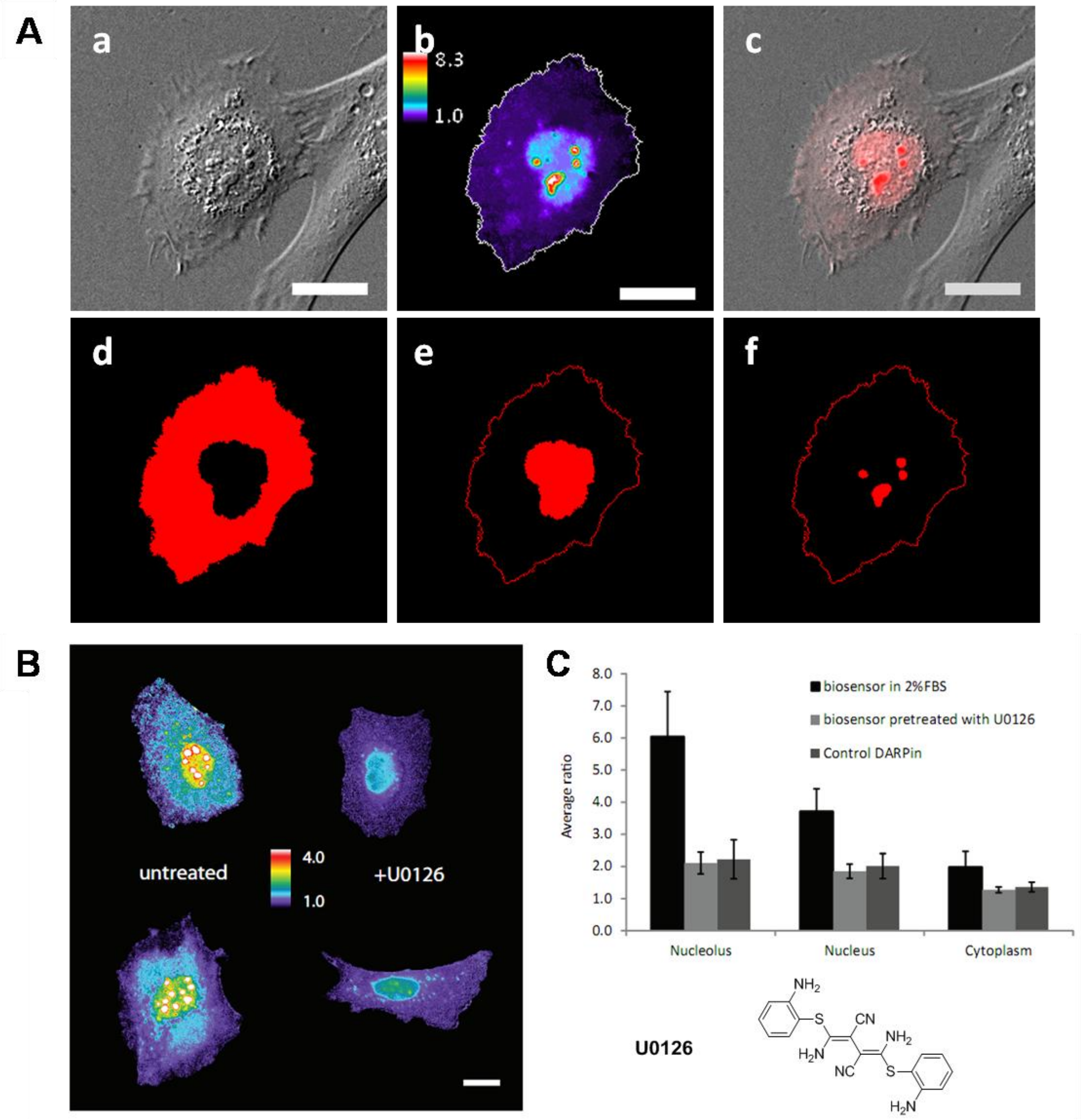

Figure 2.32 Quantification of ERK activity in living cells.

A. Average ERK activity in the cytoplasm, in the nucleus, and in the nucleoli was quantified using the intensity thresholds. **B.** Ratio images of pET59RFD in NIH 3T3 mouse embryo fibroblasts (MEF) with and without pre-treatment of 10 µM U0126, a MEK inhibitor. **C**. Comparison of the average biosensor ratios of the biosensor in 2% fetal bovine serum (13 cells), pre-treated with 10 µM U0126 (46 cells), and a control mutant sensor in 2% fetal bovine serum (60 cells).

2.4 Conclusions

Our approaches have generated sensitive biosensor designs targeting endogenous activated MEK1/2 and MKK3/6 MAPKK. The biosensor designs, based on inactivated substrates of MAPKK, utilize the capacity of inactivated MAPK protein molecules that specifically bind activated MAPKK and are labeled with a bright solvent-sensitive dye covalently attached to an engineered cysteine at the MAPKK-MAPK binding interface of the inactivated MAPK; the dye changes its fluorescence in response to the increased local hydrophobicity induced by MAPKK-MAPK binding interactions. Inactivated MAPK affinity scaffolds were obtained through introduction of multiple cysteine-to-serine mutations to remove all solvent-accessible intrinsic cysteines. In the case of biosensors based on dye-labeled ERK2, all biosensor proteins contain C63S/C159S/C164S/C252S mutations as well as an engineered cysteine for dye attachment, whereas in the case of biosensors based on dye-labeled p38α, all biosensor proteins contain C119S/C162S mutations. As a result, most dye-labeled ERK2 constructs were strongly destabilized and could not be efficiently phosphorylated by the activator MEK1, which resulted in a loss of the ability to phosphorylate ERK substrates. In contrast, the majority of the dye-labeled p38α constructs are still capable of being phosphorylated by MKK3 or MKK6, probably due to the reduction of protein destabilization effects induced by the two cysteine mutations. According to the correlation analysis of biosensor performance versus predicted protein stability of each biosensor construct, we determined that the incorporation of protein stability predictions will be crucial for future optimization of both MEK1/2 and MKK3/6 activity sensors.

2.5 Materials and Methods

DNA constructs and mutagenesis Constructs provided from outside sources or prepared by previous colleagues are listed as follows: GST-tagged *human* MEK1 WT in pGEX-2t, GST-tagged human MEK1 S218D/S222D (MEK1DD) in pGEX-2t, GST-tagged *human* MEK1 S218A/S222A (MEK1AA) in pGEX-2t, GST-tagged *human* MEK2 WT in pGEX-2t, GST-tagged *human* MEK2 S222D/S226D (MEK2DD) in pGEX-2t, GST-tagged *human* MEK2 S222A/S226A (MEK2AA) in pGEX-2t, GST-tagged *mouse* paxillin α (PXNα) 1-338 in pGEX-2t, GST-tagged *murine* KSR-1 AA383-519 in pGEX-2t, GST-tagged *murine* KSR-1 AA318-519 FSF471-473AAA in pGEX-2t, T7-tagged *human* MEK1 WT, T7-tagged *human* MEK1 S218D/S222D in pCDNA3, T7-tagged *human* MEK1 S218A/S222A in pCDNA3, HA-tagged *human* MEK2 WT in pCDNA3, HA-tagged *human* MEK2 S222D/S226D in pCDNA3, HA-tagged *human* MEK2 S222A/S226A, *human* MEK1 WT in pBabeNeo, *human* MEK1 S218D/S222D in pBabeNeo, *human* MEK1 S218A/S222A in pBabeNeo, *human* MEK2 WT in pBabeNeo, *human* MEK2 S222D/S226D in pBabeNeo and *human* MEK2 S222A/S226A in pBabeNeo were generous gifts from Dr. John Blenis at the Harvard Medical School. 6xHis-tagged *human* MEK1R4F (MEK1 ΔN3/S218E/S222D) and 6xHis-tagged ERK2/MEK1R4F in pET vectors were provided by Dr. Melanie Cobb at the UT Southwestern Medical Center. 6xHis-tagged MAPK Phosphatase-3 (MKP3) in pRSET was obtained from Dr. Alexei Toutchkine. GST-tagged ERK1 WT in pGEX-2t was provided by the Gran lab. 6xHis-tagged ELK-1 in pET22b(+), 6xHis-tagged EGFP-ERK2 WT in pET23, 6xHis-tagged EGFP-ERK2 T183A/Y185F in pET23 and 6xHistagged EGFP-ERK2 K52R in pET23 were prepared by Dr. Frédérique Gaits. 6xHis-tagged ERK DAPRin N123C in pDST67 and 6xHis-tagged ERK DAPRin D46A/R90A/N123C in pDST67 were provided by Dr. Andreas Plueckthun at the University of Zurich. The T7-tagged MEK1 constructs in pCDNA3 were sequenced using a forward primer 5'-AAGGCCGGCCACCCAAGAAGAAGCCGACGCCC-3' and a reverse primer 5'- CAAGAAGGCGCGCCTTAGACGCCAGCAGCATGGGTTG-3'. The HA-tagged MEK2 constructs in pCDNA3 were sequenced using a forward primer 5'-AAGGATCCCTGGCCCGGAGGAAGCCGGTG-3' and a reverse primer 5'-CAAGAAGGCGCGCCTCACACGGCGGTGCGCGTGGG-3'. The GST-tagged MEK1 constructs in pGEX-2t were sequenced using forward primer 5'-AAGGCCGGCCACCCAAGAAGAAGCCGACGCCC-3' and a reverse primer 5'-CAAGAAGGCGCGCCTTAGACGCCAGCAGCATGGGTTG-3'. The MEK1 constructs in pBabeNeo were sequenced using a forward primer 5'-AAGGCCGGCCACCAATGCCCAAGAAGAAGCCGACG-3' and a reverse primer 5'-CAAGAAGGCGCGCCTTAGACGCCAGCAGCATGGGTTG-3'. The MEK2 constructs in pBabeNeo were sequenced using a forward primer 5'-AAGGATCCACCAATGCTGGCCCGGAGGAAGCCG-3' and a reverse primer 5'-CAAGAAGGCGCGCCTCACACGGCGGTGCGCGTGGG-3'. Other constructs in pGEX-2t were sequenced using a forward primer 5'-GGGCTGGCAAGCCACGTTT GGTG-3' and a reverse primer 5'- CCGGGAGCTGCATGTGTCAGAGG-3'.

Site-directed mutagenesis of *rat* wild type ERK2 in pET23 was obtained by multi-step overlap extension PCR using the primers (Integrated DNA Technologies) listed in **Table 2.4**. All mutations were confirmed by sequencing (Eton Bioscience) using a forward primer of 5'-TAATACGACTCACTATAGG-3' or a reverse primer of 5'-GCTAGTTATTGCTCAGCGG-3'. The obtained constructs include ERK2 C63S/C252S, ERK2 C63S/C159S/C252S, ERK2 C63S/C164S/C252S, ERK2 C63S/C159S/C164S/S252C, ERK2 C63S/C159S/C164S/C252S/F329C, ERK2 C63S/C159S/C164S/F181C/C252S, ERK2 C63S/C159S/F181C/C252S, ERK2 I29C/C63S/C159S/C164S/C252S, ERK2 C159S/C164S/C252S, ERK2 C63S/C159S/C252S/F329C, ERK2 C63S/C159S/C252S, ERK2 K52R/C63S/C159S/C164S/C252S, ERK2 C63S/C159S/C164S/C252S/L333C, ERK2 C63S/C159S/C164S/C252S/D319N, ERK2 C63S/C159S/C164S/C252S, ERK2 C63S/C159S/C164S/C252S/F329C, ERK2 C63S/C159S/C164S/C252S/I254C, ERK2 C63S/C159S/C164S/G228C/C252S, ERK2 C63S/C159S/C164S/T183A/C252S/F329C, ERK2 C63S/C159S/C164S/Y185W/C252S/F329C, ERK2 C63S/C159S/C164S/C252S/D316A/D319A.

ERK2-EGFP fusion proteins were cloned from the two parent constructs- 6xHis-tagged ERK2 mutant in pET23 and 6xHis-tagged wild type ERK2-EGFP in pET23. The restriction enzyme cleavage sites of BamHI and NotI were added to the 6xHis-tagged ERK2 mutant in pET23 by PCR using a reverse primer 5'-CTCGAGCGCGGCCGCTTGTTAAGATCTGTATCC-3', a forward primer 5'-GATCTCGAGGGATCCATGGCACATCACCATC-3' and the Phusion High-Fidelity DNA Polymerase kit (New England BioLabs). ERK2-EGFP fusion proteins were prepared from the PCR products of the 6xHis-tagged ERK2 mutants and the entire plasmid of 6xHis-tagged wild type ERK2-EGFP in pET23 using BamHI, NotI and Quick Ligase (New England BioLabs) according to the manufacturer's instructions. The double phosphorylation site mutations T183A/Y185W were introduced to the new 6xHis-tagged

ERK2-EGFP mutants at the same time using a forward primer 5'-CATACAGGGTTCTTGGCCGAGTGGGTAGCCACGCGTTGG-3', a reverse primer 5'-CCAACGCGTGGCTACCCACTCGGCCAAGAACCCTGTATG-3' and the QuikChange Site-Directed Mutagenesis Kit (Stratagene).

Site-directed mutagenesis of *mus musculus* wild type p38α was conducted in pTriEx and pET23. p38α mutants were cloned with the help of Evan Trudeau. The useful cloning products include p38α C119S/C162S, p38α C119S/C162S/A172C, p38α C119S/C162S/A172S, p38α C119S/C162S/N196C, p38α C119S/C162S/M198C, p38α C119S/C162S/H199C, p38α C119S/C162S/Y200C and p38α C119S/C162S/C252S. Constructs were sequenced using a forward primer 5'- ATATGGATCCATGTCGCAGGAGAGGCCCAC-3' and a reverse primer 5'- ATATAAGCTTTCAGGACTCCATTTCTTCTTGG-3'.

ERK DARPin-mCerulean C49S fusion proteins were cloned assisted by Evan Trudeau. 6xHis-tagged mCerulean C49S-$(GSGS)_2$-ERK DARPin N123C and 6xHis-tagged mCerulean C49S-$(GSGS)_4$-ERK DARPin N123C were cloned into pTriEx-3 and pDST67. Constructs in pDST67 were sequenced using a forward primer 5'-GTTCTGAGGTCATTACTGG-3' and a reverse primer 5'- GTTCTGAGGTCATTACTGG-3'.

Mutation	Purpose	Primer sequence (5' to 3')	
I29C	site of dye attachment	reverse	CGTAGGCGCCTTCTCCGCAGTACGAGAGATTAGTGTAGC
		forward	GCTACACTAATCTCTCGTACTGCGGAGAAGGCGCCTACG
K52R	dominant negative	reverse	AGGACTGATTTTCCTGATAGCAACTCGAACTTTG
		forward	CGAGTTGCTATCAGGAAAATCAGTCCTTTTGAGC
R65S	dominant positive	reverse	TCTCTCTTAGGGTGCTTTGACAGTAGGTCTGGTGC
		forward	CCTACTGTCAAAGCACCCTAAGAGAGATAAAAATC
C63S	removal of intrinsic Cys	reverse	CTCTCAGGGTTCTCTGAGAGTAGGTCTGGTGCTC
		forward	GAGCACCAGACCTACTCTCAGAGAACCCTGAGAG
C63A	removal of intrinsic Cys	reverse	CAGGGTTCTCTGAGCGTAGGTCTGGTG
		forward	CACCAGACCTACGCTCAGAGAACCCTG
S63C	site of dye attachment	reverse	CAGGGTTCTCTGACAGTAGGTCTGGTG
		forward	CACCAGACCTACTGTCAGAGAACCCTG
E79A	weaken MEK-ERK binding	reverse	GCCGATGATGTTCGCATGTCTGAAGCGCAG
		forward	CGCTTCAGACATGCGAACATCATCGGCATC
S151C	site of dye attachment	reverse	GTGTTCAGCAGGAGGTTGCAAGGCTTGAGG
		forward	ACCGTGACCTCAAGCCTTGCAACCTCCTGC
C159S	removal of intrinsic Cys	reverse	GCTGAACACCACTACTGATCTCAAG
		forward	CTTGAGATCAGTAGTGGTGTTCAGC
C159A	removal of intrinsic Cys	reverse	GCTGAACACCACTAGCGATCTCAAG
		forward	CTTGAGATCAGTGCTGGTGTTCAGC
C164S	removal of intrinsic Cys	reverse	GCAACACGGGCAAGGCCAAAGTCACTGATCTTGAGATCACTAGTG
		forward	CACTAGTGATCTCAAGATCAGTGACTTTGGCCTTGCCCGTGTTGC
C164A	removal of intrinsic Cys	reverse	GGCAAGGCCAAAGTCAGCGATCTTGAG
		forward	CTCAAGATCGCTGACTTTGGCCTTGCC
A172C	site of dye attachment	reverse	CCTTGCCCGTGTTTGCGATCCAGACCATG
		forward	TCTGGATCGCAAACACGGGCAAG
T183A	phosphorylation site mutant	reverse	CGCGTGGCTACATACTCGGCCAAGAACCCTGTATGATC
		forward	GATCATACAGGGTTCTTGGCCGAGTATGTAGCCACGCG
Y185W	phosphorylation site mutant	reverse	CCAACGCGTGGCTACCCACTCTGTCAAGAACCC
		forward	GGGTTCTTGACAGAGTGGGTAGCCACGCGTTGG
T183A, Y185W	phosphorylation site mutant	reverse	CCAACGCGTGGCTACCCACTCGGCCAAGAACCCTGTATG
		forward	CATACAGGGTTCTTGGCCGAGTGGGTAGCCACGCGTTGG
F181C	site of dye attachment	reverse	TACATACTCTGTCAAGCACCCTGTATGATCATGG
		forward	CATGATCATACAGGGTGCTTGACAGAGTATGTAG
G228C	site of dye attachment	reverse	AGCTGGTCAAGGTAATGCTTGCATGGGAAGATAGGCCTG
		forward	CCAACAGGCCTATCTTCCCATGCAAGCATTACCTTGACC
H230R	weaken MEK-ERK binding	reverse	GCTGGTCAAGGTAACGCTTTCCTGGGAAG
		forward	CTTCCCAGGAAAGCGTTACCTTGACCAGC
C252S	removal of intrinsic Cys	reverse	GCTTTTAAATTTATTATAGAATTCAGATCTTCCTGTGATGG
		forward	CCATCACAGGAAGATCTGAATTCTATAATAAATTTAAAAGC
C252A	removal of intrinsic Cys	reverse	GCCGTGGTTTAAATTTATTATAGCATTCAGATCTTCCTG
		forward	CAGGAAGATCTGAATGCTATAATAAATTTAAACCACGGC
N255C	site of dye attachment	reverse	GCTTTTAAGCAGATTATAGAATTCAGATCTTCCTGTG
		forward	CTATAATCTGCTTAAAAGCTAGAAACTATTTGCTTTCTCTCCCC
Y261A	weaken MEK-ERK binding	reverse	TGCGGGAGAGAAAGCAAAGCGTTTCTAGCTTTTAAAT
		forward	AATTTAAAAGCTAGAAACGCTTTGCTTTCTCTCCCGC
S282C	site of dye attachment	reverse	CCAGTAAATCCAGAGCTTTGCAGTCAGCGTTTGGGAACAATCTG
		forward	CAGATTGTTCCCAAACGCTGACTGCAAAGCTCTGGATTTACTGG
D319N	weaken MEK-ERK binding	reverse	GCAATGGGCTCATTACTTGGGTCATAATACTGC
		forward	TTATGACCCAAGTAATGAGCCCATTGCTGAAGC
D316A, D319A	weaken MEK-ERK binding	reverse	TGGCGCTTCAGCAATGGGCTCTGCACTTGGGCCATAATAC
		forward	AGCAGTATTATGCCCCAAGTGCAGAGCCCATTGCTGAAGC
F329C	site of dye attachment	reverse	CAGCTCCATGTCACACTTGAATGGTGCT
		forward	GCACCATTCAAGTGTGACATGGAGCTGG
L333C	site of dye attachment	reverse	CCTTAGGTAAGTCGTCGCACTCCATGTCAAACTTG
		forward	CAAGTTTGACATGGAGTGCGACGACTTACCTAAGG

Table 2.4 Nucleotide sequences of primers for site-directed mutagenesis.

Expression and purification of recombinant proteins Proteins purified from *E.Coli* expression systems include 6xHis-tagged *rat* ERK2 mutants, 6xHis-tagged *rat* p38α mutants, 6xHis-tagged *rat* ERK-EGFP fusion proteins, 6xHis-tagged constitutive active MEK1 R4F, 6xHis-tagged wild type MEK1, GST-tagged wild type MEK1, GST-tagged constitutive active MEK1 S218D/S222D (MEK1DD), GST-tagged dominant negative MEK1 S218A/S222A (MEK1AA), GST-tagged wild type MEK2, GST-tagged constitutively active MEK2 S222D/S226D (MEK2DD), GST-tagged dominant negative MEK2 S222A/S226A (MEK2AA), 6xHis-tagged MKK3 wild type, 6xHis-tagged constitutively active MKK3 S189E/T193D (MKK3ED), 6xHis-tagged dominant negative MKK3 S189A/T193A (MKK3AA), 6xHis-tagged MAPK Phosphatase-3 (MKP-3), 6xHis-tagged Elk-1, GST-tagged KSR-1 AA383-519, GST-tagged KSR-1 FSF471-473AAA , GST-tagged paxillin. BL21(DE3), 6xHis-tagged ERK DARPin N123C, 6xHis-tagged ERK DARPin D46A/R90A/N123C, 6xHis-tagged mCerulean C49S-$(GSGS)_2$-ERK DARPin N123C and 6xHis-tagged mCerulean C49S-$(GSGS)_4$-ERK DARPin N123C. *Express I^q* Competent *E.coli* strains (New England BioLabs or Stratagene) were transformed with the various plasmids and plated on LB-agar plates containing 100 µg/ml carbencillin. A single fresh transformed colony from a 25 ml LB-agar plate was inoculated into a culture tube of 1 ml LB medium containing 100 µg/ml carbenicillin, grown overnight at 37 ^{o}C at 245 rpm in an orbital bacterial shake. Bacteria pellets were collected by centrifugation at room temperature at 12,000 rpm for 10 min on a benchtop centrifuge, re-suspended in 500 µl of glycerol/LB medium (1:1), and stored at -80^{o}C up to one year. 10 µl of frozen bacterial stock or a single fresh colony from a LB-agar plate were inoculated in three tubes of 5 ml of LB medium containing 100 µg/ml carbenicillin. The cultures were grown overnight at 32^{o}C at 245 rpm in an orbital bacterial shaker and then transferred to 1 L of LB medium containing 10 µg/ml carbenicillin in a 2 L sterile flask. Details of the customized expression and purification protocols for each protein of interest are described as follows.

For 6xHis-tagged MEK1R4F, 6xHis-tagged wild type MEK1, 6xHis-tagged wild type MKK3, 6xHis-tagged MKK3ED and 6xHis-tagged MKK3AA, the 1 L cultures were grown at 32 ^{o}C at 245 rpm to an optical density at 600 nm of 0.8, followed by induced-expression at 28 ^{o}C at 245 rpm for 4 hours in the presence of 0.5 mM isopropyl β-D-1-thiogalactopyranoside (IPTG) and 100 µg/ml carbenicillin. The bacterial pellets were collected by centrifugation at 4000 rpm at 4 ^{o}C for 20 min and stored at -80^{o}C prior to purification. The frozen pellet from a 1 L culture was warmed up on an ice bath and then re-suspended in 30 ml MEK lysis buffer (50 mM K_2HPO_4, 1 mM dithiothreitol, 1 mM phenylmethanesulfonylfluoride, 2 mM benzamidine.HCl, 0.25% Tween-20, 10% glycerol, pH 8.0). The lysis of the bacterial suspension was conducted on ice using an ultrasonic homogenizer (Branson Digital Sonifier) at 70% sonication strength, three cycles of 20 seconds and 30 second-intervals for cooling between each cycle. The homogenized suspension was transferred into a 35 ml tube and the supernatant was collected by centrifugation (Sorvall, model T21) at 7000 rpm under 4^{o}C for 20 min. Slurry of TALON Metal Affinity Resin (Clontech, 10 mg protein/ml resin capacity) was pre-equilibrated with lysis buffer in a 50 mL cornical tube. For 6xHis-tagged MEK1 R4F, 30 ml homogenized suspension was added into the cornical tube containing 2 ml slurry of the pre-equilibrated resin (1 ml resin plus 1 ml lysis buffer). The resulting mixture was rotated at 4^{o}C on a nutator (BD Clay Adams, model 1105) for 1 hour. The protein-bound resin was collected by centrifugation (Eppendorf, model 5810) at 1800 rpm at 4°C, washed twice with 50 ml of lysis buffer, and loaded into a polypropylene column (BioRad). The protein-bound resin was washed with 30 ml of chilled MEK wash buffer (50 mM K_2HPO_4, 10 mM imidazole, 1 mM DTT, 1 mM PMSF, 2 mM benzamidine.HCl, 0.25% Tween-20, 10% glycerol, pH 8.0) and the 6xHis-tagged protein fractions were eluted with MEK elution buffer (50 mM K_2PO_4, 150 mM imidazole, 1 mM DTT, 1 mM PMSF, 2 mM benzamidine.HCl, 0.25% Tween-20, 10% glycerol, pH 8.0). The collected fractions were combined and dialyzed at 4 °C overnight in 1 L dialysis buffer (50 mM Trizma, 0.2 M NaCl, 0.1% v/v β-mercaptoethanol, 20% glycerol, pH 7.5). Protein concentration was estimated using BCA assay and yield was calculated approximately 15 mg proteins per 1 L culture on average. The purified 6xHis-tagged MEK1 R4F protein remains active within a few days on ice and its activity is entirely lost upon any freeze-thaw cycles. Snap-freeze in liquid nitrogen or preparation in 50% glycerol prior to long-term storage at -80 °C failed to retain its activity to phosphorylated wild type ERK2 proteins as examined by *in vitro* kinase assays. Purification of 6xHis-tagged wild type MEK1, 6xHis-tagged wild type MKK3, 6xHis-tagged MKK3ED and 6xHis-tagged MKK3AA was conducted similarly to the protocol for 6xHis-tagged MEK1R4F except the use of 1 ml resin per 1 L culture. These proteins were stored in 40% glycerol at -80 °C and the constitutively active MAPKK proteins remained active after a single freeze-thaw cycle as examined by *in vitro* kinase assays. The protein concentration for each fraction was determined by BCA protein assay kits (Thermo Scientific Pierce) or absorbance at 280 nm divided by theoretical extinction coefficients (23,620 $cm^{-1}M^{-1}$ at 280 nm for MEK1 and 29,310 $cm^{-1}M^{-1}$ at 280 nm for MKK3).

For 6xHis-tagged ERK2 mutant proteins, 6xHis-tagged ERK2-EGFP fusion proteins, 6xHis-tagged p38α mutant proteins, 6xHis-tagged Elk-1 and 6xHis-tagged MKP-3, the 1 L cultures were grown at 37°C till the optical density at 600 nm of the culture is between 0.6 and 0.8. The 1 Lcultures for production of 6xHis-tagged Elk-1 and 6xHis-tagged MKP-3 were grown at 28°C at 245 rpm for 12 hours in an orbital bacterial shaker in the presence of 0.5 mM IPTG and 100 µg/ml carbencillin. Expression of 6xHis-tagged MAPK proteins were induced at 28 °C at 245 rpm for 5 hours in the presence of 0.5 mM IPTG and 100 µg/ml carbencillin. Prolonged incubation results in significant amounts of sticky bacterial debris. Bacteria pellets were collected and stored using the same protocol for 6xHis-tagged MEK1R4F. The frozen pellets were re-suspended in MAPK lysis buffer (50 mM Trizma, 500 mM NaCl, 5% glycerol, pH 8.0) and then homogenized according to the protocol for MEK1R4F. 2 ml slurry of pre-equilibrated Talon Metal Affinity Resin (Clontech) was added to the lysate from the 1 L culture and the resulting mixture was rotated at 4°C for 1 hour on a nutator. The protein-bound resin was washed with MAPK lysis buffer by centrifugation followed by gravity using MAPK lysis buffer in separation column. The 6xHis-tagged proteins were eluted by a gradient of imidazole from 0 to 250 mM in MAPK lysis buffer. The eluate containing the MAPK proteins was added 1 µLβ-mercaptoethanol (BioRad) prior to dialysis to reduce all cysteine residues of MAPK proteins. The fractions containing 6xHis-tagged Elk-1 and 6xHis-tagged MKP-3 were combined and dialyzed at 4°C overnight in dialysis buffer (50 mM Trizma, 150 mM NaCl, 1 mM EDTA, 1 mM DTT, 5% glycerol, pH 7.5) while the eluate of 6xHis-tagged MAPK proteins were dialyzed at 4 °C overnight in protein labeling buffer (50 mM Na_2HPO_4, 10% glycerol, pH 7.5). The protein concentration was determined by using absorbance at 280 nm divided by the theoretical extinction coefficients (42,230 $cm^{-1}M^{-1}$ at 280 nm for ERK2, 48,130 $cm^{-1}M^{-1}$ at 280 nm for p38α, 56,000 $cm^{-1}M^{-1}$ at 490 nm for ERK2-EGFP, 33,480 $cm^{-1}M^{-1}$ for Elk-1 and 31,190 $cm^{-1}M^{-1}$ for MKP-3) or BCA protein assay kits (Thermo Scientific Pierce). 6xHis-tagged Elk-1 and 6xHis-tagged MKP-3 proteins were adjusted to 40% glycerol in MAPK dialysis buffer and stored as aliquots in -80 ^{o}C. Portion of the reduced MAPK proteins was concentrated to 100 µM by centrifuge at 4000 rpm at 4 ^{o}C for 20 to 40 min in concentration tubes.(VivaSpin 20 MWCO 10K; Eppendorf, model 5810) and stored as 100 µl aliquots in a 0.5 ml low adhesion microcentrifuge tube (USA Scientific) at -80 ^{o}C. Some MAPK mutant proteins formed insoluble protein aggregates upon freeze-thaw cycles. All ERK2 and p38α mutant proteins for screening were freshly made and immediately used for labeling and assays without going through any freeze-thaw cycles.

For GST-tagged wild type MEK1, GST-tagged MEK1DD, GST-tagged MEK1AA, GST-tagged wild type MEK2, GST-tagged MEK2DD, GST-tagged MEK2AA, GST-tagged KSR-1 AA383-519, GST-tagged FSF471-473AAA and GST-tagged paxillin α 1-338, the 1 L cultures were grown at 32 ^{o}C to an optical density of 0.8. Expression of GST-tagged proteins was conducted at 28 ^{o}C overnight in the presence of 1.0 mM IPTG and 100 µg/ml carbencillin. The bacteria pellets were collected by centrifugation at 4000 rpm at 4 ^{o}C for 20 minutes, stored at -80 ^{o}C and re-suspended in GST lysis buffer (50 mM Trizma, 150 mM NaCl, 270 mM sucrose, 0.1 mM EGTA, 1 mM benzamidine.HCl, 1X protease cocktail, 0.1% v/v β-mercaptoethanol, 0.03% v/v Brij-35, pH 7.5). The bacteria lysate was prepared according to the protocol for 6xHis-tagged MEK1R4F. 2 ml slurry of pre-equilibrated immobilized glutathione resin (Thermo Scientific Pierce) was added to the supernatant and incubated at 4 ^{o}C for 2 hours on a nutator. The protein-bound resins were first washed three times with GST lysis buffer by centrifugation at 1800 rpm at 4 ^{o}C, loaded into a polypropylene column and washed again with 60 ml of GST lysis buffer at 4^{o}C. The GST-tagged proteins were eluted using freshly prepared GST elution buffer (33 mM glutathione, 50 mM Trizma, 150 mM NaCl, 270 mM sucrose, 0.1 mM EGTA, 1 mM benzamidine.HCl, 1X protease cocktail, 0.1% v/v β-mercaptoethanol, 0.03% v/v Brij-35, pH 7.5). The eluate was concentrated to 200 µl by centrifugation (VivaSpin 20 MWCO 10K; Eppendorf, model 5810) at 4000 rpm at 4 ^{o}C for 10 to 40 minutes depending on the initial volume. The concentrated eluate was loaded into a pre-equilibrated Dextran Desalting Column (Thermo Scientific Pierce) and eluted with MAP2K dialysis buffer (50 mM Trizma, 0.2 M NaCl, 0.1% v/v β-mercaptoethanol, 20% glycerol, pH 7.5) to remove excess glutathione molecules and to change the buffer composition for the sub sequential *in vitro* fluorescence titration experiments. Protein solutions were adjusted to 40% glycerol in the MAP2K dialysis buffer and stored at aliquots at -80 ^{o}C. Protein concentration was approximated by SDS-PAGE and Commassie staining using bovine serum albumin (New England BioLabs) as reference. Optimization of expression conditions for GST-tagged MEK1/2 and GST-tagged paxillin α 1-338 was performed in a 5 ml mini culture at various concentrations of IPTG and temperature. The bacteria pellets were collected by centrifugation at 13,200 rpm at room temperature for 10 minutes and lyzed using the BugBuster Protein Extraction Reagent (Novagen) according to the manufacturer's instructions. The soluble fractions of the bacteria lysate were analyzed by SDS-PAGE and Commassie Blue staining. Due to the substantial amounts of anomalously cleaved GST tags present in the eluate of GST-tagged MAP2K proteins, GST-MEK1DD and GST-MEK2DD were only used for *in vitro* kinase assays.

The general expression and purification protocol of 6xHis-tagged ERK DARPin N123C, 6xHis-tagged ERK DARPin D46A/R90A/N123C, 6xHis-tagged mCerulean C49S-$(GSGS)_2$-ERK DARPin and 6xHis-tagged mCerulean C49S-$(GSGS)_4$-ERK DARPin in pDST67 was adapted from the previous protocol [cite references]. *E.coli* strain I^q express (New England BioLabs) was transformed with various plasmids on LB-Agar plates containing 1% glucose and 50 µg/ml carbenicillin. A single fresh transformed colony was inoculated in 100 ml of LB medium containing 1% glucose and 50 µg/ml carbenicillin in a 250 ml sterile culture flask, and the culture was grown at 37 ^oC at 245 rpm on an orbital bacterial shaker overnight. The overnight culture was scaled up to 1 L medium in a 2 L sterile culture flask and grown at 37 ^oC at 245 rpm in an orbital bacterial shaker to an optical density at 600 nm of 0.7. Expression of ERK DARPin was conducted at 37 ^oC at 245 rpm for 5 hours in the presence of 0.5 mM IPTG, 1% glucose and 50 µg/ml carbenicillin. The bacteria pellets were collected by centrifugation at 4000 rpm at 4 ^oC for 20 min and stored at -80 ^oC.

Protein labeling Labeling reactions were conducted in the dark at room temperature for 1 hour on a rotary shaker by mixing 100 µl of 100 µM reduced MAPK proteins in protein labeling buffer and 3 µl of 20-30 mM cysteine-reactive dyes in DMF. Tested conjugatable dyes include **mero53**, **mero61**, **mero77**, **mero87**, **mero199** and **mero221**. The reactions were terminated by addition of 1 µL β-mercaptoethanol (BioRad) at room temperature for at least 10 minutes prior to separation. Excess dyes were removed by passing the reaction mixture through a pre-equilibrated Sephadex G-15 size-exclusion column (GE Healthcare). Concentration of the purified MAPK proteins were determined by using absorbance at 280 nm in protein labeling buffer and the theoretical extinction coefficients described earlier in the protein purification protocols; dye concentrations were then calculated using the extinction coefficients for each dye of interest in DMSO (140,000 $cm^{-1}M^{-1}$ for **mero53**, 93,750 $cm^{-1}M^{-1}$ for **mero61**, 12,3746 $cm^{-1}M^{-1}$ for **mero77**, 10,2520 $cm^{-1}M^{-1}$ for **mero87**, 190,000 $cm^{-1}M^{-1}$ for **mero199** and 140,000 $cm^{-1}M^{-1}$ for **mero221**). Dye-labeled proteins with labeling efficiency (dye concentration/protein concentration) greater than 100% were subjected to thermal denaturation on a heated sand bath, followed by SDS-PAGE; the relative amount of free dyes versus the amount of dye-labeled proteins were visualized by Typhoon 9410 gel and blot imager (GE Healthcare) and quantified by imageJ software.

Fluorescence titrations 50 nM dye-labeled MAPK in assay buffer (40 mM Tris, 0.08 mM EGTA, 20 mM $MgCl_2$, 0.08% v/v β-mercaptoethanol, 0.08 mg/ml bovine serum albumin, 0.05% v/v Brij-35, pH 7.5) was mixed with MAPKK proteins or other test proteins. 100 µl samples was prepared in 96-well black glass-bottom microplate (Costar) and dye emission intensity values were measured at 580/620 nm for excitation and emission on a microplate reader PHERAstar (BMG Labtech). ATP (Sigma-Aldrich) was added to the reaction mixture to make a final concentration of 0.25 mM and time-course of fluorescence change upon phosphorylation was monitored every five minutes. A solution containing the same biosensor concentration was measured to examine degrees of photobleaching or dequenching of dye excimers. Excitation and emission spectra of biosensor proteins were obtained using a SPEX Fluorolog 3 spectrometer.

In vitro kinase assays Kinase assays were conducted at 30^{o}C in heated water bath using 0.03 mg/ml wild type ELK-1, 0.03 mg/ml MAPK or dye-labeled MAPK, and 0.12 mg/ml active MEK1 (Millipore) or active MKK3ED in assay buffer (10 mM Tris, 1 mM dithiothreitol, 10 mM $MgCl_2$). 7 µl of sample was taken from a 30 µl reaction mixture at 0, 15, 30, 45 and 60 min and then diluted with 8 µl deionized water and 15 µl 2X gel loading buffer for SDS-PAGE.

SDS-PAGE and Western blot analysis Antibodies were all purchased from Cell Signaling. Samples separated by SDS-PAGE were transferred to a PVDF membrane in transfer buffer (25 mM Tris, 192 mM glycine, 20% MeOH, pH 8.3) using Panther Semi-dry Electroblotting System. Membranes were blocked with blocking solution (137 mM NaCl, 2.7 mM KCl, 10 mM Na_2HPO_4, 1.76 mM KH_2PO_4, 5% w/w milk, 3% w/w bovine serum albumin, pH 7.4) at room temperature for 1 hour or at 4^{o}C overnight. Membranes were then washed with TBST buffer (10 mM Tris, 150 mM NaCl, 0.1% v/v Tween-20, pH 7.6) three times and incubated in primary antibody solution at room temperature for 2 hours. Primary antibodies for ERK, ELK and p38 included mouse antibody for p42 MAPK (dilution 1:2000), rabbit antibody for phosphor-p44/42 MAPK (dilution 1:1000), rabbit antibody for ELK1 (dilution 1:1000), rabbit antibody for pS383 ELK1 (dilution 1:1000), rabbit antibody for p38 (dilution 1:1000) and rabbit antibody for phosphor-p38 (dilution 1:1000). The mouse p42 MAPK antibody was prepared in 5% milk in TBST; other antibodies were prepared in TBST containing 5% bovine serum album. The membranes were then washed with TBST buffer three times and incubated with secondary anti-rabbit-HRP (dilution 1:5000) or anti-mouse-HRP (dilution 1:5000) in 2.5% w/w milk in TBST at room temperature for 2 hours. Upon completion the membranes were washed three times with PBST buffer (137 mM NaCl, 2.7 mM KCl, 10 mM Na_2HPO_4, 1.76 mM KH_2PO_4, 0.1% v/v Tween-20, pH 7.4), incubated in TBST buffer at room temperature for 20 min, and dried over air. Labeled proteins were visualized using ECL western blotting substrates (Pierce) and a developer. Signals in each lane were quantified using imageJ software.

Cell culture NIH 3T3 mouse embryonic fibroblasts (MEF) were maintained in Dulbecco's modified Eagle's medium (DMEM, Cellgro) with 10% fetal bovine serum (HyClone, Thermo Scientific) and 2 mM GlutaMax (Gibco, Life Technologies) and grown in a 37 °C humidified incubator with 5% CO_2 atmosphere.

Microscopy The YPet MEF cells were plated on glass coverslips coated with fibronectin (Sigma-Aldrich) overnight. A bead loading method (425-600 microns, Sigma) was used to introduce the dye-labeled ERK or dye-labeled pET59RFD proteins (10 μl of 20 μM biosensor solution) into the YPet MEFs. Bead loaded cells were gently washed with 1 ml of phosphate saline buffer (DPBS) twice and recovered in 2ml of imaging medium in 37^oC incubator with $5\%CO_2$ for at least 30 min prior to imaging. For depleting endogenous phosphorylated ERK1/2 cells were pre-incubated with 10 μM U0126 in the culture serum containing 0.2% fetal bovine serum before bead loading. Imaging was conducted on a motorized inverted fluorescence microscope (IX81F-3, Olympus) equipped with a ZDC focus drift compensator (IX2-ZDC, Olympus), a cooled digital 14-bit CCD camera (CoolSnap ES-2, Roper Scientific), a 100 W mercury arc lamp and a 40X UPlanFLN 1.3 NA oil immersion objective. The microscope was controlled with MetaMorph imaging software (Molecule Devices). An ET-sputtered multi-band dichroic mirror (440/505/585, 89006, Chroma) was used with the band filters for YPet

(ET500/20X & ET535/30M, Chroma), **mero87** (HQ572/35X & ET632/60M, Chroma) and mCerulean (ET430/24X & ET470/24M). Images and movies were acquired and processed using the imaging routines previously described.

Estimation of solvent accessible surface area (SASA) per residue The crystal structures of inactive/unphosphorylated ERK2 (PDB: 1ERK) and active/phosphorylated ERK2 (PDB: 2ERK) and unphosphorylated p38β C119S/C162S (PDB: 3GC9) were used to calculate solvent-accessible surface area (SASA) values of each residue in proteins by Visual Molecular Dynamics (VMD), GetArea or ASAView software. The script for computing SASA values by VMD:

```
set allsel [atomselect top all]
set residlist [lsort -unique [$allsel get residue]]
foreach r $residlist {
  set sel [atomselect top "residue $r"]
  set rsasa [measure sasa 1.4 $allsel -restrict $sel]
  $sel set user $rsasa
  $sel delete
  puts "residue $r, sasa: $rsasa"
mol modcolor 0 [molinfo top] User
mol colupdate 0 [molinfo top] 1
mol scaleminmax [molinfo top] 0 auto
```

Estimation of relative protein stability of each ERK mutant The crystal structures of inactive ERK2 (PDB: 1ERK) and active ERK2 (PDB: 2ERK) were used for computation analysis of relative protein stabilities of ERK2 mutants. Effects of single point mutations in ERK2 were computed using i-Mutant Suites and Site-Directed Mutator (354). Protein stability free energy change (ΔΔG) and relative solvent accessible area caused by specified single-site mutations were both computed by SDM. Effects of multiple mutations on ERK2 were simulated using a web-based protein stability estimation program Eris (343, 344).

REFERENCES

1. Machacek M, Hodgson L, Welch C, Elliott H, Pertz O, Nalbant P, et al. Coordination of rho GTPase activities during cell protrusion. Nature. 2009 Sep 3;461(7260):99-103.

2. Ohashi K, Kiuchi T, Shoji K, Sampei K, Mizuno K. Visualization of cofilin-actin and ras-raf interactions by bimolecular fluorescence complementation assays using a new pair of split venus fragments. BioTechniques. 2012 Jan;52(1):45-50.

3. Shyu YJ, Suarez CD, Hu CD. Visualization of AP-1 NF-kappaB ternary complexes in living cells by using a BiFC-based FRET. Proc Natl Acad Sci U S A. 2008 Jan 8;105(1):151-6.

4. Grinberg AV, Hu CD, Kerppola TK. Visualization of myc/max/mad family dimers and the competition for dimerization in living cells. Mol Cell Biol. 2004 May;24(10):4294-308.

5. Kang MY, Kim HB, Piao C, Lee KH, Hyun JW, Chang IY, et al. The critical role of catalase in prooxidant and antioxidant function of p53. Cell Death Differ. 2012 Aug 24.

6. Kerppola TK. Visualization of molecular interactions using bimolecular fluorescence complementation analysis: Characteristics of protein fragment complementation. Chem Soc Rev. 2009 Oct;38(10):2876-8.

7. Newman RH, Fosbrink MD, Zhang J. Genetically encodable fluorescent biosensors for tracking signaling dynamics in living cells. Chem Rev. 2011 May 11;111(5):3614-66.

8. Hall B, McLean MA, Davis K, Casanova JE, Sligar SG, Schwartz MA. A fluorescence resonance energy transfer activation sensor for Arf6. Anal Biochem. 2008 Mar 15;374(2):243-9.

9. Aoki K, Matsuda M. Visualization of small GTPase activity with fluorescence resonance energy transfer-based biosensors. Nat Protoc. 2009;4(11):1623-31.

10. Kraynov VS, Chamberlain C, Bokoch GM, Schwartz MA, Slabaugh S, Hahn KM. Localized rac activation dynamics visualized in living cells. Science. 2000 Oct 13;290(5490):333-7.

11. Pertz O, Hodgson L, Klemke RL, Hahn KM. Spatiotemporal dynamics of RhoA activity in migrating cells. Nature. 2006 Apr 20;440(7087):1069-72.

12. Kalab P, Soderholm J. The design of forster (fluorescence) resonance energy transfer (FRET)-based molecular sensors for ran GTPase. Methods. 2010 Jun;51(2):220-32.

13. Brumbaugh J, Schleifenbaum A, Gasch A, Sattler M, Schultz C. A dual parameter FRET probe for measuring PKC and PKA activity in living cells. J Am Chem Soc. 2006 Jan 11;128(1):24-5.

14. Carrillo LD, Froemming JA, Mahal LK. Targeted in vivo O-GlcNAc sensors reveal discrete compartment-specific dynamics during signal transduction. J Biol Chem. 2011 Feb 25;286(8):6650-8.

15. Green HM, Alberola-Ila J. Development of ERK activity sensor, an in vitro, FRET-based sensor of extracellular regulated kinase activity. BMC Chem Biol. 2005 Jul 5;5:1.

16. Fosbrink M, Aye-Han NN, Cheong R, Levchenko A, Zhang J. Visualization of JNK activity dynamics with a genetically encoded fluorescent biosensor. Proc Natl Acad Sci U S A. 2010 Mar 23;107(12):5459-64.

17. Harvey CD, Ehrhardt AG, Cellurale C, Zhong H, Yasuda R, Davis RJ, et al. A genetically encoded fluorescent sensor of ERK activity. Proc Natl Acad Sci U S A. 2008 Dec 9;105(49):19264-9.

18. Lin CW, Jao CY, Ting AY. Genetically encoded fluorescent reporters of histone methylation in living cells. J Am Chem Soc. 2004 May 19;126(19):5982-3.

19. Seong J, Ouyang M, Kim T, Sun J, Wen PC, Lu S, et al. Detection of focal adhesion kinase activation at membrane microdomains by fluorescence resonance energy transfer. Nat Commun. 2011 Jul 26;2:406.

20. Sato M, Kawai Y, Umezawa Y. Genetically encoded fluorescent indicators to visualize protein phosphorylation by extracellular signal-regulated kinase in single living cells. Anal Chem. 2007 Mar 15;79(6):2570-5.

21. Ting AY, Kain KH, Klemke RL, Tsien RY. Genetically encoded fluorescent reporters of protein tyrosine kinase activities in living cells. Proc Natl Acad Sci U S A. 2001 Dec 18;98(26):15003-8.

22. Violin JD, Zhang J, Tsien RY, Newton AC. A genetically encoded fluorescent reporter reveals oscillatory phosphorylation by protein kinase C. J Cell Biol. 2003 Jun 9;161(5):899-90.

23. Wang Y, Botvinick EL, Zhao Y, Berns MW, Usami S, Tsien RY, et al. Visualizing the mechanical activation of src. Nature. 2005 Apr 21;434(7036):1040-5.

24. Ward MW, Rehm M, Duessmann H, Kacmar S, Concannon CG, Prehn JH. Real time single cell analysis of bid cleavage and bid translocation during caspase-dependent and neuronal caspase-independent apoptosis. J Biol Chem. 2006 Mar 3;281(9):5837-44.

25. DiPilato LM, Cheng X, Zhang J. Fluorescent indicators of cAMP and epac activation reveal differential dynamics of cAMP signaling within discrete subcellular compartments. Proc Natl Acad Sci U S A. 2004 Nov 23;101(47):16513-8.

26. Ding Y, Ai HW, Hoi H, Campbell RE. Forster resonance energy transfer-based biosensors for multiparameter ratiometric imaging of Ca2+ dynamics and caspase-3 activity in single cells. Anal Chem. 2011 Dec 15;83(24):9687-93.

27. Miyawaki A, Llopis J, Heim R, McCaffery JM, Adams JA, Ikura M, et al. Fluorescent indicators for Ca2+ based on green fluorescent proteins and calmodulin. Nature. 1997 Aug 28;388(6645):882-7.

28. Nikolaev VO, Gambaryan S, Lohse MJ. Fluorescent sensors for rapid monitoring of intracellular cGMP. Nat Methods. 2006 Jan;3(1):23-5.

29. Okumoto S, Looger LL, Micheva KD, Reimer RJ, Smith SJ, Frommer WB. Detection of glutamate release from neurons by genetically encoded surface-displayed FRET nanosensors. Proc Natl Acad Sci U S A. 2005 Jun 14;102(24):8740-5.

30. Truong K, Sawano A, Mizuno H, Hama H, Tong KI, Mal TK, et al. FRET-based in vivo Ca2+ imaging by a new calmodulin-GFP fusion molecule. Nat Struct Biol. 2001 Dec;8(12):1069-73.

31. Lu J, Zhang Z, Yang J, Chu J, Li P, Zeng S, et al. Visualization of beta-secretase cleavage in living cells using a genetically encoded surface-displayed [corrected] FRET probe. Biochem Biophys Res Commun. 2007 Oct 12;362(1):25-30.

32. Fujioka A, Terai K, Itoh RE, Aoki K, Nakamura T, Kuroda S, et al. Dynamics of the ras/ERK MAPK cascade as monitored by fluorescent probes. J Biol Chem. 2006 Mar 31;281(13):8917-26.

33. Akerboom J, Chen TW, Wardill TJ, Tian L, Marvin JS, Mutlu S, et al. Optimization of a GCaMP calcium indicator for neural activity imaging. J Neurosci. 2012 Oct 3;32(40):13819-40.

34. Marvin JS, Schreiter ER, Echevarria IM, Looger LL. A genetically encoded, high-signal-to-noise maltose sensor. Proteins. 2011 Nov;79(11):3025-36.

35. Shyu YJ, Suarez CD, Hu CD. Visualization of ternary complexes in living cells by using a BiFC-based FRET assay. Nat Protoc. 2008;3(11):1693-702.

36. Shu X, Royant A, Lin MZ, Aguilera TA, Lev-Ram V, Steinbach PA, et al. Mammalian expression of infrared fluorescent proteins engineered from a bacterial phytochrome. Science. 2009 May 8;324(5928):804-7.

37. Filonov GS, Piatkevich KD, Ting LM, Zhang J, Kim K, Verkhusha VV. Bright and stable near-infrared fluorescent protein for in vivo imaging. Nat Biotechnol. 2011 Jul 17;29(8):757-61.

38. Lavis LD, Raines RT. Bright ideas for chemical biology. ACS Chem Biol. 2008 Mar 20;3(3):142-55.

39. Loving GS, Sainlos M, Imperiali B. Monitoring protein interactions and dynamics with solvatochromic fluorophores. Trends Biotechnol. 2010 Feb;28(2):73-8.

40. Mie M, Naoki T, Uchida K, Kobatake E. Development of a split SNAP-tag protein complementation assay for visualization of protein-protein interactions in living cells. Analyst. 2012 Sep 17;137(20):4760-5.

41. Hahn KM, Waggoner AS, Taylor DL. A calcium-sensitive fluorescent analog of calmodulin based on a novel calmodulin-binding fluorophore. J Biol Chem. 1990 Nov 25;265(33):20335-4.

42. Hahn K, DeBiasio R, Taylor DL. Patterns of elevated free calcium and calmodulin activation in living cells. Nature. 1992 Oct 22;359(6397):736-8.

43. Garrett SC, Hodgson L, Rybin A, Toutchkine A, Hahn KM, Lawrence DS, et al. A biosensor of S100A4 metastasis factor activation: Inhibitor screening and cellular activation dynamics. Biochemistry. 2008 Jan 22;47(3):986-9.

44. Nalbant P, Hodgson L, Kraynov V, Toutchkine A, Hahn KM. Activation of endogenous Cdc42 visualized in living cells. Science. 2004 Sep 10;305(5690):1615-9.

45. Toutchkine A, Kraynov V, Hahn K. Solvent-sensitive dyes to report protein conformational changes in living cells. J Am Chem Soc. 2003 Apr 9;125(14):4132-45.

46. Gulyani A, Vitriol E, Allen R, Wu J, Gremyachinskiy D, Lewis S, et al. A biosensor generated via high-throughput screening quantifies cell edge src dynamics. Nat Chem Biol. 2011 Jun 12;7(7):437-44.

47. Demchenko AP, Mely Y, Duportail G, Klymchenko AS. Monitoring biophysical properties of lipid membranes by environment-sensitive fluorescent probes. Biophys J. 2009 May 6;96(9):3461-70.

48. Choulier L, Enander K. Environmentally sensitive fluorescent sensors based on synthetic peptides. Sensors (Basel). 2010;10(4):3126-44.

49. Stains CI, Lukovic E, Imperiali B. A p38alpha-selective chemosensor for use in unfractionated cell lysates. ACS Chem Biol. 2011 Jan 21;6(1):101-5.

50. Goguen BN, Loving GS, Imperiali B. Development of a fluorogenic sensor for activated Cdc42. Bioorg Med Chem Lett. 2011 Sep 1;21(17):5058-61.

51. Loving G, Imperiali B. Thiol-reactive derivatives of the solvatochromic 4-N,N-dimethylamino-1,8-naphthalimide fluorophore: A highly sensitive toolset for the detection of biomolecular interactions. Bioconjug Chem. 2009 Nov;20(11):2133-41.

52. Simard JR, Getlik M, Grutter C, Pawar V, Wulfert S, Rabiller M, et al. Development of a fluorescent-tagged kinase assay system for the detection and characterization of allosteric kinase inhibitors. J Am Chem Soc. 2009 Sep 23;131(37):13286-9.

53. Hansen SB, Radic' Z, Talley TT, Molles BE, Deerinck T, Tsigelny I, et al. Tryptophan fluorescence reveals conformational changes in the acetylcholine binding protein. J Biol Chem. 2002 Nov 1;277(44):41299-302.

54. Yengo CM, Chrin L, Rovner AS, Berger CL. Intrinsic tryptophan fluorescence identifies specific conformational changes at the actomyosin interface upon actin binding and ADP release. Biochemistry. 1999 Nov 2;38(44):14515-23.

55. Loving GS, Sainlos M, Imperiali B. Monitoring protein interactions and dynamics with solvatochromic fluorophores. Trends Biotechnol. 2010 Feb;28(2):73-8.

56. Toutchkine A, Nguyen DV, Hahn KM. Merocyanine dyes with improved photostability. Org Lett. 2007 Jul 19;9(15):2775-7.

57. Toutchkine A, Han WG, Ullmann M, Liu T, Bashford D, Noodleman L, et al. Experimental and DFT studies: Novel structural modifications greatly enhance the solvent sensitivity of live cell imaging dyes. J Phys Chem A. 2007 Oct 25;111(42):10849-60.

58. Toutchkine A, Nguyen DV, Hahn KM. Simple one-pot preparation of water-soluble, cysteine-reactive cyanine and merocyanine dyes for biological imaging. Bioconjug Chem. 2007 Jul-Aug;18(4):1344-8.

59. Karatan E, Merguerian M, Han Z, Scholle MD, Koide S, Kay BK. Molecular recognition properties of FN3 monobodies that bind the src SH3 domain. Chem Biol. 2004 Jun;11(6):835-44.

60. Uttamapinant C, White KA, Baruah H, Thompson S, Fernandez-Suarez M, Puthenveetil S, et al. A fluorophore ligase for site-specific protein labeling inside living cells. Proc Natl Acad Sci U S A. 2010 Jun 15;107(24):10914-9.

61. Sun X, Zhang A, Baker B, Sun L, Howard A, Buswell J, et al. Development of SNAP-tag fluorogenic probes for wash-free fluorescence imaging. Chembiochem. 2011 Sep 19;12(14):2217-26.

62. Slavoff SA, Liu DS, Cohen JD, Ting AY. Imaging protein-protein interactions inside living cells via interaction-dependent fluorophore ligation. J Am Chem Soc. 2011 Dec 14;133(49):19769-76.

63. Romanini DW, Cornish VW. Protein labelling: Playing tag with proteins. Nat Chem. 2012 Mar 22;4(4):248-50.

64. Rabuka D, Rush JS, deHart GW, Wu P, Bertozzi CR. Site-specific chemical protein conjugation using genetically encoded aldehyde tags. Nat Protoc. 2012 May 10;7(6):1052-67.

65. Lukinavicius G, Johnsson K. Switchable fluorophores for protein labeling in living cells. Curr Opin Chem Biol. 2011 Dec;15(6):768-74.

66. Keppler A, Pick H, Arrivoli C, Vogel H, Johnsson K. Labeling of fusion proteins with synthetic fluorophores in live cells. Proc Natl Acad Sci U S A. 2004 Jul 6;101(27):9955-9.

67. Liu DS, Tangpeerachaikul A, Selvaraj R, Taylor MT, Fox JM, Ting AY. Diels-alder cycloaddition for fluorophore targeting to specific proteins inside living cells. J Am Chem Soc. 2012 Jan 18;134(2):792-5.

68. Keppler A, Gendreizig S, Gronemeyer T, Pick H, Vogel H, Johnsson K. A general method for the covalent labeling of fusion proteins with small molecules in vivo. Nat Biotechnol. 2003 Jan;21(1):86-9.

69. Jing C, Cornish VW. Chemical tags for labeling proteins inside living cells. Acc Chem Res. 2011 Sep 20;44(9):784-92.

70. Jin X, Uttamapinant C, Ting AY. Synthesis of 7-aminocoumarin by buchwald-hartwig cross coupling for specific protein labeling in living cells. Chembiochem. 2011 Jan 3;12(1):65-70.

71. Beatty KE, Fisk JD, Smart BP, Lu YY, Szychowski J, Hangauer MJ, et al. Live-cell imaging of cellular proteins by a strain-promoted azide-alkyne cycloaddition. Chembiochem. 2010 Oct 18;11(15):2092-5.

72. Bertozzi CR. A decade of bioorthogonal chemistry. Acc Chem Res. 2011 Sep 20;44(9):651-3.

73. Chen Z, Jing C, Gallagher SS, Sheetz MP, Cornish VW. Second-generation covalent TMP-tag for live cell imaging. J Am Chem Soc. 2012 Aug 22;134(33):13692-9.

74. Cohen JD, Thompson S, Ting AY. Structure-guided engineering of a pacific blue fluorophore ligase for specific protein imaging in living cells. Biochemistry. 2011 Sep 27;50(38):8221-5.

75. Dieterich DC. Chemical reporters for the illumination of protein and cell dynamics. Curr Opin Neurobiol. 2010 Oct;20(5):623-30.

76. Gatzogiannis E, Chen Z, Wei L, Wombacher R, Kao YT, Yefremov G, et al. Mapping protein-specific micro-environments in live cells by fluorescence lifetime imaging of a hybrid genetic-chemical molecular rotor tag. Chem Commun (Camb). 2012 Sep 7;48(69):8694-6.

77. Gautier A, Juillerat A, Heinis C, Correa IR,Jr, Kindermann M, Beaufils F, et al. An engineered protein tag for multiprotein labeling in living cells. Chem Biol. 2008 Feb;15(2):128-36.

78. Hangauer MJ, Bertozzi CR. A FRET-based fluorogenic phosphine for live-cell imaging with the staudinger ligation. Angew Chem Int Ed Engl. 2008;47(13):2394-7.

79. Hudak JE, Barfield RM, de Hart GW, Grob P, Nogales E, Bertozzi CR, et al. Synthesis of heterobifunctional protein fusions using copper-free click chemistry and the aldehyde tag. Angew Chem Int Ed Engl. 2012 Apr 23;51(17):4161-5.

80. Lim RK, Lin Q. Photoinducible bioorthogonal chemistry: A spatiotemporally controllable tool to visualize and perturb proteins in live cells. Acc Chem Res. 2011 Sep 20;44(9):828-39.

81. Sletten EM, Bertozzi CR. A bioorthogonal quadricyclane ligation. J Am Chem Soc. 2011 Nov 9;133(44):17570-3.

82. Uttamapinant C, Tangpeerachaikul A, Grecian S, Clarke S, Singh U, Slade P, et al. Fast, cell-compatible click chemistry with copper-chelating azides for biomolecular labeling. Angew Chem Int Ed Engl. 2012 Jun 11;51(24):5852-6.

83. Yao JZ, Uttamapinant C, Poloukhtine A, Baskin JM, Codelli JA, Sletten EM, et al. Fluorophore targeting to cellular proteins via enzyme-mediated azide ligation and strain-promoted cycloaddition. J Am Chem Soc. 2012 Feb 29;134(8):3720-8.

84. Chen I, Ting AY. Site-specific labeling of proteins with small molecules in live cells. Curr Opin Biotechnol. 2005 Feb;16(1):35-40.

85. White AG, Gray BD, Pak KY, Smith BD. Deep-red fluorescent imaging probe for bacteria. Bioorg Med Chem Lett. 2012 Apr 15;22(8):2833-6.

86. Kiyose K, Hanaoka K, Oushiki D, Nakamura T, Kajimura M, Suematsu M, et al. Hypoxia-sensitive fluorescent probes for in vivo real-time fluorescence imaging of acute ischemia. J Am Chem Soc. 2010 Nov 17;132(45):15846-8.

87. Okuda K, Okabe Y, Kadonosono T, Ueno T, Youssif BG, Kizaka-Kondoh S, et al. 2-nitroimidazole-tricarbocyanine conjugate as a near-infrared fluorescent probe for in vivo imaging of tumor hypoxia. Bioconjug Chem. 2012 Mar 21;23(3):324-9.

88. Yuan L, Lin W, Yang Y, Chen H. A unique class of near-infrared functional fluorescent dyes with carboxylic-acid-modulated fluorescence ON/OFF switching: Rational design, synthesis, optical properties, theoretical calculations, and applications for fluorescence imaging in living animals. J Am Chem Soc. 2012 Jan 18;134(2):1200-11.

89. Myochin T, Kiyose K, Hanaoka K, Kojima H, Terai T, Nagano T. Rational design of ratiometric near-infrared fluorescent pH probes with various pKa values, based on aminocyanine. J Am Chem Soc. 2011 Mar 16;133(10):3401-9.

90. Tang B, Cui LJ, Xu KH, Tong LL, Yang GW, An LG. A sensitive and selective near-infrared fluorescent probe for mercuric ions and its biological imaging applications. Chembiochem. 2008 May 5;9(7):1159-64.

91. Cao X, Lin W, Wan W. Development of a near-infrared fluorescent probe for imaging of endogenous cu+ in live cells. Chem Commun (Camb). 2012 Jun 25;48(50):6247-9.

92. Xu K, Wang L, Qiang M, Wang L, Li P, Tang B. A selective near-infrared fluorescent probe for singlet oxygen in living cells. Chem Commun (Camb). 2011 Jul 14;47(26):7386-8.

93. Xu K, Sun S, Li J, Li L, Qiang M, Tang B. A near-infrared fluorescent probe for monitoring ozone and imaging in living cells. Chem Commun (Camb). 2012 Jan 18;48(5):684-6.

94. Xu K, Chen H, Tian J, Ding B, Xie Y, Qiang M, et al. A near-infrared reversible fluorescent probe for peroxynitrite and imaging of redox cycles in living cells. Chem Commun (Camb). 2011 Sep 7;47(33):9468-70.

95. Tian J, Chen H, Zhuo L, Xie Y, Li N, Tang B. A highly selective, cell-permeable fluorescent nanoprobe for ratiometric detection and imaging of peroxynitrite in living cells. Chemistry. 2011 Jun 6;17(24):6626-34.

96. Lord SJ, Conley NR, Lee HL, Nishimura SY, Pomerantz AK, Willets KA, et al. DCDHF fluorophores for single-molecule imaging in cells. Chemphyschem. 2009 Jan 12;10(1):55-6.

97. Lord SJ, Lu Z, Wang H, Willets KA, Schuck PJ, Lee HL, et al. Photophysical properties of acene DCDHF fluorophores: Long-wavelength single-molecule emitters designed for cellular imaging. J Phys Chem A. 2007 Sep 20;111(37):8934-41.

98. Wang H, Lu Z, Lord SJ, Moerner WE, Twieg RJ. Modifications of DCDHF single molecule fluorophores to impart water solubility. Tetrahedron Lett. 2007 May 7;48(19):3471-4.

99. Yin S, Yuan W, Huang J, Xie D, Liu B, Jiang K, et al. A BODIPY derivative as a colorimetric, near-infrared and turn-on chemosensor for cu(2+). Spectrochim Acta A Mol Biomol Spectrosc. 2012 Oct;96:82-8.

100. Myochin T, Hanaoka K, Komatsu T, Terai T, Nagano T. Design strategy for a near-infrared fluorescence probe for matrix metalloproteinase utilizing highly cell permeable boron dipyrromethene. J Am Chem Soc. 2012 Aug 22;134(33):13730-7.

101. Yu C, Xu Y, Jiao L, Zhou J, Wang Z, Hao E. Isoindole-BODIPY dyes as red to near-infrared fluorophores. Chemistry. 2012 May 21;18(21):6437-42.

102. Hu R, Gomez-Duran CF, Lam JW, Belmonte-Vazquez JL, Deng C, Chen S, et al. Synthesis, solvatochromism, aggregation-induced emission and cell imaging of tetraphenylethene-containing BODIPY derivatives with large stokes shifts. Chem Commun (Camb). 2012 Sep 17;48(81):10099-101.

103. Domaille DW, Zeng L, Chang CJ. Visualizing ascorbate-triggered release of labile copper within living cells using a ratiometric fluorescent sensor. J Am Chem Soc. 2010 Feb 3;132(4):1194-5.

104. Yang Y, Lowry M, Xu X, Escobedo JO, Sibrian-Vazquez M, Wong L, et al. Seminaphthofluorones are a family of water-soluble, low molecular weight, NIR-emitting fluorophores. Proc Natl Acad Sci U S A. 2008 Jul 1;105(26):8829-34.

105. Koide Y, Urano Y, Hanaoka K, Terai T, Nagano T. Evolution of group 14 rhodamines as platforms for near-infrared fluorescence probes utilizing photoinduced electron transfer. ACS Chem Biol. 2011 Jun 17;6(6):600-8.

106. Egawa T, Hanaoka K, Koide Y, Ujita S, Takahashi N, Ikegaya Y, et al. Development of a far-red to near-infrared fluorescence probe for calcium ion and its application to multicolor neuronal imaging. J Am Chem Soc. 2011 Sep 14;133(36):14157-9.

107. Koide Y, Urano Y, Hanaoka K, Terai T, Nagano T. Development of an si-rhodamine-based far-red to near-infrared fluorescence probe selective for hypochlorous acid and its applications for biological imaging. J Am Chem Soc. 2011 Apr 20;133(15):5680-2.

108. Koide Y, Urano Y, Hanaoka K, Piao W, Kusakabe M, Saito N, et al. Development of NIR fluorescent dyes based on si-rhodamine for in vivo imaging. J Am Chem Soc. 2012 Mar 21;134(11):5029-31.

109. Funabiki K, Mase H, Saito Y, Otsuka A, Hibino A, Tanaka N, et al. Design of NIR-absorbing simple asymmetric squaraine dyes carrying indoline moieties for use in dye-sensitized solar cells with pt-free electrodes. Org Lett. 2012 Mar 2;14(5):1246-9.

110. Zimmerman JD, Xiao X, Renshaw CK, Wang S, Diev VV, Thompson ME, et al. Independent control of bulk and interfacial morphologies of small molecular weight organic heterojunction solar cells. Nano Lett. 2012 Aug 8;12(8):4366-71.

111. Chang CH, Chen YC, Hsu CY, Chou HH, Lin JT. Squaraine-arylamine sensitizers for highly efficient p-type dye-sensitized solar cells. Org Lett. 2012 Sep 21;14(18):4726-9.

112. Chen G, Sasabe H, Wang Z, Wang X, Hong Z, Kido J, et al. Solution-processed organic photovoltaic cells based on a squaraine dye. Phys Chem Chem Phys. 2012 Nov 14;14(42):14661-6.

113. Oushiki D, Kojima H, Takahashi Y, Komatsu T, Terai T, Hanaoka K, et al. Near-infrared fluorescence probes for enzymes based on binding affinity modulation of squarylium dye scaffold. Anal Chem. 2012 May 15;84(10):4404-10.

114. Johnson JR, Fu N, Arunkumar E, Leevy WM, Gammon ST, Piwnica-Worms D, et al. Squaraine rotaxanes: Superior substitutes for cy-5 in molecular probes for near-infrared fluorescence cell imaging. Angew Chem Int Ed Engl. 2007;46(29):5528-31.

115. Burckstummer H, Kronenberg NM, Meerholz K, Wurthner F. Near-infrared absorbing merocyanine dyes for bulk heterojunction solar cells. Org Lett. 2010 Aug 20;12(16):3666-9.

116. Ishchenko AA, Kulinich AV, Bondarev SL, Knyukshto VN. Photodynamics of polyene-polymethine transformations and spectral fluorescent properties of merocyanine dyes. J Phys Chem A. 2007 Dec 27;111(51):13629-37.

117. Hinde E, Digman MA, Welch C, Hahn KM, Gratton E. Biosensor forster resonance energy transfer detection by the phasor approach to fluorescence lifetime imaging microscopy. Microsc Res Tech. 2012 Mar;75(3):271-8.

118. Wu YI, Frey D, Lungu OI, Jaehrig A, Schlichting I, Kuhlman B, et al. A genetically encoded photoactivatable rac controls the motility of living cells. Nature. 2009 Sep 3;461(7260):104-8.

119. Cheng ZJ, Singh RD, Holicky EL, Wheatley CL, Marks DL, Pagano RE. Co-regulation of caveolar and Cdc42-dependent fluid phase endocytosis by phosphocaveolin-1. J Biol Chem. 2010 May 14;285(20):15119-25.

120. Davis GE, Bayless KJ. An integrin and rho GTPase-dependent pinocytic vacuole mechanism controls capillary lumen formation in collagen and fibrin matrices. Microcirculation. 2003 Jan;10(1):27-44.

121. Garrett WS, Chen LM, Kroschewski R, Ebersold M, Turley S, Trombetta S, et al. Developmental control of endocytosis in dendritic cells by Cdc42. Cell. 2000 Aug 4;102(3):325-34.

122. Mettlen M, Platek A, Van Der Smissen P, Carpentier S, Amyere M, Lanzetti L, et al. Src triggers circular ruffling and macropinocytosis at the apical surface of polarized MDCK cells. Traffic. 2006 May;7(5):589-603.

123. Sabharanjak S, Sharma P, Parton RG, Mayor S. GPI-anchored proteins are delivered to recycling endosomes via a distinct cdc42-regulated, clathrin-independent pinocytic pathway. Dev Cell. 2002 Apr;2(4):411-23.

124. Veithen A, Cupers P, Baudhuin P, Courtoy PJ. V-src induces constitutive macropinocytosis in rat fibroblasts. J Cell Sci. 1996 Aug;109 (Pt 8)(Pt 8):2005-12.

125. Veithen A, Amyere M, Van Der Smissen P, Cupers P, Courtoy PJ. Regulation of macropinocytosis in v-src-transformed fibroblasts: Cyclic AMP selectively promotes regurgitation of macropinosomes. J Cell Sci. 1998 Aug;111 (Pt 16)(Pt 16):2329-35.

126. Marco E, Wedlich-Soldner R, Li R, Altschuler SJ, Wu LF. Endocytosis optimizes the dynamic localization of membrane proteins that regulate cortical polarity. Cell. 2007 Apr 20;129(2):411-22.

127. Szczur K, Xu H, Atkinson S, Zheng Y, Filippi MD. Rho GTPase CDC42 regulates directionality and random movement via distinct MAPK pathways in neutrophils. Blood. 2006 Dec 15;108(13):4205-13.

128. Fincham VJ, James M, Frame MC, Winder SJ. Active ERK/MAP kinase is targeted to newly forming cell-matrix adhesions by integrin engagement and v-src. EMBO J. 2000 Jun 15;19(12):2911-23.

129. Schlaepfer DD, Mitra SK, Ilic D. Control of motile and invasive cell phenotypes by focal adhesion kinase. Biochim Biophys Acta. 2004 Jul 5;1692(2-3):77-102.

130. Schlaepfer DD, Mitra SK. Multiple connections link FAK to cell motility and invasion. Curr Opin Genet Dev. 2004 Feb;14(1):92-101.

131. Ishibe S, Joly D, Zhu X, Cantley LG. Phosphorylation-dependent paxillin-ERK association mediates hepatocyte growth factor-stimulated epithelial morphogenesis. Mol Cell. 2003 Nov;12(5):1275-8.

132. Webb DJ, Donais K, Whitmore LA, Thomas SM, Turner CE, Parsons JT, et al. FAK-src signalling through paxillin, ERK and MLCK regulates adhesion disassembly. Nat Cell Biol. 2004 Feb;6(2):154-61.

133. DerMardirossian C, Rocklin G, Seo JY, Bokoch GM. Phosphorylation of RhoGDI by src regulates rho GTPase binding and cytosol-membrane cycling. Mol Biol Cell. 2006 Nov;17(11):4760-8.

134. Dovas A, Couchman JR. RhoGDI: Multiple functions in the regulation of rho family GTPase activities. Biochem J. 2005 Aug 15;390(Pt 1):1-9.

135. Johnson JL, Erickson JW, Cerione RA. New insights into how the rho guanine nucleotide dissociation inhibitor regulates the interaction of Cdc42 with membranes. J Biol Chem. 2009 Aug 28;284(35):23860-71.

136. Tu S, Wu WJ, Wang J, Cerione RA. Epidermal growth factor-dependent regulation of Cdc42 is mediated by the src tyrosine kinase. J Biol Chem. 2003 Dec 5;278(49):49293-300.

137. Murata T, Ohnishi H, Okazawa H, Murata Y, Kusakari S, Hayashi Y, et al. CD47 promotes neuronal development through src- and FRG/Vav2-mediated activation of rac and Cdc42. J Neurosci. 2006 Nov 29;26(48):12397-40.

138. Feng Q, Baird D, Peng X, Wang J, Ly T, Guan JL, et al. Cool-1 functions as an essential regulatory node for EGF receptor- and src-mediated cell growth. Nat Cell Biol. 2006 Sep;8(9):945-56.

139. Fukuhara T, Shimizu K, Kawakatsu T, Fukuyama T, Minami Y, Honda T, et al. Activation of Cdc42 by trans interactions of the cell adhesion molecules nectins through c-src and Cdc42-GEF FRG. J Cell Biol. 2004 Aug 2;166(3):393-405.

140. Owens DM, Keyse SM. Differential regulation of MAP kinase signalling by dual-specificity protein phosphatases. Oncogene. 2007 May 14;26(22):3203-1.

141. Zhang J, Zhou B, Zheng CF, Zhang ZY. A bipartite mechanism for ERK2 recognition by its cognate regulators and substrates. J Biol Chem. 2003 Aug 8;278(32):29901-12.

142. Tanoue T, Adachi M, Moriguchi T, Nishida E. A conserved docking motif in MAP kinases common to substrates, activators and regulators. Nat Cell Biol. 2000 Feb;2(2):110-6.

143. Tanoue T, Maeda R, Adachi M, Nishida E. Identification of a docking groove on ERK and p38 MAP kinases that regulates the specificity of docking interactions. EMBO J. 2001 Feb 1;20(3):466-79.

144. Tanoue T, Nishida E. Molecular recognitions in the MAP kinase cascades. Cell Signal. 2003 May;15(5):455-62.

145. Tanoue T, Nishida E. Docking interactions in the mitogen-activated protein kinase cascades. Pharmacol Ther. 2002 Feb-Mar;93(2-3):193-202.

146. Xu B, Stippec S, Robinson FL, Cobb MH. Hydrophobic as well as charged residues in both MEK1 and ERK2 are important for their proper docking. J Biol Chem. 2001 Jul 13;276(28):26509-15.

147. Zhang F, Strand A, Robbins D, Cobb MH, Goldsmith EJ. Atomic structure of the MAP kinase ERK2 at 2.3 A resolution. Nature. 1994 Feb 24;367(6465):704-11.

148. Huang C, Jacobson K, Schaller MD. MAP kinases and cell migration. J Cell Sci. 2004 Sep 15;117(Pt 20):4619-28.

149. Danson CM, Pocha SM, Bloomberg GB, Cory GO. Phosphorylation of WAVE2 by MAP kinases regulates persistent cell migration and polarity. J Cell Sci. 2007 Dec 1;120(Pt 23):4144-5.

150. Jia D, Gomez TS, Metlagel Z, Umetani J, Otwinowski Z, Rosen MK, et al. WASH and WAVE actin regulators of the wiskott-aldrich syndrome protein (WASP) family are controlled by analogous structurally related complexes. Proc Natl Acad Sci U S A. 2010 Jun 8;107(23):10442-7.

151. Takahashi K, Suzuki K. Membrane transport of WAVE2 and lamellipodia formation require Pak1 that mediates phosphorylation and recruitment of stathmin/Op18 to Pak1-WAVE2-kinesin complex. Cell Signal. 2009 May;21(5):695-703.

152. Takenawa T, Suetsugu S. The WASP-WAVE protein network: Connecting the membrane to the cytoskeleton. Nat Rev Mol Cell Biol. 2007 Jan;8(1):37-48.

153. Lopez-Bergami P, Huang C, Goydos JS, Yip D, Bar-Eli M, Herlyn M, et al. Rewired ERK-JNK signaling pathways in melanoma. Cancer Cell. 2007 May;11(5):447-60.

154. Carragher NO, Frame MC. Focal adhesion and actin dynamics: A place where kinases and proteases meet to promote invasion. Trends Cell Biol. 2004 May;14(5):241-9.

155. Carragher NO, Westhoff MA, Fincham VJ, Schaller MD, Frame MC. A novel role for FAK as a protease-targeting adaptor protein: Regulation by p42 ERK and src. Curr Biol. 2003 Aug 19;13(16):1442-50.

156. Tomar A, Schlaepfer DD. Focal adhesion kinase: Switching between GAPs and GEFs in the regulation of cell motility. Curr Opin Cell Biol. 2009 Oct;21(5):676-83.

157. Cuevas BD, Abell AN, Witowsky JA, Yujiri T, Johnson NL, Kesavan K, et al. MEKK1 regulates calpain-dependent proteolysis of focal adhesion proteins for rear-end detachment of migrating fibroblasts. EMBO J. 2003 Jul 1;22(13):3346-55.

158. Doshi BM, Hightower LE, Lee J. The role of Hsp27 and actin in the regulation of movement in human cancer cells responding to heat shock. Cell Stress Chaperones. 2009 Sep;14(5):445-57.

159. Xu L, Chen S, Bergan RC. MAPKAPK2 and HSP27 are downstream effectors of p38 MAP kinase-mediated matrix metalloproteinase type 2 activation and cell invasion in human prostate cancer. Oncogene. 2006 May 18;25(21):2987-98.

160. Beeram M, Patnaik A, Rowinsky EK. Raf: A strategic target for therapeutic development against cancer. J Clin Oncol. 2005 Sep 20;23(27):6771-90.

161. Duncan JS, Whittle MC, Nakamura K, Abell AN, Midland AA, Zawistowski JS, et al. Dynamic reprogramming of the kinome in response to targeted MEK inhibition in triple-negative breast cancer. Cell. 2012 Apr 13;149(2):307-21.

162. Fu P, Liang GJ, Khot SS, Phan R, Bach LA. Cross-talk between MAP kinase pathways is involved in IGF-independent, IGFBP-6-induced Rh30 rhabdomyosarcoma cell migration. J Cell Physiol. 2010 Sep;224(3):636-43.

163. Matallanas D, Birtwistle M, Romano D, Zebisch A, Rauch J, von Kriegsheim A, et al. Raf family kinases: Old dogs have learned new tricks. Genes Cancer. 2011 Mar;2(3):232-60.

164. Roskoski R,Jr. MEK1/2 dual-specificity protein kinases: Structure and regulation. Biochem Biophys Res Commun. 2012 Jan 6;417(1):5-10.

165. Roux PP, Shahbazian D, Vu H, Holz MK, Cohen MS, Taunton J, et al. RAS/ERK signaling promotes site-specific ribosomal protein S6 phosphorylation via RSK and stimulates cap-dependent translation. J Biol Chem. 2007 May 11;282(19):14056-64.

166. Sebolt-Leopold JS. Advances in the development of cancer therapeutics directed against the RAS-mitogen-activated protein kinase pathway. Clin Cancer Res. 2008 Jun 15;14(12):3651-6.

167. Shaul YD, Seger R. The MEK/ERK cascade: From signaling specificity to diverse functions. Biochim Biophys Acta. 2007 Aug;1773(8):1213-26.

168. Fremin C, Meloche S. From basic research to clinical development of MEK1/2 inhibitors for cancer therapy. J Hematol Oncol. 2010 Feb 11;3:8.

169. Zheng CF, Guan KL. Cytoplasmic localization of the mitogen-activated protein kinase activator MEK. J Biol Chem. 1994 Aug 5;269(31):19947-52.

170. Cragg MS, Jansen ES, Cook M, Harris C, Strasser A, Scott CL. Treatment of B-RAF mutant human tumor cells with a MEK inhibitor requires bim and is enhanced by a BH3 mimetic. J Clin Invest. 2008 Nov;118(11):3651-9.

171. Meng J, Fang B, Liao Y, Chresta CM, Smith PD, Roth JA. Apoptosis induction by MEK inhibition in human lung cancer cells is mediated by bim. PLoS One. 2010 Sep 27;5(9):e13026.

172. Pumiglia KM, Decker SJ. Cell cycle arrest mediated by the MEK/mitogen-activated protein kinase pathway. Proc Natl Acad Sci U S A. 1997 Jan 21;94(2):448-52.

173. Chandarlapaty S. Negative feedback and adaptive resistance to the targeted therapy of cancer. Cancer Discov. 2012 Apr;2(4):311-9.

174. Emery CM, Vijayendran KG, Zipser MC, Sawyer AM, Niu L, Kim JJ, et al. MEK1 mutations confer resistance to MEK and B-RAF inhibition. Proc Natl Acad Sci U S A. 2009 Dec 1;106(48):20411-6.

175. Little AS, Smith PD, Cook SJ. Mechanisms of acquired resistance to ERK1/2 pathway inhibitors. Oncogene. 2012 May 7.

176. Wang D, Boerner SA, Winkler JD, LoRusso PM. Clinical experience of MEK inhibitors in cancer therapy. Biochim Biophys Acta. 2007 Aug;1773(8):1248-55.

177. Tolwinski NS, Shapiro PS, Goueli S, Ahn NG. Nuclear localization of mitogen-activated protein kinase kinase 1 (MKK1) is promoted by serum stimulation and G2-M progression. requirement for phosphorylation at the activation lip and signaling downstream of MKK. J Biol Chem. 1999 Mar 5;274(10):6168-74.

178. Jaaro H, Rubinfeld H, Hanoch T, Seger R. Nuclear translocation of mitogen-activated protein kinase kinase (MEK1) in response to mitogenic stimulation. Proc Natl Acad Sci U S A. 1997 Apr 15;94(8):3742-7.

179. Slack-Davis JK, Eblen ST, Zecevic M, Boerner SA, Tarcsafalvi A, Diaz HB, et al. PAK1 phosphorylation of MEK1 regulates fibronectin-stimulated MAPK activation. J Cell Biol. 2003 Jul 21;162(2):281-9.

180. Aplin AE, Stewart SA, Assoian RK, Juliano RL. Integrin-mediated adhesion regulates ERK nuclear translocation and phosphorylation of elk-1. J Cell Biol. 2001 Apr 16;153(2):273-82.

181. Mitsushima M, Suwa A, Amachi T, Ueda K, Kioka N. Extracellular signal-regulated kinase activated by epidermal growth factor and cell adhesion interacts with and phosphorylates vinexin. J Biol Chem. 2004 Aug 13;279(33):34570-7.

182. Simard JR, Grutter C, Pawar V, Aust B, Wolf A, Rabiller M, et al. High-throughput screening to identify inhibitors which stabilize inactive kinase conformations in p38alpha. J Am Chem Soc. 2009 Dec 30;131(51):18478-8.

183. Simard JR, Getlik M, Grutter C, Pawar V, Wulfert S, Rabiller M, et al. Development of a fluorescent-tagged kinase assay system for the detection and characterization of allosteric kinase inhibitors. J Am Chem Soc. 2009 Sep 23;131(37):13286-9.

184. Fischmann TO, Smith CK, Mayhood TW, Myers JE, Reichert P, Mannarino A, et al. Crystal structures of MEK1 binary and ternary complexes with nucleotides and inhibitors. Biochemistry. 2009 Mar 31;48(12):2661-74.

185. Ohren JF, Chen H, Pavlovsky A, Whitehead C, Zhang E, Kuffa P, et al. Structures of human MAP kinase kinase 1 (MEK1) and MEK2 describe novel noncompetitive kinase inhibition. Nat Struct Mol Biol. 2004 Dec;11(12):1192-7.

186. Matsumoto T, Kinoshita T, Matsuzaka H, Nakai R, Kirii Y, Yokota K, et al. Crystal structure of non-phosphorylated MAP2K6 in a putative auto-inhibition state. J Biochem. 2012 May;151(5):541-9.

187. Matsumoto T, Kinoshita T, Kirii Y, Yokota K, Hamada K, Tada T. Crystal structures of MKK4 kinase domain reveal that substrate peptide binds to an allosteric site and induces an auto-inhibition state. Biochem Biophys Res Commun. 2010 Sep 24;400(3):369-73.

188. Brennan DF, Dar AC, Hertz NT, Chao WC, Burlingame AL, Shokat KM, et al. A raf-induced allosteric transition of KSR stimulates phosphorylation of MEK. Nature. 2011 Apr 21;472(7343):366-9.

189. Catalanotti F, Reyes G, Jesenberger V, Galabova-Kovacs G, de Matos Simoes R, Carugo O, et al. A Mek1-Mek2 heterodimer determines the strength and duration of the erk signal. Nat Struct Mol Biol. 2009 Mar;16(3):294-303.

190. Huang W, Kessler DS, Erikson RL. Biochemical and biological analysis of Mek1 phosphorylation site mutants. Mol Biol Cell. 1995 Mar;6(3):237-45.

191. Park ER, Eblen ST, Catling AD. MEK1 activation by PAK: A novel mechanism. Cell Signal. 2007 Jul;19(7):1488-96.

192. Sharma P, Veeranna, Sharma M, Amin ND, Sihag RK, Grant P, et al. Phosphorylation of MEK1 by cdk5/p35 down-regulates the mitogen-activated protein kinase pathway. J Biol Chem. 2002 Jan 4;277(1):528-34.

193. Zheng YL, Li BS, Kanungo J, Kesavapany S, Amin N, Grant P, et al. Cdk5 modulation of mitogen-activated protein kinase signaling regulates neuronal survival. Mol Biol Cell. 2007 Feb;18(2):404-13.

194. Skarpen E, Flinder LI, Rosseland CM, Orstavik S, Wierod L, Oksvold MP, et al. MEK1 and MEK2 regulate distinct functions by sorting ERK2 to different intracellular compartments. FASEB J. 2008 Feb;22(2):466-7.

195. Burack WR, Shaw AS. Live cell imaging of ERK and MEK: Simple binding equilibrium explains the regulated nucleocytoplasmic distribution of ERK. J Biol Chem. 2005 Feb 4;280(5):3832-7.

196. Zheng CF, Guan KL. Cytoplasmic localization of the mitogen-activated protein kinase activator MEK. J Biol Chem. 1994 Aug 5;269(31):19947-52.

197. Jaaro H, Rubinfeld H, Hanoch T, Seger R. Nuclear translocation of mitogen-activated protein kinase kinase (MEK1) in response to mitogenic stimulation. Proc Natl Acad Sci U S A. 1997 Apr 15;94(8):3742-7.

198. Tolwinski NS, Shapiro PS, Goueli S, Ahn NG. Nuclear localization of mitogen-activated protein kinase kinase 1 (MKK1) is promoted by serum stimulation and G2-M progression. requirement for phosphorylation at the activation lip and signaling downstream of MKK. J Biol Chem. 1999 Mar 5;274(10):6168-74.

199. Pullikuth AK, Catling AD. Scaffold mediated regulation of MAPK signaling and cytoskeletal dynamics: A perspective. Cell Signal. 2007 Aug;19(8):1621-32.

200. Jacobs D, Glossip D, Xing H, Muslin AJ, Kornfeld K. Multiple docking sites on substrate proteins form a modular system that mediates recognition by ERK MAP kinase. Genes Dev. 1999 Jan 15;13(2):163-75.

201. Kolch W. Coordinating ERK/MAPK signalling through scaffolds and inhibitors. Nat Rev Mol Cell Biol. 2005 Nov;6(11):827-3.

202. Morrison DK, Davis RJ. Regulation of MAP kinase signaling modules by scaffold proteins in mammals. Annu Rev Cell Dev Biol. 2003;19:91-118.

203. Roskoski R,Jr. ERK1/2 MAP kinases: Structure, function, and regulation. Pharmacol Res. 2012 Aug;66(2):105-43.

204. Sacks DB. The role of scaffold proteins in MEK/ERK signalling. Biochem Soc Trans. 2006 Nov;34(Pt 5):833-6.

205. Bhattacharyya RP, Remenyi A, Good MC, Bashor CJ, Falick AM, Lim WA. The Ste5 scaffold allosterically modulates signaling output of the yeast mating pathway. Science. 2006 Feb 10;311(5762):822-6.

206. Dhanasekaran DN, Kashef K, Lee CM, Xu H, Reddy EP. Scaffold proteins of MAP-kinase modules. Oncogene. 2007 May 14;26(22):3185-202.

207. Good MC, Zalatan JG, Lim WA. Scaffold proteins: Hubs for controlling the flow of cellular information. Science. 2011 May 6;332(6030):680-6.

208. Zeke A, Lukacs M, Lim WA, Remenyi A. Scaffolds: Interaction platforms for cellular signalling circuits. Trends Cell Biol. 2009 Aug;19(8):364-7.

209. Wu WS, Wu JR, Hu CT. Signal cross talks for sustained MAPK activation and cell migration: The potential role of reactive oxygen species. Cancer Metastasis Rev. 2008 Jun;27(2):303-14.

210. Harrison RE, Sikorski BA, Jongstra J. Leukocyte-specific protein 1 targets the ERK/MAP kinase scaffold protein KSR and MEK1 and ERK2 to the actin cytoskeleton. J Cell Sci. 2004 Apr 15;117(Pt 10):2151-7.

211. Ritt DA, Daar IO, Morrison DK. KSR regulation of the raf-MEK-ERK cascade. Methods Enzymol. 2006;407:224-37.

212. Kurzbauer R, Teis D, de Araujo ME, Maurer-Stroh S, Eisenhaber F, Bourenkov GP, et al. Crystal structure of the p14/MP1 scaffolding complex: How a twin couple attaches mitogen-activated protein kinase signaling to late endosomes. Proc Natl Acad Sci U S A. 2004 Jul 27;101(30):10984-9.

213. Pullikuth A, McKinnon E, Schaeffer HJ, Catling AD. The MEK1 scaffolding protein MP1 regulates cell spreading by integrating PAK1 and rho signals. Mol Cell Biol. 2005 Jun;25(12):5119-33.

214. Schaeffer HJ, Catling AD, Eblen ST, Collier LS, Krauss A, Weber MJ. MP1: A MEK binding partner that enhances enzymatic activation of the MAP kinase cascade. Science. 1998 Sep 11;281(5383):1668-71.

215. Sharma C, Vomastek T, Tarcsafalvi A, Catling AD, Schaeffer HJ, Eblen ST, et al. MEK partner 1 (MP1): Regulation of oligomerization in MAP kinase signaling. J Cell Biochem. 2005 Mar 1;94(4):708-19.

216. Duhamel S, Hebert J, Gaboury L, Bouchard A, Simon R, Sauter G, et al. Sef downregulation by ras causes MEK1/2 to become aberrantly nuclear localized leading to polyploidy and neoplastic transformation. Cancer Res. 2012 Feb 1;72(3):626-35.

217. Furthauer M, Lin W, Ang SL, Thisse B, Thisse C. Sef is a feedback-induced antagonist of ras/MAPK-mediated FGF signalling. Nat Cell Biol. 2002 Feb;4(2):170-4.

218. Philips MR. Sef: A MEK/ERK catcher on the golgi. Mol Cell. 2004 Jul 23;15(2):168-9.

219. Vomastek T, Schaeffer HJ, Tarcsafalvi A, Smolkin ME, Bissonette EA, Weber MJ. Modular construction of a signaling scaffold: MORG1 interacts with components of the

ERK cascade and links ERK signaling to specific agonists. Proc Natl Acad Sci U S A. 2004 May 4;101(18):6981-6.

220. Callaway K, Abramczyk O, Martin L, Dalby KN. The anti-apoptotic protein PEA-15 is a tight binding inhibitor of ERK1 and ERK2, which blocks docking interactions at the D-recruitment site. Biochemistry. 2007 Aug 14;46(32):9187-98.

221. Callaway K, Rainey MA, Dalby KN. Quantifying ERK2-protein interactions by fluorescence anisotropy: PEA-15 inhibits ERK2 by blocking the binding of DEJL domains. Biochim Biophys Acta. 2005 Dec 30;1754(1-2):316-23.

222. Renganathan H, Vaidyanathan H, Knapinska A, Ramos JW. Phosphorylation of PEA-15 switches its binding specificity from ERK/MAPK to FADD. Biochem J. 2005 Sep 15;390(Pt 3):729-35.

223. Acharya U, Mallabiabarrena A, Acharya JK, Malhotra V. Signaling via mitogen-activated protein kinase kinase (MEK1) is required for golgi fragmentation during mitosis. Cell. 1998 Jan 23;92(2):183-92.

224. Zhang N, Cai W, Yin G, Nagel DJ, Berk BC. GIT1 is a novel MEK1-ERK1/2 scaffold that localizes to focal adhesions. Cell Biol Int. 2009 Dec 16;34(1):41-7.

225. Yin G, Haendeler J, Yan C, Berk BC. GIT1 functions as a scaffold for MEK1-extracellular signal-regulated kinase 1 and 2 activation by angiotensin II and epidermal growth factor. Mol Cell Biol. 2004 Jan;24(2):875-8.

226. Malarkannan S, Awasthi A, Rajasekaran K, Kumar P, Schuldt KM, Bartoszek A, et al. IQGAP1: A regulator of intracellular spacetime relativity. J Immunol. 2012 Mar 1;188(5):2057-63.

227. Roy M, Li Z, Sacks DB. IQGAP1 is a scaffold for mitogen-activated protein kinase signaling. Mol Cell Biol. 2005 Sep;25(18):7940-52.

228. Roy M, Li Z, Sacks DB. IQGAP1 binds ERK2 and modulates its activity. J Biol Chem. 2004 Apr 23;279(17):17329-37.

229. Awasthi A, Samarakoon A, Chu H, Kamalakannan R, Quilliam LA, Chrzanowska-Wodnicka M, et al. Rap1b facilitates NK cell functions via IQGAP1-mediated signalosomes. J Exp Med. 2010 Aug 30;207(9):1923-38.

230. White CD, Brown MD, Sacks DB. IQGAPs in cancer: A family of scaffold proteins underlying tumorigenesis. FEBS Lett. 2009 Jun 18;583(12):1817-24.

231. Boeckeler K, Rosse C, Howell M, Parker PJ. Manipulating signal delivery - plasma-membrane ERK activation in aPKC-dependent migration. J Cell Sci. 2010 Aug 15;123(Pt 16):2725-32.

232. Ku H, Meier KE. Phosphorylation of paxillin via the ERK mitogen-activated protein kinase cascade in EL4 thymoma cells. J Biol Chem. 2000 Apr 14;275(15):11333-40.

233. Ishibe S, Joly D, Liu ZX, Cantley LG. Paxillin serves as an ERK-regulated scaffold for coordinating FAK and rac activation in epithelial morphogenesis. Mol Cell. 2004 Oct 22;16(2):257-6.

234. Pribic J, Brazill D. Paxillin phosphorylation and complexing with erk and FAK are regulated by PLD activity in MDA-MB-231 cells. Cell Signal. 2012 Aug;24(8):1531-40.

235. Ge L, Ly Y, Hollenberg M, DeFea K. A beta-arrestin-dependent scaffold is associated with prolonged MAPK activation in pseudopodia during protease-activated receptor-2-induced chemotaxis. J Biol Chem. 2003 Sep 5;278(36):34418-26.

236. Luttrell LM, Roudabush FL, Choy EW, Miller WE, Field ME, Pierce KL, et al. Activation and targeting of extracellular signal-regulated kinases by beta-arrestin scaffolds. Proc Natl Acad Sci U S A. 2001 Feb 27;98(5):2449-54.

237. Min J, Defea K. Beta-arrestin-dependent actin reorganization: Bringing the right players together at the leading edge. Mol Pharmacol. 2011 Nov;80(5):760-8.

238. Liu ZX, Yu CF, Nickel C, Thomas S, Cantley LG. Hepatocyte growth factor induces ERK-dependent paxillin phosphorylation and regulates paxillin-focal adhesion kinase association. J Biol Chem. 2002 Mar 22;277(12):10452-8.

239. Segarra J, Balenci L, Drenth T, Maina F, Lamballe F. Combined signaling through ERK, PI3K/AKT, and RAC1/p38 is required for met-triggered cortical neuron migration. J Biol Chem. 2006 Feb 24;281(8):4771-8.

240. White A, Pargellis CA, Studts JM, Werneburg BG, Farmer BT,2nd. Molecular basis of MAPK-activated protein kinase 2:p38 assembly. Proc Natl Acad Sci U S A. 2007 Apr 10;104(15):6353-8.

241. ter Haar E, Prabhakar P, Liu X, Lepre C. Crystal structure of the p38 alpha-MAPKAP kinase 2 heterodimer. J Biol Chem. 2007 Mar 30;282(13):9733-9.

242. Lukas SM, Kroe RR, Wildeson J, Peet GW, Frego L, Davidson W, et al. Catalysis and function of the p38 alpha.MK2a signaling complex. Biochemistry. 2004 Aug 10;43(31):9950-6.

243. Burkhard KA, Chen F, Shapiro P. Quantitative analysis of ERK2 interactions with substrate proteins: Roles for kinase docking domains and activity in determining binding affinity. J Biol Chem. 2011 Jan 28;286(4):2477-85.

244. Robinson FL, Whitehurst AW, Raman M, Cobb MH. Identification of novel point mutations in ERK2 that selectively disrupt binding to MEK1. J Biol Chem. 2002 Apr 26;277(17):14844-52.

245. Chang CI, Xu BE, Akella R, Cobb MH, Goldsmith EJ. Crystal structures of MAP kinase p38 complexed to the docking sites on its nuclear substrate MEF2A and activator MKK3b. Mol Cell. 2002 Jun;9(6):1241-9.

246. Remenyi A, Good MC, Bhattacharyya RP, Lim WA. The role of docking interactions in mediating signaling input, output, and discrimination in the yeast MAPK network. Mol Cell. 2005 Dec 22;20(6):951-62.

247. Liu S, Sun JP, Zhou B, Zhang ZY. Structural basis of docking interactions between ERK2 and MAP kinase phosphatase 3. Proc Natl Acad Sci U S A. 2006 Apr 4;103(14):5326-31.

248. Zhou T, Sun L, Humphreys J, Goldsmith EJ. Docking interactions induce exposure of activation loop in the MAP kinase ERK2. Structure. 2006 Jun;14(6):1011-9.

249. Ma W, Shang Y, Wei Z, Wen W, Wang W, Zhang M. Phosphorylation of DCC by ERK2 is facilitated by direct docking of the receptor P1 domain to the kinase. Structure. 2010 Nov 10;18(11):1502-11.

250. Kuzu G, Keskin O, Gursoy A, Nussinov R. Constructing structural networks of signaling pathways on the proteome scale. Curr Opin Struct Biol. 2012 Jun;22(3):367-7.

251. Xu B, Wilsbacher JL, Collisson T, Cobb MH. The N-terminal ERK-binding site of MEK1 is required for efficient feedback phosphorylation by ERK2 in vitro and ERK activation in vivo. J Biol Chem. 1999 Nov 26;274(48):34029-35.

252. Biondi RM, Nebreda AR. Signalling specificity of ser/thr protein kinases through docking-site-mediated interactions. Biochem J. 2003 May 15;372(Pt 1):1-13.

253. Dimitri CA, Dowdle W, MacKeigan JP, Blenis J, Murphy LO. Spatially separate docking sites on ERK2 regulate distinct signaling events in vivo. Curr Biol. 2005 Jul 26;15(14):1319-24.

254. Legewie S, Schoeberl B, Bluthgen N, Herzel H. Competing docking interactions can bring about bistability in the MAPK cascade. Biophys J. 2007 Oct 1;93(7):2279-88.

255. Remenyi A, Good MC, Bhattacharyya RP, Lim WA. The role of docking interactions in mediating signaling input, output, and discrimination in the yeast MAPK network. Mol Cell. 2005 Dec 22;20(6):951-62.

256. Sharrocks AD, Yang SH, Galanis A. Docking domains and substrate-specificity determination for MAP kinases. Trends Biochem Sci. 2000 Sep;25(9):448-53.

257. Burack WR, Sturgill TW. The activating dual phosphorylation of MAPK by MEK is nonprocessive. Biochemistry. 1997 May 20;36(20):5929-33.

258. Aoki K, Yamada M, Kunida K, Yasuda S, Matsuda M. Processive phosphorylation of ERK MAP kinase in mammalian cells. Proc Natl Acad Sci U S A. 2011 Aug 2;108(31):12675-80.

259. Bardwell AJ, Abdollahi M, Bardwell L. Docking sites on mitogen-activated protein kinase (MAPK) kinases, MAPK phosphatases and the elk-1 transcription factor compete for MAPK binding and are crucial for enzymic activity. Biochem J. 2003 Mar 15;370(Pt 3):1077-85.

260. Boutros T, Chevet E, Metrakos P. Mitogen-activated protein (MAP) kinase/MAP kinase phosphatase regulation: Roles in cell growth, death, and cancer. Pharmacol Rev. 2008 Sep;60(3):261-310.

261. Camps M, Nichols A, Gillieron C, Antonsson B, Muda M, Chabert C, et al. Catalytic activation of the phosphatase MKP-3 by ERK2 mitogen-activated protein kinase. Science. 1998 May 22;280(5367):1262-5.

262. Caunt CJ, Armstrong SP, Rivers CA, Norman MR, McArdle CA. Spatiotemporal regulation of ERK2 by dual specificity phosphatases. J Biol Chem. 2008 Sep 26;283(39):26612-23.

263. Caunt CJ, Rivers CA, Conway-Campbell BL, Norman MR, McArdle CA. Epidermal growth factor receptor and protein kinase C signaling to ERK2: Spatiotemporal regulation of ERK2 by dual specificity phosphatases. J Biol Chem. 2008 Mar 7;283(10):6241-52.

264. Huang CY, Tan TH. DUSPs, to MAP kinases and beyond. Cell Biosci. 2012 Jul 9;2(1):24.

265. Junttila MR, Li SP, Westermarck J. Phosphatase-mediated crosstalk between MAPK signaling pathways in the regulation of cell survival. FASEB J. 2008 Apr;22(4):954-65.

266. Tamura Y, Simizu S, Osada H. The phosphorylation status and anti-apoptotic activity of bcl-2 are regulated by ERK and protein phosphatase 2A on the mitochondria. FEBS Lett. 2004 Jul 2;569(1-3):249-55.

267. Mustelin T, Tautz L, Page R. Structure of the hematopoietic tyrosine phosphatase (HePTP) catalytic domain: Structure of a KIM phosphatase with phosphate bound at the active site. J Mol Biol. 2005 Nov 18;354(1):150-63.

268. Murphy LO, Blenis J. MAPK signal specificity: The right place at the right time. Trends Biochem Sci. 2006 May;31(5):268-75.

269. Ramos JW. The regulation of extracellular signal-regulated kinase (ERK) in mammalian cells. Int J Biochem Cell Biol. 2008;40(12):2707-19.

270. Caunt CJ, Finch AR, Sedgley KR, McArdle CA. Seven-transmembrane receptor signalling and ERK compartmentalization. Trends Endocrinol Metab. 2006 Sep;17(7):276-83.

271. Aplin AE, Hogan BP, Tomeu J, Juliano RL. Cell adhesion differentially regulates the nucleocytoplasmic distribution of active MAP kinases. J Cell Sci. 2002 Jul 1;115(Pt 13):2781-90.

272. Mor A, Philips MR. Compartmentalized ras/MAPK signaling. Annu Rev Immunol. 2006;24:771-800.

273. Goldsmith EJ, Akella R, Min X, Zhou T, Humphreys JM. Substrate and docking interactions in serine/threonine protein kinases. Chem Rev. 2007 Nov;107(11):5065-81.

274. Gonzalez FA, Raden DL, Davis RJ. Identification of substrate recognition determinants for human ERK1 and ERK2 protein kinases. J Biol Chem. 1991 Nov 25;266(33):22159-63.

275. Chuderland D, Konson A, Seger R. Identification and characterization of a general nuclear translocation signal in signaling proteins. Mol Cell. 2008 Sep 26;31(6):850-61.

276. Costa M, Marchi M, Cardarelli F, Roy A, Beltram F, Maffei L, et al. Dynamic regulation of ERK2 nuclear translocation and mobility in living cells. J Cell Sci. 2006 Dec 1;119(Pt 23):4952-63.

277. Fukuda M, Gotoh Y, Nishida E. Interaction of MAP kinase with MAP kinase kinase: Its possible role in the control of nucleocytoplasmic transport of MAP kinase. EMBO J. 1997 Apr 15;16(8):1901-8.

278. Gu Z, Kordowska J, Williams GL, Wang CL, Hai CM. Erk1/2 MAPK and caldesmon differentially regulate podosome dynamics in A7r5 vascular smooth muscle cells. Exp Cell Res. 2007 Mar 10;313(5):849-66.

279. Khokhlatchev AV, Canagarajah B, Wilsbacher J, Robinson M, Atkinson M, Goldsmith E, et al. Phosphorylation of the MAP kinase ERK2 promotes its homodimerization and nuclear translocation. Cell. 1998 May 15;93(4):605-1.

280. Shibayama S, Shibata-Seita R, Miura K, Kirino Y, Takishima K. Identification of a C-terminal region that is required for the nuclear translocation of ERK2 by passive diffusion. J Biol Chem. 2002 Oct 4;277(40):37777-82.

281. Tanimura S, Nomura K, Ozaki K, Tsujimoto M, Kondo T, Kohno M. Prolonged nuclear retention of activated extracellular signal-regulated kinase 1/2 is required for

hepatocyte growth factor-induced cell motility. J Biol Chem. 2002 Aug 2;277(31):28256-64.

282. Abramczyk O, Rainey MA, Barnes R, Martin L, Dalby KN. Expanding the repertoire of an ERK2 recruitment site: Cysteine footprinting identifies the D-recruitment site as a mediator of ets-1 binding. Biochemistry. 2007 Aug 14;46(32):9174-86.

283. Babu GJ, Lalli MJ, Sussman MA, Sadoshima J, Periasamy M. Phosphorylation of elk-1 by MEK/ERK pathway is necessary for c-fos gene activation during cardiac myocyte hypertrophy. J Mol Cell Cardiol. 2000 Aug;32(8):1447-5.

284. Cruzalegui FH, Cano E, Treisman R. ERK activation induces phosphorylation of elk-1 at multiple S/T-P motifs to high stoichiometry. Oncogene. 1999 Dec 23;18(56):7948-57.

285. Davis S, Vanhoutte P, Pages C, Caboche J, Laroche S. The MAPK/ERK cascade targets both elk-1 and cAMP response element-binding protein to control long-term potentiation-dependent gene expression in the dentate gyrus in vivo. J Neurosci. 2000 Jun 15;20(12):4563-72.

286. Hauge C, Frodin M. RSK and MSK in MAP kinase signalling. J Cell Sci. 2006 Aug 1;119(Pt 15):3021-3.

287. McCoy CE, Campbell DG, Deak M, Bloomberg GB, Arthur JS. MSK1 activity is controlled by multiple phosphorylation sites. Biochem J. 2005 Apr 15;387(Pt 2):507-1.

288. Zhang HM, Li L, Papadopoulou N, Hodgson G, Evans E, Galbraith M, et al. Mitogen-induced recruitment of ERK and MSK to SRE promoter complexes by ternary complex factor elk-1. Nucleic Acids Res. 2008 May;36(8):2594-607.

289. Marampon F, Ciccarelli C, Zani BM. Down-regulation of c-myc following MEK/ERK inhibition halts the expression of malignant phenotype in rhabdomyosarcoma and in non muscle-derived human tumors. Mol Cancer. 2006 Aug 9;5:31.

290. Serra JM, Gutierrez A, Alemany R, Navarro M, Ros T, Saus C, et al. Inhibition of c-myc down-regulation by sustained extracellular signal-regulated kinase activation prevents the antimetabolite methotrexate- and gemcitabine-induced differentiation in non-small-cell lung cancer cells. Mol Pharmacol. 2008 Jun;73(6):1679-87.

291. Shi Y, Frost P, Hoang B, Yang Y, Fukunaga R, Gera J, et al. MNK kinases facilitate c-myc IRES activity in rapamycin-treated multiple myeloma cells. Oncogene. 2012 Feb 27.

292. Athineos D, Marshall L, White RJ. Regulation of TFIIIB during F9 cell differentiation. BMC Mol Biol. 2010 Mar 12;11:21.

293. Felton-Edkins ZA, Fairley JA, Graham EL, Johnston IM, White RJ, Scott PH. The mitogen-activated protein (MAP) kinase ERK induces tRNA synthesis by phosphorylating TFIIIB. EMBO J. 2003 May 15;22(10):2422-3.

294. Huang H, Petkova SB, Cohen AW, Bouzahzah B, Chan J, Zhou JN, et al. Activation of transcription factors AP-1 and NF-kappa B in murine chagasic myocarditis. Infect Immun. 2003 May;71(5):2859-67.

295. Chalmers CJ, Gilley R, March HN, Balmanno K, Cook SJ. The duration of ERK1/2 activity determines the activation of c-fos and fra-1 and the composition and quantitative transcriptional output of AP-1. Cell Signal. 2007 Apr;19(4):695-704.

296. Monje P, Marinissen MJ, Gutkind JS. Phosphorylation of the carboxyl-terminal transactivation domain of c-fos by extracellular signal-regulated kinase mediates the transcriptional activation of AP-1 and cellular transformation induced by platelet-derived growth factor. Mol Cell Biol. 2003 Oct;23(19):7030-43.

297. Vial E, Marshall CJ. Elevated ERK-MAP kinase activity protects the FOS family member FRA-1 against proteasomal degradation in colon carcinoma cells. J Cell Sci. 2003 Dec 15;116(Pt 24):4957-63.

298. Liu Y, Yang Y, Ye YC, Shi QF, Chai K, Tashiro S, et al. Activation of ERK-p53 and ERK-mediated phosphorylation of bcl-2 are involved in autophagic cell death induced by the c-met inhibitor SU11274 in human lung cancer A549 cells. J Pharmacol Sci. 2012;118(4):423-32.

299. Dong C, Waters SB, Holt KH, Pessin JE. SOS phosphorylation and disassociation of the Grb2-SOS complex by the ERK and JNK signaling pathways. J Biol Chem. 1996 Mar 15;271(11):6328-32.

300. Zhang M, Liu J, Cheng A, Deyoung SM, Chen X, Dold LH, et al. CAP interacts with cytoskeletal proteins and regulates adhesion-mediated ERK activation and motility. EMBO J. 2006 Nov 15;25(22):5284-93.

301. Nguyen DH, Catling AD, Webb DJ, Sankovic M, Walker LA, Somlyo AV, et al. Myosin light chain kinase functions downstream of ras/ERK to promote migration of urokinase-type plasminogen activator-stimulated cells in an integrin-selective manner. J Cell Biol. 1999 Jul 12;146(1):149-64.

302. Zhou X, Liu Y, You J, Zhang H, Zhang X, Ye L. Myosin light-chain kinase contributes to the proliferation and migration of breast cancer cells through cross-talk with activated ERK1/2. Cancer Lett. 2008 Nov 8;270(2):312-27.

303. De Cesare D, Jacquot S, Hanauer A, Sassone-Corsi P. Rsk-2 activity is necessary for epidermal growth factor-induced phosphorylation of CREB protein and transcription of c-fos gene. Proc Natl Acad Sci U S A. 1998 Oct 13;95(21):12202-7.

304. Wang Y, Prywes R. Activation of the c-fos enhancer by the erk MAP kinase pathway through two sequence elements: The c-fos AP-1 and p62TCF sites. Oncogene. 2000 Mar 9;19(11):1379-85.

305. Cargnello M, Roux PP. Activation and function of the MAPKs and their substrates, the MAPK-activated protein kinases. Microbiol Mol Biol Rev. 2011 Mar;75(1):50-83.

306. Wang X, Flynn A, Waskiewicz AJ, Webb BL, Vries RG, Baines IA, et al. The phosphorylation of eukaryotic initiation factor eIF4E in response to phorbol esters, cell stresses, and cytokines is mediated by distinct MAP kinase pathways. J Biol Chem. 1998 Apr 17;273(16):9373-7.

307. Hay N. Mnk earmarks eIF4E for cancer therapy. Proc Natl Acad Sci U S A. 2010 Aug 10;107(32):13975-6.

308. Walsh D, Mohr I. Phosphorylation of eIF4E by mnk-1 enhances HSV-1 translation and replication in quiescent cells. Genes Dev. 2004 Mar 15;18(6):660-72.

309. Waskiewicz AJ, Flynn A, Proud CG, Cooper JA. Mitogen-activated protein kinases activate the serine/threonine kinases Mnk1 and Mnk2. EMBO J. 1997 Apr 15;16(8):1909-20.

310. Gaestel M. Specificity of signaling from MAPKs to MAPKAPKs: Kinases' tango nuevo. Front Biosci. 2008 May 1;13:6050-9.

311. Tanimura S, Nomura K, Ozaki K, Tsujimoto M, Kondo T, Kohno M. Prolonged nuclear retention of activated extracellular signal-regulated kinase 1/2 is required for hepatocyte growth factor-induced cell motility. J Biol Chem. 2002 Aug 2;277(31):28256-64.

312. Komatsu N, Aoki K, Yamada M, Yukinaga H, Fujita Y, Kamioka Y, et al. Development of an optimized backbone of FRET biosensors for kinases and GTPases. Mol Biol Cell. 2011 Dec;22(23):4647-56.

313. Eblen ST, Slack-Davis JK, Tarcsafalvi A, Parsons JT, Weber MJ, Catling AD. Mitogen-activated protein kinase feedback phosphorylation regulates MEK1 complex formation and activation during cellular adhesion. Mol Cell Biol. 2004 Mar;24(6):2308-17.

314. Han WG, Liu T, Himo F, Toutchkine A, Bashford D, Hahn KM, et al. A theoretical study of the UV/visible absorption and emission solvatochromic properties of solvent-sensitive dyes. Chemphyschem. 2003 Oct 17;4(10):1084-9.

315. Carter CW,Jr, LeFebvre BC, Cammer SA, Tropsha A, Edgell MH. Four-body potentials reveal protein-specific correlations to stability changes caused by hydrophobic core mutations. J Mol Biol. 2001 Aug 24;311(4):625-38.

316. Sherman DB, Zhang S, Pitner JB, Tropsha A. Evaluation of the relative stability of liganded versus ligand-free protein conformations using simplicial neighborhood analysis of protein packing (SNAPP) method. Proteins. 2004 Sep 1;56(4):828-3.

317. Tropsha A, Carter CW,Jr, Cammer S, Vaisman II. Simplicial neighborhood analysis of protein packing (SNAPP): A computational geometry approach to studying proteins. Methods Enzymol. 2003;374:509-44.

318. Zhang S, Kaplan AH, Tropsha A. HIV-1 protease function and structure studies with the simplicial neighborhood analysis of protein packing method. Proteins. 2008 Nov 15;73(3):742-53.

319. Cobb MH, Goldsmith EJ. Dimerization in MAP-kinase signaling. Trends Biochem Sci. 2000 Jan;25(1):7-9.

320. Wilsbacher JL, Juang YC, Khokhlatchev AV, Gallagher E, Binns D, Goldsmith EJ, et al. Characterization of mitogen-activated protein kinase (MAPK) dimers. Biochemistry. 2006 Nov 7;45(44):13175-82.

321. Emrick MA, Hoofnagle AN, Miller AS, Ten Eyck LF, Ahn NG. Constitutive activation of extracellular signal-regulated kinase 2 by synergistic point mutations. J Biol Chem. 2001 Dec 7;276(49):46469-7.

322. Zhou B, Zhang J, Liu S, Reddy S, Wang F, Zhang ZY. Mapping ERK2-MKP3 binding interfaces by hydrogen/deuterium exchange mass spectrometry. J Biol Chem. 2006 Dec 15;281(50):38834-4.

323. Emrick MA, Lee T, Starkey PJ, Mumby MC, Resing KA, Ahn NG. The gatekeeper residue controls autoactivation of ERK2 via a pathway of intramolecular connectivity. Proc Natl Acad Sci U S A. 2006 Nov 28;103(48):18101-6.

324. Levin-Salomon V, Kogan K, Ahn NG, Livnah O, Engelberg D. Isolation of intrinsically active (MEK-independent) variants of the ERK family of mitogen-activated protein (MAP) kinases. J Biol Chem. 2008 Dec 12;283(50):34500-1.

325. Zhou T, Sun L, Humphreys J, Goldsmith EJ. Docking interactions induce exposure of activation loop in the MAP kinase ERK2. Structure. 2006 Jun;14(6):1011-9.

326. Tarrega C, Rios P, Cejudo-Marin R, Blanco-Aparicio C, van den Berk L, Schepens J, et al. ERK2 shows a restrictive and locally selective mechanism of recognition by its tyrosine phosphatase inactivators not shared by its activator MEK1. J Biol Chem. 2005 Nov 11;280(45):37885-94.

327. Yazicioglu MN, Goad DL, Ranganathan A, Whitehurst AW, Goldsmith EJ, Cobb MH. Mutations in ERK2 binding sites affect nuclear entry. J Biol Chem. 2007 Sep 28;282(39):28759-67.

328. Lee T, Hoofnagle AN, Kabuyama Y, Stroud J, Min X, Goldsmith EJ, et al. Docking motif interactions in MAP kinases revealed by hydrogen exchange mass spectrometry. Mol Cell. 2004 Apr 9;14(1):43-55.

329. Polychronopoulos S, Verykokakis M, Yazicioglu MN, Sakarellos-Daitsiotis M, Cobb MH, Mavrothalassitis G. The transcriptional ETS2 repressor factor associates with active and inactive erks through distinct FXF motifs. J Biol Chem. 2006 Sep 1;281(35):25601-1.

330. Delaney AM, Printen JA, Chen H, Fauman EB, Dudley DT. Identification of a novel mitogen-activated protein kinase kinase activation domain recognized by the inhibitor PD 184352. Mol Cell Biol. 2002 Nov;22(21):7593-602.

331. Whitehurst AW, Robinson FL, Moore MS, Cobb MH. The death effector domain protein PEA-15 prevents nuclear entry of ERK2 by inhibiting required interactions. J Biol Chem. 2004 Mar 26;279(13):12840-7.

332. Mahalingam M, Arvind R, Ida H, Murugan AK, Yamaguchi M, Tsuchida N. ERK2 CD domain mutation from a human cancer cell line enhanced anchorage-independent cell growth and abnormality in drosophila. Oncol Rep. 2008 Oct;20(4):957-62.

333. Robbins DJ, Zhen E, Cheng M, Xu S, Vanderbilt CA, Ebert D, et al. Regulation and properties of extracellular signal-regulated protein kinases 1, 2, and 3. J Am Soc Nephrol. 1993 Nov;4(5):1104-10.

334. Bhattacharyya RP, Remenyi A, Good MC, Bashor CJ, Falick AM, Lim WA. The Ste5 scaffold allosterically modulates signaling output of the yeast mating pathway. Science. 2006 Feb 10;311(5762):822-6.

335. Wortzel I, Seger R. The ERK cascade: Distinct functions within various subcellular organelles. Genes Cancer. 2011 Mar;2(3):195-209.

336. Barrett LE, Van Bockstaele EJ, Sul JY, Takano H, Haydon PG, Eberwine JH. Elk-1 associates with the mitochondrial permeability transition pore complex in neurons. Proc Natl Acad Sci U S A. 2006 Mar 28;103(13):5155-60.

337. Besnard A, Galan-Rodriguez B, Vanhoutte P, Caboche J. Elk-1 a transcription factor with multiple facets in the brain. Front Neurosci. 2011 Mar 16;5:35.

338. Fukuda M, Gotoh I, Gotoh Y, Nishida E. Cytoplasmic localization of mitogen-activated protein kinase kinase directed by its NH2-terminal, leucine-rich short amino acid sequence, which acts as a nuclear export signal. J Biol Chem. 1996 Aug 16;271(33):20024-8.

339. Wolf I, Rubinfeld H, Yoon S, Marmor G, Hanoch T, Seger R. Involvement of the activation loop of ERK in the detachment from cytosolic anchoring. J Biol Chem. 2001 Jul 6;276(27):24490-7.

340. Ray RM, Vaidya RJ, Johnson LR. MEK/ERK regulates adherens junctions and migration through Rac1. Cell Motil Cytoskeleton. 2007 Mar;64(3):143-56.

341. Smith SD, Jaffer ZM, Chernoff J, Ridley AJ. PAK1-mediated activation of ERK1/2 regulates lamellipodial dynamics. J Cell Sci. 2008 Nov 15;121(Pt 22):3729-36.

342. Viala E, Pouyssegur J. Regulation of tumor cell motility by ERK mitogen-activated protein kinases. Ann N Y Acad Sci. 2004 Dec;1030:208-1.

343. Yin S, Ding F, Dokholyan NV. Modeling backbone flexibility improves protein stability estimation. Structure. 2007 Dec;15(12):1567-76.

344. Yin S, Ding F, Dokholyan NV. Eris: An automated estimator of protein stability. Nat Methods. 2007 Jun;4(6):466-7.

345. ter Haar E, Prabhakar P, Liu X, Lepre C. Crystal structure of the p38 alpha-MAPKAP kinase 2 heterodimer. J Biol Chem. 2007 Mar 30;282(13):9733-9.

346. Amstutz P, Koch H, Binz HK, Deuber SA, Pluckthun A. Rapid selection of specific MAP kinase-binders from designed ankyrin repeat protein libraries. Protein Eng Des Sel. 2006 May;19(5):219-2.

347. Kummer L, Parizek P, Rube P, Millgramm B, Prinz A, Mittl PR, et al. Structural and functional analysis of phosphorylation-specific binders of the kinase ERK from designed ankyrin repeat protein libraries. Proc Natl Acad Sci U S A. 2012 Aug 21;109(34):E2248-57.

348. Wang Z, Zhang B, Wang M, Carr BI. Persistent ERK phosphorylation negatively regulates cAMP response element-binding protein (CREB) activity via recruitment of CREB-binding protein to pp90RSK. J Biol Chem. 2003 Mar 28;278(13):11138-44.

349. Mendoza MC, Er EE, Blenis J. ERK-MAP kinase signaling in the cytoplasm. Methods Mol Biol. 2010;661:185-203.

350. Yoon S, Seger R. The extracellular signal-regulated kinase: Multiple substrates regulate diverse cellular functions. Growth Factors. 2006 Mar;24(1):21-44.

351. Legewie S, Schoeberl B, Bluthgen N, Herzel H. Competing docking interactions can bring about bistability in the MAPK cascade. Biophys J. 2007 Oct 1;93(7):2279-88.

352. Shin SY, Rath O, Choo SM, Fee F, McFerran B, Kolch W, et al. Positive- and negative-feedback regulations coordinate the dynamic behavior of the ras-raf-MEK-ERK signal transduction pathway. J Cell Sci. 2009 Feb 1;122(Pt 3):425-3.

353. Mendoza MC, Er EE, Zhang W, Ballif BA, Elliott HL, Danuser G, et al. ERK-MAPK drives lamellipodia protrusion by activating the WAVE2 regulatory complex. Mol Cell. 2011 Mar 18;41(6):661-7.

354. Worth CL, Preissner R, Blundell TL. SDM--a server for predicting effects of mutations on protein stability and malfunction. Nucleic Acids Res. 2011 Jul;39(Web Server issue):W215-22.